FROM QUARKS TO COLD ATOMS: THE PHASES OF STRONGLY-INTERACTING SYSTEMS

BY

PHILIP D. POWELL

DISSERTATION

Submitted in partial fulfillment of the requirements
for the degree of Doctor of Philosophy in Physics
in the Graduate College of the
University of Illinois at Urbana-Champaign, 2013

Urbana, Illinois

Doctoral Committee:

Professor Eduardo Fradkin, Chair
Professor Gordon Baym, Director of Research
Professor Gregory MacDougall
Professor Matthias Grosse Perdekamp

Abstract

In this thesis we investigate the phase structure of dense quark matter, the structure and stability of neutron and quark stars, and the phases of ultracold fermions in the presence of an artificial spin-orbit coupling. While spanning an extraordinary twenty orders of magnitude in energy scales, these systems exhibit some remarkable similarities including non-perturbative many-body interactions, perfect fluid behavior, the formation of Cooper pairs, and the possibility of BCS-BEC crossovers between weakly and strongly interacting regimes. Moreover, due to phenomenal advancements in laser cooling techniques and the ability to exert an unprecedented level of control over the interactions of ultracold atomic gases, the possibility of using these systems to simulate the complex behavior of systems not easily realized in the laboratory (e.g., non-Abelian gauge fields, quantum chromodynamics) is becoming increasingly real.

Despite the widespread success of quantum chromodynamics (QCD), the theory of the strong nuclear force, much remains unknown about the properties of strongly-interacting quark matter. In large part, this continued ignorance is a result of the mathematical intractability of QCD and the limitations of current numerical techniques to very low densities. In the first part of this thesis, in order to gain some insight into the phase structure of dense quark matter we therefore apply an effective field theory which is built upon the symmetries of QCD, the Polyakov–Nambu–Jona-Lasinio (PNJL) model. We construct the QCD phase diagram for two and three quark flavors, giving special attention to the effect of the intermediate strange quark mass on the preferred quark pairing structure at intermediate to high density. In addition, we investigate the impact of the strange quark mass and axial anomaly on a recently proposed low temperature critical point, which may allow for a smooth crossover between hadronic and color superconducting matter. Finally, we investigate the impact of a local color neutrality constraint on phases of asymmetric quark pairing.

While the Relativistic Heavy Ion Collider (RHIC) continues to probe the QCD phase diagram at ever-higher temperatures and researchers await the completion of the highly anticipated Facility for Antiprotons and Ion Research (FAIR), the only known "laboratories" in which low temperature dense quark matter is encountered are the cores of neutron stars. Fortunately, the structure of these astrophysical objects is highly dependent upon the properties of the dense matter in their cores, and observations of the mass-radius relationship of these stars impose constraints on the quark matter equation of state. In the second part of this thesis we investigate the possibility of realizing massive neutron stars, such as the recently

observed PSRs J1614-2230, J0348+0432, and J1311-3430 with $M = (1.97 \pm 0.04)M_\odot$, $M = (2.01 \pm 0.04)M_\odot$, and $M = (2.4 \pm 0.3)M_\odot$, respectively, by including a flavor-symmetric vector coupling within an NJL model description of quark matter. By extracting the quark matter equation of state we show that in the absence of diquark pairing, a reasonable magnitude vector repulsion can to stabilize neutron stars against gravitational collapse up to $M \approx 2.34M_\odot$. We also investigate the possibility of realizing stable quark stars with densities much higher than those obtained in conventional neutron stars, but find that stars with central densities $\rho_c \gg 10\rho_0$ are always unstable to gravitational collapse.

In the third part of this thesis we study the properties of ultracold atomic gases in the presence of artificial gauge fields. While neutral atoms do not naturally couple to the gauge fields in nature (e.g., magnetic fields, the strong nuclear force), recent advancements in laser techniques have led to the realization of *synthetic* gauge fields in which ultracold atoms behave as if they were charged. Combined with the Feshbach resonance, through which the two-body interactions which dominate these dilute gases can be arbitrarily tuned, these gases can be used to simulate a wide variety of systems, including those that occur naturally and those that do not. We study the phase structure of a two-species mixture of fermions in the presence of Rashba-Dresselhaus (RD) spin-orbit coupling, which is induced by a specific type of non-Abelian gauge field. In particular, we compute the dependence of the superfluid critical temperature on the RD coupling strength and the tunable two-body interaction. We also investigate the effects of the spin-orbit coupling on the crossover between weakly bound (BCS) atomic pairs and strongly bound (BEC) molecules and the effects of fluctuations on the stability of the superfluid phase.

To my father,

I changed my mind.

Acknowledgements

This thesis is the product of many years of work in which I have received the invaluable help and support of an immense number of people. First, I must thank my research advisor Gordon Baym for his endless guidance, insight, and patience. It has been said that life consists of things we know, things we know we don't know, and things we don't know we don't know [1]. As with many of life's most challenging tasks, throughout my time as a graduate student I have constantly discovered how much falls within the third category. Throughout these challenges, Gordon has unhesitatingly shared his wealth of knowledge and experience, through which I have learned far more than I could have conceived when I first set foot in Urbana seven years ago.

I must also thank my family for the endless love and support they have provided throughout my graduate career, and long before it. Long before I knew the word "physics," my father and mother personified for me the love of truth and its pursuit, of which this work is a part, however small. I am also grateful to my brother, James, for the wildly varying but always interesting conversations which we have shared, as well as for the programming expertise which has so often proved the linchpin of my work. Despite the fact that I have yet to convince him an electric field is real, he has not hesitated to help me in whatever I have asked, and for that I am thankful. To my sister, Beth, I am thankful for the persistent phone calls which inevitably interrupted the most crucial part of my calculation. We will never know how much more success I might have had if she had left me alone, but I am quite glad she did not.

I am also immensely grateful to my wife, Lila, and daughter, Clara, for their unconditional support and the joy and perspective that they provide. I came to Urbana for a premier institution of fundamental research, but having come, I have found as well a premier institution of the human race–a family, which will forever be the greatest gift I have received in this life. On that note, I am also particularly in debt to my in-laws, Salim, Judy, Eli, and Mario. I shudder to think what these last few years would have been without their love and support, and if not for Judy's computer and countless free baby-sittings this thesis would likely never have seen the light of day.

I am also especially thankful for the constant friendship, insight, and conversation provided by Eric Smith over the past fifteen years. It is rare to find a person who actually wants an answer when he asks how my work is progressing, and it is a joy to know that someone cares and wants to understand what I understand. I am only sorry that the latter category is so limited.

I am thankful too for Fr. James Ellison and the wonderful extended family of St. Nicholas Orthodox Church, which has done so much to make me truly at home in central Illinois. Their presence and support has been a blessing far beyond my expectations, and it is a joy to know that on their account I will always have a home in Urbana. I am especially grateful for the stimulating conversation and true friendship which I have come to expect from Ryan McDaniel, to whom I never have to justify the pursuit of knowledge simply for its own sake. I have also enjoyed the company and distractions provided by Michele McDaniel, Matthew Sutton, Maria Cucuras, Elizabeth Betten, Hannah Stapleton, Marianna Ruggerio, Matthew and Angie Isaacs, David and Ashley Purpura, and the Kelley family.

In addition to all these, there is an almost endless list of friends and fellow graduate students who have made the last seven years both far more productive and enjoyable. It has been several years since we bonded over liquid xenon, but I remain particularly indebted to Wade DeGottardi, Stephanie Law Toner, and Tomoki Ozawa for the laughter and conversation that we have shared over the years. In addition, I have truly enjoyed the friendship and conversation on all conceivable topics which was shared with Tomoki and Soheil Baharian in the climatically erratic environment of Loomis 341. I am also grateful to Jaron and JulieAnn Krogel for their friendship and for repeatedly opening their home to me. Finally, I would like to thank John Nichol, David McKay, Sarang Gopalakrishnan, Benjamin Hsu, Mingwu Lu, and Jeremy McMinis.

One of my great sources of enjoyment aside from physics over the last several years has come from the friendships I have developed within the vibrant community of soccer referees in Champaign-Urbana. In particular, I am grateful to Dave Gire for providing a constant reminder that a bit of sanity still exists in this world, even if you have to drive to Camargo to find it. I also thank Ed Schell and Thomas Ayala for their selfless help and encouragement. Whatever the players may say, I am a much better referee now than I was seven years ago, and it is these men I have to thank.

The physics department at the University of Illinois must surely be one of the most friendly and supportive environments in which a graduate student could find himself, and there are a great number of its members to whom I am indebted. I am especially grateful to John Stack, Lance Cooper, Nigel Goldenfeld, Philip Phillips, Laura Greene, Paul Kwiat, Sue Berndt, Shannon Cardaronella, Melodee Schweighart, and Wendy Wimmer. I would also like to thank all of the students I have had the pleasure of teaching over the last seven years. I hope that they have learned as much as I have from our interaction and I will truly miss teaching at the University of Illinois. I am also grateful to the National Science Foundation, which enabled me to perform much of this work through Grants No. PHY05-00914, PHY07-01611, and PHY09-69790.

Finally, I am sincerely grateful to Carlos Sá de Melo for his selfless guidance and support over the past

eight years. Since he first introduced me to the world of physics research in the summer of 2005, he has not hesitated to share his immense knowledge and experience in both physics and the often confounding world of practicalities which surrounds it. His wisdom and support have been invaluable to my development as a student of physics, and as I hope, to a productive member of the physics community.

Table of Contents

Chapter 1

Introduction

In this thesis we discuss three topics concerning matter under extreme conditions. First, we construct the phase diagram of quantum chromodynamics (QCD) by applying effective field theory at finite temperature and density. Second, we investigate the effects of quark thermodynamics on the structure and stability of neutron and dense quark stars. Third, we study the properties of Fermi gas mixtures in the presence of artificial spin-orbit coupling and a tunable s-wave contact interaction. While spanning an extraordinary twenty orders of magnitude in energy scales, these systems exhibit remarkable similarities which will be the subject of our investigation, including non-perturbative many-body interactions, perfect fluid behavior, the formation of Cooper pairs, and the possibility of BCS-BEC crossovers between weakly and strongly interacting regimes. In the following sections we briefly introduce each of these topics. Much of this work is based on the author's publications [2–5].

1.1 QCD Phase Diagram

Since its inception in the mid-1960s, the theory of quantum chromodynamics (QCD) has cemented its place as one of the most robust and successful theories of modern physics. Modeled after the unprecedented success of quantum electrodynamics (QED), for which Feynman, Schwinger, and Tomonaga received the 1965 Nobel Prize in Physics, QCD describes the strong nuclear interaction in terms of a fundamental quark field which interacts via the exchange of gauge bosons known as *gluons*. As suggested in 1965 by Nambu with Han, and independently by Greenberg, it was possible to explain the observed hadronic structure of protons and neutrons, an antisymmetric orbital s-state of three quarks, by positing a new quantum number *color*, which belongs to the fundamental representation of SU(3). In order for the theory to retain the local SU(3) color symmetry expected of relativistic field theories, it also demanded the existence of an octet of gauge bosons which mediated the strong interaction, in the same way that virtual photon exchange mediates the U(1) theory of QED.

While QCD has certainly obtained a secure footing in the contemporary physics community, it is unique among such "successful" theories in that, while it has passed all experimental tests, there are an extremely wide variety of conditions under which we are, nearly fifty years after its inception, still completely incapable of discerning its predictions. This practical barrier is a consequence the strength of the aptly named strong

interaction, namely that in contrast to the QED coupling constant $\alpha = e^2/4\pi \approx 1/137$, the strong coupling constant $\alpha_s = g^2/4\pi$ is not small. As a result, the perturbative techniques which have proven so effective in QED are much less useful in QCD, applying only in the limit of asymptotically large energies, where the renormalized coupling $\alpha_s(\mu_R)$ becomes small. Thus, we find ourselves in the unique circumstance of possessing a theory which we believe to be a complete and accurate description of strongly interacting matter, but which is intractable in the majority of the phase diagram.

In our present undertaking we wish to construct the QCD phase diagram, which displays the ground state phases of quark matter over a range of quark chemical potentials μ and temperatures T. Thus, we are fundamentally required to assess the properties of strongly interacting matter under a wide variety of conditions. As a starting point, we note that at asymptotically large densities, as the distance between quarks becomes small and asymptotic freedom is obtained, quark matter becomes weakly-interacting and the perturbative techniques developed in QED can be applied. However, except in this special region of the phase diagram, we have no analytical method for ascertaining the predictions of QCD. At present, there are two methods by which one may then proceed. First, by defining a discrete space-time *lattice* and solving the equations of QCD on it, one may extrapolate to the continuum limit and thereby approximate the properties of strongly interacting matter. Such lattice techniques have seen an explosion of interest and precision thanks to the corresponding explosion in computing power over the decades since their initial development in the 1980s [6–10]. At present, these techniques are our sole method for performing non-perturbative QCD calculations, and are therefore invaluable both for the direct insight they provide to strongly interacting systems, as well as in testing and verifying any approximation scheme one might apply.

Unfortunately, despite its successes, lattice QCD is largely restricted to zero quark density by the "fermion sign problem" [6, 7]. In constructing the QCD phase diagram, we therefore have "exact" lattice results at zero density and perturbative results at asymptotically large densities, but we are left with very little insight regarding the properties of quark matter in between. Thus, we are led to consider the second method of studying strongly interacting matter, through the use of effective field theories (EFTs). Such theories are constructed to retain the symmetry-breaking properties of QCD while dispensing with the full complexities that render QCD intractable. Naturally, such a theory will have a limited region of applicability, namely the region of phase space in which the symmetry-breaking properties it contains dominate the system. Fortunately for our present undertaking, this symmetry breaking is precisely what determines the phase boundaries of the system, so that the EFT approach is well-suited to an analysis of the QCD phase diagram. In addition, an effective theory has the advantage of analytic tractability which may yield insight into the basic mechanisms at work in the system, and which may be obscured by a brute force numerical treatment

or hidden entirely in the full "parent" theory.

In Chapters 2, 3, and 4, we construct the phase diagram of two and three flavor QCD by employing the Polyakov–Nambu–Jona-Lasinio (PNJL) model, an effective field theory built upon the spontaneous chiral symmetry breaking exhibited by QCD. The earliest form of this model, which did not include the Polyakov loop, an effective order parameter for confinement, was developed prior to the discovery of quarks and provided a method for dynamically generating nucleon mass from a massless fundamental field [11, 12]. After the discovery of quarks and the full theory of the strong interaction, the NJL model was reinterpreted in terms of a massless fundamental quark field [13–16]. Since then, the model has been extended in a variety of ways by including the effects of the QCD axial anomaly, diquark pairing, and confinement, among others [2, 17–22].

We observe that for three quark flavors the chiral phase transition at $T = 176$ MeV, which is first-order in the massless quark limit, becomes a smooth crossover at $\mu = 0$ for non-zero quark masses. A line of first-order transitions and an associated high temperature critical end point does persist, however, at non-zero baryon density within a certain parameter regime, namely when the coupling between the chiral and diquark condensates is not too strong. At low temperatures, we find that when the chiral and diquark condensate coupling is sufficiently strong, the first-order transition between the hadronic and color superconducting phases becomes second-order and the system develops a BEC-BCS crossover between strongly bound diquark molecules and weakly coupled pairs consisting of up and down quarks (e.g., within a 2SC phase). In addition, while the presence of the 2SC phase eliminates the possibility of continuity between hadronic and color-flavor-locked (CFL) superconducting matter, we find that for certain parameter sets there exists a line of first-order BEC-BCS transitions within the 2SC phase, and an associated low temperature critical end point. Finally, in the presence of a local color neutrality constraint, we find that certain phases of asymmetric quark pairing are suppressed, which tends to decrease the 2SC portion of the phase diagram.

In order to motivate the PNJL model we now briefly discuss the symmetries upon which it is built and the general properties which follow.

1.1.1 Symmetries of QCD

Having described the complexities inherent in QCD that prevent us from directly discerning its implications, we now briefly discuss the symmetries of QCD, which motivate the NJL model. We begin by writing the QCD Lagrangian density:

$$\mathcal{L}_{QCD} = \overline{q}\left(i\partial\!\!\!/ - \hat{m}\right) q - g\overline{q}\gamma^{\mu}\mathcal{A}^{a}_{\mu}T_{a}q - \frac{1}{4}\,\mathcal{G}^{a}_{\mu\nu}\mathcal{G}^{\mu\nu}_{a}, \tag{1.1}$$

Symmetry	Name	Transformation	Manifestation
$\mathrm{SU}(N_f)_V$	isospin	$q \to e^{-iT_a\theta_a}q$	approximately realized
$\mathrm{SU}(N_f)_A$	chiral	$q \to e^{-iT_a\omega_a\gamma_5}q$	spontaneously broken
$\mathrm{U}(1)_V$	baryon	$q \to e^{-i\alpha}q$	exactly realized
$\mathrm{U}(1)_A$	axial	$q \to e^{-i\beta\gamma_5}q$	broken by anomaly

Table 1.1: Exact and approximate symmetries of QCD with N_f quark flavors of approximately equal mass. Also shown are the respective quark field transformations and their manifestation in nature. Adapted from [15].

where q is a quark field with Dirac, color, and flavor indices, $\hat{m}$ is the bare quark mass matrix, $A_\mu = \mathcal{A}^a_\mu T_a$ is the gluon field where T_a ($a = 1...8$) are the generators of the local SU(3) color symmetry,[1] g is the strong coupling constant, and the gluon field strength is defined by

$$\mathcal{G}^a_{\mu\nu} = \partial_\mu \mathcal{A}^a_\nu - \partial_\nu \mathcal{A}^a_\mu - g f_{abc} \mathcal{A}^b_\mu \mathcal{A}^c_\nu, \tag{1.2}$$

where f_{abc} are the structure constants of SU(3), defined by the commutation relations $[T_a, T_b] = i f_{abc} T_c$. These coefficients are antisymmetric under the interchange of any two indices and are explicitly given by

$$\begin{aligned} f_{123} &= 1, \\ f_{147} &= f_{246} = f_{257} = f_{345} = -f_{156} = -f_{367} = \frac{1}{2}, \\ f_{458} &= f_{678} = \frac{\sqrt{3}}{2}, \end{aligned} \tag{1.3}$$

and where the coefficients not related to those above by cyclic permutation of the indices vanish. In addition, we employ the Feynman slash notation, $\partial\!\!\!/ \equiv \gamma^\mu \partial_\mu \equiv \gamma_\mu \eta^{\mu\nu} \partial_\nu$, where we adopt the metric $\eta = \mathrm{diag}(1, -1, -1, -1)$.

In analyzing QCD, there are three types of symmetries that one encounters. First, there are the symmetries of the Poincaré group and CPT invariance, which are characteristic of all relativistic quantum field theories. These will certainly be maintained in any effective field theory which we might wish to consider, but are sufficiently general that they will not play a defining role in our analysis and we will not discuss them further. Second, there is the local SU(3) color symmetry which plays a defining role in QCD. It is evident that this symmetry, which gives rise to the gluon field and thereby the complexities which render QCD largely intractable, must be dispensed with (or approximated) to some degree. The specific way in

[1] While the majority of this thesis concerns systems exhibiting the local SU(3) color symmetry realized in nature, for analytical purposes we also briefly consider a two color, two flavor system in Chapter 2. In this case, the T_a ($a = 1...3$) are instead the generators of the local SU(2) color symmetry and the structure constants are simply given by the antisymmetric tensor $f_{abc} = \varepsilon_{abc}$.

which we shall deal with this symmetry will be a topic of the next subsection. Third, there are approximate "accidental" symmetries of QCD which are not built into the structure of the QCD Lagrangian, but are instead the result of the particular parameter values observed in nature (e.g., quark masses). These approximate symmetries play a crucial role in QCD phenomenology and the observed hadronic spectrum, and so will play a correspondingly important role in the construction of any effective field theory which we hope to reproduce this phenomenology. Let us now turn to this third category of symmetries and discuss the properties of QCD in more detail.

1.1.2 Approximate Symmetries of QCD

In order to identify the approximate symmetries of QCD it is helpful to first rewrite the QCD Lagrangian in terms of quark fields of definite chirality. Defining the projection operators

$$P_R \equiv \frac{1+\gamma_5}{2}, \qquad\qquad P_L \equiv \frac{1-\gamma_5}{2}, \tag{1.4}$$

where $\gamma_5 = i\gamma^0\gamma^1\gamma^2\gamma^3$, and the corresponding chirality states $q_R = P_R q$ and $q_L = P_L q$, we can rewrite $\mathcal{L}_{QCD}$ as

$$\mathcal{L} = \overline{q}_R i\partial\!\!\!/ q_R + \overline{q}_L i\partial\!\!\!/ q_L - \overline{q}_R \hat{m} q_L - \overline{q}_L \hat{m} q_R - g\overline{q}_R \gamma^\mu \mathcal{A}^a_\mu T_a q_R - g\overline{q}_L \gamma^\mu \mathcal{A}^a_\mu T_a q_L - \frac{1}{4}\mathcal{G}^a_{\mu\nu}\mathcal{G}^{\mu\nu}_a. \tag{1.5}$$

In this form, one immediately recognizes that only the mass terms couple states of different chirality. As a consequence, for massless quarks the Lagrangian is invariant under independent unitary transformations of right- and left-handed quarks (i.e. $q_R = U_R q_R$ and $q_L = U_L q_L$, where $U_R^\dagger U_R = U_L^\dagger U_L = I$). More generally, for N_f massless flavors the states of different chirality corresponding to those flavors remain uncoupled and so the QCD Lagrangian possesses the symmetry group $\mathcal{G} = U(N_f)_L \otimes U(N_f)_R$.

In order to make the connection between the symmetries of the QCD vacuum and its phase structure we now decompose the symmetry group of the QCD Lagrangian in terms of those symmetries which are physically realized (or broken) in nature. To this end, we first note that an element of $U(N_f)$ can always be decomposed into the product of elements of $SU(N_f)$ and $U(1)$ so that[2]

$$\mathcal{G} = \left[SU(N_f) \otimes U(1)\right]_L \otimes \left[SU(N_f) \otimes U(1)\right]_R. \tag{1.6}$$

Next, by considering that a finite $SU(N_f)$ or $U(1)$ transformation can be built up from infinitesimal trans-

[2] If $U \in U(N_f)$ then $U^\dagger U = 1$ so that $\det(U) = e^{i\alpha}$. Defining $\tilde{U} = e^{-i\alpha}U$, factorization of the determinant yields $\det(\tilde{U}) = 1$ so that $U \in SU(N_f)$. Thus, by writing $U = e^{i\alpha}\tilde{U}$, we find that $U(N_f) = SU(N_f) \otimes U(1)$.

formations, one can show that $SU(N_f)_L \otimes SU(N_f)_R = SU(N_f)_V \otimes SU(N_f)_A$ and $U(1)_L \otimes U(1)_R = U(1)_V \otimes U(1)_A$, where the vector (V) and axial (A) transformations are defined by

$$\begin{aligned} U(1)_V &: q \to e^{-i\alpha} q & SU(N_f)_V &: q \to e^{-i\theta_a T_a} q \\ U(1)_A &: q \to e^{-i\alpha\gamma_5} q & SU(N_f)_A &: q \to e^{-i\theta_a T_a \gamma_5} q, \end{aligned} \tag{1.7}$$

where the T_a are here understood to be the generators of $SU(N_f)$. Thus, we may write the symmetry group of the QCD Lagrangian with N_f massless flavors as

$$\mathcal{G} = SU(N_f)_V \otimes SU(N_f)_A \otimes U(1)_V \otimes U(1)_A. \tag{1.8}$$

Having now expressed the symmetry group in terms of those symmetries which are physically realized (or broken) in nature we shall now briefly discuss the four components of $\mathcal{G}$.

The first component of $\mathcal{G}$, $SU(N_f)_V$, is a simple rotation in the space of massless flavors and is known as *isospin* symmetry. While this symmetry is only approximate, owing to the only approximately equal masses of the up and down quarks, and to a lesser extent the strange quark, this symmetry remains unbroken in nature and is reflected in the spectrum of the light hadrons [23, 24].

The second component of $\mathcal{G}$, $SU(N_f)_A$, is known as *chiral* symmetry, and is spontaneously broken in the hadronic phase of QCD, giving rise to the large effective quark masses present in the proton and neutron.[3] We note that many authors use the term chiral symmetry to refer to either the entire symmetry group $U(N_f)_L \otimes U(N_f)_R$, or the slightly smaller group $SU(N_f)_L \otimes SU(N_f)_R$. For any of these definitions, it is certainly correct to say that chiral symmetry is broken in the hadronic phase. However, with our definition we isolate the particular $SU(N_f)_V$ symmetry which is *completely* broken in the hadronic phase, thus avoiding the question of what subgroups might yet be realized.

The third component of $\mathcal{G}$, $U(1)_V$, corresponds to baryon number conservation and is believed to be realized exactly in nature.

Finally, the fourth component of $\mathcal{G}$, $U(1)_A$, is known as the *axial* symmetry and as shown by 't Hooft, is broken by instanton effects via the QCD axial anomaly [25]. Thus, while this group is a symmetry of the QCD Lagrangian (i.e., "classical" QCD), it is not a true symmetry of QCD under any circumstances.

[3] The bare up and down quark masses are approximately $m_u = 2.3$ MeV and $m_d = 4.8$ MeV, while the proton (uud) and neutron (udd) have masses of $m_p = 938$ MeV and $m_n = 940$ MeV, respectively. One important observation from this data is that despite the fact that $m_u, m_d \neq 0$, so that chiral symmetry is not truly present in the system, the effective quark mass in the hadronic phase is nonetheless orders of magnitude larger than the quark bare masses. By attributing the large dynamically generated masses to the same chiral symmetry breaking mechanism at work in the massless (bare) quark case, we may still refer to (approximate) chiral symmetry breaking, and define the hadronic phase in terms of a chiral condensate which is much larger than that stemming from the non-zero bare quark masses.

1.1.3 Polyakov–Nambu–Jona-Lasinio Model

Having discussed the symmetries of QCD, we are now in a position to construct an effective field theory which will approximate the behavior of QCD in at least some portion of the phase diagram. As noted in the prior subsection, we must begin by dispensing with QCD's local SU(3) color symmetry, which gives rise to the gluonic degrees of freedom. Thus, we replace the local symmetry with a *global* SU(3) symmetry, and correspondingly eliminate the gluon field altogether. Next, having eliminated the mechanism for coupling the quark fields, we must introduce an effective interaction which retains isospin and $U(1)_V$ symmetry, while providing a mechanism for spontaneous chiral symmetry breaking. Finally, we must also introduce an effective interaction which plays the role of the QCD instanton and explicitly breaks the $U(1)_A$ symmetry of the QCD Lagrangian.

While the specific form of the NJL model Lagrangian depends both on the number of quark colors and flavors considered as well as the types of interactions one wishes to study, in this thesis we will study models which can be generally written in the form

$$\mathcal{L}_{NJL} = \overline{q}\left(i\partial\!\!\!/ - \hat{m}\right) q + \mathcal{L}^{(4)} + \mathcal{L}^{(6)}, \tag{1.9}$$

where $\mathcal{L}^{(4)}$ is an effective four-quark interaction which is invariant under the full symmetry group $\mathcal{G}$, but allows for the spontaneous breaking of chiral symmetry and diquark pairing, and $\mathcal{L}^{(6)}$ is an effective six-quark interaction that is present for three quark flavors and reflects the QCD axial anomaly by explicitly breaking the $\mathrm{U}(1)_A$ symmetry.

While the NJL model accounts for many of the defining properties of QCD, there remains one crucial property of strongly interacting matter which we have thus far neglected, namely the phenomenon of confinement. As with the chiral symmetry breaking and diquark pairing already mentioned, the confinement of quarks into color singlets at low temperatures, and their "melting" into the quark-gluon plasma (QGP) is the result of an extraordinarily complex exchange of gluons, as well as a variety of gluon-gluon interactions, which we have necessarily dispensed with in our effective theory. In fact, an analytic proof that QCD is color confining has so successfully eluded the physics community that since 2000 it has been the subject of a Millennium Prize, and the corresponding $1 million which accompanies the six such outstanding problems [26]. Nonetheless, given that all known QCD phenomenology at low energies exhibits such confinement, it remains a property which we wish to include in any effective theory of the strong interaction.

A quantity which will prove most useful in discussing confinement both in the full theory of QCD and in modeling it in our present effective theory is the *Polyakov loop*, or thermal Wilson line with periodic

boundary conditions, which is defined as [27–29]

$$L(\mathbf{r}) = \exp\left(i\int_0^\beta d\tau\, A_0(\mathbf{r},\tau)\right), \tag{1.10}$$

where $A_0(\mathbf{r},\tau)$ is the time-like component of the gluon field. We note that the Polyakov loop $L(\mathbf{r})$ inherits any non-Dirac indices from the gauge field and so in the case of QCD, it is a matrix in color space. Tracing over these indices yields the "traced Polyakov loop," often itself simply referred to as the Polyakov loop:

$$\Phi(\mathbf{r}) = \frac{1}{N_c}\,\mathrm{tr}L(\mathbf{r}), \tag{1.11}$$

where N_c is the number of colors. The utility of this object is found in the fact that in the limit of infinitely massive quarks the partition function of a static quark pair separated by $\mathbf{r}$ can be simply expressed in terms of Φ:

$$e^{-\beta F_{qq}(\mathbf{r})} \sim \left\langle \overline{\Phi}(\mathbf{r})\Phi(\mathbf{0})\right\rangle, \tag{1.12}$$

where $F_{qq}(\mathbf{r})$ is the free energy of the quark-quark pair and $\langle\cdots\rangle$ denotes the thermal expectation value. In the absence of long-range order we expect the correlations in Eq. (1.12) to fall off as a power of r. Thus, by taking the quark separation to infinity the expectation value can be factored to yield

$$e^{-\beta F_{qq}(\infty)} \sim \left\langle \overline{\Phi}(\mathbf{r})\right\rangle \langle\Phi(\mathbf{0})\rangle = |\langle\Phi(\mathbf{0})\rangle|^2, \tag{1.13}$$

where we have used the fact that $\overline{\Phi}(\mathbf{r}) = \overline{\Phi}(\mathbf{0})$, which follows from the symmetry of the two-quark system. Thus, assuming a spatially homogeneous $\langle\Phi\rangle$ we obtain

$$\langle\Phi\rangle \sim e^{-\beta F_{qq}(\infty)/2}. \tag{1.14}$$

In the confined phase it requires an infinite energy to separate the two quarks to infinity so that $\langle\Phi\rangle = 0$, while in a non-confining phase $F_{qq}(\infty)$ remains finite and $\langle\Phi\rangle \neq 0$. Thus, $\langle\Phi\rangle$ serves as an order parameter for confinement, and after normalizing we obtain

$$\langle\Phi\rangle = \begin{cases} 0 & \text{confined} \\ 1 & \text{deconfined} \end{cases}. \tag{1.15}$$

A careful reader will note that we prefaced Eq. (1.12) by assuming infinitely massive quarks so that the quark dynamics were suppressed. Thus, $\langle\Phi\rangle$ is a true order parameter for confinement only in this limit. In fact, as has been observed in both lattice and EFT calculations such as those which follow, for finite quark masses there need not be a true deconfinement phase transition at all. Rather, the system may undergo a more or less rapid and smooth crossover from $\langle\Phi\rangle \sim 0$ to $\langle\Phi\rangle \sim 1$ with increasing temperature. Thus, given the phenomenological character of our model and the rough correspondence of these limiting values to the confining and deconfining phases of QCD, we will employ the Polyakov loop as an effective parameter for confinement.

Finally, we note that we will treat the PNJL model in the mean field approximation throughout this thesis, replacing the traced Polyakov loop and its conjugate with their thermal expectation values. For the sake of notational simplicity, we will continue to use Φ to represent this expectation value, not writing the brackets explicitly.

As seen in Eq. (1.10), the Polyakov loop is defined in terms of the time-like component of the gluon field A_0. Thus, if one were computing true QCD thermodynamics, one can imagine determining the equilibrium gluon field configuration for a system, and from it calculating the Polyakov loop, thereby determining whether the system is in a confined phase or not. However, having begun our search for an EFT by dispensing with the dynamical gluon field, we no longer have either the field A_0 nor a means to define the Polyakov loop. Thus, our first step in incorporating confinement into the NJL model is to re-introduce a static homogeneous gauge field A_μ and the corresponding covariant derivatives into the NJL Lagrangian:

$$D_\mu = \partial_\mu - iA_\mu, \qquad\qquad A_\mu = \delta^0_\mu A_0, \tag{1.16}$$

where we have absorbed any coupling strength which would otherwise multiply A_μ into the definition of the gauge field.

One crucial aspect of the Polyakov loop's place in an EFT is the fact that unlike in QCD, its value is no longer the byproduct of the theory's dynamical degrees of freedom. Rather, we must treat Φ (or equivalently, A_0) as a variable on par with the chiral and diquark condensates, with respect to which we will minimize the thermodynamic potential. As a result, we must also introduce an effective potential $\mathcal{U}(\overline{\Phi}, \Phi)$, which will govern the deconfinement phase transition in the pure gauge sector (i.e., in the absence of quarks). The precise form of the potential will depend on the number of quark colors, but will allow us to write the PNJL model Lagrangian generally in the form

$$\mathcal{L}_{PNJL} = \overline{q}\left(i\partial\!\!\!/ - \hat{m} + A_0\gamma^0\right)q + \mathcal{L}^{(4)} + \mathcal{L}^{(6)} - \mathcal{U}(\overline{\Phi}, \Phi). \tag{1.17}$$

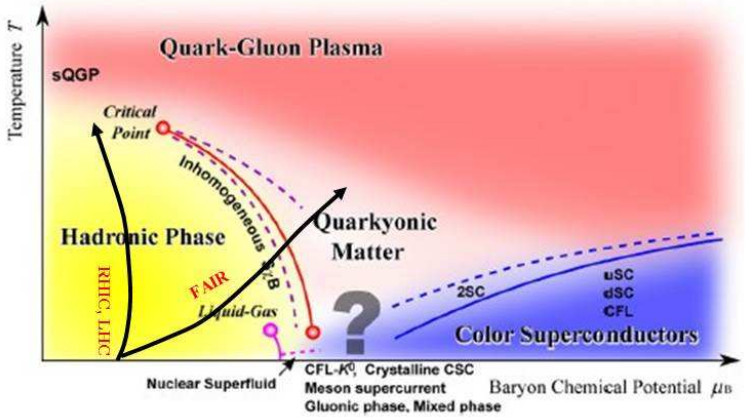

Figure 1.1: Schematic QCD phase diagram showing the regions probed by current heavy ion colliders as well as the low temperature region applicable to neutron stars. Adapted from [30].

1.2 Structure of Neutron and Dense Quark Stars

While much of our current observational study of the QCD phase diagram is restricted to the high temperature, low density matter created in heavy ion collisions, nature itself provides us an indirect method for the study of low temperature quark matter in neutron stars. These astrophysical objects have temperatures $T \lesssim 1$ MeV and are thought to obtain central densities of $\rho_c \sim 5 - 10\rho_0$, where $\rho_0 \approx 2.3 \times 10^{14}$ g /cm^3 is nuclear density. As a result, the cores of neutron stars are thought to have precisely the conditions necessary to reach into the rich, but highly uncertain, region of the QCD phase diagram (see Fig. 1.1).

Unfortunately, while neutron stars may hold the key to understanding the structure of dense quark matter, our observations of the quark matter that comprises them are necessarily indirect, owing both to their distance (~ 100 ly to the nearest [31,32], and ~ 4000 ly to the most massive [33]) and to their intense gravitational and rotational properties. Thus, we are led to consider what observable properties of a neutron star is capable of providing insight into the thermodynamic properties of its core [34–36].

The connection between neutron star thermodynamics and structure is contained in the Tolman-Oppenheimer-Volkov (TOV) equation, which describes spherically symmetric solutions of the Einstein field equations of general relativity [37,38]:

$$\frac{dP(r)}{dr} = -G\,\frac{\left[\rho(r) + P(r)/c^2\right]\left[M(r) + 4\pi r^3\,P(r)/c^2\right]}{r^2 - 2GM(r)/c^2\,r}, \tag{1.18}$$

where $P(r)$ and $\rho(r)$ are the pressure and energy density at a radius r from the star's center, G is Newton's

gravitational constant, and the mass contained within a shell of radius r is given by

$$M(r) = \int_0^r dr' \, 4\pi r'^2 \rho(r'). \tag{1.19}$$

In order to solve Eq. (1.18) we must specify the *equation of state* of the matter comprising the star, which gives the matter's pressure as a function of its mass density, $P(\rho)$. Once this ingredient is supplied by a thermodynamic analysis of the quark matter which comprises the star, the relationship between neutron star mass and radius is determined. Working in reverse, by making astronomical observations of the mass-radius relationship of neutron stars one can constrain the possible quark matter equations of state and thereby gain insight into the microscopic properties of dense quark matter.

One reason that observing the masses of neutron stars is so useful is that for a given equation of state there exists a maximum total mass (M_{max}), beyond which a star would be unstable to gravitational collapse. Thus, by observing the neutron star masses obtained in nature, one can eliminate those candidate equations of state which do not permit the realization of such massive stars. One can understand the existence of M_{max} by considering the simpler case of a much lower density white dwarf, which is supported against gravitational collapse by *electron* (rather than neutron) degeneracy pressure. For simplicity, we assume the star is comprised of highly relativistic electrons and stationary nuclei. Taking into account the spin degeneracy, the kinetic energy of the electrons is

$$E_{kin} \quad = \quad 2V \int_0^{p_F} \frac{d^3\mathbf{p}}{(2\pi\hbar)^3} \sqrt{(pc)^2 + (m_e c^2)^2}, \tag{1.20}$$

where m_e is the electron mass, $p_F = \hbar(3\pi^2 N_e/V)^{2/3}$ is the Fermi momentum of the electrons, N_e is the number of electrons in the star, and V is the star's volume. In the highly relativistic limit ($p_F \gg m_e c$) the electrons' rest energy is a small correction to their kinetic energy so that we can expand the square root in Eq. (1.20) and after performing the integrals obtain

$$E_{kin}(R) \sim \frac{B}{R} + CR, \tag{1.21}$$

where R is the star's radius and we define the constants

$$B = \frac{3}{4}\left(\frac{9\pi}{4}\right)^{1/3}\left(\frac{Z}{A}\right)^{4/3}\left(\frac{M}{m_p}\right)^{4/3}\hbar c \qquad C = \frac{3}{4}\left(\frac{9\pi}{4}\right)^{-1/3}\left(\frac{Z}{A}\right)^{2/3}\left(\frac{M}{m_p}\right)^{2/3}\left(\frac{mc}{\hbar}\right)^{2}\hbar c, \tag{1.22}$$

where m_p is the proton mass and $M \approx (A/Z)N_e m_p$ is the total star mass, with A and Z the mass and

atomic numbers, respectively. Meanwhile, the gravitational potential energy of the star is $V = -D/R$ where we take $D = 3GM^2/5$, assuming a constant density star.[4] The total energy of the star is therefore

$$E(R) = \frac{B - D}{R} + CR. \tag{1.23}$$

The equilibrium radius of the star is the radius at which the pressure $P = -(\partial E/\partial V)_{S,N} = 0$, so that $E'(R_*) = 0$. However, if $B < D$ then the star's energy is a monotonically decreasing function of R; in this situation the degeneracy pressure of the electrons is insufficient to balance the gravitational force, and the star is unstable to collapse. Setting $B = D$ thus yields the maximum white dwarf mass:

$$M_{max} = \frac{15\sqrt{5\pi}}{16}\left(\frac{Z}{A}\right)^2\left(\frac{\hbar c}{G}\right)^{3/2}\frac{1}{m_p^2} \approx 6.87\left(\frac{Z}{A}\right)^2 M_\odot, \tag{1.24}$$

where $M_\odot = 2.0 \times 10^{33}$ g is a solar mass. The appearance of the ratio Z/A in this expression can be traced to the fact that while protons contribute to both the gravitational and degeneracy pressures of the star (the latter indirectly, through the presence of a neutralizing electron), neutrons do not. Thus, a star composed of neutron rich nuclei ($A > 2Z$) will become unstable before a star with equal numbers of protons and neutrons. In practice, white dwarfs primarily consist of low atomic number nuclei with roughly equal numbers of protons and neutrons (e.g., ^{12}C, ^{16}O) and using a value of $A/Z \approx 2.2$ yields the *Chandrasekhar limit* of $M_{max} = 1.41M_\odot$ [39, 40].

Looking back at Eq. (1.23) we see that while the coefficient D, which stems from the gravitational pressure of the star, is independent of the type of particles which comprise the star, the coefficient B is highly dependent on the detailed properties of the gas' constituents. In particular, it can be derived from the equation of state for the star's constituent matter, which for a free ultra-relativistic Fermi gas is simply $P(\rho) = \rho/3$. Thus, if by careful astronomical observation we are able to identify a white dwarf with $M_{obs} > M_{max}$ then we can conclude that we must modify our equation of state in order to raise M_{max} above M_{obs}.

In Chapter 5 we investigate the constraints placed on the equation of state of dense quark matter by the recent observation of massive neutron stars with $M \gtrsim 2M_\odot$ [33, 41, 42]. By introducing a flavor-symmetric vector repulsion within an NJL model of dense quark matter we construct a quark matter equation of state which stabilizes neutron stars up to $M \approx 2.34M_\odot$. Such an interaction can therefore explain the recent observations of PSRs J1614-2230 and J0348+0432 with $M = (1.97 \pm 0.04)M_\odot$ and $(2.01 \pm 0.04)M_\odot$ respectively [33, 42], though its capacity to account for PSR J1311-3430 with $M = (2.4 \pm 0.3)M_\odot$ is unclear,

[4] This approximation is not necessary, but simplifies the present calculation without affecting the qualitative result.

given the large uncertainty in its observed mass [41]. We then consider observational data from non-maximally massive neutron stars and find that our equation of state is in marked agreement with the observational constraints imposed by this data for quite reasonable magnitudes of the vector coupling.

We also investigate the stability of neutron stars and the proposed ultra-dense *quark stars*, whose central densities are thought to be $\rho_c \gg 10\rho_0$ [43, 44]. We construct density profiles and determine the mass-radius relationships for these dense stars in the presence of a vector repulsion and study the impact of this coupling on the stability limits of quark and neutron stars. We find that the vector coupling is not capable of stabilizing the ultra-dense matter of quark stars against gravitational collapse, so that if such stars are to be realized in nature, additional physics is required.

1.3 Artificial Gauge Fields in Ultracold Atoms

In the past two decades the study of ultracold atomic gases has quickly become one of the most rapidly developing fields of science, due in large part to these systems' remarkable ability to simulate other widely disparate physical systems. The explosion in both interest and application of these systems has been largely precipitated by the technological developments which have recently allowed experimentalists to reach the extremely low temperatures ($T \sim 100$ nK) required to observe macroscopic quantum mechanical behavior. In particular, the development of laser cooling techniques which earned Phillips, Cohen-Tannoudji, and Chu the 1997 Nobel Prize in physics, paved the way for researchers to probe the lowest energy states of matter [45].

The realization of the first man-made atomic Bose-Einstein condensate (BEC) in 1995 [46] and the first degenerate Fermi gas four years later [47] opened these prototypical quantum systems to experimental probes for the first time, seventy years after they were postulated [48, 49]. Soon after, the first signs of the wide application of these systems began to appear, and in 1998 Ketterle *et al.* demonstrated the ability to arbitrarily tune a two-body atomic interaction by means of an external magnetic field, via a mechanism known in nuclear physics as a Feshbach resonance [50, 51]. Five years later, beginning with a gas of weakly bound Bardeen-Cooper-Schrieffer (BCS) pairs of fermions, Jin *et al.* induced the formation of strongly bound diatomic molecules which then condensed to form a *molecular* BEC, as shown in Fig. 1.2 [52, 53]. Thus, a mere eight years after creating the first BEC, researchers were able to create and probe either Bose or Fermi systems with arbitrary two-body interactions, and remarkably, to move continuously between the two regimes via a BEC-BCS crossover.

The ability to prepare and measure the properties of strongly interacting systems in a controlled manner ensure sustained interest in ultracold gases and has inevitably led researchers to pursue methods of simulating

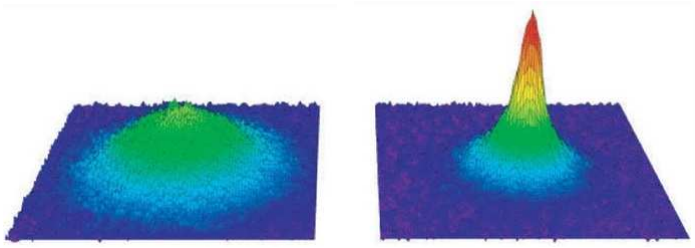

(a) (b)

Figure 1.2: Momentum distribution (a) above and (b) below the critical temperature T_c for Bose-Einstein condensation of a $^{40}K_2$ molecular gas. Above T_c the gas has a thermal Boltzmann distribution, while below T_c a large peak in the distribution forms, indicating the presence of a macroscopic number of molecules in the zero-momentum ground state. Image is courtesy of [53].

other systems that are difficult to study in their naturally occurring forms. One such application which has garnered particular attention is the simulation of both Abelian gauge fields (e.g., magnetic fields) in which the symmetry group generators commute, and non-Abelian fields (e.g., QCD) in which they do not. For example, in order to simulate a charged particle in a magnetic field, we must design a system described by a Hamiltonian of the form

$$H = \frac{1}{2m}\left(\mathbf{p} - \frac{q}{c}\mathbf{A}\right)^2, \tag{1.25}$$

where $\mathbf{p}$ is the particle's momentum and $\mathbf{B} = \nabla \times \mathbf{A}$ is the magnetic field. The remaining variables m and q are the particle's effective mass and charge, while c is the speed of light. Of course, the reason we cannot use a cold atomic gas to probe a magnetic field directly is that $q = 0$ so that the atoms do not couple to the gauge field $\mathbf{A}$. Thus, we must devise a way in which to construct a Hamiltonian of the form in Eq. (1.25) without a true electric charge. At present, two such methods have been successfully implemented. The first, which is capable of simulating constant Abelian gauge fields (i.e., magnetic fields), is through mechanical rotation. The second, through which it is possible to simulate both spatially varying and non-Abelian gauge fields, employs carefully tuned laser techniques. Though it is the second technique which we will be concerned with in this thesis, we will first briefly review the rotation method, as it is technically less complex and provides insight to the general approach of gauge field simulation.

Consider an atom with Hamiltonian $H_0 = \mathbf{p}^2/2m + V_0$, where V_0 is an unspecified external potential. If we place the atom in a frame rotating at an angular velocity $\boldsymbol{\omega} = \omega\mathbf{z}$ the Hamiltonian in the rotating frame is

$$H' = H_0 - \boldsymbol{\omega} \cdot \mathbf{L}, \tag{1.26}$$

where $\mathbf{L} = \mathbf{r} \times \mathbf{p}$ is the particle's angular momentum in the lab frame. Writing out the components explicitly, the rotating-frame Hamiltonian becomes

$$\begin{aligned} H' &= \frac{p_x^2 + p_y^2 + p_z^2}{2m} - \omega(xp_y - yp_x) + V_0, \\ &= \frac{(p_x + m\omega y)^2 + (p_y - m\omega x)^2 + p_z^2}{2m} - \frac{1}{2}\, m\omega^2(x^2 + y^2) + V_0, \\ &\equiv \frac{1}{2m}\left(\mathbf{p} - \frac{q}{c}\mathbf{A}\right)^2 + V', \end{aligned} \tag{1.27}$$

where we define the *artificial gauge field* $\mathbf{A}$ and rotating frame external potential V'

$$q\mathbf{A} = mc\omega\,(-y\mathbf{x} + x\mathbf{y}) \qquad V' = V_0 - \frac{1}{2}\, m\omega^2(x^2 + y^2). \tag{1.28}$$

Thus, measured in the rotating frame, the neutral atom responds as if it were a charged particle subject to the vector potential $\mathbf{A}$ as well as an additional scalar potential which gives rise to the centrifugal force. Incidentally, very often the external potential is a harmonic trap of the form $V_0 = m\Omega^2 r^2/2$ so that if the system is tuned to $\Omega = \omega$, the centrifugal and trapping potentials precisely cancel in the plane perpendicular to the rotation, and one is left only with a trapping potential $V' = m\omega^2 z^2/2$ in the plane perpendicular to the rotation. Also, note that by equating Eqs. (1.25) and (1.27) we are only able to determine the product $q\mathbf{A}$, which is as expected, since both q and $\mathbf{A}$ are artificial "effective" quantities, and only their product appears in the Hamiltonian.

From the vector potential $\mathbf{A}$ we can compute the artificial magnetic field $\mathbf{B} = \nabla \times \mathbf{A}$. Since only the product $q\mathbf{B}$ is fixed by Eq. (1.28) we are free to choose $q = e$ for simplicity so that

$$\mathbf{B} = \frac{2mc}{e}\,\boldsymbol{\omega} \approx 10^{-13} A\boldsymbol{\omega} \text{ gauss}, \tag{1.29}$$

where $A = m/m_p$ is the mass number of the atom and ω is measured in Hertz. The magnetic field is necessarily constant in space and while its magnitude can be tuned arbitrarily in principle, in practice the attainable fields are limited by achievable rotation rates. As a result, researchers have recently developed optical techniques for creating synthetic gauge fields which are much more versatile than mechanical rotation [54–56]. In particular, these methods do not face the technical limitations associated with high rotation rates and therefore allow for the realization of much larger synthetic field strengths. Moreover, these methods also allow for the simulation of both spatially varying and non-Abelian gauge fields, with which we are concerned in this thesis.

In Chapters 6 and Appendix A we investigate the properties of a mixture of two hyperfine species of

fermions coupled to a *non-Abelian* gauge field, induced by spatially-varying lasers. In particular, we consider a spin-orbit coupling of the Rashba-Dresselhaus (RD) form:

$$H = \frac{\kappa}{m} k_x \sigma_x + \frac{\eta\kappa}{m} k_y \sigma_y, \tag{1.30}$$

where m and $\mathbf{k}$ are the atom's mass and momentum respectively, $\boldsymbol{\sigma} = (\sigma_x, \sigma_y, \sigma_z)$ is the vector of Pauli matrices in hyperfine space, κ is the overall strength of the spin-orbit coupling, and η is the anisotropy of the Rashba and Dresselhaus components. The special cases $\eta = 1$ and $\eta = 0$ were first encountered in the study of two-dimensional semiconductors [57,58], and this class of Hamiltonians has recently gained attention as the first type of experimentally realized artificial non-Abelian gauge field [59]. With the addition of a Zeeman field (h_z) and a tunable s-wave contact interaction this system exhibits a very rich phase structure including a variety of topologically distinct superfluid phases, a BEC-BCS crossover, and the emergence of Majorana and Dirac excitations [59–63].

In Chapter 6 we investigate the phase structure of artificially spin-orbit coupled systems in the mean field approximation, which yields the general phase structure of these systems and reveals many important properties. We compute the critical superfluid temperature as a function of the RD coupling strength and anisotropy, as well as the applied Zeeman field. We observe a continuous BEC-BCS crossover with increasing two-body coupling strength, indicating a movement from a gas of weakly bound fermions to a composite gas of strongly bound Bose molecules. We also find that the critical temperature for superfluidity can either be enhanced or suppressed by the presence of a Zeeman field, depending on the system's location in phase space, namely whether the system is dominated by singlet or triplet pairing and the form of the density of states.

In Appendix A we study the effects of fluctuations on the phase diagram of spin-orbit coupled fermions, which play an increasingly important role as the system approaches phase transitions. In particular, we focus on the BEC regime in which the Fermi gas is largely composed of composite Bose molecules. We compute the coefficients of the Ginzburg-Landau thermodynamic potential, which can be used to obtain the superfluid critical temperature in this limit. Thus, one can show that the formation of bosonic molecules strongly suppresses the critical temperature relative to the mean field result by replacing the energetically costly pair-breaking excitations of the BCS limit with excitations of the strongly bound diatomic molecules from their bosonic ground state.

Chapter 2

Phase Diagram of Two Flavor QCD

2.1 Introduction

The reasons for the great sustained interest in the QCD phase diagram are many, but two factors in particular have contributed to its long-standing status among theoreticians. First, QCD's phase structure has the potential to be nearly arbitrarily rich, owing to the complexities of the gluon-mediated interaction, the wide variety of potential quark pairing structures, and the asymptotic freedom which is obtained at large densities. Second, until very recently it has been nearly impossible to probe the phase diagram experimentally and thereby constrain the number of "good" models. As a result, within the general bounds provided by the structure of QCD, each theoretician is limited only by his imagination as regards the varied exotic phases in which quark matter might exist, particularly at intermediate to large densities. Examples of such postulated phases include the color superconducting 2SC and CFL phases, superconducting phases with condensed mesons (e.g., CFLK$^{\pm}$, CFLK^{0}, CFL$\pi^{\pm}$), strange quark matter (e.q., stranglets, strange stars), and quarkyonic matter, among others [8, 30, 64–71].

In principle, a complete QCD phase diagram would involve an exhaustive analysis of the phases of the six quark flavors over all energy scales. Fortunately, nature has provided a convenient method for approaching the complete phase structure systematically. In particular, the six flavors of quarks are spread out over a wide range of masses so that at chemical potentials below a given threshold, quarks whose masses are greater than that threshold may be neglected. Conveniently, given the masses observed in nature, only the two lightest quarks (up and down) are relevant at the densities observed in our everyday world. Thus, the case of $N_f = 2$ provides a very useful and physically meaningful starting place from which to study the QCD phase diagram.

In this chapter we begin our study of the QCD phase diagram by considering the two flavor PNJL model for both two and three colors. In doing so, we pay special attention to how the addition of the third quark color and confinement affects the phase structure of strongly interacting matter. In particular, we find that the existence of a third quark color suppresses color superconductivity at low chemical potentials, thereby greatly increasing the hadronic region of the phase diagram. In fact, while the two flavor model yields a phase structure incorporating the rough features of more elaborate models (e.g., a hadronic phase, color

superconductivity, and a deconfined quark gluon plasma), for $N_c = 3$ the onset of color superconductivity is delayed to chemical potentials large enough that the strange quark can no longer be consistently neglected. Thus, we are naturally led to consider the three flavor PNJL model, which is the subject of Chapters 3 and 4.

2.2 Two Flavor NJL Model

Recalling the general NJL Lagrangian of Eq. (1.9) and noting that the six-quark interaction is absent in the two flavor system, we write the two flavor NJL Lagrangian in the form

$$\mathcal{L}_{2F} = \overline{q}\left(i\partial\!\!\!/ - \hat{m} + \mu\gamma^0\right)q + \mathcal{L}_\sigma^{(4)} + \mathcal{L}_d^{(4)}, \tag{2.1}$$

$$\mathcal{L}_\sigma^{(4)} = G\Big[\left(\overline{q}q\right)^2 + \left(\overline{q}i\gamma_5\boldsymbol{\tau}q\right)^2\Big], \tag{2.2}$$

$$\mathcal{L}_d^{(4)} = H\Big[\left(\overline{q}i\gamma_5\tau_2\lambda_2 C\overline{q}^T\right)\left(q^T C i\gamma_5\tau_2\lambda_2 q\right) + \left(\overline{q}\tau_2\lambda_2 C\overline{q}^T\right)\left(q^T C\tau_2\lambda_2 q\right)\Big], \tag{2.3}$$

where we have introduced the quark chemical potential μ, and $\mathcal{L}_\sigma^{(4)}$ and $\mathcal{L}_d^{(4)}$ are responsible for spontaneous chiral symmetry breaking and diquark pairing, respectively. The coupling coefficients are $G, H > 0$, corresponding to attractive quark-quark interactions, while $\boldsymbol{\tau} = (\tau_1, \tau_2, \tau_3)$ is the vector of Pauli matrices in flavor space, λ_2 is the second Pauli (for $N_c = 2$ colors) or Gell-Mann (for $N_c = 3$) matrix in color space, and C is the charge conjugation operator. We now make two observations regarding this Lagrangian. First, the coefficients G and H subsume all of the gluon-mediated interactions of QCD into themselves. Second, by using four-quark point interaction vertices, our theory is no longer renormalizable and therefore requires the introduction of a high-momentum cutoff (Λ) to regulate the theory. This cutoff will serve as a parameter of our model and will be determined along with the other parameters (namely, $\hat{m}$, G, and H) by fitting to various experimentally determined, or otherwise known, quantities. We are free to choose either a 3- or 4-momentum cutoff, but in order to maintain contact with the majority of the literature and to remain applicable in the finite temperature formalism, we will choose the former.

In order to complete the definition of our model, we must now specify a method for fixing the parameters $\hat{m}$, G, H, and Λ. For simplicity, we treat the situation of equal up and down quark masses and follow the standard prescription in which m, G, and Λ are fixed by fitting to the pion mass ($m_\pi = 139.3$ MeV) and decay constant ($f_\pi = 92.3$ MeV) in vacuum, along with the chiral condensate determined from QCD sum rules [$\langle\overline{u}u\rangle \approx \langle\overline{d}d\rangle = -(240 \pm 20)$ MeV$)^3$] [16, 20]. The diquark coupling H can be related to G by means of a Fierz transformation which connects the $\mathcal{L}_\sigma^{(4)}$ and $\mathcal{L}_d^{(4)}$ vertices so that for $N_c = 2$ we have $H = G$, while for $N_c = 3$ we have $H = 3G/4$. The result of this fitting procedure is given in Table 2.1, which is taken

N_c	m [MeV]	$G\Lambda^2$	$H\Lambda^2$	Λ	M [MeV]
2	4.5	3.13	3.13	780	360
3	5.5	2.13	1.60	650	323

Table 2.1: Parameters for the two flavor NJL model: the bare quark mass m, chiral and diquark couplings G and H, and the spatial momentum cutoff Λ [72, 73]. Also shown is the effective quark mass M at $\mu = T = 0$.

from [72, 73].

2.3 Mean Field Approximation

The condensates preferred by our chosen interaction are the flavor symmetric chiral and diquark condensates in the spin-parity 0^+ channel [2, 20]:

$$\sigma = \langle \overline{q} q \rangle \,, \qquad d = \left\langle q^T C \gamma_5 \tau_2 \lambda_2 q \right\rangle , \tag{2.4}$$

where σ represents the degree to which the system has spontaneously broken $SU(3)_A$ chiral symmetry and d is the amplitude of quark Cooper pairing. In particular, by writing out the color and flavor indices explicitly, one finds

$$d = -\left\langle u_r^T C \gamma_5 d_g \right\rangle + \left\langle u_g^T C \gamma_5 d_r \right\rangle + \left\langle d_r^T C \gamma_5 u_g \right\rangle - \left\langle d_g^T C \gamma_5 u_r \right\rangle , \tag{2.5}$$

where (u, d) and (r, g) denote up and down flavors and red and green colors, respectively. Thus, the structure of d ensures that a quark pair will be a color and flavor singlet consisting of one quark of each color and flavor. Working in mean field and neglecting quadratic fluctuations of the fields, we expand the products of operators appearing in the Lagrangian as

$$\begin{aligned} XY &= [\langle X \rangle + (X - \langle X \rangle)][\langle Y \rangle + (Y - \langle Y \rangle)], \\ &= \langle X \rangle \langle Y \rangle + \langle X \rangle (Y - \langle Y \rangle) + (X - \langle X \rangle) \langle Y \rangle + (X - \langle Y \rangle)(X - \langle Y \rangle), \\ &\approx \langle X \rangle \langle Y \rangle + \langle X \rangle (Y - \langle Y \rangle) + (X - \langle X \rangle) \langle Y \rangle , \\ &= \langle X \rangle Y + X \langle Y \rangle - \langle X \rangle \langle Y \rangle . \end{aligned} \tag{2.6}$$

The mean field Lagrangian thus becomes

$$\mathcal{L}_{2F} = \overline{q} \left(i\partial\!\!\!/ - \hat{m} + 2G\sigma + \mu\gamma^0 \right) q - H d^* (q^T C \gamma_5 \tau_2 \lambda_2 q) + H d (\overline{q} \gamma_5 \tau_2 \lambda_2 C \overline{q}^T) - \mathcal{V}_{2F}(\sigma, d), \tag{2.7}$$

where $\mathcal{V}_{2F}(\sigma, d) = G\sigma^2 + H|d|^2$ prevents double-counting the degrees of freedom in our mean field treatment.

Next, in order to transform the Lagrangian to Gaussian form we introduce the Nambu-Gor'kov spinor

$$\Psi = \frac{1}{\sqrt{2}} \begin{pmatrix} q \\ q^C \end{pmatrix}, \tag{2.8}$$

where $q^C \equiv C\overline{q}^T$ is the charge-conjugate quark field. Symmetrizing the first term in Eq. (2.7) with respect to the Nambu-Gor'kov indices and defining the effective mass and gap

$$\hat{M} = \hat{m} - 2G\sigma, \qquad \Delta = -2Hd, \tag{2.9}$$

we can write the Lagrangian in the form

$$\mathcal{L}_{2F} = \overline{\Psi} S^{-1} \Psi - \mathcal{V}_{2F}(\sigma, d), \tag{2.10}$$

where the inverse propagator is

$$S^{-1}(x) = \begin{pmatrix} i\partial\!\!\!/ - \hat{M} + \mu\gamma^0 & \Delta\gamma_5\tau_2\lambda_2 \\ -\Delta^*\gamma_5\tau_2\lambda_2 & i\partial\!\!\!/ - \hat{M} - \mu\gamma^0 \end{pmatrix}. \tag{2.11}$$

Thus, we have cast the mean field NJL model in the form of a free theory which can be solved exactly. In particular, the quasiparticle dispersion relations are simply the poles of the propagator in Eq. (2.11). We now proceed to calculate these eigenvalues in both the two- and three-color cases.

2.3.1 Eigenvalues for $N_c = 2$

In order to compute the eigenvalues for $N_c = 2$ we first transform the inverse propagator in Eq. (2.11) to momentum space:

$$S^{-1}(k) = \begin{pmatrix} k\!\!\!/ - \hat{M} + \mu\gamma^0 & \Delta\gamma_5\tau_2\lambda_2 \\ -\Delta^*\gamma_5\tau_2\lambda_2 & k\!\!\!/ - \hat{M} - \mu\gamma^0 \end{pmatrix}. \tag{2.12}$$

We note that while the Nambu-Gor'kov indices are written explicitly, each of the four elements appearing in $S^{-1}(k)$ is itself a 16×16 matrix, having 4 Dirac, 2 color, and 2 flavor indices. The eigenvalues of the system are given by the roots of the equation $\det[S^{-1}(k_0)] = 0$. As shown in Appendix D.2.1, the determinant of

Eq. (2.12) can be written in terms of its blocks:

$$\det[S^{-1}(k)] = \det\left[\not{k} - \hat{M} + \mu\gamma^0 - (\Delta\gamma_5\tau_2\lambda_2)(\not{k} - \hat{M} - \mu\gamma^0)^{-1}(-\Delta^*\gamma_5\tau_2\lambda_2)\right]\det(\not{k} - \hat{M} - \mu\gamma^0). \quad (2.13)$$

Assuming equal mass up and down quarks ($\hat{m} = mI_2$), the argument of the first determinant above can be simplified significantly by commuting $\tau_2\lambda_2$ through the inverted Dirac matrix (which is both color and flavor independent) and noting that $\tau_2^2 = \lambda_2^2 = I_2$. In addition, it is easily verified that

$$(\not{k} - \hat{M} - \mu\gamma^0)^{-1} = \frac{\not{k} + \hat{M} - \mu\gamma^0}{(k_0 - \mu)^2 - E_k^2}, \quad (2.14)$$

where $E_k = \sqrt{\mathbf{k}^2 + M^2}$ is the energy of a free quark of mass M. Using these facts and taking the now trivial determinant over color and flavor indices, we obtain

$$\det[S^{-1}(k)] = \det\left[\not{k} - M + \mu\gamma^0 - |\Delta|^2\,\frac{\not{k} - M - \mu\gamma^0}{(k_0 - \mu)^2 - E_k^2}\right]^4 \det(\not{k} - M - \mu\gamma^0)^4. \quad (2.15)$$

After writing out the Dirac indices and a bit of algebra (see Appendix D for details) we obtain the eigenvalues:

$$E_{1,2} = \sqrt{(E_k \pm \mu)^2 + |\Delta|^2}, \quad (2.16)$$

each with multiplicity 16, though we note that the Nambu-Gor'kov formalism has doubled the number of degrees of freedom, so that only 8 of each eigenvalue are "physical" (4 Dirac $\times$ 2 color $\times$ 2 flavor indices). Thus, we find that for $N_c = 2$ all 16 eigenvalues of the system are gapped, half corresponding to quasiparticles ($-$), and half to quasiholes ($+$).

2.3.2 Eigenvalues for $N_c = 3$

In the $N_c = 3$ case, the momentum-space inverse propagator is again given by Eq. (2.12), but with λ_2 the second Gell-Mann matrix, rather than the second Pauli matrix. Thus, each block is now a 24×24 matrix. The expression in Eq. (2.13) similarly holds for the $N_c = 3$ case, but while we can commute the $\tau_2\lambda_2$ and utilize the fact that $\tau_2^2 = I_2$ as before, it is no longer true that $\lambda_2^2 = I_2$. Rather, we now have $\lambda_2^2 = \mathrm{diag}(1, 1, 0)$, so that the eigenvalues will fall into two classes. Two-thirds of the eigenvalues (those corresponding to the first and second diagonal elements of λ_2^2) will be of the form of Eq. (2.16), while the

remaining third will be ungapped. The detailed calculation is given in Appendix D.3, and the result is:

$$E_{1,2} = \sqrt{(E_k \pm \mu)^2 + |\Delta|^2} \qquad \text{multiplicity 16,} \tag{2.17}$$

$$E_{3,4} = |E_k \pm \mu| \qquad \text{multiplicity 8.} \tag{2.18}$$

We can understand the appearance of ungapped excitations in the $N_c = 3$ case by considering the explicit form of the diquark pairing amplitude, given in Eq. (2.5). In this form we see that the system pairs up (red) with down (green) quarks, as well as up (green) with down (red), while blue quarks remain unpaired. Thus, in the $N_c = 2$ case, in which there are no blue quarks, all quark colors and flavors participate in the pairing, thereby inducing gaps into all quasiparticle excitations. In the $N_c = 3$ case, however, blue quarks are unpaired and the corresponding one-third of the eigenvalues are the ungapped excitations of free particles.

Having computed the eigenvalues for both the $N_c = 2$ and $N_c = 3$ cases, we are now in a position to evaluate the thermodynamic potential of the system, from which we can construct the QCD phase diagram.

2.3.3 Thermodynamic Potential

The partition function of the system can be expressed in path-integral formalism as

$$\mathcal{Z} = \int D[\overline{q}, q]\, e^{-S_E[\overline{q},q]}, \tag{2.19}$$

where the Euclidean action is defined as

$$S_E[\overline{q}, q] = \int_0^\beta d\tau \int d^3\mathbf{x} \left(\overline{q}\gamma^0 \partial_\tau q + \mathcal{H}\right), \tag{2.20}$$

with $\beta = 1/T$ the inverse temperature (and $k_B = 1$ throughout). Thus, having cast the Lagrangian in the quadratic form of Eq. (2.10), the Gaussian integral over the quark fields can be performed exactly so that we obtain

$$\begin{aligned}
\mathcal{Z} &= \int D[\overline{q}, q]\, e^{-\int_0^\beta d\tau \int d^3\mathbf{r} \left(\overline{\Psi} S^{-1} \Psi + \mathcal{V}_{2F}\right)}, \\
&= e^{-\beta V \mathcal{V}_{2F}} \sqrt{\int D[\overline{\Psi}, \Psi]\, e^{-\int_0^\beta d\tau \int d^3\mathbf{r}\, \overline{\Psi} S^{-1} \Psi}}, \\
&= e^{-\beta V \mathcal{V}_{2F}} \sqrt{\det(\beta S^{-1})}, \\
&= e^{-\beta V \mathcal{V}_{2F} + \frac{1}{2} \ln \det(\beta S^{-1})},
\end{aligned} \tag{2.21}$$

where V is the volume of the system and we have used the identity $\mathrm{tr}\ln A = \ln\det A$ to rewrite the last line above. In addition, the square root in the second line comes from doubling the number of degrees of freedom in the path integral from $(\overline{q}, q)$ to $(\overline{\Psi}, \Psi)$. The thermodynamic potential per unit volume ($\Omega = -T\ln\mathcal{Z}/V$) is therefore

$$\Omega = -\frac{T}{2V}\,\mathrm{tr}\ln(\beta S^{-1}) + \mathcal{V}_{2F}. \tag{2.22}$$

The trace in Eq. (2.22) is taken over the discrete indices (Dirac, color, flavor, and Nambu-Gor'kov) as well as the continuous labels $(\tau, \mathbf{r})$, or equivalently $(i\omega_n, \mathbf{k})$, where $\omega_n = (2n+1)\pi T$ are the fermionic Matsubara frequencies. Choosing the latter set of variables, by virtue of our interest in finite temperature effects, and writing out the trace over $(i\omega_n, \mathbf{k})$ explicitly, we obtain

$$\Omega = -\frac{T}{2}\sum_n \int \frac{d^3\mathbf{k}}{(2\pi)^3}\,\mathrm{tr}\ln\left[\beta S^{-1}(i\omega_n, \mathbf{k})\right] + \mathcal{V}_{2F}. \tag{2.23}$$

This result is of the standard form except for the unusual factor of $1/2$ present in the first term, which accounts for the double-counting of the degrees of freedom inherent in the Nambu-Gor'kov formalism. We can take our expression a step further by noting that the eigenvalues of the system $E_j(\mathbf{k})$ are the poles of $S^{-1}(i\omega_n, \mathbf{k})$ so that

$$\det\left[\beta S^{-1}(i\omega_n, \mathbf{k})\right] = \prod_j \beta\left[i\omega_n - E_j(\mathbf{k})\right].$$

Inserting this expression into Eq. (2.22) and performing the Matsubara sum (see Appendix C for details) we obtain

$$\Omega = -\frac{T}{2}\sum_j \int \frac{d^3\mathbf{k}}{(2\pi)^3}\left[\ln(1+e^{-\beta E_j}) + \frac{1}{2}\beta\Delta E_j\right] + \mathcal{V}_{2F}, \tag{2.24}$$

where $\Delta E_j = E_j - E_j^{free}$ is the difference between the eigenvalue and its value in the non-interacting case (without absolute values). This term is required to ensure that $\Omega = 0$ when all condensates are set to zero at $T = 0$, so that Ω is measured with respect to the ground state of the non-interacting Dirac sea.

Having obtained the thermodynamic potential, we now proceed to minimize it with respect to the condensates σ and d at each point (μ, T), and thereby obtain the phase diagram in both the two and three color cases.

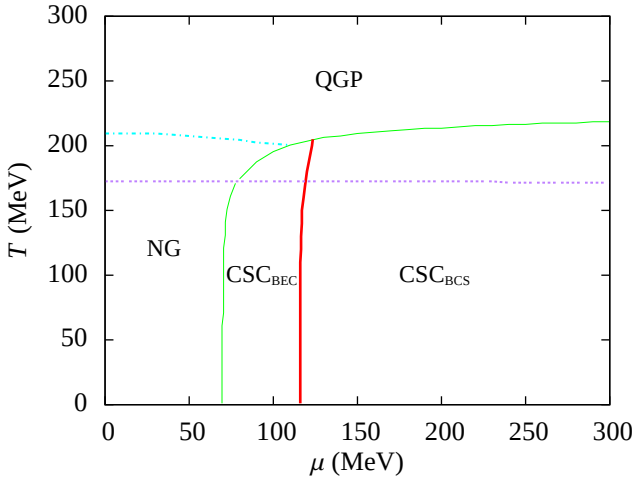

Figure 2.1: Phase diagram for the two flavor, two color NJL model. Solid (green) lines denote second-order transitions while the dash-dotted (cyan) and dotted (blue) lines denote the chiral and BEC-BCS crossovers respectively. The BEC-BCS crossover is defined by $M(\mu, T) = \mu$.

2.4 Two Color NJL Phase Diagram

The eigenvalues in the case $N_c = 2$ are given in Eq. (2.16), so that recalling Eq. (2.24), the thermodynamic potential becomes

$$\Omega(\sigma, d) = -8T \sum_{j=1}^{2} \left[\ln(1 + e^{-\beta E_j}) + \frac{1}{2} \beta \Delta E_j \right] + \mathcal{V}_{2F}(\sigma, d). \tag{2.25}$$

Having fixed the parameters m, G, and Λ, as described in subsection 2.2, we now minimize Ω with respect to σ and d, which yields the phase diagram in Fig. 2.1. The three phases are the chirally broken Nambu-Goldstone (NG) phase with $\sigma \neq 0$ and $d = 0$, a color superconducting (CSC) phase with $d \neq 0$, and which may or may not be chirally broken, and the quark-gluon plasma (QGP) with $\sigma \sim 0$ and $d = 0$. We note that while in the chiral ($m \to 0$) limit the QGP is defined by $\sigma = d = 0$, the presence of a non-zero bare quark mass ($m = 4.5$ MeV) turns the chiral phase transition into a smooth crossover, blurring the distinction between the NG and QGP phases. Nonetheless, while no longer a true phase transition, we define the crossover temperature T_c as the location of the maximum in the $d\sigma/dT$, as shown in Fig. 2.2.

At low temperatures the NG-CSC phase transition occurs at a critical chemical potential $\mu_c = m_\pi/2 = 70$ MeV, precisely half of the pion mass m_π, as is expected from general considerations [72]. Roughly speaking, the system will begin pairing as soon as there is sufficient energy to generate a pion (i.e. a quark pair) from the vacuum.

In addition to the three phases just discussed, we also make a distinction within the CSC phase between

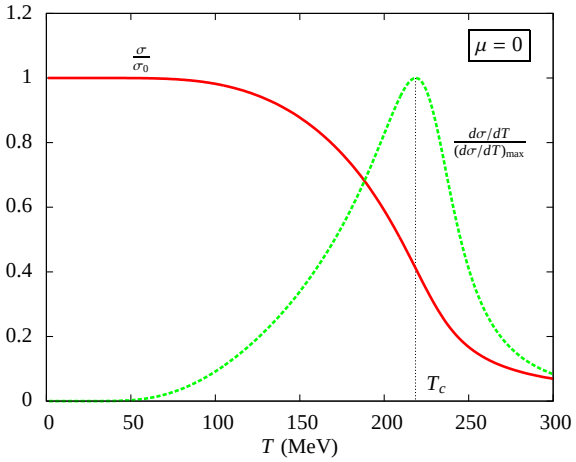

Figure 2.2: Normalized $d\sigma/dT$ vs. temperature at $\mu = 0$ in the two flavor, two color NJL model.

regions characterized by tightly bound diquark molecules (BEC) and delocalized weakly bound quark Cooper pairs (BCS). The blue dotted line in Fig. 2.1 demarks the boundary between these regions, which is defined by $M(\mu, T) = \mu$, and is smooth crossover at all temperatures. As this BEC-BCS crossover will be a topic of interest throughout the remainder of our work, let us now investigate the transition in more detail.

2.4.1 BEC-BCS Crossover

In order to begin our discussion of the crossover from tightly bound diquark molecules to weakly bound Cooper pairs we first consider the quasiparticle excitation spectrum given in Eq. (2.16). In particular, we ask the question, "At what momentum is the quasiparticle energy minimized?" Noting that E_1 corresponds to the quasihole energy, while E_2 is the quasiparticle energy, we set $dE_2/dk = 0$ and solve for the momentum, which yields two possible minima:

$$(1)\ \ k_1 = 0 \qquad\qquad E_2(k_1) = \sqrt{(\mu - M)^2 + |\Delta|^2}\ ,$$

$$(2)\ \ k_2 = \sqrt{\mu^2 - M^2} \qquad\qquad E_2(k_2) = |\Delta|\ ,$$

where the first solution always exists, but the second exists only for $\mu > M$. If this condition is met then $E_2(k_2) < E_2(k_1)$ and the quasiparticle energy is minimized for $k = \sqrt{\mu^2 - M^2} \equiv k_F$, which we recognize as the quark Fermi momentum. This corresponds to a weakly bound (BCS) Cooper pair whose component quarks have momenta $\mathbf{k}$ and $-\mathbf{k}$, where $|\mathbf{k}| = k_F$. On the other hand, if $\mu < M$ then only the first solution exists and the quasiparticle energy is minimized for $k = 0$. In this case, the paired quarks are at rest with respect to one another, and the excitation energy is simply the gap $|\Delta|$. This corresponds to a tightly bound diquark molecule, the low energy excitations of which simply involve the quarks moving together at non-zero momentum.

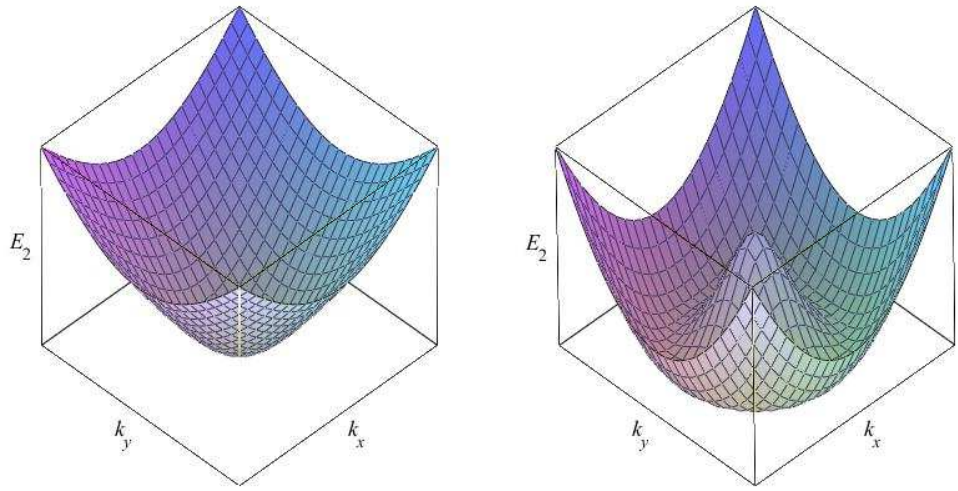

Figure 2.3: Quasiparticle dispersion for the CSC phase of the two flavor, two color NJL model, Eq. (2.16). The dependence on k_z, which is identical to that of k_x and k_y is neglected for the sake of representation . (a) For $\mu < M(\mu, T)$ the dispersion's minimum is at $k = 0$ and the diquark pair is a tightly bound (BEC) molecule. (b) For $\mu > M(\mu, T)$, the dispersion's minimum is at $k = \sqrt{\mu^2 - M^2}$ and the diquark pair is a weakly bound (BCS) Cooper pair.

Having identified the BEC and BCS regimes of quark pairing, it is instructive to consider the low-energy excitations in each regime. First, in the BEC regime we expand $E_2(k)$ about $k = 0$, which gives

$$E_2(k) \approx E_2(0) + \frac{M - \mu}{E_2(0)} \frac{k^2}{2M} + \cdots \tag{2.26}$$

In this form, we see that at low energies, the quasiparticle dispersion is of the form of a free particle with an effective mass

$$M_{\text{eff}}^{\text{BEC}} = \left(\frac{E_2(0)}{M - \mu} \right) M = M \sqrt{1 + \frac{|\Delta|^2}{(M - \mu)^2}}. \tag{2.27}$$

The free particle-like dispersion is consistent with our picture of a tightly bound molecule in which the diquark ground state consists of two quarks at rest ($k = 0$), while the low energy excitations involve the quarks moving together at small $k \neq 0$, with an effective mass that is modified by their interaction strength $|\Delta|$.

Turning now to the BCS regime, expanding Eq. (2.16) about $k = k_F$ yields

$$E_2(k) \approx |\Delta| + \frac{\mu^2 - M^2}{2\mu^2 |\Delta|} (k - k_F)^2 + \cdots \tag{2.28}$$

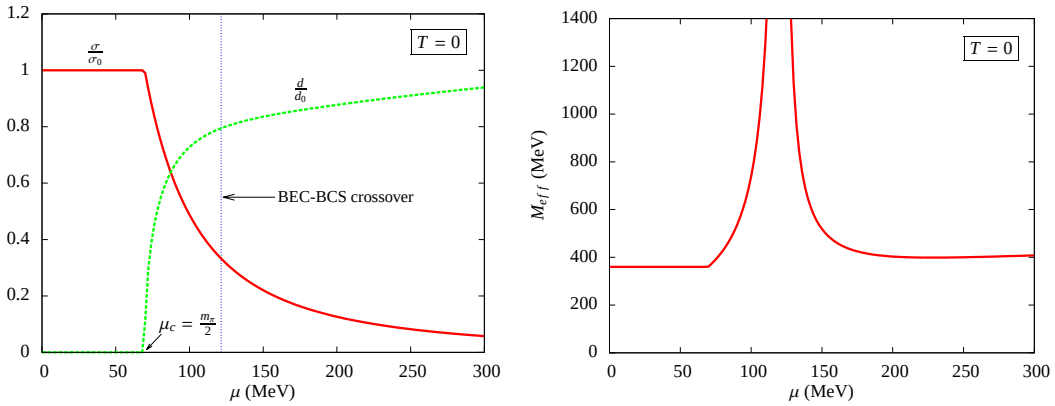

Figure 2.4: Properties of the two flavor, two color NJL model at $T = 0$. (a) Normalized chiral and diquark condensates, where σ_0 and d_0 are the condensates' maximum values. Note both the second-order NG-CSC transition at $\mu_c = m_\pi/2$ and the smooth crossover from the BEC to BCS pairing regimes at $\mu = 121$ MeV. (b) Effective quark mass, $M_{\text{eff}} = (\partial^2 E_2/\partial k^2)^{-1}|_{k=0}$, across the BEC-BCS crossover.

This expression is again consistent with a weakly bound quark Cooper pair with momenta $(\mathbf{k}, -\mathbf{k})$ and $|\mathbf{k}| = k_F$ and binding energy $|\Delta|$. In order to excite the diquark pair, one must first expend an energy $|\Delta|$ to break the Cooper pair, and then give the liberated quark a small "kick," modifying its momentum from its unperturbed position on the Fermi surface. Nonetheless, even after its liberation from the Cooper pair, the quark's effective mass is still modified by the presence of the other quarks surrounding it, and becomes

$$M_{\text{eff}}^{\text{BCS}} = \left(\frac{\mu^2}{\mu^2 - M^2}\right)|\Delta|. \tag{2.29}$$

As indicated in Fig. 2.4(a), at low μ when the system is in the NG phase, the chiral condensate, and therefore the constituent quark mass $M = m - 2G\sigma$, remains constant. Further, since quarks are unpaired ($\Delta = 0$), the effective quark mass M_{eff} and constituent quark mass M are identical. In the opposite limit, at large μ, chiral symmetry is asymptotically restored so that $M \to m \approx 0$, while the BCS pairing gap plateaus so that M_{eff} also approaches a constant value. As shown in Fig. 2.4(b), in between these two limits as the system moves through the BEC-BCS crossover at $\mu = 121$ MeV, one observes a divergence in M_{eff}. Physically, this implies that even a finite momentum quasiparticle carries a vanishingly small kinetic energy.[1]

Having observed the phase structure of the two flavor, two color QCD phase diagram, let us now move on to observe the modifications made by the addition a third color, as is realized in nature.

[1]Care must be taken in applying the expansions Eqs. (2.26) and (2.28) very near the crossover. It is straightforward to show that these expansions are valid only for $|k - k_0| \ll \sqrt{\mu|M - \mu|}$, where $k_0 = 0$ on the BEC side and $k_0 = k_F$ on the BCS side of the transition. Thus, precisely at the crossover when $M = \mu$, the radius of convergence of the expansions goes to zero.

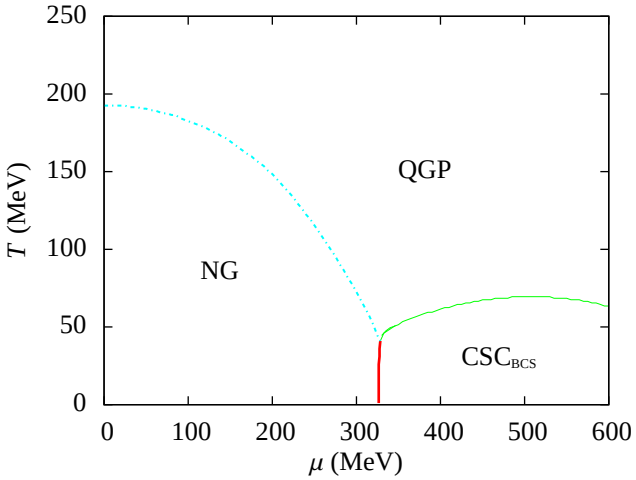

Figure 2.5: Phase diagram for the two flavor, three color NJL model. Line types are the same as in Fig. 2.1, with the additional thick (red) line denoting a first-order transition.

2.5 Three Color NJL Phase Diagram

While two color QCD provides an instructive introduction to the phases and characteristics of strongly interacting matter that we will observe throughout this work, the $N_c = 3$ case which we now consider moves us much closer to "real world" QCD. In particular, while QCD's SU(3) color symmetry guarantees that quark masses are independent of color, and there is therefore no physical basis on which to eliminate one of the three colors, no such fundamental flavor symmetry exists. Rather, the existence of two light flavors ($m_{u,d} \sim 5$ MeV), an intermediate mass flavor ($m_s \sim 100$ MeV), and three heavy flavors ($m_{c,b,t} \gtrsim 1,300$ MeV) of quarks implies that two flavor QCD is a very physically meaningful limit. In particular, for $\mu \ll m_s$ a strongly interacting system will have insufficient energy to generate strange quarks and the two light flavors will be the only physically relevant degrees of freedom. Thus, in this regime, two flavor QCD will be precisely the governing theory of the system.

Having previously computed the eigenvalues in the case $N_c = 3$, which are given in Eq. (2.18), the three color thermodynamic potential becomes

$$\begin{aligned}\Omega(\sigma,d) &= -4T\int\frac{d^3\mathbf{k}}{(2\pi)^3}\Big[2\ln(1+e^{-\beta E_1})+\beta\Delta E_1+2\ln(1+e^{-\beta E_2}) \\ &\quad +\beta\Delta E_2+\ln(1+e^{-\beta E_3})+\frac{1}{2}\beta\Delta E_3+\ln(1+e^{-\beta E_4})+\frac{1}{2}\beta\Delta E_4\Big]+\mathcal{V}_{2F}(\sigma,d). \quad (2.30)\end{aligned}$$

Minimizing the thermodynamic potential yields the phase diagram shown in Fig. 2.5. Comparing this phase diagram to the $N_c = 2$ case (Fig. 2.1), we observe a few notable differences.

First, we note that the inclusion of a third quark color significantly reduces the transition temperature to

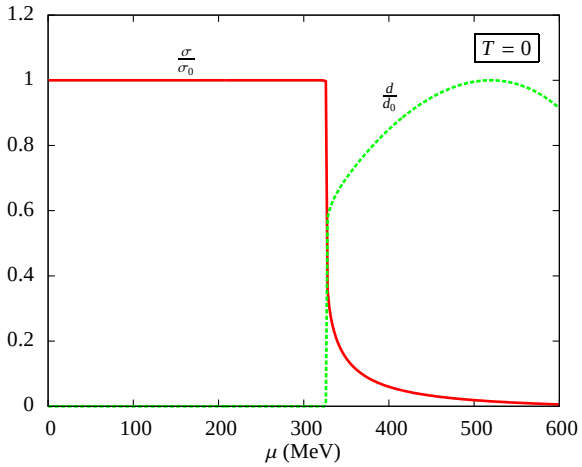

Figure 2.6: Normalized chiral and diquark condensates vs. μ at $T = 0$ in the NJL model with $N_f = 2$, $N_c = 3$. The discontinuous jump at $\mu = 327$ MeV indicates a first-order NG-CSC phase transition.

the QGP phase, particularly at large chemical potentials. While the CSC-QGP phase boundary is relatively independent of μ in both cases, the transition now occurs at $T_c^{N_c=3} \sim 65$ MeV, approximately one third the value of the two color transition temperature $T_c^{N_c=2} \sim 215$ MeV. Thus, the region dominated by quark pairing is significantly smaller for $N_c = 3$ than for $N_c = 2$.

The second significant difference between the $N_c = 2$ and $N_c = 3$ phase diagrams is that in the latter case there exists no BEC region of color superconductivity. Instead, the NG phase gives way immediately to a weakly-coupled $\mathrm{CSC}_{\mathrm{BCS}}$ phase via a *first*-order transition, as shown in Fig. 2.6. In addition, the critical chemical potential at which the NG-CSC transition occurs has increased by nearly a factor of 5 to $\mu_c = 327$ MeV, so that where the $\mathrm{CSC}_{\mathrm{BEC}}$ region existed in the $N_c = 2$ case, it is now energetically favorable to remain in the chirally broken NG phase.

2.6 Mean Field PNJL Model

Having constructed the phase diagram for the two flavor NJL model with both $N_c = 2$ and $N = 3$, we now investigate the effects of confinement by introducing the Polyakov loop. From Eq. (1.17) we observe that the static gauge field A_0 associated with the Polyakov loop enters the Lagrangian in the form of a color-dependent chemical potential, resulting in the modification $\mu \to \mu + iA_0$. Thus, the inverse propagator Eq. (2.11) now becomes

$$S^{-1}(x) = \begin{pmatrix} i\partial\!\!\!/ - \hat{M} + (\mu + iA_0)\gamma^0 & \Delta\gamma_5\tau_2\lambda_2 \\ -\Delta^*\gamma_5\tau_2\lambda_2 & i\partial\!\!\!/ - \hat{M} - (\mu + iA_0)\gamma^0 \end{pmatrix}. \tag{2.31}$$

Before constructing the phase diagram, we next compute the eigenvalues in both the $N_c = 2$ and $N_c = 3$ cases in order to observe how they are modified by the presence of the Polyakov loop.

2.6.1 Eigenvalues for $N_c = 2$

The eigenvalues in the $N_c = 2$ case are the poles of the momentum space propagator

$$S^{-1}(k) = \begin{pmatrix} \not{k} - \hat{M} + (\mu + iA_0)\gamma^0 & \Delta\gamma_5\tau_2\lambda_2 \\ -\Delta^*\gamma_5\tau_2\lambda_2 & \not{k} - \hat{M} - (\mu + iA_0)\gamma^0 \end{pmatrix}, \tag{2.32}$$

where λ_2 is the second Pauli matrix in color space. The field A_0 is a matrix in color space so in order to write down the inverse propagator explicitly we must fix the gauge. For convenience, we choose the *Polyakov gauge*, in which A_0 is diagonal and can therefore be expressed in the form $A_0 = \phi_3\lambda_3$. Computing the $4_D \times 2_c \times 2_f \times 2_{NG} = 32$ eigenvalues yields

$$E_{1,2} = \sqrt{(E_k + \mu)^2 + |\Delta|^2} \pm i\phi_3 \qquad \text{multiplicity 8,} \tag{2.33}$$

$$E_{3,4} = \sqrt{(E_k - \mu)^2 + |\Delta|^2} \pm i\phi_3 \qquad \text{multiplicity 8.} \tag{2.34}$$

Comparing this result to Eq. (2.16), we note that the presence of the Polyakov loop introduces an imaginary part to the eigenvalues. However, the fact that the eigenvalues appear in conjugate pairs will ensure that the thermodynamic potential is real so that its minimization remains well defined.

Before moving on to the $N_c = 3$ case, we now pause to briefly consider the Polyakov loop itself. While our discussion in Section 1.1.3 concerned the quantity $\Phi = \mathrm{tr}L/N_c$, which serves as an order parameter for confinement, the eigenvalues above have been expressed in terms of the variable ϕ_3. Thus, we must ask how these two quantities are related. From Eqs. (1.10) and (1.11) we observe that for the homogeneous gauge field we have adopted we obtain $\Phi = \mathrm{tr}(e^{i\beta A_0})/2$. Evaluating the matrix exponential with $A_0 = \phi_3\lambda_3$ leads to the relation

$$\Phi = \cos(\beta\phi_3). \tag{2.35}$$

From this expression we find that the physically relevant range $0 \leq \Phi \leq 1$ corresponds to $0 \leq \phi_3 \leq \pi T/2$, with $\phi_3 = 0$ ($\Phi = 1$) denoting a completely deconfined phase and $\phi_3 = \pi T/2$ ($\Phi = 0$) a completely confined phase. In between these limiting values the system can be interpreted as being either more or less confined, as we will discuss in more detail in Sections 2.7 and 2.8.

2.6.2 Eigenvalues for $N_c = 3$

In Sections 2.3.2 we found that the addition of blue quarks, which do not participate in pairing as a result of the color-flavor locking of $\mathcal{L}_d^{(4)}$, leads to a set of non-gapped eigenstates, while leaving unchanged the gapped quasiparticle excitations corresponding to red and green quark pairs. Unfortunately, we cannot apply this same reasoning to the three color PNJL model because in exchanging $\mathrm{SU}(2)_c$ for $\mathrm{SU}(3)_c$, we have introduced a second diagonal generator and so in the three color Polyakov gauge we have $A_0 = \phi_3\lambda_3 + \phi_8\lambda_8$. Thus, the Polyakov loop now involves two independent fields, ϕ_3 and ϕ_8. Solving for the eigenvalues in terms of these fields, we obtain

$$\begin{aligned}
E_{1,2} &= \sqrt{\left(E_k + \mu + \frac{i\phi_8}{\sqrt{3}}\right)^2 + |\Delta|^2} \pm i\phi_3 \qquad \text{multiplicity 8,} \\
E_{3,4} &= \sqrt{\left(E_k - \mu - \frac{i\phi_8}{\sqrt{3}}\right)^2 + |\Delta|^2} \pm i\phi_3 \qquad \text{multiplicity 8,} \\
E_{5,6} &= |E_k + \mu| \pm \frac{2i\phi_8}{\sqrt{3}} \qquad \text{multiplicity 4,} \\
E_{7,8} &= |E_k - \mu| \pm \frac{2i\phi_8}{\sqrt{3}} \qquad \text{multiplicity 4.}
\end{aligned} \tag{2.36}$$

We note that as expected on physical grounds, and as observed in the $N_c = 3$ NJL model, one-third of the eigenvalues are ungapped, corresponding to the unpaired blue quarks. The remaining two-thirds of the 48 eigenvalues consist of gapped quasiparticle and quasihole excitations with complex chemical potential $\mu_{qp} = -\mu_{qh} = \mu + i\phi_8/\sqrt{3}$. In addition, the gapped eigenvalues have an imaginary part of the same form as observed in the $N_c = 2$ case, while the ungapped eigenvalues are modified by the new field ϕ_8.

Next, we must again determine the relationship between the quantities ϕ_3 and Φ, this time for $N_c = 3$. Since A_0 is diagonal in the Polyakov gauge its exponentiation is trivial and we obtain the relation

$$\Phi = \frac{1}{3}\left(e^{i(\phi_3+\phi_8/\sqrt{3})} + e^{i(-\phi_3+\phi_8/\sqrt{3})} + e^{2i\phi_8/\sqrt{3}}\right). \tag{2.37}$$

At this point, we must say a few words about the traced Polyakov loop and its properties in our mean field treatment. First, it is evident from the definition of the thermal expectation values

$$\langle\Phi\rangle = \frac{1}{\mathcal{Z}}\,\mathrm{tr}\left(\Phi e^{-\beta H}\right), \qquad \langle\overline{\Phi}\rangle = \frac{1}{\mathcal{Z}}\,\mathrm{tr}\left(\overline{\Phi} e^{-\beta H}\right), \tag{2.38}$$

that we need *not* have $\langle\overline{\Phi}\rangle = \langle\Phi\rangle^*$. This follows from the fact that the Hamiltonian density corresponding

to Eq. (1.17) is

$$\mathcal{H} = \overline{q}\left(i\boldsymbol{\gamma}\cdot\nabla + \hat{m} - (\mu + iA_0)\gamma^0\right)q + \mathcal{H}_{int} + \mathcal{U}(\overline{\Phi},\Phi), \tag{2.39}$$

where $\boldsymbol{\gamma} = (\gamma_1,\gamma_2,\gamma_3)$. In particular, the quark-Polyakov loop coupling term $\overline{q}iA_0\gamma^0 q$ is *anti*-Hermitian, and is responsible for the complex eigenvalues obtained in Eqs. (2.34) and (2.36).[2]

Having observed that the PNJL model Hamiltonian is not Hermitian, it follows that

$$\left\langle\overline{\Phi}\right\rangle = \left[\frac{1}{\mathcal{Z}^\dagger}\,\mathrm{tr}\left(\Phi e^{-\beta H^\dagger}\right)\right]^* \neq \langle\Phi\rangle^*. \tag{2.40}$$

Despite this complexity, it is quite generally true that the thermal expectation values $\langle\Phi\rangle$ and $\left\langle\overline{\Phi}\right\rangle$ are both real quantities [74]. As a result, in mean field where we make the replacements $\Phi \to \langle\Phi\rangle$ and $\overline{\Phi} \to \left\langle\overline{\Phi}\right\rangle$, the imaginary part of Eq. (2.37) must vanish, which requires $\phi_8 = 0$.[3] Incidentally, this result also allows us to avoid the rather confounding prospect of a complex thermodynamic potential which would result from the presence of a non-zero ϕ_8 [21, 77–79].

Having eliminated ϕ_8, the eigenvalues in Eq. (2.36) reduce to

$$E_{1,2} = \sqrt{(E_k+\mu)^2 + |\Delta|^2} \pm i\phi_3 \qquad \text{multiplicity 8,} \tag{2.41}$$

$$E_{3,4} = \sqrt{(E_k-\mu)^2 + |\Delta|^2} \pm i\phi_3 \qquad \text{multiplicity 8,} \tag{2.42}$$

$$E_{5,6} = |E_k \pm \mu| \qquad \text{multiplicity 8,} \tag{2.43}$$

where we have redefined the subscripts as indicated. In fact, we might have expected these eigenvalues on the basis of the argument at the beginning of this section. That is, having eliminated ϕ_8, the Polyakov loop now couples only to red and green quarks, which happen to be the same colors which give rise to the gapped quasiparticle states. As a result, we would expect the Polyakov loop to generate an imaginary part of the gapped eigenvalues as in the $N_c = 2$ case, while leaving the ungapped (blue) eigenvalues unchanged. Finally, we note that after setting $\phi_8 = 0$, Eq. (2.37) reduces to

$$\Phi = \frac{1 + 2\cos(\beta\phi_3)}{3}. \tag{2.44}$$

[2] Any Hermitian operator possesses only real eigenvalues, so if we had not noticed at the outset, the appearance of complex eigenvalues in Eqs. (2.34) and (2.36) indicate that the PNJL Hamiltonian is decidedly non-Hermitian.

[3] In some of the literature authors attempt to account for the beyond-mean field effects of $\left\langle\overline{\Phi}\right\rangle \neq \langle\Phi\rangle^*$ by treating $\overline{\Phi}$ and Φ as independent quantities (interchangeable with ϕ_3 and ϕ_8) and minimizing Ω with respect to the full set $(\sigma, d, \overline{\Phi}, \Phi)$ [73, 75, 76]. However, as noted in [21], this treatment results in certain unphysical features and does not substantially improve any quantitative aspects of the model. Therefore, we do not consider such extensions of the PNJL model in this thesis.

Thus, the range $0 \leq \Phi \leq 1$ corresponds to $0 \leq \phi_3 \leq 2\pi T/3$, with $\phi_3 = 0$ corresponding to a completely deconfined phase and $\phi_3 = 2\pi T/3$ corresponding to a completely confined phase.

2.7 Two Color PNJL Phase Diagram

Having solved for the $N_f = N_c = 2$ eigenvalues in Eq. (2.34), the thermodynamic potential becomes

$$\Omega(\sigma, d, \Phi) = -4T \sum_{j=1}^{4} \int \frac{d^3\mathbf{k}}{(2\pi)^3} \left[\ln(1 + e^{-\beta E_j}) + \frac{1}{2}\beta \Delta E_j \right] + \mathcal{V}_{2F}(\sigma, d) + \mathcal{U}_{2C}(\Phi), \tag{2.45}$$

where, as the notation suggests, we have made use of the mean field relation $\langle \overline{\Phi} \rangle = \langle \Phi \rangle$, and have represented both by a single Φ in the argument of the Polyakov loop potential $\mathcal{U}_{2C}(\Phi)$. Following Brauner, we write this potential in the form [80, 81]

$$\frac{\mathcal{U}_{2C}(\overline{\Phi}, \Phi)}{T} = -b_2 \left[24\, \overline{\Phi}\Phi e^{-\beta a_2} + \ln\left(1 - \overline{\Phi}\Phi\right) \right], \tag{2.46}$$

where a_2 and b_2 are coefficients fixed by matching with two color lattice data at $\mu = 0$ [8, 21, 73, 82]. We can rewrite Eq. (2.45) in a somewhat more transparent form by defining the quantities $E_\pm = \sqrt{(E_k \pm \mu)^2 + |\Delta|^2}$ and combining the logarithms from the $j = 1, 2$ terms as follows:

$$\begin{aligned} \ln(1 + e^{-\beta E_1}) + \ln(1 + e^{-\beta E_2}) &= \ln(1 + e^{-\beta E_+} e^{-i\beta\phi_3}) + \ln(1 + e^{-\beta E_+} e^{+i\beta\phi_3}), \\ &= \ln\left[1 + \left(e^{i\beta\phi_3} + e^{-i\beta\phi_3}\right) e^{-\beta E_+} + e^{-2\beta E_+}\right], \\ &= \ln\left(1 + 2\Phi\, e^{-\beta E_+} + e^{-2\beta E_+}\right). \end{aligned} \tag{2.47}$$

Similarly combining the $j = 3, 4$ logarithms, the thermodynamic potential becomes

$$\Omega(\sigma, d, \Phi) = -4T \sum_{\pm} \int \frac{d^3\mathbf{k}}{(2\pi)^3} \left[\ln(1 + 2\Phi\, e^{-\beta E_\pm} + e^{-2\beta E_\pm}) + \beta \Delta E_\pm \right] + \mathcal{V}_{2F}(\sigma, d) + \mathcal{U}_{2C}(\Phi). \tag{2.48}$$

We can interpret this form of the thermodynamic potential by first noting that the logarithm in Ω has its physical origin in the entropy of the system since $\Omega = \varepsilon - Ts - \mu n$ and $s = V^{-1} \sum_k [f_k \ln f_k + (1 - f_k)\ln(1 - f_k)]$, where f_k is the Fermi distribution function. Since the logarithm in Eq. (2.48) is the result of adding logarithms corresponding to two distinct eigenvalues, the result is related to the entropy of two quasi-quarks. In a confined phase ($\Phi = 0$) there will be no isolated quarks to contribute to the system's entropy so that the terms weighted by $e^{-\beta E_\pm}$ vanish. On the other hand, in a deconfined phase ($\Phi = 1$) the two quarks may either be free (corresponding to the term $2e^{-\beta E_\pm}$) or "paired" (corresponding to the term $e^{-2\beta E_\pm}$).

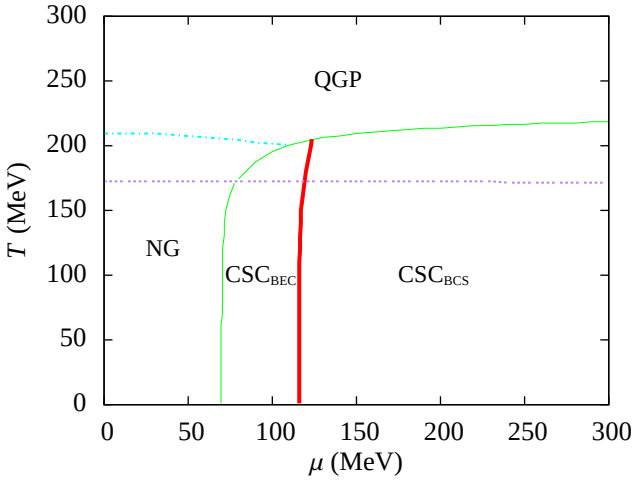

Figure 2.7: Phase diagram for the two flavor, two color PNJL model. Line types are the same as in Fig. 2.5, with the additional dotted (purple) line denoting the deconfinement crossover, defined as a maximum in $d\Phi/dT$.

Before constructing the phase diagram, we must now fix the Polyakov loop parameters a_2 and b_2 in Eq. (2.46). It is straightforward to show that in the pure gauge sector, where $\Omega = \mathcal{U}_{2C}(\Phi)$, the critical temperature for the first-order deconfinement transition is $T_c = a/\ln(24)$. Thus, one common method of parameter fixing is to determine a_2 by matching this pure gauge transition to the lattice QCD value of $T_\Phi^{N_f=0} = 270$ MeV [19, 80, 83]. The second parameter b_2, which is known with less certainty, can be fixed independently in order to ensure coincident chiral and deconfinement transitions [19] or related to a_2 via the QCD string tension, $b_2 = (\sigma_s/a_2)^3$, where $\sigma_s = (425 \text{ MeV})^2$ [80]. However, fixing a_2 in the pure gauge sector results in a deconfinement transition temperature approximately 30 MeV higher than the lattice QCD value of $T_\Phi^{N_f=2} = 173$ MeV. Since our present goal is to model the $N_f = N_c = 2$ QCD phase diagram, we therefore choose $a_2 = 565$ MeV in order to reproduce the two flavor lattice transition temperature and subsequently set $b_2 = (320 \text{ MeV})^3$ to reproduce the QCD string tension.

Minimizing Eq. (2.48) with respect to σ, d, and Φ yields the phase diagram in Fig. 2.7. Comparing to Fig. 2.1, we find that the inclusion of the Polyakov loop does not significantly alter the structure of the two color QCD phase diagram. Indeed, we appear to have simply overlaid a μ-independent deconfinement transition onto our previous non-confining (NJL) model. However, it is important to note that given our parameter choice for a_2, in the absence of quarks the deconfinement transition is first-order and occurs at $T_\Phi = 177$ MeV. Thus, the coupling between the quarks and the Polyakov loop has transformed the deconfinement transition from first-order to a smooth crossover, and has pulled the critical temperature for this transition down slightly. In fact, the difference between the chiral and deconfinement crossover temperatures at low μ is very nearly constant at $\Delta T_c = T_\sigma - T_\Phi = 35$ MeV, as shown in Fig. 2.8. So, while

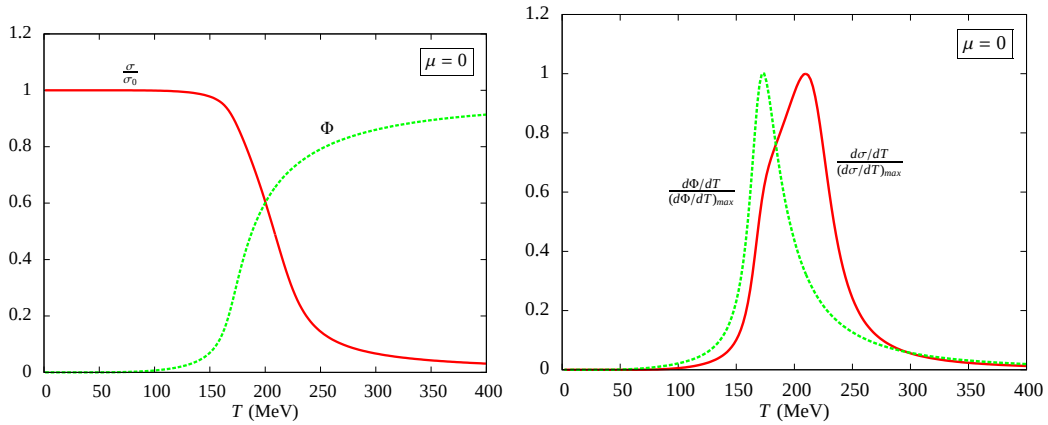

Figure 2.8: Near coincidence of the chiral and deconfinement crossovers at $\mu = 0$ in the $N_f = N_c = 2$ PNJL model. (a) Normalized chiral condensate and traced Polyakov loop. (b) Normalized $d\sigma/dT$ and $d\Phi/dT$. The transitions are nearly coincident, with $\Delta T = T_\sigma - T_\Phi \approx 21.5$ MeV, independent of μ.

the two crossovers are not coincident, they are certainly correlated.

Before moving on to consider the $N_c = 3$ phase diagram, we note one subtle feature of Fig. 2.8(b), namely the slight "bump" in $d\sigma/dT$ which accompanies the local maximum in $d\Phi/dT$. We will see a much more pronounced correlation between the two derivatives in the $N_c = 3$ case, but it is interesting to note that while the chiral and deconfinement crossovers do not coincide in the PNJL model, they do nonetheless influence one another.

2.8 Three Color PNJL Phase Diagram

Having solved for the $N_f = 2$, $N_c = 3$ eigenvalues in Eq. (2.42), the three color thermodynamic potential is

$$\Omega(\sigma, d, \Phi) = -4T \sum_{j=1}^{6} \int \frac{d^3\mathbf{k}}{(2\pi)^3} \left[\ln(1 + e^{-\beta E_j}) + \frac{1}{2}\beta \Delta E_j \right] + \mathcal{V}_{2F}(\sigma, d) + \mathcal{U}_{3C}(\Phi), \tag{2.49}$$

where, following Fukushima, we use the three color Polyakov loop potential [17, 21]

$$\frac{\mathcal{U}_{3C}(\overline{\Phi}, \Phi)}{T^4} = -\frac{a(T)}{2}\overline{\Phi}\Phi + b(T) \ln\left[1 - 6\,\overline{\Phi}\Phi + 4(\overline{\Phi}^3 + \Phi^3) - 3(\overline{\Phi}\Phi)^2\right], \tag{2.50}$$

where the temperature-dependent coefficients are

$$a(T) = a_0 + a_1\left(\frac{T_0}{T}\right) + a_2\left(\frac{T_0}{T}\right)^2, \qquad b(T) = b_3\left(\frac{T_0}{T}\right)^3, \tag{2.51}$$

a_0	a_1	a_2	b_3
3.51	-2.47	15.2	-1.75

Table 2.2: Coefficients of the three color Polyakov-loop potential $\mathcal{U}_{3C}(\Phi)$, given in Eq. (2.50) [21].

and where the coefficients a_i, and b_3 are determined by fitting to three color lattice data at $\mu = 0$. The constant T_0, which is the critical temperature for deconfinement in the pure gauge sector, has a value of $T_0 = 270$ MeV [17]. However, we will treat T_0 as a parameter of the theory, along with the various NJL couplings, and will fix its value by matching the $\mu = 0$ deconfinement transition from lattice QCD.

Combining the logarithms corresponding to $j = 1, 2$ and $j = 3, 4$, we can rewrite the thermodynamic potential in terms of Φ:

$$\begin{aligned}\Omega(\sigma, d, \Phi) &= -4T \int \frac{d^3\mathbf{k}}{(2\pi)^3} \Big[\ln\left[1 + (3\Phi - 1)e^{-\beta E_+} + e^{-2\beta E_+}\right] + \ln\left[1 + (3\Phi - 1)e^{-\beta E_-} + e^{-2\beta E_-}\right] \\ &\quad + \ln(1 + e^{-\beta E_5}) + \ln(1 + e^{-\beta E_6}) + \beta\Delta E_+ + \beta\Delta E_- + \frac{1}{2}\beta\Delta E_5 + \frac{1}{2}\beta\Delta E_6 \Big] \\ &\quad + \mathcal{V}_{3F}(\sigma, d) + \mathcal{U}_{3C}(\Phi), \end{aligned} \tag{2.52}$$

Comparing this expression to the $N_c = 2$ case in Eq. (2.48) we note that the coefficient of $e^{-\beta E_\pm}$ appearing in the logarithmic terms is now $3\Phi - 1$ instead of 2Φ.

Before constructing the three color phase diagram, we must also fit the parameter T_0 which appears in the Polyakov loop potential $\mathcal{U}_{3C}(\Phi)$. As in the $N_c = 2$ case, we fix T_0 in order to reproduce the lattice QCD deconfinement transition of $T_\Phi = 173$ MeV, which leads us to choose $T_0 = 200$ MeV. We must also address a certain ambiguity in the definition of the chiral crossover for $N_c = 3$ that did not exist in the $N_c = 2$ case. As shown in Fig. 2.9(b), the normalized $d\sigma/dT$ now has *two* local maxima, and we must determine which of these we will designate the chiral crossover. To a certain extent our choice is arbitrary, since the ambiguity arises from the fact that there is, in fact, no true chiral phase transition for $m \neq 0$. However, from Fig. 2.9(a), we see that the first (sharp) peak in $d\sigma/dT$ corresponds to the initial "drop off" of σ from its maximum value σ_0, which persists for $0 < T < 172$ MeV. That is, the chiral condensate (and consequently the constituent quark mass) is constant up to $T = 172$ MeV, but as the temperature increases further, the condensate decreases, and begins its descent with an infinite slope, akin to a square root divergence. While certainly an interesting feature, this behavior does not correspond to our notion of a crossover. Thus, we define the chiral crossover temperature T_σ as the location of the broader, smooth maximum at somewhat higher temperature than the slight discontinuity. As a result, the chiral and deconfinement crossovers will not coincide, but we shall discover that as μ increases, the difference between the crossover temperatures

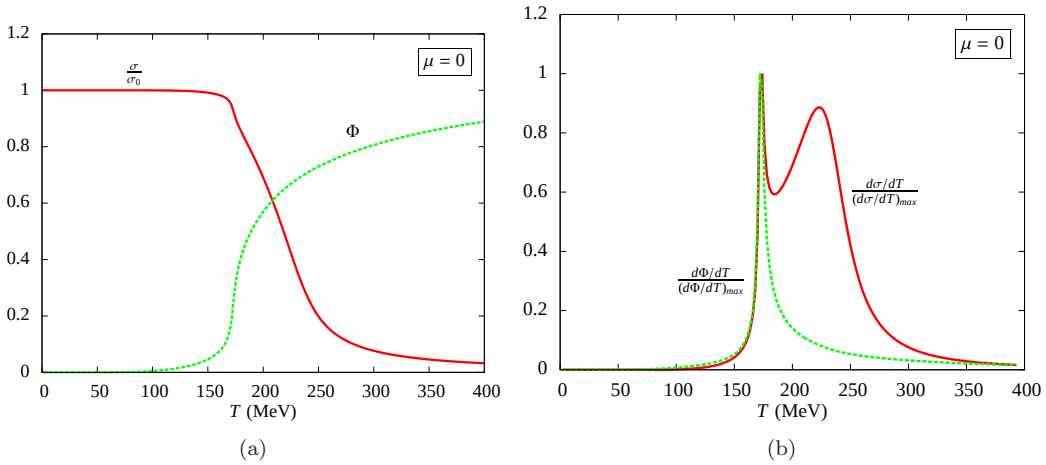

Figure 2.9: Near coincidence of the chiral and deconfinement crossovers at $\mu = 0$ in the $N_f = 2$, $N_c = 3$ PNJL model. (a) Normalized chiral condensate and traced Polyakov loop. (b) Normalized $d\sigma/dT$ and $d\Phi/dT$. Note the presence of two local maxima in $d\sigma/dT$: (1) a sharp maximum coincident with the deconfinement crossover, and (2) a broader, smooth maximum at a higher temperature ($\Delta T \approx 52$ MeV).

will decrease and eventually they will in fact coincide.

Minimizing the thermodynamic potential with respect to σ, d, and Φ yields the phase diagram in Fig. 2.10. Comparing to Fig. 2.5, we see that the coupling of the Polyakov loop to the quarks significantly increases the region of chiral symmetry breaking and diquark pairing. In the case of the NG phase, the crossover temperature to the QGP at $\mu = 0$ has increased by $\Delta T_\sigma = 31$ MeV. Meanwhile, the temperature to which diquark pairs exist has nearly doubled from $T_c^{NJL} \sim 65$ MeV to $T_c^{PNJL} \sim 125$ MeV. This suggests that the system has a strong aversion to simultaneously undergoing chiral symmetry breaking or diquark pairing on the one hand, and deconfinement on the other. Thus, deep in the NG phase where confinement is a dominant property, the system strongly prefers to obtain $\sigma \neq 0$. Similarly, at large μ the small value of Φ drives diquark pairing to persist to a much higher temperature than in the non-confining NJL model.

A second observation we make from Fig. 2.10 is that the deconfinement transition, while still not highly dependent on μ, is more obviously correlated with the chiral crossover, as well as the diquark pairs, than in the $N_c = 2$ case. While $\Delta T_c = 51$ MeV at $\mu = 0$, this difference decreases as the system moves to higher density, and the deconfinement crossover is very nearly coincident with the CSC-QGP transition at large μ.

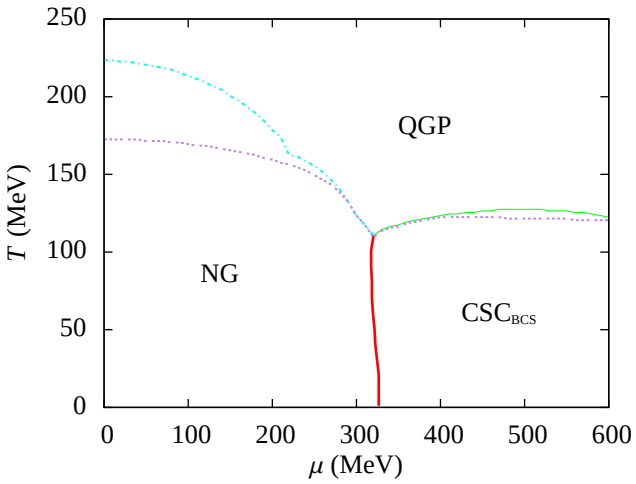

Figure 2.10: Phase diagram for the two flavor, three color PNJL model. Line types are the same as in Fig. 2.7.

Chapter 3

Phase Diagram of Massless Three Flavor QCD

3.1 Introduction

In the prior chapter we analyzed the phase structure of two flavor QCD, which is a useful approximation to the full theory at energies less than the strange quark mass $m_s \sim 100$ MeV. However, as shown in Fig. 2.5, our two flavor model predicts the realization of color superconducting phases for $\mu \gtrsim 320$ MeV, well above the density at which strange quarks may be expected to play an important role in QCD thermodynamics. Thus, if we hope to obtain a reliable picture of strongly interacting matter at these densities we are necessarily led to consider the three flavor system. The content of this chapter is based on [2].

The inclusion of the strange quark in our theory greatly enhances the richness of the possible QCD phase diagram in two ways. First, the number of possible quark pairing structures is expanded. For example, while the two flavor system is restricted to forming ud pairs, the three flavor system may also form us and ds pairs. As a consequence, the system may realize phases in which only one set of quark flavors pairs (e.g., 2SC, uSC, dSC), a color-flavor-locked (CFL) phase in which all flavors pair with equal magnitude, or an asymmetric CFL (ACFL) phase in which all flavors pair, but with unequal magnitudes [30, 83, 84].

The second way in which the strange quark affects the QCD phase diagram is by its role in the instanton-induced QCD axial anomaly. In particular, the axial anomaly, which in three flavor QCD gives rise to the Kobayashi-Maskawa, 't Hooft (KMT) effective six-quark interaction, plays a crucial role in determining both the properties of the light mesons and the phase structure of quark matter. In the first case, the anomaly is responsible for breaking the $\mathrm{U}(1)_A$ symmetry of QCD and giving rise to the anomalously large mass of the η' meson. In the second, recent work by Hatsuda *et al.* has demonstrated the importance of the axial anomaly in determining the topology of the QCD phase diagram [18, 85]. Specifically, they have shown that under the right circumstances the anomaly-induced attraction between chiral and diquark condensates leads to a low temperature critical point and a corresponding BCS-BEC crossover between the chirally broken Nambu-Goldstone phase and a color superconducting phase.

In this chapter we investigate the phases of dense quark matter by considering the massless three flavor PNJL model. We pay special attention to the impact of the axial anomaly-induced KMT interaction on the structure of the low temperature QCD phase diagram, and particularly the possibility of realizing a

low temperature critical point. We also carefully consider the combined effects of the axial anomaly and confinement by performing an expansion of the thermodynamic potential of the Ginzburg-Landau form and computing the lowest-order couplings between the quark condensates and the Polyakov loop.

3.2 Three Flavor PNJL Model

Following Abuki *et al.* and introducing the Polyakov loop via the standard prescription we write the three flavor PNJL Lagrangian [20]

$$\mathcal{L} = \overline{q}(i\partial\!\!\!/ - \hat{m} + (\mu + iA_0)\gamma^0)q + \mathcal{L}^{(4)} + \mathcal{L}^{(6)} - \mathcal{U}_{3C}(\overline{\Phi}, \Phi), \tag{3.1}$$

where we have introduced a factor of i to the gauge field A_0, as required at finite temperature (see Appendix B). The standard form of the three flavor four-quark interaction $\mathcal{L}^{(4)}$ is chosen to respect the full symmetry group of classical QCD and contains color-flavor-locked quark-quark interactions [65, 86]

$$\begin{aligned}
\mathcal{L}^{(4)} &= \mathcal{L}_\sigma^{(4)} + \mathcal{L}_d^{(4)}, && (3.2)\\
\mathcal{L}_\sigma^{(4)} &= G\sum_{a=0}^{8}[(\overline{q}\tau_a q)^2 + (\overline{q}i\gamma_5\tau_a q)^2], && (3.3)\\
\mathcal{L}_d^{(4)} &= H\sum_{A,A'=2,5,7}[(\overline{q}i\gamma_5\tau_A\lambda_{A'}C\overline{q}^T)(q^TCi\gamma_5\tau_A\lambda_{A'}q) + (\overline{q}\tau_A\lambda_{A'}C\overline{q}^T)(q^TC\tau_A\lambda_{A'}q)], && (3.4)
\end{aligned}$$

where τ_a are the U(3) flavor generators ($a = 0...8$), and τ_A and λ_A are the antisymmetric flavor and SU(3) color generators ($A, A' = 2, 5, 7$). We also find it useful to define the chiral and diquark operators

$$\begin{aligned}
\phi_{ij} &= (\overline{q}_R)_a^j(q_L)_a^i, && (3.5)\\
(d_L)_{ai} &= \epsilon_{abc}\epsilon_{ijk}(q_L)_b^jC(q_L)_c^k, && (3.6)\\
(d_R)_{ai} &= \epsilon_{abc}\epsilon_{ijk}(q_R)_b^jC(q_R)_c^k, && (3.7)
\end{aligned}$$

where i, j, k and a, b, c are flavor and color indices respectively and q_L and q_R denote states of left and right handed chirality. In terms of these operators, the four-quark interactions can be written in the compact form

$$\begin{aligned}
\mathcal{L}_\sigma^{(4)} &= 8G\mathrm{tr}(\phi^\dagger\phi), && (3.8)\\
\mathcal{L}_d^{(4)} &= 2H\mathrm{tr}(d_L^\dagger d_L + d_R^\dagger d_R). && (3.9)
\end{aligned}$$

$G\Lambda^2$	$H\Lambda^2$	$K\Lambda^5$	M (MeV)
1.926	1.74	12.36	355.1

Table 3.1: Coupling constants and dynamical quark mass for the massless three flavor NJL model. The high momentum cutoff is $\Lambda = 602.3$ MeV [16, 20].

The six-quark interaction can also be written as the sum of two terms

$$\mathcal{L}^{(6)} = \mathcal{L}^{(6)}_{\sigma} + \mathcal{L}^{(6)}_{\sigma d}, \tag{3.10}$$

$$\mathcal{L}^{(6)}_{\sigma} = -8K(\det\phi + \text{h.c.}), \tag{3.11}$$

$$\mathcal{L}^{(6)}_{\sigma d} = K'\left(\text{tr}[(d^{\dagger}_R d_L)\phi] + \text{h.c.}\right). \tag{3.12}$$

The first term, $\mathcal{L}^{(6)}_{\sigma}$, is the standard KMT interaction, which is the result of the instanton-induced QCD axial anomaly [25, 87]. The second term, $\mathcal{L}^{(6)}_{\sigma d}$, is the effective interaction between the chiral and diquark fields, mediated by the QCD instanton [18, 85].

To complete our model we must now fix the NJL parameters of our theory. The couplings G and K, as well as the cutoff Λ are fixed by fitting to experimentally determined mesonic properties, while H is related to G via a Fierz transformation, as discussed by Buballa [16], and are given in Table 3.1. The second anomaly coupling K' will be adjusted "by hand" to determine its effect on the QCD phase structure, and in particular the realization of a low T critical point. In addition, the Polyakov loop parameters a_i and b_3 are unchanged from the two flavor case, while the parameter T_0 is chosen to match our model's deconfinement transition at $\mu = 0$ to the massless lattice value of $T_{\Phi}^{N_f=3} = 154$ MeV [30, 82]. Throughout this chapter we assume that the bare masses of the quarks are zero.

3.3 Mean Field Approximation

The condensates favored by $\mathcal{L}^{(4)}$ and $\mathcal{L}^{(6)}$ are the flavor-symmetric chiral and diquark condensates in the spin-parity 0^+ channel:

$$\left\langle \overline{q}^i_a q^j_a \right\rangle = \sigma\delta_{ij}, \qquad \left\langle q^T C\gamma_5\tau_A\lambda_{A'} q\right\rangle = d\delta_{AA'}. \tag{3.13}$$

Expanding about these condensates and neglecting quadratic fluctuations, we obtain the mean field Lagrangian

$$\mathcal{L} = \overline{q}(i\partial\!\!\!/ - M + (\mu + iA_0)\gamma^0)q - \frac{1}{2}(\Delta^* q^T C\gamma_5\tau_A\lambda_A q + \text{H.c.}) - \mathcal{V}_{3F}(\sigma, d) - \mathcal{U}_{3C}(\overline{\Phi}, \Phi), \tag{3.14}$$

where H.c. denotes the Hermitian conjugate, the sum over $A = 2, 5, 7$ is implied, and the effective quark mass and BCS pairing gap are

$$M = m - 4G\sigma + 2K\sigma^2 + \frac{K'}{4}|d|^2, \qquad \Delta = -2d\left(H - \frac{K'}{4}\sigma\right). \tag{3.15}$$

In addition, the condensates contribute to the system's potential directly an amount

$$\mathcal{V}_{3F}(\sigma_i, d_i) = 2G\sum_{i=1}^{3}\sigma_i^2 - 4K\sigma_1\sigma_2\sigma_3 + \sum_{i=1}^{3}\left(H - \frac{K'}{2}\sigma_i\right)|d_i|^2. \tag{3.16}$$

In terms of the Nambu-Gor'kov spinor $\Psi = (q \;\; q^C)/\sqrt{2}$, we can now cast the Lagrangian in the quadratic form $\mathcal{L} = \overline{\Psi}S^{-1}\Psi - \mathcal{V}_{3F} - \mathcal{U}_{3C}$, where the inverse propagator in Nambu-Gor'kov space is

$$S^{-1}(k) = \begin{pmatrix} \not{k} - M + (\mu + iA_0)\gamma^0 & \Delta\gamma_5\tau_A\lambda_A \\ -\Delta^*\gamma_5\tau_A\lambda_A & \not{k} - M - (\mu + iA_0)\gamma^0 \end{pmatrix}, \tag{3.17}$$

Having cast the Lagrangian in Gaussian form, we may integrate over the fields $\overline{\Psi}$ and Ψ to obtain the thermodynamic potential:

$$\Omega = -\frac{T}{2}\sum_{i=1}^{72}\int^{\Lambda}\frac{d^3\mathbf{k}}{(2\pi)^3}\left[\ln(1 + e^{-\beta E_i}) + \frac{1}{2}\beta\Delta E_i\right] + \mathcal{V}_{3F}(\sigma_i, d_i) + \mathcal{U}_{3C}(\overline{\Phi}, \Phi), \tag{3.18}$$

where the E_i ($i = 1...72$) are the poles of Eq. (3.17). Working in the Polyakov gauge in which $A_0 = \phi_3\lambda_3 + \phi_8\lambda_8$, our next task is to compute these eigenvalues, from which we may obtain the thermodynamic potential.

3.4 Eigenvalues

From Eq. (3.17) we see that the presence of the Polyakov loop induces an effectively color-dependent chemical potential. We therefore define the effective chemical potential matrix $\hat{\mu}_{\text{eff}} = \mu + iA_0 = \text{diag}(\mu_1, \mu_2, \mu_3)$ where

$$\mu_1 = \mu + i\left(\phi_3 + \frac{\phi_8}{\sqrt{3}}\right), \qquad \mu_2 = \mu + i\left(-\phi_3 + \frac{\phi_8}{\sqrt{3}}\right), \qquad \mu_3 = \mu - \frac{2i\phi_8}{\sqrt{3}}. \tag{3.19}$$

Obtaining the 72 roots of Eq. (3.17)'s characteristic polynomial is a laborious calculation involving the properties of block matrices, the details of which are given in Appendix D. The resulting 18 distinct eigenvalues, each with multiplicity 4 (2 spin $\times$ 2 Nambu-Gor'kov), fall into two classes. The first class,

consisting of 12 distinct eigenvalues, can be written in the form

$$E_{1-12} = \sqrt{\left(E_k \pm \frac{\mu_i + \mu_j}{2}\right)^2 + |\Delta|^2} \pm \frac{\mu_i - \mu_j}{2}, \qquad i, j, = 1, 2, 3 \quad (i \neq j), \tag{3.20}$$

where $E_k = \sqrt{\mathbf{k}^2 + M^2}$, and the two $\pm$ are independent. The remaining six distinct eigenvalues are the roots of the polynomials $F(\omega_n, \pm E_k)$ which satisfy $\lim_{k\to\infty} E_i = \infty$, where

$$\begin{aligned} F(\omega_n, E_k) \;=\; & (\omega_n + E_k + \mu_1)(\omega_n - E_k - \mu_1)(\omega_n + E_k + \mu_2)(\omega_n - E_k - \mu_2)(\omega_n + E_k + \mu_3)(\omega_n - E_k - \mu_3) \\ & -|\Delta|^2(\omega_n + E_k + \mu_1)(\omega_n + E_k + \mu_2)(\omega_n - E_k - \mu_3)[(\omega_n - E_k - \mu_1) + (\omega_n - E_k - \mu_2)] \\ & -|\Delta|^2(\omega_n + E_k + \mu_1)(\omega_n + E_k + \mu_3)(\omega_n - E_k - \mu_2)[(\omega_n - E_k - \mu_1) + (\omega_n - E_k - \mu_3)] \\ & -|\Delta|^2(\omega_n + E_k + \mu_2)(\omega_n + E_k + \mu_3)(\omega_n - E_k - \mu_1)[(\omega_n - E_k - \mu_2) + (\omega_n - E_k - \mu_3)] \\ & +|\Delta|^4[(\omega_n + E_k + \mu_1) + (\omega_n + E_k + \mu_2) + (\omega_n + E_k + \mu_3)] \\ & \quad \times[(\omega_n - E_k - \mu_1) + (\omega_n - E_k - \mu_2) + (\omega_n - E_k - \mu_3)] - 4|\Delta|^6. \end{aligned} \tag{3.21}$$

The function $F(\omega_n, E_k)$ is an even sixth-order polynomial and therefore reducible to a cubic polynomial, whose solutions can be obtained exactly.[1] Thus, all of the model's eigenvalues can be obtained explicitly and the thermodynamic potential computed via Eq. (3.18).

In light of the eigenvalues' dependence on the Polyakov loop variables ϕ_3 and ϕ_8, by comparing Eq. (3.18) to the two-flavor expression in Eq. (2.30) we note that Ω is no longer a simple function of the traced Polyakov loop Φ, but rather depends on ϕ_3 and ϕ_8 independently. Thus, in order to construct the phase diagram we must now minimize $\Omega(\sigma, d, \phi_3, \phi_8)$ with respect to all variables, then compute Φ via Eq. (2.37). However, as shown in Section 2.6.2, the self-consistency of our mean field approximation requires us to set $\phi_8 = 0$. In this case, $\mu_1^\dagger = \mu_2$ and $\mu_3 = \mu$, so the eigenvalues come in conjugate pairs. This fact, together with the assurance that Φ is now real ensures that the thermodynamic potential is also real and that the minimization procedure is well-defined.

In order to assess the effects of confinement on the QCD phase structure we first construct the phase diagram for $\Phi = 1$ (no confinement), and then compare to the results for the full PNJL model.

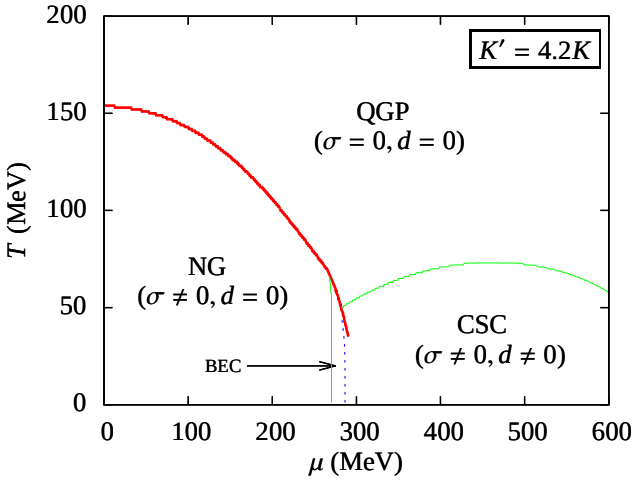

Figure 3.1: Phase diagram for the three flavor NJL model (no confinement). Thick (red) lines represent first-order phase transitions while thin (green) lines represent second-order transitions. The dotted (blue) vertical line is a BEC-BCS crossover, defined by $M(\mu, T) = \mu$. The low T critical point is at $(\mu, T) =$ (291 MeV, 35 MeV).

3.5 Phase Diagram without Confinement

In the absence of confinement we set $A_0 = \phi_3 = 0$ so that $\Phi = 1$ (see Eq. (2.37)) and eliminate $\mathcal{U}_{3C}(\Phi, \overline{\Phi})$ from the thermodynamic potential, which then reduces to

$$\Omega_{NJL} = \mathcal{V}_{3F}(\sigma, d) - 2T \sum_{\pm} \int \frac{d^3\mathbf{k}}{(2\pi)^3} \left[8 \ln(1 + e^{-\beta E_1^{\pm}}) + \ln(1 + e^{-\beta E_2^{\pm}}) + 4\beta\Delta E_1^{\pm} + \frac{1}{2}\beta\Delta E_2^{\pm} \right], \tag{3.22}$$

where the eigenvalues are now

$$E_1^{\pm} = \sqrt{(E_k \pm \mu)^2 + |\Delta|^2}, \tag{3.23}$$

$$E_2^{\pm} = \sqrt{(E_k \pm \mu)^2 + 4|\Delta|^2}, \tag{3.24}$$

and where $\sum_{\pm}$ denotes summation over $E_{1,2}^{+}$ and $E_{1,2}^{-}$.

The minimization of Ω with respect to σ and d yields the phase diagram shown in Fig. 3.1. The critical temperature for the chiral transition at $\mu = 0$ is found to be $T_c^{NJL} = 153$ MeV, in agreement with Abuki *et al.*, and within the margin of error of current lattice results [9, 10, 20]. Note that this temperature is determined entirely by the couplings G and K and the high momentum cut-off Λ, which were in turn fixed

[1] While the remaining six distinct eigenvalues can in principle now be written down explicitly, due to the complicated and opaque nature of these expressions, we decline to do so. It is a straightforward exercise to rewrite $F(\omega, E_k)$ as a cubic polynomial in ω^2, read off the polynomial's coefficients, and insert the coefficients into the formula for the roots of a general cubic polynomial. Having spent several hours in this endeavor himself, the author encourages the reader who feels compelled to do so to share any insight he thereby gains!

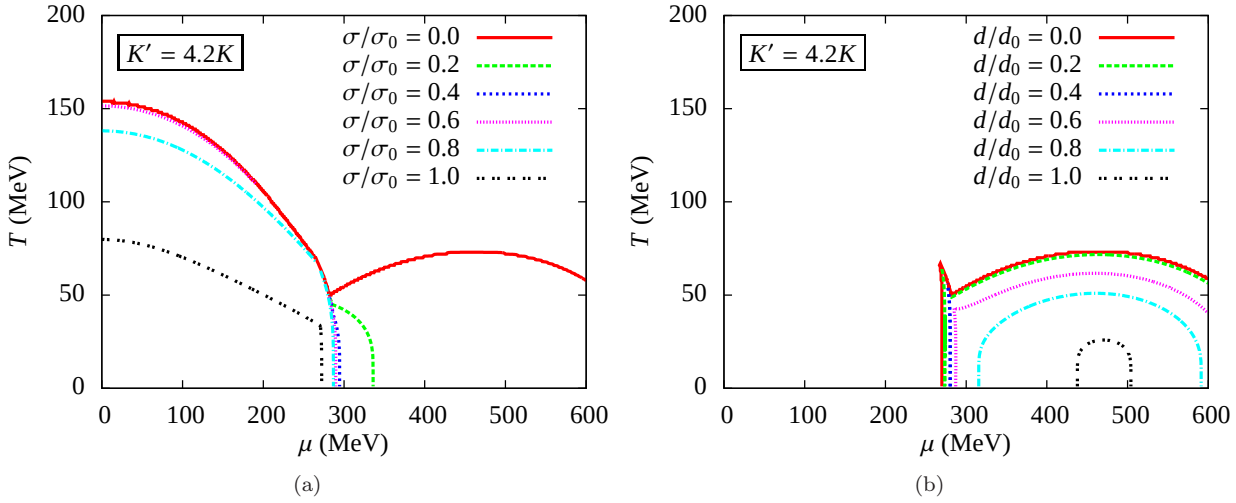

Figure 3.2: (a) Contour plot for the chiral condensate in the three flavor NJL model, showing contours of $\sigma = 0.2$, 0.4, 0.6, 0.8 and 1.0 σ_0, where σ_0 is the maximum value of the diquark condensate. (b) Contour plot for the diquark condensate in the NJL model, showing contours of $d = 0.2$, 0.4, 0.6, 0.8 and 1.0 d_0, where d_0 is the maximum value of the diquark condensate.

by empirical mesonic properties (T_c^{NJL} proves independent of H and K', which are related to diquark pairing, since $d = 0$ in this portion of the phase diagram).

As reported by Abuki *et al.*, the topology of the phase diagram depends critically on the ratio of the anomaly couplings $\kappa = K'/K$ [20]. We find, in agreement with their results, that for $\kappa < 4.2$, the transition out of the Nambu-Goldstone (NG) phase is first-order for all temperatures, while for $\kappa \geq 4.2$, a low-T critical point emerges, below which there is a smooth crossover from the NG phase to a CSC phase, in which both chiral symmetry breaking and diquark pairing persist (see Fig. 3.1).

We find that as κ increases above the critical value of 4.2, the low T critical point moves up the NG-CSC phase boundary (to higher T and lower μ) until it vanishes into the NG-QGP phase boundary at $\kappa = 4.8$. We therefore find that there are three distinct structures of the NJL phase diagram, determined by the value of κ: (1) $\kappa < 4.2$, (2) $4.2 \leq \kappa \leq 4.7$, and (3) $\kappa \geq 4.8$. Since we are particularly interested in the existence of the low T critical point, we are interested primarily in structure (2). Therefore, in displaying our results, we choose $\kappa = 4.2$ as a representative value for which the critical point is realized.

Considering the contour plot of σ, shown in Fig. 3.2(a), we see that the chiral condensate is relatively slowly varying within the NG phase, which implies a relatively constant effective quark mass. Near the phase boundaries, however, σ varies rapidly, either falling discontinuously (NG-QGP or NG-CSC, above the critical point) or undergoing a very rapid, though smooth, crossover (NG-CSC, below the critical point).

Similarly, the contours of d show that while d is not maximized over as great a portion of the phase diagram as σ, it is relatively constant throughout the CSC region, dropping rapidly only near the second-

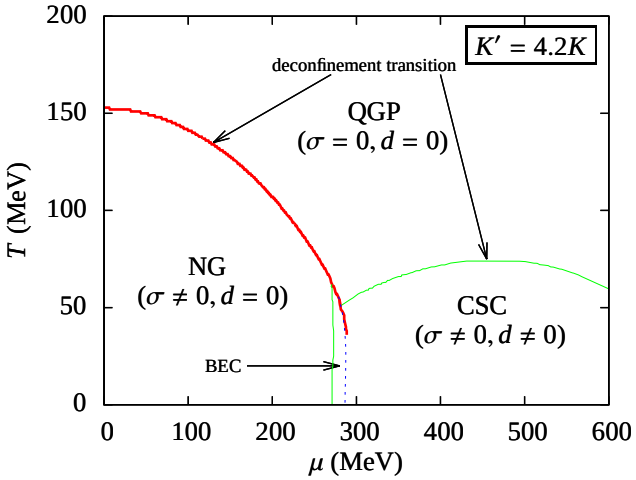

Figure 3.3: Phase diagram for the three-flavor PNJL model. Line types are the same as in Fig. 3.1, and the deconfinement transition coincides with the chiral phase transition at all values of μ. The low T critical point is at $(\mu, T) = (288 \text{ MeV}, 36 \text{ MeV})$.

order CSC-QGP phase transition and the NG-CSC crossover (Fig. 3.2(b)).

3.6 Phase Diagram with Confinement

Before constructing the three-flavor QCD phase diagram with confinement, we fix the Polyakov loop parameter T_0 by matching the deconfinement temperature at $\mu = 0$ with current lattice data. With massive quarks, the definition of T_c in this context would be, as noted by Aoki *et al.*, ambiguous, there being at least three standard choices: (1) a maximum of the chiral susceptibility, (2) a maximum of the quark number susceptibility, and (3) a maximum in $d\Phi/dT$ [9, 10].[2] While these transitions are coincident in the NJL and PNJL models, current lattice calculations with non-zero current quark masses yield slightly different values for the three critical temperatures. However, for massless quarks, all three transitions are coincident and there is no ambiguity. Thus, we choose to match the deconfinement transition at $T_c = 154$ MeV [30], which leads us to set $T_0 = 50$ MeV.

Minimizing Ω in the presence of the Polyakov loop yields the phase diagram shown in Fig. 3.3. Comparing to Fig. 3.1 we now assess the effects of confinement on the phase structure of QCD. As in the nonconfining NJL model, the topology of the phase diagram depends critically on κ. We find that this dependence is unaffected by the inclusion of confinement, and that the critical point continues to appear for $4.2 \leq \kappa \leq 4.7$, while it vanishes into the NG-QGP phase boundary for $\kappa \geq 4.8$. The location in the phase diagram at which

[2] There is a slight ambiguity in this definition at low μ. For $\mu \lesssim 288$ MeV, as the system moves to higher T, Φ first undergoes a smooth, though rapid, crossover, which is followed by a slight discontinuity coincident with the chiral phase transition, as shown in Fig. 3.5(b). Whether one chooses to identify the deconfinement transition with the maximum finite value of $d\Phi/dT$ (rapid crossover) or with the absolute maximum of $d\Phi/dT$ (discontinuity) is a matter of convention. Here, we choose the latter definition. For large μ there is no such ambiguity, since the CSC-QGP transition is second-order and no discontinuity exists.

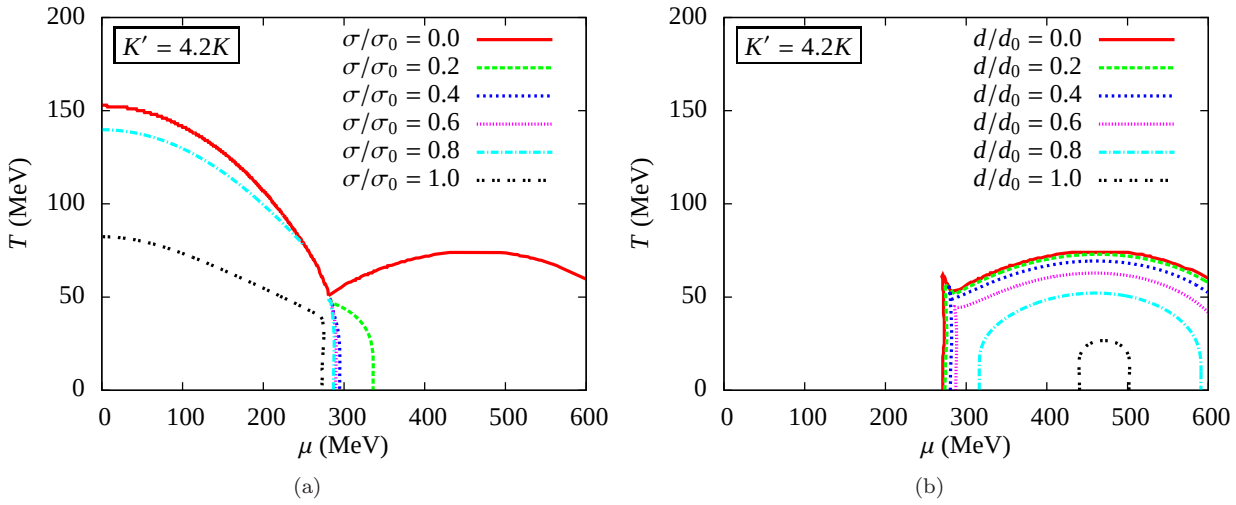

Figure 3.4: (a) Contour plot for the chiral condensate in the three flavor PNJL model, showing contours of $\sigma = 0.2$, 0.4, 0.6, 0.8 and 1.0 σ_0, where σ_0 is the maximum value of the diquark condensate. (b) Contour plot for the diquark condensate in the PNJL model, showing contours of $d = 0.2$, 0.4, 0.6, 0.8 and 1.0 d_0, where d_0 is the maximum value of the diquark condensate.

the critical point vanishes (for $\kappa = 4.8$) is at marginally higher temperature in the PNJL model ($T = 54$ MeV) than in the NJL model ($T = 50$ MeV). This reflects the fact that the Polyakov loop causes a slight shift (between 2 and 4 MeV) of the NG-QGP and CSC-QGP phase boundaries to higher temperatures, at intermediate to high μ (note that the critical temperature at $\mu = 0$ is unchanged).

Given that deconfinement is a high T effect, it might be unsurprising that it does not materially affect the low T critical point. However, it is important to note that were possible μ dependence included in the Polyakov loop potential, Eq. (2.50), the present inclusion of confinement could have a greater effect on the phase structure of QCD. Unfortunately, because lattice calculations are restricted to $\mu = 0$, we are unable to discern any μ dependence of $\mathcal{U}(\overline{\Phi}, \Phi)$.

We also note that while prior work has demonstrated that inclusion of the Polyakov loop pulls the NG-QGP and CSC-QGP phase transitions, as well as the low-T critical point, to higher temperatures [21,88,89], our results do not demonstrate such a shift. This apparent disparity is a result of the aforementioned fitting of $T_0 = 50$ MeV, which we choose to reproduce the $\mu = 0$ deconfinement transition for massless three-flavor QCD. Had we instead chosen to match the transition in the pure-gauge sector (as in [21]) and set $T_0 = 270$ MeV, both the NG-QGP and CSC-QGP transitions, as well as the low-T critical point, would have been shifted to significantly higher temperatures.

Comparing the contour plot of the chiral condensate (Fig. 3.4(a)) to that from the NJL model (Fig. 3.2(a)), we note that the Polyakov loop encourages larger values of σ, most notably near the phase boundaries. This is clear from the absence of a $\sigma = 0.6\sigma_0$ contour at low μ in the PNJL model, as well as the termination of

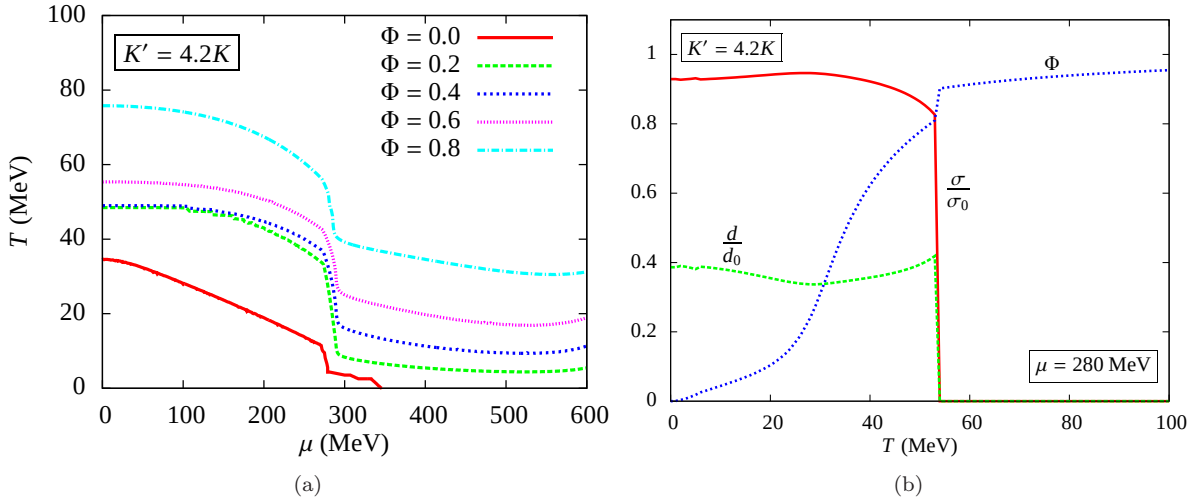

Figure 3.5: (a) Contour plot for the traced Polyakov loop in the three flavor PNJL model, showing contours of Φ = 0.2, 0.4, 0.6, 0.8 and 1.0. (b) Plot of the normalized chiral and diquark condensates and Polyakov loop for $\mu = 280$ MeV.

the $\sigma = 0.8\sigma_0$ contour into the NG-QGP phase boundary at lower chemical potential ($\mu = 250$ MeV) than in the NJL model ($\mu = 266$ MeV). This effect can be traced to an effective $\sigma^2\Phi$ coupling, which favors the coexistence of a chiral condensate and confinement, and which is discussed in more detail in Sec. 3.7. In the same vein, from Fig. 3.5(a) we note that Φ tends to decrease in the presence of σ. As a result, curves of constant Φ are "pulled" to higher temperatures in the NG phase than they would be in the absence of the effective $\sigma^2\Phi$ coupling. On the other hand, inspecting the contours of the diquark condensate (Fig. 3.4(b)), we find that the Polyakov loop has no appreciable effect on d.

Finally, Fig. 3.5(a) demonstrates that Φ is only weakly dependent on chemical potential, being primarily an increasing function of temperature, and what μ dependence does exist is almost entirely restricted to the NG phase. In the CSC phase, the Φ contours line up roughly parallel to the d contours, suggesting an effective $|d|^2\Phi$ coupling. However, it does not appear that this coupling affects the deconfinement transition significantly, since Φ has already achieved nearly its maximum value at much lower temperatures than where $d \to 0$. We find that Φ is discontinuous across the first-order NG-QGP and NG-CSC transitions (e.g. note the jump in the $\Phi = 0$ contour at $\mu = 267$ MeV), but the relative magnitude of the discontinuity is much less than that of σ (Fig. 3.5(b)).

3.7 Ginzburg-Landau Coefficients

Having constructed the PNJL phase diagram, we next seek to understand the lowest-order effects of the condensate-Polyakov loop couplings by expanding the thermodynamic potential Ω in a Ginzburg-Landau

form

$$\begin{aligned}\Omega &= \left(\frac{a}{2}\,\sigma^2 - \frac{c}{3}\,\sigma^3 + \frac{b}{4}\,\sigma^4\right) + \left(\frac{\alpha}{2}\,|d|^2 + \frac{\beta}{4}\,|d|^4\right) + \left(A\Phi + \frac{B}{2}\Phi^2 + \frac{C}{3}\,\Phi^3\right) - \gamma\sigma|d|^2 \\ &\quad + \frac{a'}{2}\,\sigma^2\Phi - \frac{c'}{3}\,\sigma^3\Phi + \frac{\alpha'}{2}\,|d|^2\Phi - \gamma'\sigma|d|^2\Phi + \cdots \end{aligned} \tag{3.25}$$

While prior work by Hatsuda *et al.* focused on the topological consequences of a thermodynamic potential of this form (without the Polyakov loop), here we are in a position to compute the coefficients explicitly as functions of temperature and chemical potential [18]. For example, the coefficient a can be computed from Eq. (3.18) via the relation

$$a = \left.\frac{\partial^2\Omega}{\partial\sigma^2}\right|_{\sigma=d=\Phi=0}, \tag{3.26}$$

while similar expressions hold for the other coefficients.

In the following calculations, for the sake of convenience the coefficients a, c, γ, etc. will be taken to refer to their dimensionless versions, where they are scaled by the appropriate power of Λ (as in Table 3.1). This ensures that the coefficients are of roughly the same order of magnitude and facilitates comparison of their relative importance. For the purposes of these comparisons, note that the dimensionless chiral and diquark condensates have maximum values of $\sigma_0 = 0.0636$ and $d_0 = 0.0548$. In addition, in order to express the coefficients compactly, we define the following quantities:

$$f^\pm = \frac{1}{\cosh(\beta E_0^\pm) - \frac{1}{2}}, \qquad g^\pm = \frac{1}{\cosh(\beta E_0^\pm) + 1}, \qquad h^\pm = \frac{1}{9(\beta E_0^\pm)^2 + \pi^2}, \tag{3.27}$$

where $E_0^\pm = k \pm \mu$ are the eigenvalues (without absolute values) in the absence of any interactions.

3.7.1 Noncoupling terms

In computing the coefficients of simple powers of σ, we may set $d = \Phi = 0$ prior to taking the necessary derivatives. Thus, the 18 distinct eigenvalues shown in Eqs. (3.20) and (3.21) reduce to the six distinct values: $E_{1-4} = |E_k \pm \mu| \pm 2\pi i T/3$ (with the two $\pm$ independent) and $E_{5,6} = |E_k \pm \mu|$. In this way, we obtain the first three LG coefficients:

$$a(\mu, T) = 12G - 48G^2 \sum_\pm \int \frac{d^3\mathbf{k}}{(2\pi)^3} \frac{\sinh(\beta E_0^\pm)}{k} (2f^\pm + g^\pm), \tag{3.28}$$

$$c(\mu, T) = 12K - 72GK \sum_\pm \int \frac{d^3\mathbf{k}}{(2\pi)^3} \frac{\sinh(\beta E_0^\pm)}{k} (2f^\pm + g^\pm), \tag{3.29}$$

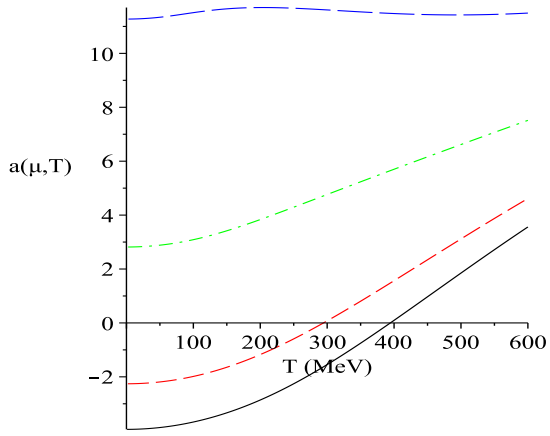

Figure 3.6: Coefficient of σ^2, $a(\mu, T)$, for various values of the chemical potential (solid black = 0, dashed red = 150 MeV, dot-dashed green = 300 MeV, long-dashed blue = 450 MeV).

We note that the σ^3 term is proportional to the coupling K, which stems from the axial anomaly. This proves true for all odd powers of σ so that in the absence of the axial anomaly the thermodynamic potential is an even function of σ.

Figure 3.6 shows that the coefficient a changes sign, becoming negative at low temperatures and chemical potentials. As a result, in the low-μ, low-T portion of the phase diagram, the σ^2 term in the thermodynamic potential tends to favor chiral condensation. In fact, we see that if the σ^2 term were dominant, this transition would occur at $\mu = 0$ at the extremely high temperature of $T = 395$ MeV. However, by looking at Eq. (3.29) we can assess the relative magnitude of c, and whether it will play a significant role in determining the order of the NG-QGP phase transition. In fact, noting that the integrals appearing in c are identical to those in a, we can write

$$c = \frac{3K}{2G}(a - 4G). \tag{3.30}$$

Thus, we find that at $\mu = 0$, $|c/a| \gtrsim 6K \sim 60$, while as noted above, $\sigma_0 \sim 1/16$. As expected from the results of the prior section then, we find that the σ^3 term cannot be ignored in determining the order of the NG-QGP transition. In fact, the inclusion of higher-order terms coupling σ and Φ leads to a first-order transition at a more modest temperature of $T_c = 154$ MeV.

Next, the coefficients of terms involving only powers of $|d|$ may be obtained by setting $\sigma = \Phi = 0$ at the outset and taking the appropriate derivatives. Unlike the prior calculation, in which setting $d = 0$ reduced the number of distinct eigenvalues from 18 to 6, in this case, no such simplification occurs and the full 18 eigenvalues must be evaluated. Doing so yields the $|d|^2$ coefficient:

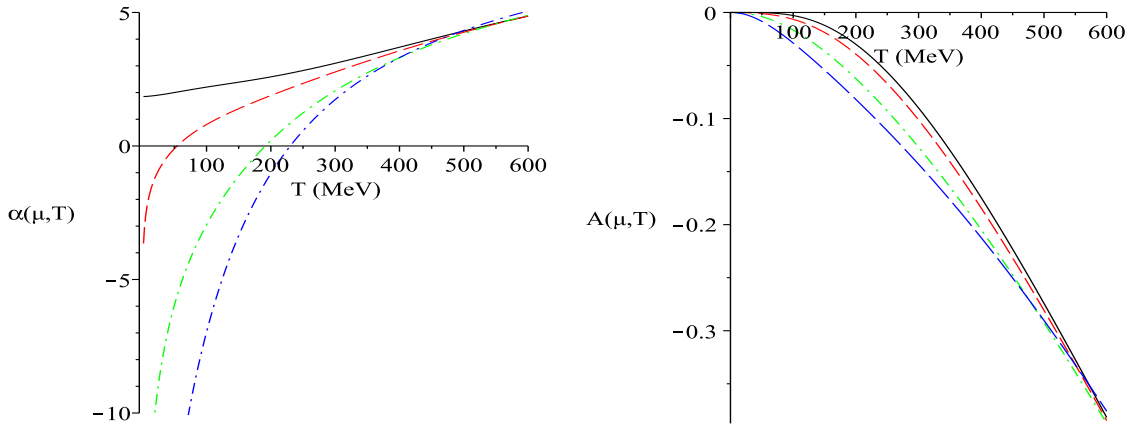

(a) (b)

Figure 3.7: (a) Coefficient of $|d|^2$, $\alpha(\mu, T)$, for various values of the chemical potential (same as Fig. 3.6). (b) Coefficient of Φ, $A(\mu, T)$.

$$\alpha(\mu,T) = 6H - 4H^2 \sum_{\pm} \int \frac{d^3\mathbf{k}}{(2\pi)^3} \Bigg\{ \frac{4\sinh(\beta E_0^{\pm}) f^{\pm}}{E_0^{\pm}} + 9\beta[6\beta E_0^{\pm} \sinh(\beta E_0^{\pm}) + \sqrt{3}\pi] f^{\pm} h^{\pm} + 36\beta^2 E_0^{\pm} \sinh(\beta E_0^{\pm}) g^{\pm} h^{\pm} \Bigg\}. \tag{3.31}$$

As shown in Fig. 3.7(a), for sufficiently large μ, the sign of the $|d|^2$ term becomes negative at low T. Since no odd powers of the diquark condensate appear in Ω the phase transition is of second-order. This transition produces a color superconducting phase of quark Cooper pairs in the low T, high μ portion of the phase diagram, as has been widely reported [16, 21, 66]. The precise location of the diquark condensate formation is affected by the chiral-diquark condensate coupling, but for $T \sim 0$, we find that α becomes negative at $\mu \sim 120$ MeV.

Next, we compute the coefficients of powers of Φ. Setting $\sigma = d = 0$ again reduces the 18 eigenvalues to six eigenvalues analogous to those involved in the calculation of the σ^n coefficients (with $E_k \to k$). Computing the necessary derivatives yields:

$$A(\mu,T) = -9T \sum_{\pm} \int \frac{d^3\mathbf{k}}{(2\pi)^3} f^{\pm}, \tag{3.32}$$

$$B(\mu,T) = -T^4 [a(T) + 12b(T)] + \frac{27T}{2} \sum_{\pm} \int \frac{d^3\mathbf{k}}{(2\pi)^3} (f^{\pm})^2, \tag{3.33}$$

$$C(\mu,T) = 24b(T) - \frac{81T}{4} \sum_{\pm} \int \frac{d^3\mathbf{k}}{(2\pi)^3} (f^{\pm})^3. \tag{3.34}$$

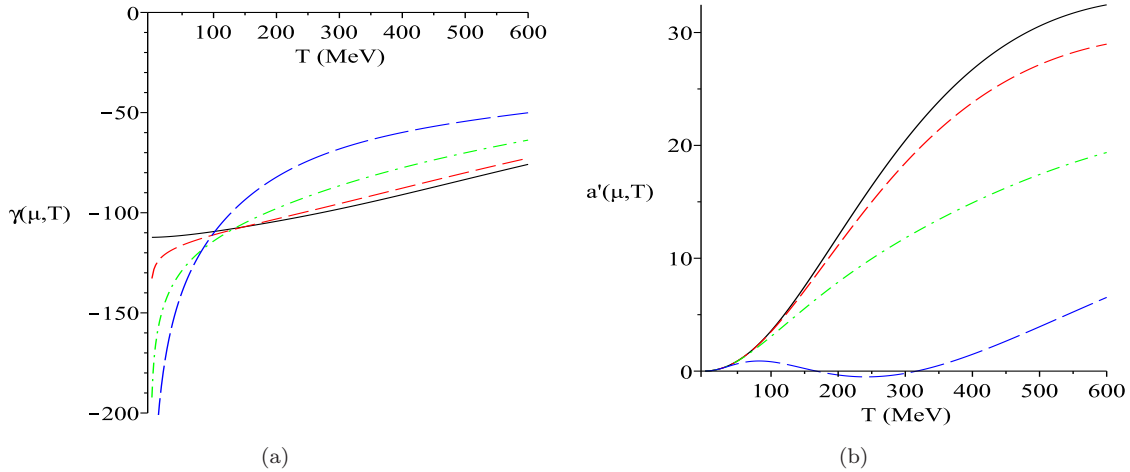

Figure 3.8: (a) Coefficient of $\sigma|d|^2$, $\gamma(\mu, T)$, for various values of the chemical potential (same as Fig. 3.6). (b) Coefficient of $\sigma^2\Phi$, $a'(\mu, T)$.

Significantly, while in the pure-gauge sector the lowest-order term in $\mathcal{U}_{3C}(\Phi, \overline{\Phi})$ is quadratic (see Eq. (2.50)), the existence of quarks generates a term linear in Φ. Further, A is negative at all points in the phase diagram except at $T = 0$. As a result, even for very small non-zero temperatures, the Polyakov loop will take on a finite value. This behavior stands in marked contrast to that of the pure-gauge sector, in which Φ undergoes a large discontinuous jump at $T_0 = 270$ MeV, below which $\Phi = 0$.

3.7.2 Coupling terms

Having computed the coefficients of the pure condensate and Polyakov loop terms in Eq. (3.25), we now consider the lowest-order couplings between these variables. Beginning with the chiral and diquark condensates, we note from Figs. 3.4(a) and 3.4(b) that there is only a small region near $\mu \sim 280 - 320$ MeV in which both σ and d are significant. Thus, the primary condensate coupling is the lowest-order coupling, of the form $\sigma|d|^2$. Setting $\Phi = 0$ at the outset and performing the necessary derivatives yields

$$\begin{aligned}\gamma(\mu, T) \;=\; & \frac{3}{2}K' - 2GK' \sum_{\pm} \int \frac{d^3\mathbf{k}}{(2\pi)^3} \Bigg\{ \frac{3G \sinh(\beta E_0^{\pm})}{k} (2f^{\pm} + g^{\pm}) + \frac{2H \sinh(\beta E_0^{\pm}) f^{\pm}}{E_0^{\pm}} \\ & + 3H\beta[\beta E_0^{\pm} \sinh(\beta E_0^{\pm}) + \sqrt{3}\pi] f^{\pm} h^{\pm} + 18H\beta^2 E_0^{\pm} \sinh(\beta E_0^{\pm}) h^{\pm} g^{\pm} \Bigg\}. \quad (3.35)\end{aligned}$$

In Fig. 3.8(a) we see that γ is negative at all points in the phase diagram, and therefore the $\sigma|d|^2$ coupling universally encourages coexistence of the chiral and diquark condensates. In the prior section we observed that this term is the critical factor in determining the nature of the NG-CSC transition at low temperatures. Since the $\sigma|d|^2$ coupling does not involve the Polyakov loop, Eq. (3.35) is the same as that obtained by Abuki *et al.*, although they did not compute it explicitly, but only observed its consequences in the numerical

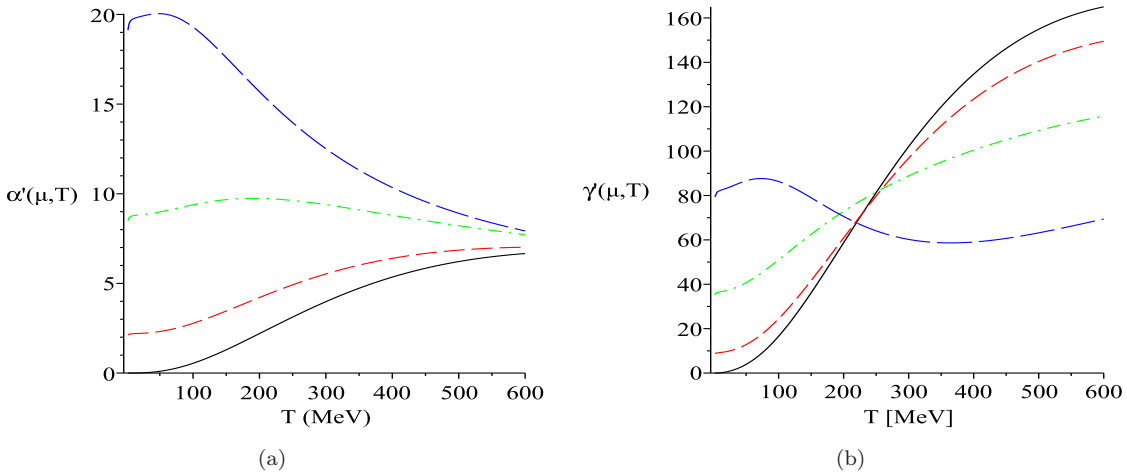

(a) (b)

Figure 3.9: (a) Coefficient of $|d|^2\Phi$, $\alpha'(\mu,T)$, for various values of the chemical potential (same as Fig. 3.6). For $\alpha' < 0$, the $|d|^2\Phi$ term favors the coexistence of a diquark condensate and deconfinement. (b) Coefficient of $\sigma|d|^2\Phi$, $\gamma'(\mu,T)$. For $\gamma' < 0$, the system favors the coexistence of σ, d, and Φ.

construction of the QCD phase diagram [20].

Having computed the lowest-order noncoupling terms, we consider the effective modifications to these terms that arise from the inclusion of the Polyakov loop. The coefficients of the lowest-order couplings between the condensates and the Polyakov loop, $\sigma^2\Phi$, $\sigma^3\Phi$, and $|d|^2\Phi$ are:

$$a' = 144G^2 \sum_{\pm} \int \frac{d^3\mathbf{k}}{(2\pi)^3} \frac{\sinh(\beta E_0^{\pm})(f^{\pm})^2}{k}, \tag{3.36}$$

$$c' = 216GK \sum_{\pm} \int \frac{d^3\mathbf{k}}{(2\pi)^3} \frac{\sinh(\beta E_0^{\pm})(f^{\pm})^2}{k}, \tag{3.37}$$

$$\alpha' = 12H^2 \sum^{\pm} \int \frac{d^3\mathbf{k}}{(2\pi)^3} \left\{ \frac{2\sinh(\beta E_0^{\pm})(f^{\pm})^2}{E_0^{\pm}} - 36\sqrt{3}\pi\beta^2 E_0^{\pm} \sinh(\beta E_0^{\pm})(h^{\pm})^2 g^{\pm}, \right.$$
$$\left. -2\sqrt{3}\pi\beta f^{\pm} h^{\pm} + 3\sqrt{3}\beta \left[2\sqrt{3}\beta E_0^{\pm} \sinh(\beta E_0^{\pm}) + \pi \right] (f^{\pm})^2 h^{\pm} \right\}. \tag{3.38}$$

As shown in Fig. 3.8(b), except for at very large chemical potential ($\mu \gtrsim 445$ MeV) both a' and $c' = (3K'/2G)a'$ are positive, and therefore tend to disfavor simultaneous chiral condensation and deconfinement. Since σ is only appreciable for $\mu \lesssim 300$ MeV, this means that to lowest-order, the presence of a chiral condensate will tend to maintain a confined state, and vice versa. We note, however, that this finding does not preclude the realization of a spatially inhomogeneous "quarkyonic" phase at large μ, as has been suggested recently [30, 83, 84, 90, 91], since we have explicitly assumed a homogeneous condensate.

We also note that the magnitude of a' decreases with increasing chemical potential, and is therefore largest (most strongly opposing deconfinement) in the NG region of the phase diagram where σ dominates.

This effect is visible in Fig. 3.5(a), where the curves of constant Φ are pulled to higher temperatures in the NG phase by virtue of the presence of a non-zero σ. The NG-QGP transition is therefore the result of two competing effects. On one hand, in the pure-gauge sector confinement tends to become weaker at higher temperatures, eventually giving way to a deconfined QGP. On the other hand, as temperature increases, the system has an increasing aversion to a state in which both σ and Φ are non-zero, so the presence of the chiral condensate tends to suppress the deconfinement transition.

Similarly, as shown in Fig. 3.9(a), the coefficient α' is positive throughout the phase diagram and its magnitude increases with increasing μ. Thus, the presence of a diquark condensate also tends to maintain a confined state with $\Phi \sim 0$, and does so more strongly at high chemical potentials, where d is appreciable. This can be understood by noting that in order to satisfy the gap equation, $\partial\Omega/\partial\Delta = 0$, with increasing Φ, one must decrease the magnitude of the gap.

The final coefficient that we compute is of the term $\sigma|d|^2\Phi$, the lowest-order term coupling all three variables:

$$\begin{aligned}\gamma' &= 6K' \sum_{\pm} \int \frac{d^3\mathbf{k}}{(2\pi)^3} \Big\{ -18\sqrt{3}\pi H \beta^2 E_0^{\pm} (h^{\pm})^2 \sinh(\beta E_0^{\pm}) g^{\pm} + \left(\frac{3G}{k} + \frac{H}{E_0^{\pm}} \right) \sinh(\beta E_0^{\pm}) (f^{\pm})^2 \\ &\qquad -\sqrt{3}\pi H \beta f^{\pm} h^{\pm} + \frac{3\sqrt{3} H \beta}{2} \left[2\sqrt{3} \beta E_0^{\pm} \sinh(\beta E_0^{\pm}) + \pi \right] (f^{\pm})^2 h^{\pm} \Big\}. \end{aligned} \tag{3.39}$$

As shown in Fig. 3.9(b), γ' is positive throughout the phase diagram, so that once again, we find that condensation and deconfinement tend to disfavor one another. Thus, we find that in general, the existence of a condensate (either σ or d) tends to encourage confinement, and the greater the number or magnitude of the condensate(s) present, the greater the effect.

3.8 Low temperature critical point

Having computed the lowest-order Landau-Ginzburg coefficients, we are now in a position to assess the effect of the Polyakov loop on the low temperature critical point. As noted in the prior section, in order for the critical point to appear the ratio of the axial anomaly couplings $\kappa = K'/K$ must exceed 4.2. In the presence of the Polyakov loop, the values of these couplings are effectively modified by terms proportional to Φ, as well as higher-order terms, which can be neglected to first-order. Comparing Eqs. (3.16) and (3.25) we

define

$$K_{\rm eff} \equiv K_0 \left(1 + \frac{c'}{c}\,\Phi\right), \tag{3.40}$$

$$K'_{\rm eff} \equiv K'_0 \left(1 + \frac{\gamma'}{\gamma}\,\Phi\right). \tag{3.41}$$

Taking the ratio and expanding to linear order in Φ yields

$$\kappa_{\rm eff} = \kappa_0 \left[1 + \left(\frac{\gamma'}{\gamma} - \frac{c'}{c}\right)\Phi\right]. \tag{3.42}$$

The effect of the Polyakov loop can be assessed in terms of the sign of $\delta \equiv \gamma'/\gamma - c'/c$. For $\delta > 0$, the effective ratio $\kappa_{\rm eff}$ is increased, which will tend to encourage the emergence of the critical point, while for $\delta < 0$ the critical point will tend to be suppressed. The condition for Eq. (3.42) to remain valid is $\delta \ll \Phi^{-1} \sim 2$, which follows from the fact that $\Phi \sim 0.4$ at the critical point. Noting that for $\kappa_0 = 4.2$ the critical point is at $(\mu, T) = (288\ \text{MeV}, 36\ \text{MeV})$, we find that $\delta_{cp} = -0.16$. Thus, the presence of the Polyakov loop decreases the effective coupling ratio κ by approximately 6%.

Chapter 4

Phase Diagram of Three Flavor QCD with Realistic Masses

4.1 Introduction

In the prior chapter we began our investigation of the three flavor QCD phase diagram by studying the massless PNJL model. While we have gained a number of insights by this work, there are several important factors which we have thus far neglected. In particular, while we have found that the addition of a third quark flavor may give rise to a low temperature critical point, we have not yet assessed the impact of a realistic strange quark mass on the realization of this critical point. Thus, in this chapter we investigate the effects of realistic quark masses on the QCD phase diagram and the "freezing-out" of the strange quark as the system moves to lower chemical potentials where the light up and down quarks dominate. The material in this chapter is based on [3].

Another aspect of the QCD phase diagram of particular interest is the nature of quark pairing at intermediate chemical potential. While it is known that for three quark flavors a color-flavor-locked (CFL) phase, in which all quark flavors and colors pair, is energetically favorable for asymptotically large μ, the preferred pairings for μ not asymptotically large are not determined. Calculations indicate phases in which only two colors and flavors pair (2SC) [92], in which one flavor pairs with all others (uSC, dSC) [64], and a spatially inhomogeneous phase which has properties of both free quarks and hadrons (quarkyonic) [30, 83, 84].

In this chapter we build on prior studies of the effects of confinement on quark pairing in the three flavor PNJL model by considering a wider range of pairing schemes than the CFL and 2SC phases previously considered [2, 92]. In particular, by permitting distinct ud, us, and ds pairing amplitudes we allow for the possibility that the confining mechanism of QCD may not treat all quark flavors on an equal footing, even for equal masses. Thus, we are led to consider the possibility of a new homogeneous asymmetric CFL (ACFL) phase characterized by *breached* pairing in which all quark flavors pair, but with unequal magnitudes [93–95]. Further, by considering a range of strange quark masses we investigate the combined effects of this potential asymmetry and the decoupling of the strange quark sector with increasing strange quark mass.

We also investigate the implications of a local color neutrality constraint on the phase structure of dense quark matter. While QCD has the capacity to dynamically achieve local color neutrality by means of a gluon field condensate $\langle A_a^0 \rangle$, the PNJL model lacks the necessary gluonic degrees of freedom to achieve

such neutrality in a phase of asymmetric quark pairing (e.g., 2SC, uSC, dSC). Thus, one must impose such neutrality "by hand" in order to avoid the large color-electric forces which would result from color accumulation [68,96–99]. Prior studies of the axial anomaly's influence on the phase structure of dense quark matter in NJL-type models have either focused on pairing structures which are trivially color neutral [2, 20] or have allowed for locally colored phases [92]. By introducing an effectively color-dependent chemical potential we impose local color neutrality and study its effects on the low temperature portion of the QCD phase diagram, most notably its suppression of the 2SC phase and the potential for realizing quark-hadron continuity.

4.2 Three Flavor PNJL Model with Realistic Masses

Recalling the three flavor PNJL Lagrangian in Eq. (3.1) and anticipating the effects of unequal quark masses we consider chiral and diquark condensates of the form

$$\langle \overline{q}^i_a q^j_a \rangle = \sigma_i \delta_{ij}, \qquad \langle q^T C\gamma_5 t_i l_j q \rangle = d_i \delta_{ij}, \tag{4.1}$$

where the sum over a is implied and we define $t_{1,2,3} = \tau_{7,5,2}$ and $l_{1,2,3} = \lambda_{7,5,2}$. Note also that there is no sum over i in Eq. (4.1); rather, the right sides of the equations are diagonal matrices in flavor space with three distinct elements. Writing out the diquark condensates explicitly, we have

$$d_1 = -\langle d^T_g C\gamma_5 s_b\rangle + \langle d^T_b C\gamma_5 s_g\rangle + \langle s^T_g C\gamma_5 d_b\rangle - \langle s^T_b C\gamma_5 d_g\rangle, \tag{4.2}$$

$$d_2 = -\langle u^T_r C\gamma_5 s_b\rangle + \langle u^T_b C\gamma_5 s_r\rangle + \langle s^T_r C\gamma_5 u_b\rangle - \langle s^T_b C\gamma_5 u_r\rangle, \tag{4.3}$$

$$d_3 = -\langle u^T_r C\gamma_5 d_g\rangle + \langle u^T_g C\gamma_5 d_r\rangle + \langle d^T_r C\gamma_5 u_g\rangle - \langle d^T_g C\gamma_5 u_r\rangle. \tag{4.4}$$

Thus, we see that while σ_1, σ_2, and σ_3 represent the up, down, and strange chiral condensates respectively, d_1, d_2, and d_3 represent the magnitudes of ds, us, and ud pairing. In addition, the color-flavor-locking of the interaction $\mathcal{L}^{(4)}_d$ means that while d_3, for example, describes the pairing of red up and green down quarks (as well as red down and green up quarks), blue quarks of either flavor do not participate in this pairing.

With our chosen condensate structure, working in mean field the Lagrangian Eq. (3.1) becomes

$$\mathcal{L} = \overline{q}(i\partial\!\!\!/ - \hat{M} + (\mu + iA_0)\gamma^0)q - \frac{1}{2}\sum_{i=1}^{3}\left[\Delta^*_i(q^T C\gamma_5 t_i l_i q) + \text{H.c.}\right] - \mathcal{V}_{3F}(\sigma_i, d_i) - \mathcal{U}_{3C}(\Phi), \tag{4.5}$$

where the ith effective quark mass and BCS gap are

$$M_i = m_i - 4G\sigma_i + K|\varepsilon_{ijk}|\sigma_j\sigma_k + \frac{K'}{4}|d_i|^2, \qquad \Delta_i = -2d_i\left(H - \frac{K'}{4}\sigma_i\right), \tag{4.6}$$

with $|\varepsilon_{ijk}| = 1$ if i, j, k are all distinct and zero otherwise, and where the condensates' direct contribution to Ω is

$$\mathcal{V}'_{3F}(\sigma_i, d_i) = 2G\sum_{i=1}^{3}\sigma_i^2 - 4K\sigma_1\sigma_2\sigma_3 + \sum_{i=1}^{3}\left(H - \frac{K'}{2}\sigma_i\right)|d_i|^2. \tag{4.7}$$

Writing the Lagrangian in terms of the Nambu-Gor'kov spinor $\Psi = (q \;\; q^C)/\sqrt{2}$, we cast the Lagrangian in the form $\mathcal{L} = \overline{\Psi}S^{-1}\Psi - \mathcal{V}'_{3F} - \mathcal{U}_{3C}$, where the inverse propagator in Nambu-Gor'kov space is

$$S^{-1}(k) = \begin{pmatrix} \not{k} - M + (\mu + iA_0)\gamma^0 & \Delta_i\gamma_5 t_i l_i \\ -\Delta_i^*\gamma_5 t_i l_i & \not{k} - M - (\mu + iA_0)\gamma^0 \end{pmatrix}, \tag{4.8}$$

and where the sum over i in the off-diagonal elements is implied. Integrating over the fermionic fields then yields the thermodynamic potential:

$$\Omega = -\frac{T}{2}\sum_{i=1}^{72}\int^{\Lambda}\frac{d^3\mathbf{k}}{(2\pi)^3}\left[\ln(1 + e^{-\beta E_i}) + \frac{1}{2}\beta\Delta E_i\right] + \mathcal{V}'_{3F}(\sigma_i, d_i) + \mathcal{U}_{3C}(\overline{\Phi}, \Phi), \tag{4.9}$$

where the E_j ($j = 1...72$) are the poles of Eq. (4.8).

Unfortunately, owing to the size of $S^{-1}(k)$ (72×72) and the asymmetry of its constituent blocks, it is not possible to obtain explicit forms for the system's eigenvalues in either the case of unequal quark masses or condensates. Thus, in the general case we are left to proceed by constructing the phase diagram numerically.

Before proceeding to our construction of the phase diagram, we must say a brief word concerning our parameter fits for this model. The values of Λ, H, and K remain unchanged from the massless case considered in the prior chapter and are given in Table 3.1. However, in order to observe the gradual decoupling of the strange quark from the up-down sector, we will consider several strange quark masses in the range $0 < m_s < 80$ MeV; if G were to remain independent of m_s, the result would be quite unreasonably large effective quark masses at $\mu = 0$. Thus, following Abuki *et al.*, as we adjust the strange quark mass and coupling K' (see Table 4.1), rather than recalculating G by again fitting the mesonic quantities, for the sake of simplicity we choose G to yield a fixed value for $(M_u + M_d)/2 = 367.5$ MeV [20]. The quantitative effects of this choice are negligible for the present purposes.

As noted in Table 4.1, we consider two values of K': (1) $K' = K$, which is suggested by applying a Fierz

	m_s (MeV)	$G\Lambda^2$	$K'\Lambda^5$	T_0 (MeV)	M_s (MeV)
I*	0	1.926	12.36	210	355.1
II	5	1.928	12.36	208	369.4
III	5	1.928	51.91	208	369.4
IV	20	1.915	12.36	207	392.2
V	20	1.915	51.91	207	392.2
VI	40	1.899	12.36	206	417.5
VII	40	1.899	51.91	206	417.5
VIII	80	1.877	12.36	204	476.6
IX	80	1.877	51.91	204	476.6

Table 4.1: Parameter sets for the three flavor PNJL model: the strange quark bare mass m_s, coupling constants G and K', and Polyakov loop parameter T_0, with a spatial momentum cutoff $\Lambda = 602.3$ MeV [16]. The remaining parameters, which are constant across all parameters sets, are $H = 1.74/\Lambda^2$ and $K = 12.36/\Lambda^5$ [20, 21, 73].. Also shown is the constituent strange quark mass at $\mu = T = 0$. *Parameter set I, which was studied in Chapter 3 and in which all bare quark masses are set to zero is listed here for comparison. In all subsequent data sets we take $m_u = 2.5$ MeV and $m_d = 5.0$ MeV [24].

transformation to the instanton vertex [20], and (2) $K' = 4.2K$, which allows the realization of the low T critical point and facilitates comparison with the results of the prior chapter and current literature [20, 92]. Finally, the parameter T_0 is chosen for each parameter set to match our model's deconfinement transition at $\mu = 0$ to the lattice value of $T_\Phi^{N_f=3} = 176$ MeV [9, 10].

In order to study the effects of an increasing strange quark mass on the preferred quark pairing structures at intermediate μ, we begin by again constructing the massless QCD phase diagram, now with the more general condensate structure given in Eq. (4.1). Afterwards, we adopt realistic up and down quark masses, while gradually increasing the strange quark mass in order to observe its effects. In addition, to facilitate a comparison with the current literature, which largely ignores the complication of a local color neutrality constraint, we begin by constructing the phase diagrams without enforcing color neutrality, deferring a discussion of the effects of this constraint to Sec. 4.6. We also note that while a variety of spatially inhomogeneous phases (e.g., crystalline color superconductors, FFLO phases) may be energetically preferred in certain high density regions of the phase diagram [100, 101], in this thesis we consider only homogeneous phases.

4.3 Massless QCD Phase Diagram

4.3.1 Without Confinement

In this section we discuss the phase structure of massless QCD before moving on to consider the case of three different mass quarks. This will allow us to investigate both the general effects of quark mass on the phase diagram, as well its particular influence on a possible ACFL phase. We note that we do not impose color neutrality in either this section or the following, in order that we may consider the effects of this additional

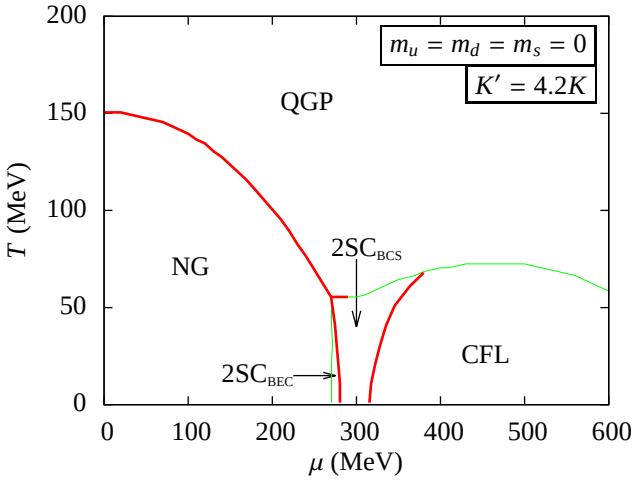

Figure 4.1: Phase diagram of the NJL model (no confinement) with three massless quark flavors. Red lines denote first-order transitions while green lines denote second-order transitions.

constraint in Sec. 4.6.

When we turn off confinement by setting $\phi_3 = 0$ and dropping the potential $\mathcal{U}_{3C}(\overline{\Phi}, \Phi)$ the thermodynamic potential reduces to that considered by Basler and Buballa [92]. The only significant difference between the massless NJL model considered here and the massive case is that for massless quarks the chiral phase transition is first-order for all μ, rather than a smooth crossover at low μ (Fig. 4.1). Basler and Buballa have shown that for $K' \gtrsim 3.5K$ a 2SC$_{\rm BEC}$ phase appears, in which only up and down quarks pair ($d_1 = d_2 = 0$, $d_3 \neq 0$). This phase is similarly visible in Fig 4.1, separated from the hadronic NG phase by a second-order phase transition, and from the 2SC$_{\rm BCS}$ phase by a first-order transition.

Anticipating the ACFL phase discussed in Secs. 4.4 and 4.5, in Fig. 4.2 we show the single diquark condensate of the CFL phase as a function of temperature for $\mu = 500$ MeV. We note that it is roughly constant for $T \lesssim 30$ MeV, and then falls as $d \sim \sqrt{T_c - T}$ for 30 MeV $\lesssim T < 71$ MeV, before finally vanishing as $d \sim (T_c - T)$, due to the effective $\sigma|d|^2$ coupling induced by the axial anomaly [2, 18, 85].

4.3.2 With Confinement

In order to construct the phase diagram in the presence of the Polyakov loop, we first fix T_0 by matching the model's deconfinement transition at $\mu = 0$ to the lattice value of $T_c^{QGP} = 176$ MeV. The resulting value of T_0 varies slightly with m_s, and is given for the various parameter sets used in Table 3.1. Minimizing Ω with respect to the condensates and Polyakov loop, we obtain the phase diagram shown in Fig. 4.3(a). As has been widely reported, the inclusion of the Polyakov loop pulls the chiral transition to higher temperatures (from 151 MeV to 193 MeV), significantly enlarging the region of symmetry breaking [21, 73].[1]

[1]Note that in our prior work [2], we did not observe such an increase in the region of chiral symmetry breaking. This was due to our defining the deconfinement transition as the (slight) discontinuity in $d\Phi/dT$, which is coincident with the chiral

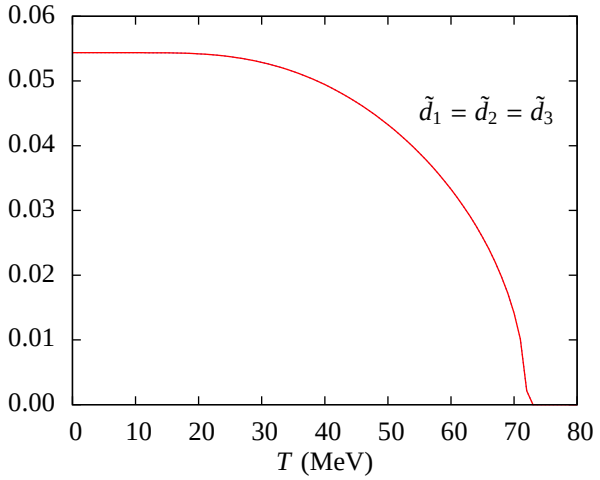

Figure 4.2: Dimensionless diquark condensate $\tilde{d}_i = d_i/\Lambda^3$ for $\mu = 500$ MeV in the massless three flavor NJL model. As indicated in Fig. 4.1, the system undergoes a second-order CFL-QGP phase transition at 73 MeV. The linear approach to zero for 71 MeV $< T <$ 73 MeV is due to an effective $\sigma|d|^2$ coupling (see Sec. 3.7) [2, 18, 85].

One important consequence of the increase of $T_c^{\rm QGP}$ is that the Polyakov loop gives rise to a much larger region of $2SC_{\rm BCS}$, which we define as a 2SC phase ($d_1 = d_2 = 0$, $d_3 \neq 0$) in which $M_{u,d} < \mu$. In particular, this phase now persists to much higher μ than in the NJL model, where it is constrained to roughly 270 MeV $\lesssim \mu \lesssim$ 350 MeV.

Figure 4.3(b) shows the two distinct diquark condensates $d_1 = d_2$ and d_3 for $\mu = 500$ MeV. We find that for $T \lesssim 20$ MeV, the results are not significantly altered from the NJL model. However, for $T \gtrsim 20$ MeV we find that $d_1 = d_2$ falls with increasing T, while d_3 increases until the system undergoes a second-order phase transition to the $2SC_{\rm BCS}$ phase at 70 MeV, slightly below the location of the CFL-QGP transition in the absence of confinement. Thus, the ground state of the system at intermediate μ is no longer a symmetric CFL phase, but rather an asymmetric CFL phase characterized by $0 < d_1 = d_2 < d_3$.

4.4 Realistic Mass QCD Phase Diagram

Having observed the emergence of an ACFL phase in massless QCD, we now consider the effects of realistic bare quark masses on both this phase and the phase diagram generally. To this end we construct phase diagrams for $m_s = 0$, 20, 40, and 80 MeV. In all cases we take $m_u = 2.5$ MeV and $m_d = 5.0$ MeV, while the coupling G is adjusted in order to maintain $(M_u + M_d)/2 = 367.5$ MeV at $\mu = T = 0$.

As shown in Figs. 4.4 and 4.5, as the strange quark mass increases, the region of ACFL moves to higher μ, effectively decoupling the strange quark from the up/down sector. This is due to the fact that in the

phase transition, rather than its maximum finite value. Here, we use the latter definition as it more naturally extends to the case of non-zero quark masses in which $d\Phi/dT$ is continuous and the deconfinement "transition" is unquestionably a smooth crossover.

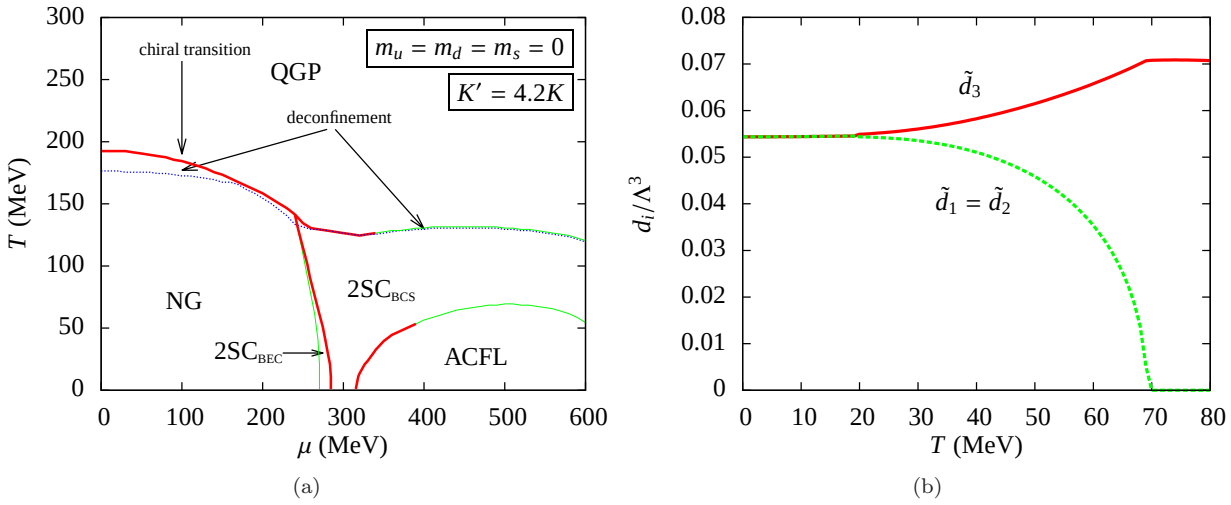

Figure 4.3: (a) Phase diagram of the PNJL model with three massless quark flavors. Line types have the same meaning as in Fig. 4.1, with the additional dotted (blue) line representing the deconfinement crossover. (b) Dimensionless diquark condensates in the massless PNJL model for $\mu = 500$ MeV.

limit $m_s \to \infty$, there is insufficient energy to generate strange quarks and we are left with an effectively two flavor system. We also note that while for small m_s, the deconfinement transition at large μ essentially coincides with the breaking of up/down quark Cooper pairs (the 2SC-QGP transition), as m_s increases the deconfinement temperature moves down somewhat.

Also noteworthy is the fact that except for small m_s and K', a critical point appears on the ACFL-2SC phase boundary, separating a first-order transition at lower μ from a second-order transition at higher μ. One can summarize the situation by noting that the ACFL-2SC transition is first-order when $T_c \lesssim 50$ MeV, and second-order when $T_c \gtrsim 50$ MeV. Thus, for example, for $m_s = 5$ and 20 MeV and $K' = K$, the phase boundary never drops below $T \approx 50$ MeV and the transition is always second-order. We note, however, that while the phase boundary has a negative slope for large μ, the transition does not again become first-order when the boundary drops below $T \approx 50$ MeV.

As shown by Abuki *et al.* in the non-confining NJL model and by the authors for the massless PNJL model, we find that for $K' \geq 4.2K$, a low T critical point emerges [2, 64]. Also, as shown by Basler and Buballa, when one allows for 2SC pairing this critical point acts as the termination of a line of first-order BEC-BCS transitions, above which a smooth crossover develops [92]. Interestingly, as shown in Fig. 4.5, when the $2SC_{BEC}$ phase exists, we find that for $m_s = 5$, 20, and 40 MeV the BEC-BCS transition is first-order at zero temperature, while for $m_s = 80$ MeV the critical point drops below the T-axis and one obtains a smooth BEC-BCS crossover at all temperatures.

While not visible in Figs. 4.4 and 4.5, for unequal mass quarks much of the ACFL-2SC phase boundary

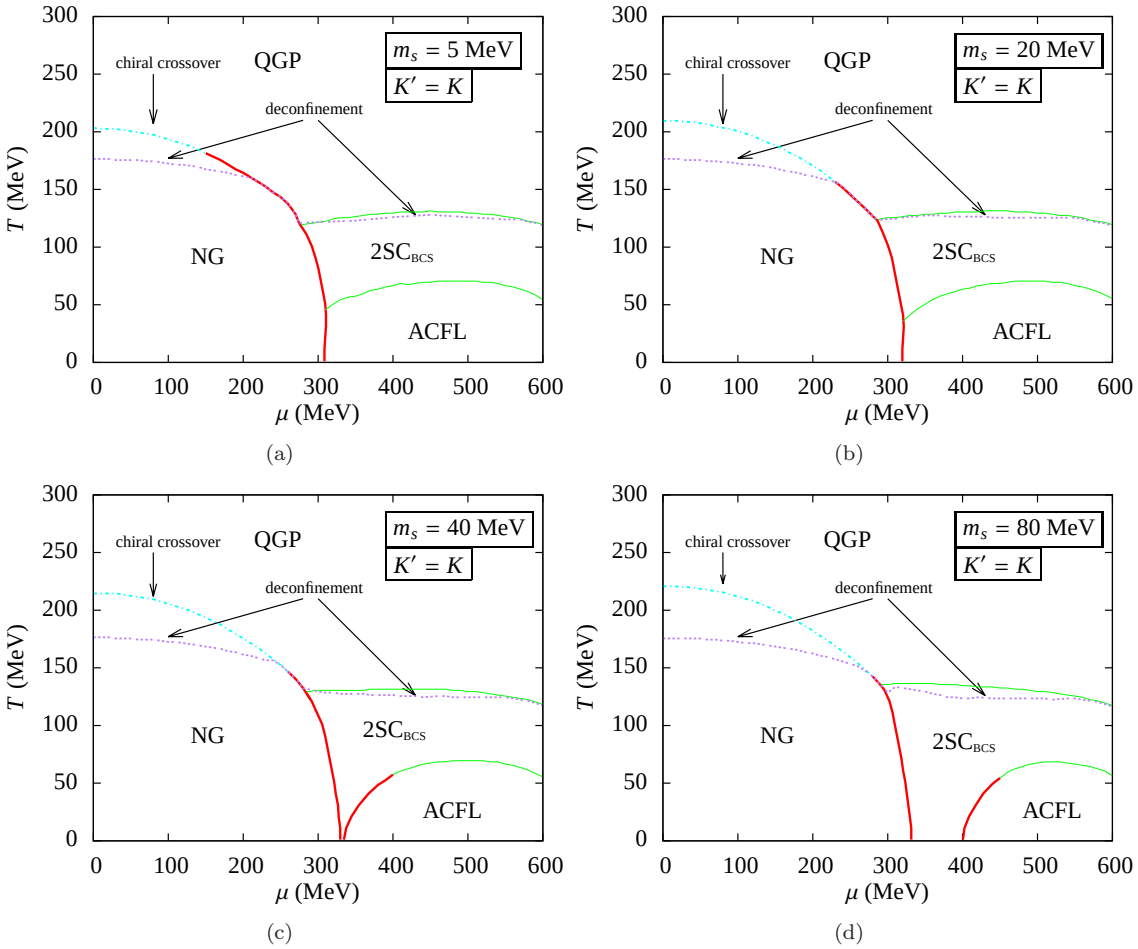

Figure 4.4: Phase diagrams for the PNJL model with realistic up and down quark masses and various strange quark masses, where the axial anomaly couplings are taken to be equal ($K' = K$). Line types have the same meaning as in Fig. 4.3(a).

is actually two distinct, but very closely spaced phase boundaries. The first boundary, at slightly lower temperature, separates the ACFL phase from a sliver of a uSC phase in which up/down and up/strange quarks pair, but down/strange quarks do not. Thus, crossing this phase boundary corresponds to breaking the down/strange quark Cooper pairs. The second boundary separates the uSC phase from the 2SC and corresponds to the breaking of the up/strange quark pairs. Figure 4.6 shows these two distinct transitions for exaggerated up and down quark masses ($m_u = 0$, $m_d = 40$ MeV, $m_s = 80$ MeV), in order to make the distinct phase boundaries visible.

We note that while the precise value of K' is unknown, on the basis the Fierz transformation mentioned in Sec. 4.1 it is expected that $K' \sim K$, and it is unclear if any mechanism might increase K' above the $4.2K$ threshold required to realize the low temperature critical point and BEC-BCS crossover. Therefore, it seems likely that Fig. 4.4(d) is closest to the true QCD phase diagram.

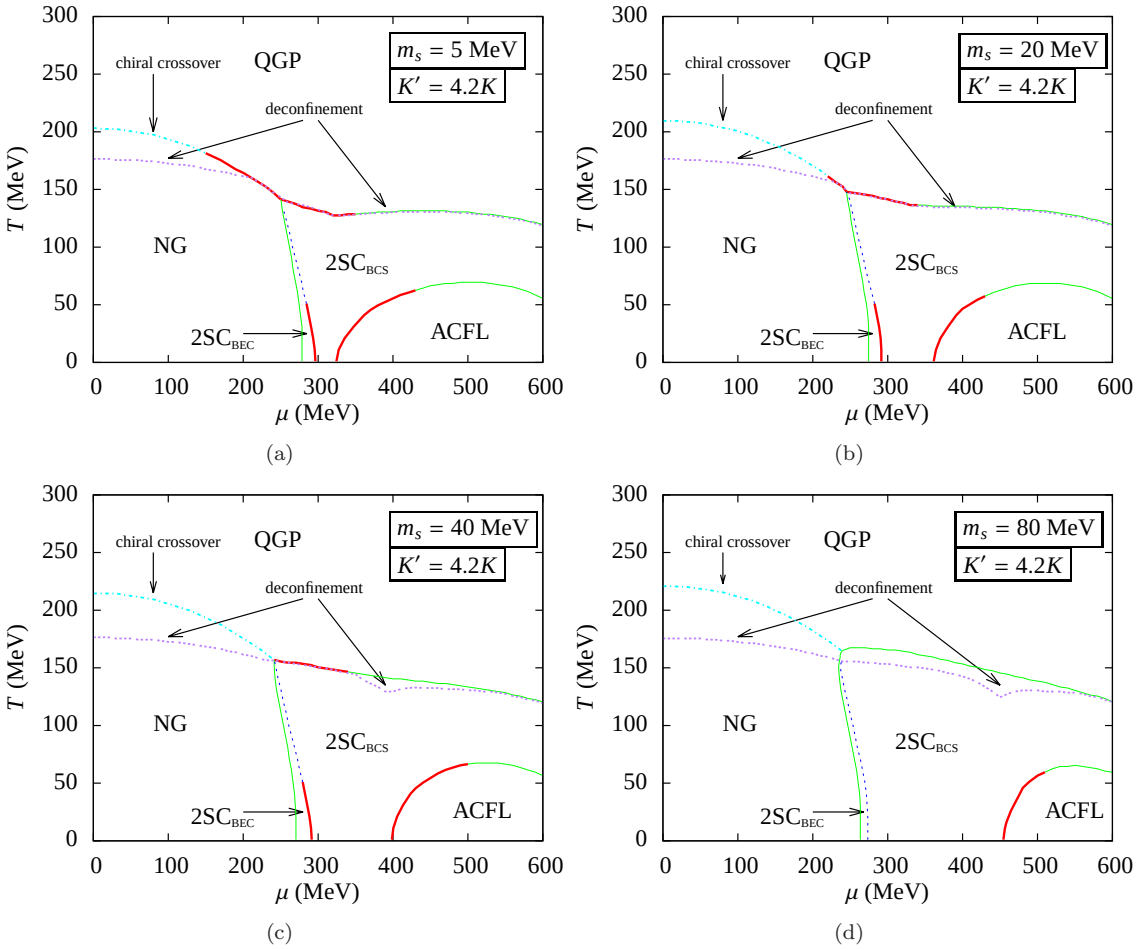

Figure 4.5: Phase diagrams for the PNJL model with realistic up and down quark masses and various strange quark masses, where $K' = 4.2K$. Line types have the same meaning as in Fig. 4.3(a).

Finally, a word is required regarding quark pairing in the ACFL phase for realistic quark masses. While the splitting of up and down quark masses is quite small relative to the chemical potential at which the ACFL phase is obtained ($\mu \sim 400$ MeV), the mass splitting between the strange quark and the two light flavors is indeed large ($M_s - M_{u,d} \gtrsim 100$ MeV). This mass difference results in significantly mismatched Fermi surfaces, which acts as a barrier to quark pairing in the conventional BCS picture of superconductivity. However, with the assumption of spatially uniform pairing, the different dispersion relations of the ultrarelativistic light quarks on the one hand, and the much slower strange quarks on the other, can lead to a situation in which quarks on the strange quark Fermi surface pair with quarks on the *interior* of the light flavors' Fermi spheres, as shown in [93]. This *breached* pairing corresponds to a situation in which the $T = 0$ state of the system consists of both superfluid and normal Fermi liquid components with both gapped and ungapped quasiparticle excitations [94]. Thus, as shown in [95], it is indeed possible to form a stable homogeneous superfluid phase out of the mismatched Fermi spheres, as we observe.

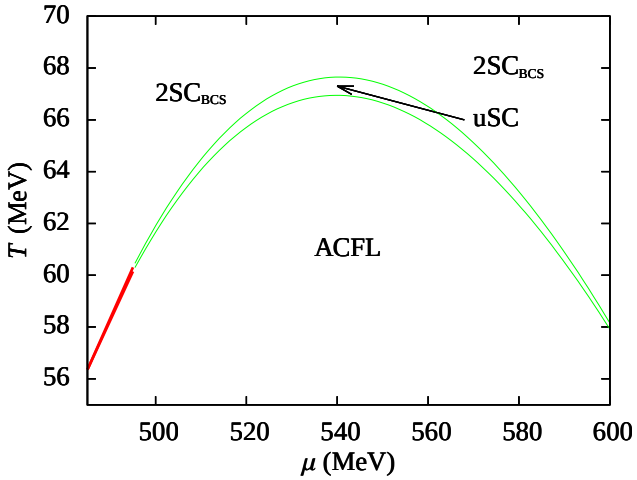

Figure 4.6: Partial phase diagram of the three flavor PNJL model with $K' = 4.2K$. Exaggerated bare quark masses of $m_u = 0$, $m_d = 40$ MeV, and $m_s = 80$ MeV are used to make the uSC region more visible. Line types have the same meaning as in Fig. 4.1.

4.5 Asymmetric CFL (ACFL) Phase

4.5.1 Quark Pairing Amplitudes

The evolution of color superconducting quark matter with increasing temperature can be inferred from Fig. 4.7. At low temperatures, the ACFL phase is essentially identical with the CFL phase, with $d_1 = d_2 \approx d_3$, and has a thermodynamic potential well below the QGP. At high temperatures, the ACFL phase morphs continuously into the $2SC_{BCS}$ phase, with $d_1 = d_2 = 0$, via a second-order phase transition. In between these two limiting cases, for 20 MeV $< T <$ 70 MeV, the ACFL phase is distinct from both the 2SC and QGP phases, and has a thermodynamic potential below both.

We also note that while not clearly visible in Fig. 4.3(b), our calculations indicate that for $T > 6$ MeV it is always energetically favorable to adopt unequal pairing amplitudes. Thus, while we cannot exclude the possibility of a low temperature CFL-ACFL phase transition, it seems very likely that the unequal pairing amplitudes persist to arbitrarily low temperatures, and that a symmetric CFL phase at intermediate μ is restricted to $T = 0$.

We can understand the asymmetric behavior of the quark pairing by noting that in our chosen gauge (and with $\phi_8 = 0$) the quark-Polyakov loop coupling is of the form

$$\overline{q}A_0\gamma^0 q = \phi_3(\overline{r}\gamma^0 r - \overline{g}\gamma^0 g), \tag{4.10}$$

where we have written the color indices explicitly, so that the Polyakov loop couples only to red and green

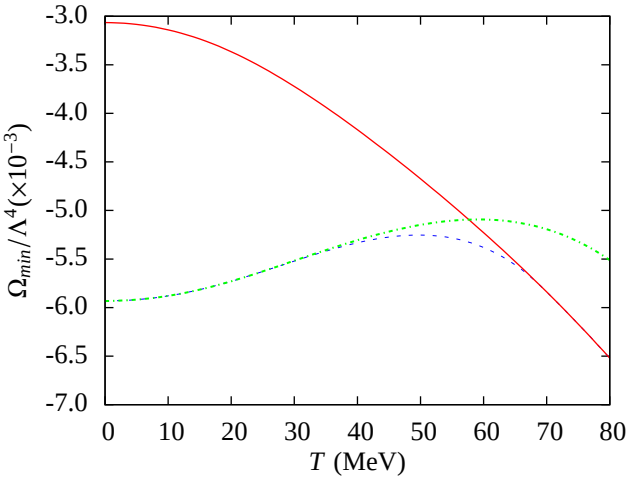

Figure 4.7: Minimum Ω/Λ^4 vs. T at $\mu = 500$ MeV for the phases: CFL (green), ACFL (blue), and QGP (red) in the massless PNJL model.

quarks. Thus, the condensates d_1 (which involves green and blue quarks) and d_2 (red and blue) are only singly-coupled to the Polyakov loop, while d_3 (green and red) is doubly-coupled.

One may inquire whether this phase of unequal quark pairing is simply an artifact of our choice of $\phi_8 = 0$, or whether such a phase might actually be realized in QCD. Unfortunately, in the present model, allowing $\phi_8 \neq 0$ renders the thermodynamic potential complex so that its minimization is no longer a well-posed problem. Nevertheless, our results do demonstrate the possibility of obtaining a phase characterized by unequal quark pairing, and they present a challenge to other models of dense quark matter to address the question of its realization.

In addition to local color charge, asymmetric quark pairing in both the ACFL and 2SC phases can give rise to a net local *electric* charge. In quark matter in neutron stars such a charge is neutralized by a net electron (and possibly muon) density, and indeed in deriving an equation of state for neutron stars, we must include charge neutrality. On the other hand, matter encountered in heavy ion collisions is electrically charged and the collisions occur on sufficiently short time scales that while the matter reaches equilibrium with respect to the strong nuclear force, it does not reach charge equilibrium. While we discuss color neutrality in Sec. 4.6, we defer a discussion of the effects of electrical neutrality in neutron stars to Chapter 5.

4.5.2 Symmetry Breaking Pattern

Having identified the region of the phase diagram occupied by the ACFL phase as well as the order of the associated phase transitions, we next study the symmetry breaking pattern of this phase. We begin by

noting that the symmetry groups of the 2SC and CFL states are [66, 67]

$$\begin{aligned} \text{2SC}: &\quad \mathrm{SU}(2)_{rg} \otimes \mathrm{SU}(2)_L \otimes \mathrm{SU}(2)_R \otimes \mathrm{U}(1)_{\bar{B}} \otimes \mathrm{U}(1)_S, \\ \text{CFL}: &\quad \mathrm{SU}(3)_{c+L+R} \otimes Z_2, \end{aligned}$$

where $\mathrm{SU}(2)_{rg}$ denotes a rotation in the color subspace of red and green quarks, $\mathrm{U}(1)_{\bar{B}}$ is a rotated baryon conserving symmetry with conserved quantity

$$\overline{B} = \overline{Q} + I_3 \quad \text{with} \quad \overline{Q} = Q - \frac{1}{2\sqrt{3}}\lambda_8, \tag{4.11}$$

and where I_3 is the isospin operator, Q and $\overline{Q}$ are the standard and rotated (conserved) electromagnetic charge operators in the 2SC phase, and $\mathrm{U}(1)_S$ corresponds to multiplying the strange quark by an arbitrary phase.

Since both the CFL and 2SC phases are special cases of the ACFL phase, the symmetry group of the ACFL phase must be a subset of the symmetry groups of these respective phases. Thus, the color-flavor-locking aspect of the CFL phase requires that there be no unbroken independent color or chiral rotations in the ACFL phase, while the $\mathrm{SU}(2)_{rg}$ symmetry of the 2SC phase requires that there be no unbroken symmetry which mixes blue quarks with red or green quarks. A direct calculation demonstrates that none of the remaining symmetries are broken and we are left with the symmetry group

$$\text{ACFL}: \mathrm{SU}(2)_{rg+L+R} \otimes Z_2.$$

In fact, the symmetry group of the ACFL phase is simply the intersection of the symmetry groups of the 2SC and CFL phases. Moreover, this symmetry group is identical to that of the CFL phase with unequal strange quark mass.[2] Finally, we note that we expect 14 Goldstone bosons in the ACFL phase, which follows from the $8_R + 8_L + 1_B = 17$ generators of the Lagrangian's symmetry group and the three generators of the ACFL symmetry group.

4.6 Color Neutrality

In the prior sections we have constructed the phase diagram of the PNJL model for both massless and massive quarks and have observed the emergence of a new ACFL phase at large μ. If our model is to

[2] While one often refers to a CFL phase in the case of unequal strange quark mass, it is implicitly assumed that $\mu \gg m_s$ so that $d_1 = d_2 \approx d_3$. If μ is not much larger than m_s then the quark pairing amplitudes will no longer be approximately equal and the CFL phase gives way to the ACFL phase.

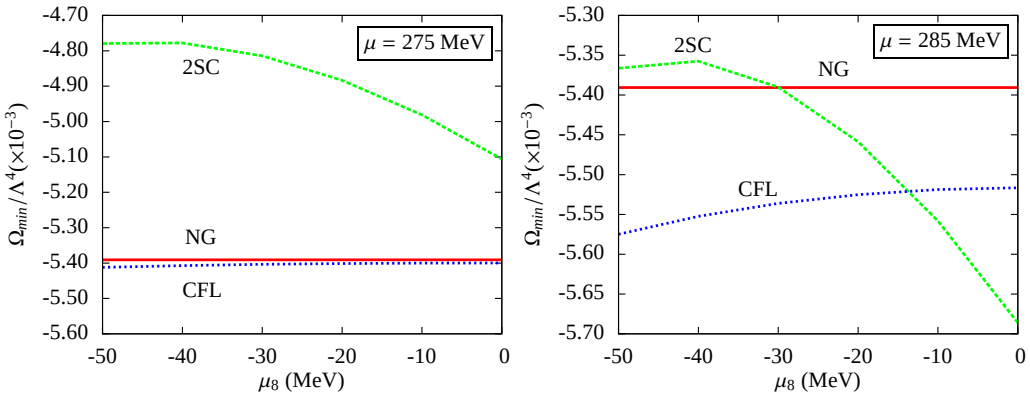

Figure 4.8: Minimum thermodynamic potentials in the NG, 2SC, and CFL phases as a function of μ_8 at $T = 0$ for (a) $\mu = 275$, and (b) $\mu = 285$ MeV, in the three flavor PNJL model with massless quarks and $K' = 4.2K$.

accurately reflect the behavior of dense QCD, however, for the homogeneous phases which we consider here we must also investigate the effects of the requirement of local color neutrality. In fact, both the 2SC phase previously reported by Basler and Buballa [92] and the new ACFL phase possess non-zero color densities which would, if left unchecked, induce large color-electric forces in the superconducting quark matter.

The origin of the net color density, in both the 2SC and ACFL phases, is the modification of the quark dispersion relations which results from unequal pairing amplitudes for red and green quarks compared with blue quarks. In the 2SC phase, for example, at fixed particle number the pairing of red and green quarks results in a decrease in the Fermi energy of these colors. In a system at fixed quark chemical potential μ, this results in an increase in the density of red and green quarks compared to the unpaired blue quarks, and a corresponding net anti-blue color density. In QCD, this quark color density is exactly cancelled by the development of a non-zero expectation value of the gluon field (i.e., tadpole diagrams), and so the homogeneous 2SC phase remains color neutral [96, 97]. However, having replaced the local SU(3) color symmetry of QCD with the global symmetry of the PNJL model we now lack the means for dynamically realizing a neutral ground state.

The standard method for imposing color neutrality in the NJL model is to introduce a set of color chemical potentials μ_a, which are chosen to ensure vanishing color densities [68, 98, 99]:

$$n_a = \left\langle q^\dagger T_a q \right\rangle = -\frac{\partial \Omega}{\partial \mu_a} = 0, \tag{4.12}$$

where $T_a = \lambda_a/2$. In light of our discussion above, we see that the equilibrium value of μ_a (i.e., the value required to achieve color neutrality) is proportional to $\left\langle A_a^0 \right\rangle$ in QCD. In both the 2SC and ACFL phases red

and green quarks pair symmetrically, so we need only include μ_8, in order to ensure that $n_8 = n_r + n_g - 2n_b = 2(n_r - n_b) = 0$.[3] Thus, we modify the Lagrangian from Eq. (3.14) to

$$\mathcal{L} = \overline{q}(i\partial\!\!\!/ - \hat{m} + (\mu + iA_0)\gamma^0 + \mu_8\lambda_8\gamma^0)q + \mathcal{L}^{(4)} + \mathcal{L}^{(6)} - \mathcal{U}_{3C}(\overline{\Phi}, \Phi). \tag{4.13}$$

In order to obtain the locally color neutral phase diagram we now minimize the thermodynamic potential with respect to the condensates σ_i and d_i, and Polyakov loop variable ϕ_3 as before, while imposing the additional neutrality constraint

$$n_8 = -\frac{\partial\Omega}{\partial\mu_8} = 0, \tag{4.14}$$

along with the stability condition

$$\frac{\partial n_8}{\partial\mu_8} = -\frac{\partial^2\Omega}{\partial\mu_8^2} > 0. \tag{4.15}$$

Thus, our solution is a saddle point of Ω, minimized with respect to the condensates, and maximized with respect to μ_8.

Due to the computational intensity of the saddle point problem for our eight variable thermodynamic potential we do not perform a complete assessment of the effects of color neutrality, together with the strange quark mass and confinement, at present. However, we report two important results from the *massless* quark limit at $T = 0$, which give insight into the structure of the full color neutral QCD phase diagram.

First, in the massless quark limit the color neutrality constraint eliminates the 2SC phase from a large portion of the phase diagram, in favor of a CFL phase. We can understand this effect by considering Fig. 4.8. At $\mu = 275$ MeV the thermodynamic potentials of the color neutral NG and CFL phases ($\mu_8 = 0$) are nearly equal, indicating the location of a phase transition between the NG phase, which exists at low μ, and the CFL phase which exists at high μ. As the system moves to higher density the energy of the NG phase is essentially constant, while both the 2SC and CFL phases decrease in energy, becoming more favorable.

The crucial effect of the color neutrality constraint is visible in the thermodynamic potentials at $\mu = 285$ MeV. In the absence of a local color neutrality constraint ($\mu_8 = 0$), we find that the 2SC phase is indeed the lowest energy, and therefore the preferred, phase of the system. However, in imposing color neutrality, we require the 2SC phase to take on a nonzero $\mu_8 \approx -40$ MeV, which results in a (physical) 2SC state which is

[3] Strictly speaking, because of the small mass splitting between up and down quarks there is a slight imbalance in the light quarks' Fermi seas, which in principle leads to $d_1 \neq d_2$ and requires the introduction of additional color-dependent chemical potentials, beyond the μ_8 considered here. However, because the up-down mass splitting is extremely small compared to the light quark Fermi energies, this effect is negligible.

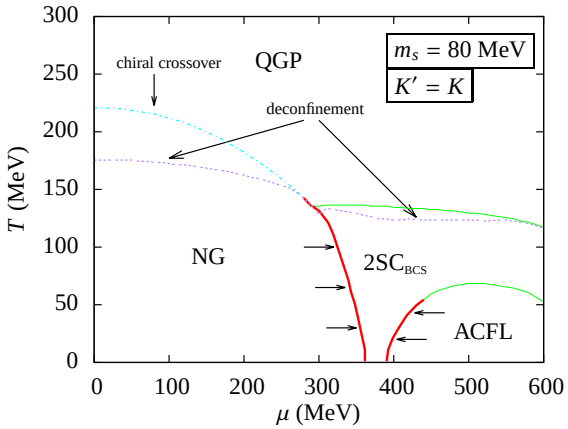

Figure 4.9: (color online) Proposed phase diagram for three flavor QCD with spatially homogeneous color neutral phases. The arrows indicate the movement of the phase boundaries due to the enforcement of local color neutrality (compare to Fig. 4.4(d)).

.

formally higher in energy than the colored state. This "additional" energy is sufficient to raise Ω_{2SC} above both Ω_{NG} and Ω_{CFL}, with the lower energy CFL phase being the color neutral ground state. As the system moves to yet higher μ, both the 2SC and CFL phases continue to move to lower energies, with the latter always maintaining a slight energetic advantage. Thus, at $T = 0$ enforcing local color neutrality eliminates the 2SC phase altogether.

A second important effect of color neutrality, which is a corollary of the suppression of the 2SC phase is the "re-emergence" of a low temperature critical point [2, 18]. As shown in [92] and confirmed in Fig. 4.5, when one allows for 2SC quark pairing (rather than simply a CFL structure) in the absence of a local color neutrality constraint this critical point is eliminated in favor of a second-order NG-2SC phase transition at intermediate μ. However, with the 2SC phase eliminated by the color neutrality constraint, the system once again realizes quark-hadron continuity via a smooth crossover between the NG and ACFL phases at low temperatures.

In the case of realistic quark masses, the 2SC phase remains intact after imposing local color neutrality, but the location of the low temperature NG-2SC transition is moved to the right by $\Delta\mu \approx 30$ MeV. This shift in the phase boundary is not surprising in light of the additional energy required to maintain a non-zero μ_8. Indeed, the 2SC phase still becomes more favorable (i.e., Ω_{2SC} decreases) as the system moves to higher μ, but the non-zero value of μ_8 results in an overall shift of Ω_{2SC} to larger values. As a result, the NG-2SC phase boundary defined by $\Omega_{2SC} = \Omega_{NG}$ is shifted to larger μ.

While an exhaustive analysis of the effects of color neutrality and realistic quark masses is beyond the scope of this thesis, based on the results obtained here we can propose an educated hypothesis for the QCD phase diagram under the assumptions adopted here, namely the restriction to spatially homogeneous

phases. Figure 4.9 shows the proposed QCD phase diagram, which should be compared to Fig. 4.4(d), in which color neutrality was not enforced. We expect the essential effect of the color neutrality constraint to be the reduction in size of the 2SC phase, due to the additional energy required to generate the neutralizing gluon condensate. In particular, the lines of first-order NG-2SC and ACFL-2SC transitions will encroach upon the 2SC region due to the upward shift of Ω_{2SC}, as indicated by the arrows in Fig. 4.9. Second-order transition lines, however, will remain largely unaffected as $\mu_8 \to 0$ on these boundaries.

A number of outstanding questions exist regarding the PNJL model and the QCD phase diagram which have yet to be addressed. Foremost among them is a complete construction of the QCD phase diagram which incorporates local color neutrality along with realistic quark masses. Also, the effects of charge neutrality and β-equilibrium, which are important in the study of stable quark matter at low temperatures in neutron stars, and which is the subject of the next chapter, remain to be completely elucidated in the context of the PNJL model.

Chapter 5

Structure and Stability of Neutron and Dense Quark Stars

5.1 Introduction

After several decades of speculation, the Large Hadron Collider (LHC) and the Relativistic Heavy Ion Collider (RHIC) are finally providing the first significant experimental probes of the phase diagram of quantum chromodynamics (QCD) [102–107]. Unfortunately, despite their successes and the promise of yet higher density probes at the Facility for Antiproton and Ion Research (FAIR), accelerators are by their nature restricted to investigating high temperature matter due to the extreme heating inherent in high energy collisions. Indeed, there is no conceivable method by which the rich structure of cold dense quark matter will ever be obtainable in a laboratory, due to the extreme pressures which must be sustained to produce such matter. As a result, the only opportunity to probe the low temperature region of the QCD phase diagram is provided by nature herself, in the neutron stars which are fortuitously spread throughout our galaxy, and beyond.

While neutron stars may hold the key to understanding the properties of dense quark matter, our observations of the quark matter that comprises them are necessarily indirect, owing both to their distance (~ 100 ly to the nearest [31, 32], and ~ 4000 ly to the most massive [33]) and to their intense gravitational and rotational properties. Thus, we are led to consider what observable properties of neutron stars are capable of providing insight into the thermodynamic properties of their constituent matter [34–36, 108].

Two astrophysical observables which are intimately connected to the thermodynamic properties of quark matter are neutron stars' maximum stable masses (M_{max}) and their mass-radius (M-R) relationship. In particular, for a given equation of state (EoS), which specifies the pressure (P) of the star's constituent matter as a function of its density (ρ), both M_{max} and the M-R relationship are uniquely determined by the Tolman-Oppenheimer-Volkov (TOV) equation [37, 38]. As a result, much work has been done to model the equation of state of the dense quark matter of which neutron stars are composed, in order that we may better understand the structure of these astrophysical objects. While a wide variety of nuclear equations of state have been proposed, until very recently all such models have yielded maximum neutron star masses less than $2M_\odot$ [109–115]. The recent observation of several neutron stars with $M \sim 2M_\odot$ has thus prompted a revisiting of our understanding of the basic structure of dense quark matter and the search for a mechanism

Neutron Star	Discovery	Mass ($M_\odot$)	Distance
J1614 - 2230	Demorest (2010)	1.97 ± 0.04	3,900 ly
J0348+0432	Antoniadis (2013)	2.01 ± 0.04	6,800 ly
J1311 - 3430	Romani (2012)	2.4 ± 0.3	TBD

Table 5.1: Currently known massive neutron stars with $M \gtrsim 2M_\odot$, together with the date of their discovery and distance from Earth [33, 41, 42].

by which such massive stars might be obtained [33, 41, 42]. Meanwhile, from an observational standpoint, astrophysical measurements of the masses and radii of neutron stars place strict constraints on the equation of state of dense quark matter [36, 116].

Neutron stars with central densities of $\rho \sim 5-10\rho_0$ (where nuclear density is $\rho_0 \approx 2.3\times10^{14}$ g/cm^3) have traditionally been studied under the assumption that they are largely composed of matter whose fundamental degrees of freedom are hadrons. However, as discussed in Chapters 3 and 4, the phase transition from confined hadrons to color superconducting phases occurs at a density of roughly $\rho \sim 2\rho_0$, and as a star's central density increases beyond this range, an increasingly large portion of the star is described by matter whose fundamental degrees of freedom are the quarks themselves. As a result, the structure and stability of these dense neutron stars is particularly dependent on the *quark matter* equation of state [43, 44, 117–119]. Moreover, as shown in [120,121], strange matter is expected to emerge at baryon densities of $n_b \sim 4n_0$ (where nuclear baryon density is $n_0 \approx 0.17/\text{fm}^3$), at which point the nuclei comprising the star will have percolated, rendering a nucleonic description of matter quite tenuous. We therefore take as our starting point a Nambu–Jona-Lasinio model description of *quark*, rather than hadronic matter, and investigate the possibility of realizing massive neutron stars of $M \gtrsim 2M_\odot$. In particular, we include a tunable flavor-symmetric vector repulsion and compute M_{max}, as well as the stars' M-R relationship, as a function of the magnitude of the vector coupling.

In addition to the question of how nature might realize massive neutron stars, the possibility of extremely dense *quark stars* has been raised [122–124]. Such stars would have masses typical of observed neutron stars, but would consist of an extremely dense core (perhaps with $\rho_c \sim 100$ or more) possibly surrounded by a thin crust ($\delta R \sim 1$ km) of hadronic matter of more typical neutron star densities. For such stars, even more than typical neutron stars, their stability is determined by the equation of state in the quark sector. In the next section we derive a quark matter equation of state at $T = 0$ from the NJL model discussed in Chapters 3 and 4. After interpolating this equation of state with a hadronic equation of state at low densities we then proceed to investigate the density profiles and mass-radius relationship of both neutron stars and the proposed ultra-dense quark stars. The content of this chapter is based largely on [4].

5.2 Quark Matter Equation of State

The pressure in a homogeneous system in equilibrium is given by the thermodynamic identity $P = n^2\partial(\Omega/n)/\partial n$, where $n = N/V$ is the baryon density and $\Omega = (E - TS - \mu N)/V$ is the thermodynamic potential per unit volume. Since Ω is an intensive quantity it follows that $P = -\Omega$ and it is possible to obtain the pressure for the three flavor PNJL model trivially from Eq. (4.9). However, since the Polyakov loop does not significantly impact quark thermodynamics at low temperatures, for simplicity we work instead with the non-confining NJL model. In addition, we consider the effects of a flavor-symmetric vector repulsion of the form [120, 121, 125, 126]

$$\mathcal{L}_V^{(4)} = -g_V \left(\overline{q}\gamma^\mu q\right)^2, \tag{5.1}$$

where $g_V > 0$, which increases the quark matter pressure at fixed mass density ρ. Since a star's radius is determined by the equilibrium of gravitational and internal pressures, this additional pressure tends to counteract the tendency toward gravitational collapse that increases with mass and thereby permits the realization of more massive neutron stars than would otherwise be stable.

Next, we note that while color superconducting phases are thought likely to exist in the cores of neutron stars, as discussed in Chapters 2, 3, and 4, the preferred quark pairing structures at neutron star densities are not known. Thus, by investigating a variety of potential pairing structures and computing the maximum stable star masses for each, it may be possible to infer aspects of the QCD phase diagram directly from astrophysical observations. Regardless of the precise pairings realized, however, color superconductivity will always act to *soften* the quark matter equation of state, reducing $P(\rho)$, and thereby making it more difficult to realize massive neutron stars. As a first approximation, we therefore neglect quark pairing entirely in order to determine whether a vector repulsion is capable of stabilizing massive neutron stars even in the absence of this softening. Future work will be dedicated to a more complete analysis of quark pairing and its effects on the stability of massive neutron stars.

In the absence of diquark pairing we describe the quark matter of neutron stars with the NJL model Lagrangian

$$\mathcal{L}_q = \overline{q}\left(i\partial\!\!\!/ - \hat{m}\right)q + \mathcal{L}_\sigma^{(4)} + \mathcal{L}_V^{(4)} + \mathcal{L}_\sigma^{(6)}, \tag{5.2}$$

where $\mathcal{L}_\sigma^{(4)}$ and $\mathcal{L}_\sigma^{(6)}$ are defined in Eqs. (3.3) and (3.11). In order to describe the stable quark matter which comprises a neutron or quark star we must also impose the conditions of fixed particle number, charge

neutrality, and β-equilibrium. The first two conditions are incorporated in the standard way by introducing quark and electron chemical potentials μ and μ_e as Lagrange multipliers so that

$$\mathcal{L}_q \to \mathcal{L}_q + \mu q^\dagger q - \mu_e q^\dagger Q q, \tag{5.3}$$

where $Q = \mathrm{diag}(2/3, -1/3, -1/3)$ is the quark charge matrix in flavor space (in units of e, where we take $e > 0$). Meanwhile, the β-equilibrium $u \leftrightarrow d + e^- + \overline{\nu}_e$ requires that $\mu_u = \mu_d + \mu_e$, where we neglect $\mu_{\overline{\nu}_e}$ since the neutrinos' extremely small scattering cross section allows them to escape the star so their number is not conserved.[1] The presence of the electrons required to maintain charge neutrality also requires that we include the corresponding Dirac Lagrangian $\mathcal{L}_e = \overline{\psi}_e(i\partial\!\!\!/ - m_e + \mu_e\gamma^0)\psi_e$, where ψ_e is the electron field.[2]

Having defined our model, we now work at the mean field level by neglecting quadratic fluctuations about the average chiral condensates $\sigma_i = \langle \overline{q}_i q_i \rangle$ and quark densities $n_i = \langle q_i^\dagger q_i \rangle$ $(i = u, d, s)$. Thus, we obtain the Lagrangian

$$\mathcal{L} = \overline{q}(i\partial\!\!\!/ - \hat{M} + \hat{\mu}\gamma^0)q + \overline{\psi}_e\left(i\partial\!\!\!/ - m_e + \mu_e\gamma^0\right)\psi_e - V(\sigma_i, n), \tag{5.4}$$

where $\hat{M}$ and $\hat{\mu}$ are flavor-dependent effective quark masses and chemical potentials:

$$M_i = m_i - 4G\sigma_i + 2K|\epsilon_{ijk}|\sigma_j\sigma_k, \qquad \mu_i = \mu - Q_i\mu_e - 2g_V n_q, \tag{5.5}$$

and where $n_q = \sum_i n_i$ is the net quark density. Writing the partition function as $\mathcal{Z} = \int D[\overline{q}, q, \overline{\psi}_e, \psi_e]e^{-S_E}$ where $S_E = \int_0^\beta d\tau \int d^3\mathbf{r}\left\{q^\dagger\partial_\tau q + \psi^\dagger\partial_\tau\psi + \mathcal{H}\right\}$ and integrating out the fermionic degrees of freedom yields the thermodynamic potential per unit volume

$$\begin{aligned}\Omega &= -\frac{T}{2}\sum_{i=1}^{72}\int\frac{d^3\mathbf{k}}{(2\pi)^3}\left[\ln(1 + e^{-\beta E_{qi}}) + \frac{1}{2}\beta\Delta E_{qi}\right] \\ &\quad -2T\sum_{i=1}^{2}\int\frac{d^3\mathbf{k}}{(2\pi)^3}\left[\ln(1 + e^{-\beta E_{ei}}) + \frac{1}{2}\beta\Delta E_{ei}\right] + V(\sigma_i, n),\end{aligned} \tag{5.6}$$

where $V(\sigma_i, n)$ is defined below, the quark and electron eigenvalues E_{qi} and E_{ei} are the poles of their

[1] This approximation is very nearly exact in all stable astrophysical objects. However, the $\overline{\nu}_e$ *are* believed to play an important role in the dynamics of stellar core collapse, which occurs on such short time scales that the large quantities of $\overline{\nu}_e$ produced are unable to escape the star [127–130].

[2] One can also allow for the possibility of muon production in neutron stars by introducing an analogous term $\mathcal{L}_\mu = \overline{\psi}_\mu(i\partial\!\!\!/ - m_\mu + \mu_\mu\gamma^0)\psi_\mu$. However, as noted in [120, 121], within the present model muons are produced neither at low densities where they are suppressed due to their relatively large masses ($m_\mu \approx 200m_e$), nor at high densities where the appearance of strange quarks achieves charge neutrality without lepton generation. Thus, we do not consider the possibility of muon production further.

Λ (MeV)	$G\Lambda^2$	$K'\Lambda^5$	$m_{u,d}$ (MeV)	m_s (MeV)
631.4	1.835	9.29	5.5	135.7

Table 5.2: NJL parameters in the 2+1 flavor NJL model, which we use to construct the quark matter equation of state [14].

respective single particle Green's functions $S_q(k) = (\not{k} - \hat{M} + \mu\gamma^0)^{-1}$ and $S_e(k) = (\not{k} - m_e + \mu_e\gamma^0)^{-1}$:

$$E_{qi} = |E_{\mathbf{k},i} \pm \mu_i| \qquad \text{where} \qquad E_{\mathbf{k},i} = \sqrt{\mathbf{k}^2 + M_i^2}, \tag{5.7}$$

$$E_{ei} = |E_{\mathbf{k},e} \pm \mu_e| \qquad \text{where} \qquad E_{\mathbf{k},e} = \sqrt{\mathbf{k}^2 + m_e^2}, \tag{5.8}$$

and $\Delta E_i = E_i - E_i^{free}$, where E_i^{free} is the given eigenvalue in the non-interacting case, and measures Ω with respect to the non-interacting Dirac sea.

The potential $V(\sigma_i, n)$, which prevents the double-counting the degrees of freedom in our mean field treatment is

$$V(\sigma_i, n) = 2G\sum_{i=1}^{3}\sigma_i^2 - 4K\sigma_1\sigma_2\sigma_3 - g_V n_q^2. \tag{5.9}$$

Finally, because neutron star temperatures ($T \sim 1 - 10$ MeV) are very small compared to the energy scales of QCD we may consider the limit $T \to 0$ and obtain the quark matter equation of state:

$$P_q = \frac{1}{4}\sum_{i=1}^{72}\int^{\Lambda}\frac{d^3\mathbf{k}}{(2\pi)^3}\Delta E_{qi} + \sum_{i=1}^{2}\int^{\Lambda}\frac{d^3\mathbf{k}}{(2\pi)^3}\Delta E_{ei} - V(\sigma_i, n), \tag{5.10}$$

where we have introduced the usual high-momentum cutoff Λ to regulate the theory. We note that the total weighting of the quark degrees of freedom in Eq. (5.10) is $72/4 = 3$ (color) $\times$ 3 (flavor) $\times$ 2 (spin), while the electrons contribute a factor of 2 (spin). This is what we expect at $T = 0$ as the antiparticle excitations are frozen out, reducing the Dirac degeneracy from four to two.

In order to fully define the quark matter equation of state, we must also fix the NJL parameters $\hat{m}$, G, K, and Λ. For the sake of simplicity, as well as to facilitate a comparison of our results with the current literature, we work in the 2+1 flavor NJL model where $m_u = m_d \neq m_s$ and adopt the parameters of Hatsuda and Kunihiro, which are shown in Table 5.2 [14]. While we have now obtained the equation of state for quark matter, which is valid for high densities at which quarks are no longer confined into hadrons, non-trivial portions of neutron stars consist of hadronic matter for which Eq. (5.10) will not be valid. Thus, we must devise a method for extending the region of validity of our equation of state to low densities, which is the topic of the next section.

5.3 Quark-Hadron Hybrid Equation of State

While the equations of state for quark matter at very low (hadronic) and very high (liberated quark) densities are well studied, very little is known of the detailed crossover between these two regimes. As a result, there is no unique method for extending our quark matter equation of state to low densities. Therefore, following [120,121] we adopt a simple, qualitatively valid interpolation scheme in which the pressure is given by

$$P(n) = f_h(n)P_h(n) + f_q(n)P_q(n), \tag{5.11}$$

where $n = n_q/3$ is the net baryon density, $P_h(n)$ and $P_q(n)$ are the pressures as given by the hadronic and quark equations of state, respectively, and we define the weighting functions

$$f_{q,h}(n) = \frac{1}{2}\left[1 \pm \tanh\left(\frac{n-\overline{n}}{\Gamma}\right)\right], \tag{5.12}$$

where $\overline{n}$ and Γ are the center and characteristic size of the "crossover region," and following [120, 121], we choose $(\overline{n}, \Gamma) = (3n_0, n_0)$. In order to compute the mass (or energy) density in a thermodynamically consistent way, we integrate the identity $P = n^2\partial(\rho c^2/n)/\partial n$ to obtain

$$\rho(n) = f_h(n)\rho_h(n) + f_q(n)\rho_q(n) + \Delta\rho(n), \tag{5.13}$$

where $\Delta\rho/n$ is an additional mass density per baryon which stems from the interpolation scheme:

$$\Delta\rho(n) = n\int_{\overline{n}}^{n} dn' \, \frac{\rho_h(n') - \rho_q(n')}{2\Gamma}\frac{g(n')}{n'}, \tag{5.14}$$

and where $g(n) = \mathrm{sech}^2[(n-\overline{n})/\Gamma]$. In order to apply our interpolation scheme we must of course choose an equation of state $P_h(n)$ valid in the hadronic regime. Many candidates have been proposed to describe nuclear matter at low densities [112–115], but here we employ the Akmal-Pandaripande-Ravenhall (APR) equation of state to describe matter in the low density hadronic regime [111].

Figure 5.1(a) shows the interpolation scheme between the hadronic and quark equations of state for $g_V = G$. As we found in Chapters 2–4, in the NJL model, in which the quarks themselves are the fundamental degrees of freedom, for $\mu \lesssim 275$ MeV the effective quark masses are sufficiently large to suppress their generation so that $n_q = 0$. Thus, below this critical chemical potential (and the corresponding density) $P_q = 0$, while above it $P_q \neq 0$. As a result, the quark matter equation of state is only relevant above a

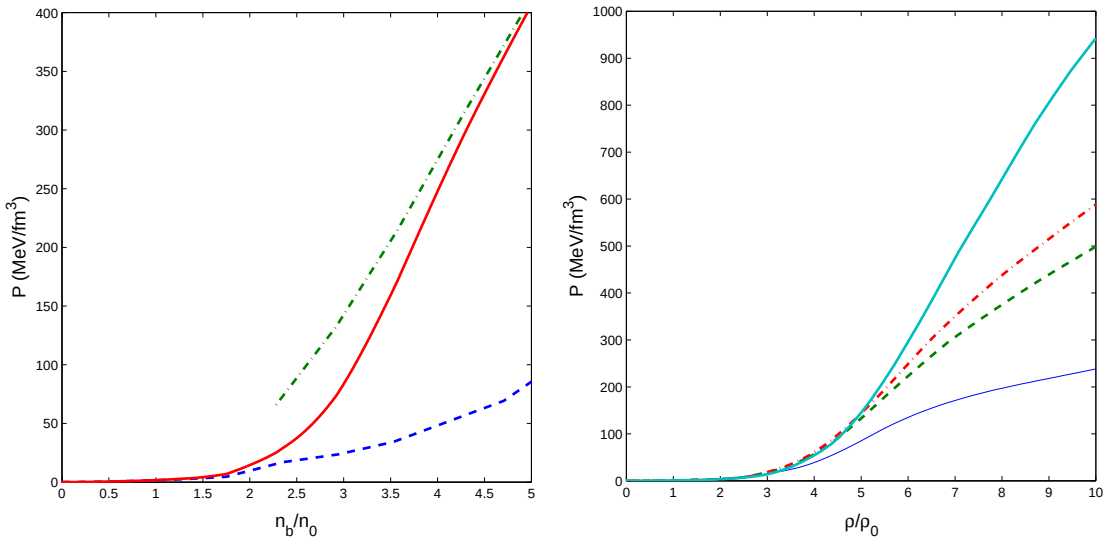

(a) (b)

Figure 5.1: (a) Hadronic (dashed blue), quark (dot-dashed green), and interpolated (solid red) equations of state $P(n)$ for $g_V = G$. For $n_b \lesssim 1.5n_0$ the NJL model's ground state is the vacuum so that $P_{interp} = P_h$ [110]. (b) Hybrid equation of state $P(\rho)$ for $g_V = 0$ (thin blue), G (dashed green), $1.5G$ (dot-dashed red), and $5G$ (solid teal).

critical density, as depicted in the green curve. For lower densities, the interpolated equation of state is identical to the hadronic equation of state, while at higher densities it moves smoothly between the hadronic and free quark limits.

Figure 5.1(b) shows the interpolated quark matter equation of state for $g_V = 0$, G, and $1.5G$. As anticipated, the presence of the vector repulsion acts to increase the pressure of the quark gas at fixed ρ. This effect is most pronounced at small g_V, while for $g_V \gtrsim 1.5G$ the marginal effect of increasing g_V diminishes. Having now obtained the equation of state we are in a position to determine the structure of neutron and quark stars by solving the Tolman-Oppenheimer-Volkov equation, to which we now turn.

5.4 Massive Neutron Star Structure

Having specified the quark matter equation of state for all densities, the pressure (and thus density) profiles of neutron and hybrid quark stars are determined by the Tolman-Oppenheimer-Volkov (TOV) equation, which is the solution of the Einstein field equations for a static spherically symmetric body:

$$\frac{dP(r)}{dr} = -G\frac{\left[\rho(r) + P(r)/c^2\right]\left[M(r) + 4\pi r^3 P(r)/c^2\right]}{r^2 - 2GM(r)/c^2\, r}, \tag{5.15}$$

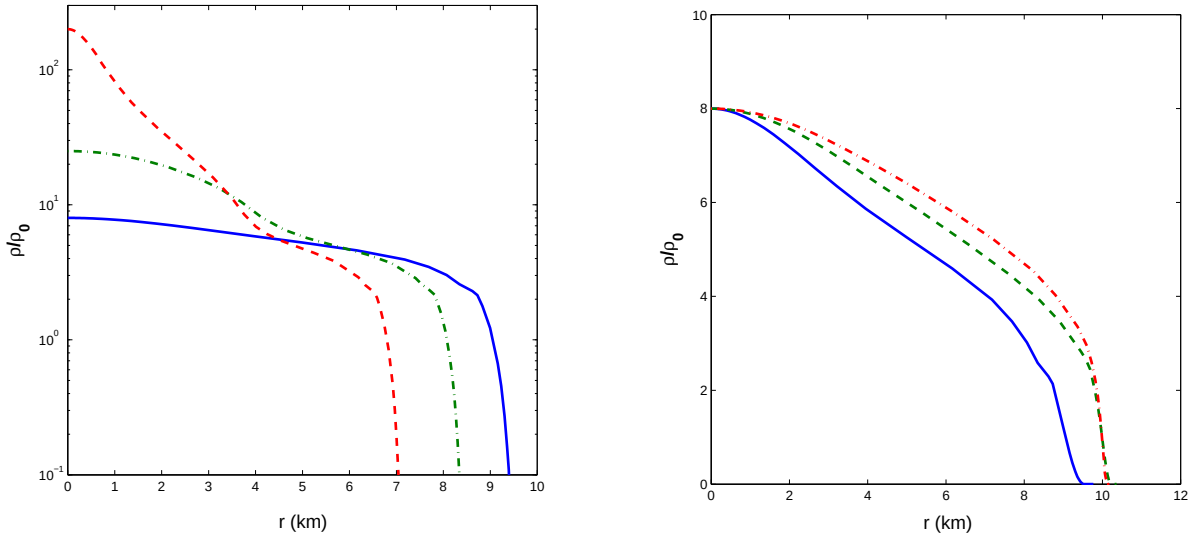

(a) (b)

Figure 5.2: Quark star density profiles $\rho(r)$ for (a) $g_V = 0$ with $\rho_c = 8\rho_0$ (solid blue), $25\rho_0$ (dot-dashed green), and $200\rho_0$ (dashed red); (b) $\rho_c = 8\rho_0$ with $g_V = 0$ (solid blue), $1.5G$ (dashed green), and $5G$ (dot-dashed red). Note that the vertical axis in (a) is logarithmic, while that in (b) is linear.

where G is Newton's gravitational constant, the equation of state gives $\rho(r) = \rho(P(r))$, and

$$M(r) = \int_0^r dr'\, 4\pi r'^2 \rho(r') \tag{5.16}$$

is the total mass inside a shell of radius r. Given a central density $\rho_c \equiv \rho(r = 0)$, Eq. (5.15) can be integrated numerically to yield $P(r)$, which can then be transformed into the density profile via the equation of state.

Figure 5.2(a) shows the density profile for three quark stars with different central densities and $g_V = 0$. The red curve (with $\rho_c = 8\rho_0$) represents a typical neutron star while the green ($\rho_c = 25\rho_0$) and blue ($\rho_c = 200\rho_0$) curves represent quark stars with central densities above those of known astrophysical objects.[3] One feature of these stars which immediately stands out is the fact that at least for these values of ρ_c, the equilibrium star radius *decreases* with increasing central density. This is due to the increasing gravitational force which accompanies the increase in ρ_c, and which tends to decrease the size of the star. In addition, while stars with intermediate central densities ($\rho \lesssim 10\rho_c$) have relatively constant density profiles outside of a thin crust of thickness $\delta R \sim 1$ km, as ρ_c increases the larger gravitational force induces larger density gradients and a smaller fraction of the star's volume realizes densities of $\rho \sim \rho_c$. As a result, for $\rho \gtrsim 10\rho_0$ the total star mass is actually a *decreasing* function of ρ_c, as shown in Fig. 5.3(a).

Figure 5.2(b) shows the density profile for a star with $\rho_c = 8\rho_0$, for three different values of g_V. We see that as the vector coupling increases, the stiffening of the equation of state tends to raise the density

[3] Black holes are, of course, an exception that we do not attempt to describe in this thesis.

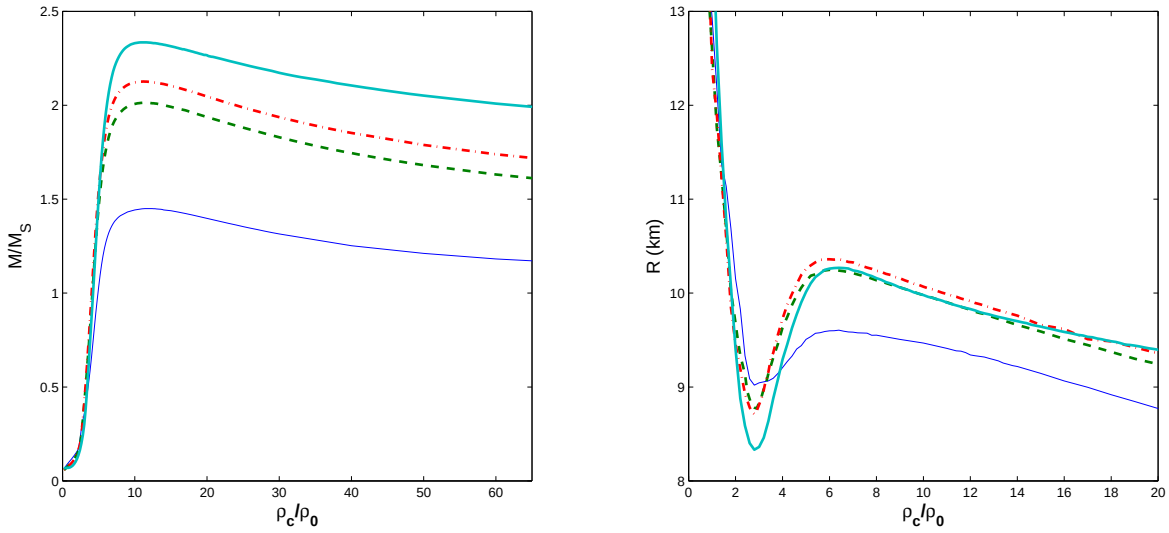

(a) (b)

Figure 5.3: Neutron star (a) mass (in solar masses) and (b) radius vs. central density for $g_V = 0$ (blue), G (green), $1.5G$ (red), and $5G$ (teal). As g_V increases, the additional pressure due to the vector coupling allows neutron stars to become larger and more massive before succumbing to gravitational collapse.

at a given radius. As a result, the density profile "bows out," tending to give rise to larger, more massive stars for a specified central density. We also find that while the star radius increases by ~ 1 km when g_V/G increases from 0 (blue curve) to 1.5 (green), there is no further increase in star size as the vector coupling increases to $g_V/G = 5$. However, the density profile does continue to bow out, indicating a further mass increase, since $M = \int_0^R dr'\, 4\pi r'^2 \rho(r')$.

In Fig. 5.3(b) we display the neutron star radius as a function of its central density for $g_V/G = 0$, 1, 1.5, and 5. For low ρ_c, where the hadronic equation of state dominates, the star's structure is relatively independent of g_V. However, as ρ_c increases, the vector repulsion plays a progressively more significant role in the stellar equilibrium, and for $\rho_c \gtrsim 5\rho_0$ a value of $g_V \gtrsim G$ increases the star radius by ~ 0.5 km.

While Fig. 5.3(a) indicates that increasing the vector coupling increases the maximum stable neutron star mass, this situation does not continue indefinitely, as shown in Fig. 5.4(a). The reason for the vector coupling's limited capacity to increase M_{max} can be understood by considering the effect of an increasing g_V on the interpolation of the equation of state $P(\rho)$. As discussed in Section 5.3, we interpolate between the hadronic and quark sector equations of state over the domain $2n_0 \lesssim n_b \lesssim 4n_0$, based on the percolation of quark matter at these baryon densities. As g_V increases, the hybrid equation of state stiffens, and $\rho(n)$ (i.e., the mass density at specified baryon density) decreases. Thus, while the crossover region in baryon density is fixed, as g_V increases the corresponding crossover region in mass density is shifted to progressively

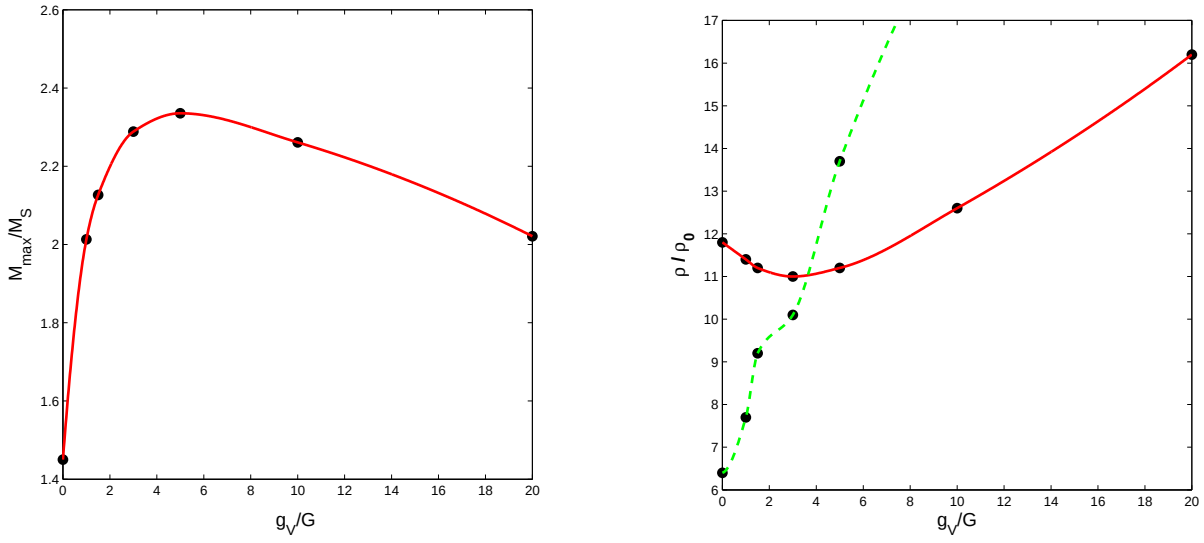

(a) (b)

Figure 5.4: (a) Maximum stable neutron star mass as a function of the vector coupling strength g_V/G. (b) Central density for maximally massive stars (red) and critical density for onset of strangeness (green) as a function of g_V/G. The curves intersect at $g_V/G = 3.19$, indicating that for $g_V/G > 3.19$, maximally massive neutron stars have no strange quark content. Black dots denote calculated values while the red curves are interpolated fits.

larger values of ρ (see the green curve in Fig. 5.4(b) which roughly corresponds with the end of the crossover region). In other words, while larger values of g_V stiffen the hybrid equation of state at large ρ, they *soften* it at low ρ. The net effect of the vector coupling is therefore to exchange stiffness at low mass density for stiffness at high density.

As shown in Fig. 5.2(a), the density profiles of neutron stars with central densities of $\rho_c \lesssim 10\rho_0$ are relatively flat except for very near the stars' crusts, where $\rho(r)$ decreases rapidly. As a result, very little of these stars' constituent matter exists at low densities. This means that when g_V is small, the equation of state's stiffening at high ρ impacts a large portion of the star's constituent matter, while the softening at low ρ is negligible except in a very thin shell near the star's surface. In this case, the net effect of g_V is therefore to increase the maximum stable star mass. When g_V is large, however, the crossover region is at a correspondingly high ρ, and for a specified ρ_c a greater portion of the star is described by the softened, low ρ portion of the equation of state, tending to lead to lower mass stars. Moreover, increasing ρ_c does not counteract this effect, for as shown in Fig. 5.2(a), as ρ_c increases, so too does the gradient $dP/d\rho$, so that it is no longer possible to form a star whose constituent matter is described primarily, by the high ρ equation of state.

The end result of the vector coupling's ability to shift stiffness between low and high density quark matter is that, as shown in Fig. 5.4(a), for $g_V/G \lesssim 5$ the high density stiffening dominates the star, while

for $g_V/G \gtrsim 5$ low density softening is the dominant feature. Thus, the maximum stable neutron star mass for *any* vector coupling is $M_{max} = 2.34M_\odot$, which is obtained for $g_V/G \approx 5$.

Figure 5.4(b) shows the central density for maximally massive stars (ρ_c^*), as well as the critical density for strange quark production (ρ_s^*), as a function of g_V. Noting that the critical *baryon* density for the onset of strangeness ($n_b^* \sim 4.3n_0$) is independent of g_V, ρ_s^* roughly corresponds to the end of the interpolation region ($4n_0$), and so its rapid increase with g_V is anticipated from our prior discussion. Meanwhile, we find that as g_V is increased from zero, ρ_c^* initially decreases slightly, as the stiffening of the high density equation of state is exploited most effectively by "flattening" the density profile of the star, thereby rendering a greater portion of the star described by the stiff high density equation of state. As g_V increases, however, ρ_c^* must likewise increase if a significant portion of the star is to take advantage of the stiff high density region.

Comparing Fig. 5.4(a) to the masses observed in Table 5.1, we find that our equation of state is capable of generating stable neutron stars consistent with J1614-2230 ($M = 1.97M_\odot$) and J0348+0432 ($M = 2.01M_\odot$) for quite reasonable values of the vector coupling ($g_V/G \gtrsim 1$). The status of J1311-3430 [$M = (2.4 \pm 0.3)M_\odot$] is less clear, owing to the large uncertainty in its observed mass, but our calculated value of $M_{max} \approx 2.34M_\odot$ is well within the quoted mass range, with the lower limit on its mass requiring $1.4 \lesssim g_V/G \lesssim 17.0$, and the mean estimate yielding $3.6 \lesssim g_V/G \lesssim 8.0$. Perhaps in the near future, improved observational data will reduce the uncertainty in this massive neutron star's properties and the discovery of additional massive neutron stars will further constrain the quark matter equation of state.

5.5 Stability of Neutron and Ultra-Dense Quark Stars

In the previous section we computed the maximum obtainable masses of neutron and hybrid quark stars as a function of the vector coupling g_V. However, we have yet to assess the stability of these massive stars against gravitational collapse and the formation of black holes. In addition, there has been much interest recently in the prospect of stable quark stars for which $\rho_c \gg 10\rho_0$. In particular, it is suggested that while neutron stars become unstable to collapse beyond a critical central density, by continuing to increase ρ_c well beyond the densities obtained in conventional neutron stars one might arrive at another region of stability. This ultra-high density matter would consist of equal densities of the three light flavors of quarks, as shown in Fig. 5.5, and could be *absolutely stable*, or the true lowest energy state of quark matter [122, 124]. It is the stability of the neutron stars studied in the prior chapter and the possibility of realizing such ultra-dense quark stars to which we now turn.

Before assessing the stability of dense quark stars we first briefly discuss the properties of the matter

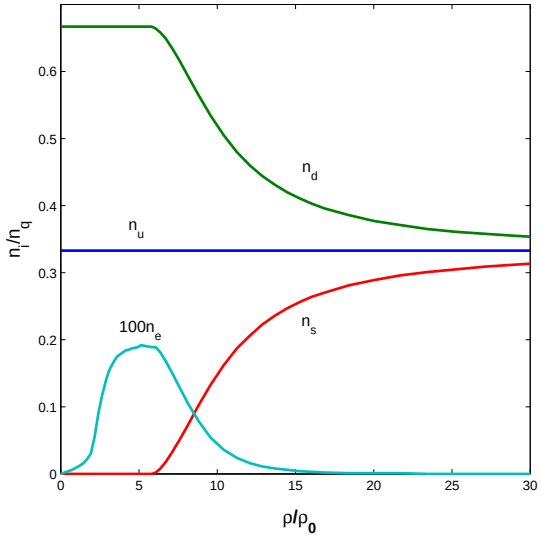

Figure 5.5: Fractional quark and electron number densities vs. ρ for electrically neutral matter with $g_V = 0$, where $n_q = n_u + n_d + n_s$.

which makes up these proposed objects. Charge neutrality requires that

$$\frac{2}{3}\,n_u - \frac{1}{3}\,n_d - \frac{1}{3}\,n_s - n_e = 0, \tag{5.17}$$

so that defining the fractional densities $\tilde{n}_i = n_i/n_q$ (where n_q is the net quark density) we obtain the relations

$$\tilde{n}_u = \frac{1}{3} + \tilde{n}_e, \qquad \text{or equivalently,} \qquad \tilde{n}_d + \tilde{n}_s = \frac{2}{3} - \tilde{n}_e. \tag{5.18}$$

At low densities there is insufficient energy to generate the intermediate mass strange quark and the electron density is always much smaller than the net quark density ($n_e \sim n/100$) so that charge neutrality enforces $n_d \approx 2n_u$. At the high densities anticipated in quark stars, however, the quark mass splittings are negligible relative to the large Fermi energies obtained so that the matter becomes flavor symmetric ($n_u \approx n_d \approx n_s$) and the electrons are suppressed entirely ($n_e \to 0$).

One way of assessing the stability of high density quark stars is by constructing the M-R diagram shown in Fig. 5.6. The structure of neutron stars with low central densities ($\rho_c \lesssim 2\rho_0$) are determined entirely by the hadronic equation of state and are therefore independent of the magnitude of the (quark) vector coupling g_V. Further, the low densities of these stars result in correspondingly small density gradients via the TOV equation so that these stars have relatively large radii of $R \sim 20$ km for $\rho_c = 0.2\rho_0$. As ρ_c increases the equilibrium radius falls and for $\rho \gtrsim 2\rho_0$ the vector coupling begins to play an important role in the star's

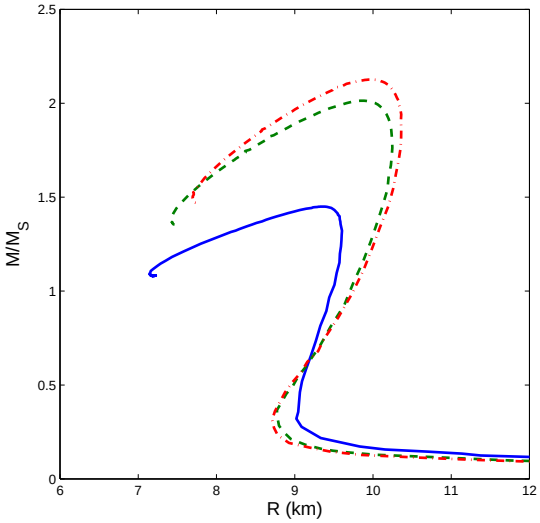

Figure 5.6: Mass-radius relationship for neutron and quark stars for $g_V = 0$ (blue), G (green), and $1.5G$ (red). The stars' central densities increase from ρ_0 to $400\rho_0$ as one moves from right (large R) to left (small R), tracing out the curves in a counterclockwise fashion.

equilibrium, causing the M-R curves for different values of g_V to begin to separate (see the "kink" in Fig. 5.6 at $M \sim 0.3M_\odot$, after which the stars' masses begin to increase dramatically with ρ_c).

As indicated in Figs. 5.3(a) and 5.4(b), for $g_V/G \lesssim 5$ the maximum stable neutron star mass is obtained for $\rho_c \approx 11\rho_0$. Thus, as ρ_c increases from $3\rho_0$ to $10\rho_0$ in Fig. 5.6, the stars' positions in M-R space move from the "kink" at $M \approx 0.3M_\odot$ to the respective peaks at $M_{max} = 1.44M_\odot$, $2.01M_\odot$, and $2.14M_\odot$, with $R \approx 9 - 10$ km. As the central densities increase further, the stars trace out the curves in Fig. 5.6 in a counterclockwise fashion, but do so at a decreasing rate (i.e., $dM/d\rho_c \to 0^-$, as indicated in Fig. 5.3(a)). The stability of high density quark stars depends on the direction in which the M-R curves bend as ρ_c becomes large. Due to the small values of $dM/d\rho_c$ one must consider central densities as high as $400\rho_0$ in order to obtain the curves shown in Fig. 5.6, but having done so, we find that while at extremely high densities the stars' radii do begin to increase, the masses continue to fall, indicating the onset of a second unstable mode, rather than a recovery of stability. Thus, while the presence of a vector repulsion does allow neutron stars to obtain larger stable masses, it does not (within the NJL model, at least) provide sufficient pressure to stabilize the ultra-high density matter against gravitational collapse and thereby allow for the realization of high density quark stars.

5.6 Observational Constraints and the Equation of State

Having seen that our equation of state is consistent with the most massive neutron stars yet observed, we now proceed to consider the constraints placed on our equation of state by observations of other, non-

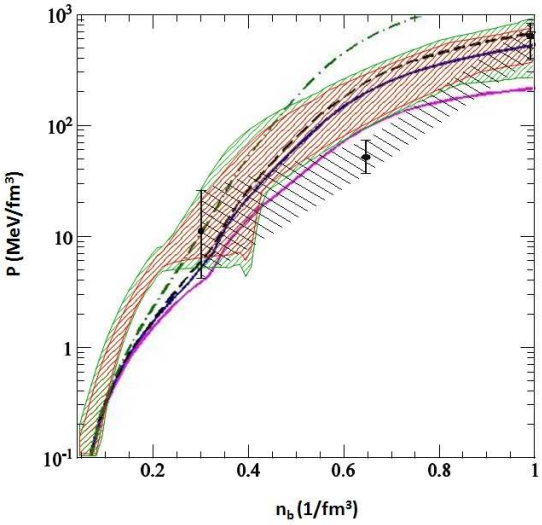

Figure 5.7: Comparison of our equation of state, Eq. (5.11), with constraints from astrophysical observations. Curves show our equation of state (in order of increasing stiffness) for $g_V/G = 0$ (solid magenta), 1 (solid blue), 1.5 (dashed black), and 5 (dot-dashed green). The shaded region with data points shown is from [36] while the larger (red and green) shaded regions are 68% and 95% confidence regions, respectively, from [116].

maximally massive neutron stars. As discussed in the prior section, a given equation of state uniquely determines the neutron star M-R relationship. As a result, astrophysical measurements of these parameters allow one to place strict constraints on the quark matter equation of state. While this connection between quark thermodynamics and neutron star structure has been discussed for some time, it is only recently that significant efforts have begun to put this connection into practice [36, 116].

Figure 5.7 shows our hybrid equation of state as a function of baryon density, along with the observational constraints imposed by the analyses in [36, 116]. While in the absence of the vector coupling (dotted red curve) our equation of state is too soft to be consistent with the eleven neutron stars analyzed in these studies, and $g_V/G = 5$ results in an equation of state which is significantly too stiff at high density, vector couplings of $1.3 \lesssim g_V/G \lesssim 1.7$ yield quite marked agreement with the observational constraints. Moreover, this range of vector couplings is consistent with the constraints imposed by the massive neutron star observations discussed in the prior section, which required $g_V/G \gtrsim 1.4$.

An important question which we have not yet addressed is the role of quark pairing in the structure of neutron and dense quark stars, particularly its impact on the astrophysical observables discussed here [119]. While we are hopeful that by combining observational data with future analysis of the effects of quark pairing we may gain further insight into the low temperature QCD phase diagram, regardless of the preferred pairing structures of dense QCD, color superconductivity will always act to *soften* the quark matter equation of state, thereby making it more difficult to realize either massive neutron or ultra-dense quark stars. It is

important, however, to determine how significantly quark pairing reduces the maximum obtainable neutron star masses. In addition, we have so far neglected the effects of the rapid rotation which many neutron stars undergo and which tends to stabilize these stars to somewhat greater masses.

Chapter 6

Artificial Gauge Fields in Ultracold Atoms

6.1 Introduction

Over the past decade the study of cold atomic gases has rapidly become one of the most dynamic and quickly evolving fields of physics, largely due to the ability of these systems to simulate a wide variety of quantum systems [131, 132]. One particular type of system which is not easily probed in its naturally occurring forms, but which is of great theoretical interest is that of both Abelian and non-Abelian gauge fields. While homogeneous Abelian gauge fields (i.e., magnetic fields) can be simulated via mechanical rotation, as discussed in Section 1.3, the ability to obtain synthetic fields with large magnitudes is limited by achievable rotation rates and this method is also incapable of producing spatially varying fields. Further, given the extreme difficulty of probing the rich phase structure of naturally occurring non-Abelian gauge fields (e.g., QCD) the ability to simulate non-Abelian gauge fields in ultracold atoms is of both great theoretical and experimental interest.

Fortunately, in the last five years researchers have developed optical techniques for achieving both inhomogeneous and non-Abelian gauge fields, greatly expanding the number of systems that can be experimentally probed [54, 55, 59, 133–135]. In particular, studies are no longer limited to simulating naturally occurring systems, but are now extended to systems never before realized in nature, but having the capacity to greatly advance our understanding of the complexities of non-Abelian theories.

In this chapter we investigate the properties of a mixture of two hyperfine species of fermions subject to a particular non-Abelian gauge field of the Rashba-Dresselhaus (RD) form, which couples the atoms' momenta and spins ($H \sim \mathbf{p} \cdot \boldsymbol{\sigma}$). This type of anisotropic spin-orbit coupling is of practical interest due to its realization in certain two dimensional semiconductors [57, 58]. It is also of great theoretical interest due to the recently acquired ability to create artificial gauge fields of this type in the laboratory, and perhaps in the near future, to tune the anisotropy in order to study a wide range of systems which do not naturally occur, thereby broadening our general understanding of these system's properties [136–139].

In the next section we begin by reviewing the phenomenon of *Berry's phase*, the exploitation of which allows for the realization of spatially varying and non-Abelian gauge fields by optical methods. We then move on to discuss Rashba-Dresselhaus coupling specifically, which will be the focus of the rest of this thesis.

The background presented in these two sections is largely based on [56, 140]. Finally, we construct the mean field phase diagram for spin-orbit coupled fermions whose interactions can be arbitrarily tuned via a Feshbach resonance.

6.2 Berry's Phase

Berry's phase is a quite general quantum phase which emerges in systems described by two sets of variables which evolve on different time scales [141]. For example, in order to describe a metal fully one must in principle solve the Schrödinger equation for the many-particle Hamiltonian that describes both the nuclear and electronic degrees of freedom. However, due to the electrons' much smaller mass they are able to respond to internal (and external) forces, and thereby reach dynamical equilibrium, much more rapidly than the relatively heavy nuclei. Therefore, to a first approximation one may treat the slowly varying nuclei positions as fixed, solve for the quickly varying electron distribution, and then use this electron distribution in order to solve for the new positions of the nuclei. In this particular context, this approximation is known as the *Born-Oppenheimer approximation* [142].

In the case of the laser-induced artificial gauge fields which we will study in this chapter, the slowly varying variables are the positions of the atoms ($\mathbf{r}$) while the quickly varying variables are the internal pseudo-spins $|\chi(\mathbf{r})\rangle$ (i.e., hyperfine states, which we will henceforth refer to simply as "spins"), where, as the notation suggests, the spin configuration will be solved for as a function of the positions $\mathbf{r}$, which are taken as fixed. According to the *adiabatic theorem* of quantum mechanics, as long as the time scale characterizing the motion of the atoms is long enough compared to the time scale characterizing the spin dynamics, the eigenstates of the system will continuously evolve from their unperturbed states. In particular, this means that the coupling of the quickly and slowly varying degrees of freedom will not couple eigenstates of different energies. Thus, in considering the evolution of an atom which begins in a particular eigenstate $|\chi_i(\mathbf{r})\rangle$ of the "fast" Hamiltonian H_F, we need only consider the subspace of eigenstates which are degenerate (or nearly degenerate) with $|\chi_i(\mathbf{r})\rangle$.

We can write the Hamiltonian of our atomic system quite generally in the form

$$H = \left(-\frac{\nabla^2}{2m} + U(\mathbf{r})\right)\mathbf{I} + H_F(\mathbf{r}), \tag{6.1}$$

where ∇ is the gradient with respect to the slowly varying variables $\mathbf{r}$, $U(\mathbf{r})$ is an external potential, and $H_F(\mathbf{r})$ is the Hamiltonian describing the quickly varying spin variables. In addition, $\mathbf{I}$ is the identity operator in spin space. Assuming that our atom begins in an eigenstate $|\chi_i(\mathbf{r})\rangle$, the total state of the atom at a later

time t can be written as

$$|\Psi(\mathbf{r},t)\rangle = \sum_{i=1}^{N} \psi_i(\mathbf{r},t)\,|\chi_i(\mathbf{r})\rangle\,, \tag{6.2}$$

where $\{|\chi_i(\mathbf{r})\rangle\}$ $(i = 1...N)$ is an orthonormal set of eigenstates of $H_F(\mathbf{r})$ with the nearly degenerate eigenvalues $E_1...E_N$ and $\{\psi_i(\mathbf{r},t)\}$ are the atomic position eigenstates. The Schrödinger equation therefore yields (with $\hbar = 1$)

$$i\frac{\partial}{\partial t}\,|\Psi(\mathbf{r},t)\rangle = \sum_{i=1}^{N}\left(-\frac{\nabla^2}{2m} + U(\mathbf{r}) + E_i\right)\psi_i(\mathbf{r})\,|\chi_i(\mathbf{r})\rangle\,. \tag{6.3}$$

We can pick out the time evolution of the jth component of $|\Psi(\mathbf{r},t)\rangle$ by taking the inner product of this equation with $\langle\chi_j(\mathbf{r})|$ and using the orthogonality of the eigenstate to obtain

$$\begin{aligned}
i\frac{\partial}{\partial t}\,\psi_j(\mathbf{r},t) &= -\frac{1}{2m}\sum_{i=1}^{N}\left\langle \chi_j(\mathbf{r})\middle|\left(\nabla^2\,|\chi_i(\mathbf{r})\rangle\,\psi_i(\mathbf{r},t)\right)\right\rangle + (U(\mathbf{r}) + E_j)\,\psi_j(\mathbf{r},t),\\
&= \left(-\frac{\nabla^2}{2m} + U(\mathbf{r}) + E_j\right)\psi_j(\mathbf{r},t) - \frac{1}{m}\sum_{i=1}^{N}\langle\chi_j(\mathbf{r})|\nabla|\chi_i(\mathbf{r})\rangle\,\nabla\psi_i(\mathbf{r},t)\\
&\qquad -\frac{1}{2m}\sum_{i=1}^{N}\left\langle\chi_j(\mathbf{r})|\nabla^2|\chi_i(\mathbf{r})\right\rangle\psi_i(\mathbf{r},t),\\
&= \frac{1}{2m}\sum_{i=1}^{N}\Big(-\delta_{ji}\nabla^2 + 2\,\langle\chi_j(\mathbf{r})|\nabla|\chi_i(\mathbf{r})\rangle\,\nabla\Big)\psi_j(\mathbf{r},t) + (U(\mathbf{r}) + E_j)\,\psi_j(\mathbf{r},t)\\
&\qquad -\frac{1}{2m}\sum_{i=1}^{N}\left\langle\chi_j(\mathbf{r})|\nabla^2|\chi_i(\mathbf{r})\right\rangle\psi_i(\mathbf{r},t),\\
&= \frac{1}{2m}\sum_{i,k=1}^{N}\Big(-i\delta_{ji}\nabla - i\,\langle\chi_j(\mathbf{r})|\nabla|\chi_i(\mathbf{r})\rangle\Big)\cdot\Big(-i\delta_{ik}\nabla - i\,\langle\chi_i(\mathbf{r})|\nabla|\chi_k(\mathbf{r})\rangle\Big)\psi_k(\mathbf{r},t)\\
&\qquad + (U(\mathbf{r}) + E_j)\,\psi_j(\mathbf{r},t) - \frac{1}{2m}\sum_{i,k=1}^{N}\langle\chi_j(\mathbf{r})|\nabla|\chi_i(\mathbf{r})\rangle\,\langle\chi_i(\mathbf{r})|\nabla|\chi_k(\mathbf{r})\rangle\\
&\qquad + \frac{1}{2m}\sum_{i=1}^{N}\left(\langle\chi_j(\mathbf{r})\nabla|\right)\cdot\left(\nabla\,|\chi_i(\mathbf{r})\rangle\right)\psi_i(\mathbf{r}),
\end{aligned} \tag{6.4}$$

where $(\langle\chi_j(\mathbf{r})\nabla|)$ indicates ∇ acting to the left on $\langle\chi_j(\mathbf{r})|$. Next, we write $\hat{p} = -i\nabla$ and define the quantities

$$\vec{A}_{ij}(\mathbf{r}) = i\,\langle\chi_i(\mathbf{r})|\nabla|\chi_j(\mathbf{r})\rangle\,, \tag{6.5}$$

where the notation indicates that for each pair (i,j), $\vec{A}_{ij}$ is a three component vector, with the components corresponding to the three "components" of the gradient operator. Thus, writing Eq. (6.4) in vector notation

we obtain

$$i\frac{\partial}{\partial t}\vec{\psi}(\mathbf{r},t) = \left[\frac{1}{2m}\left(\hat{p}\mathbf{I}-\vec{\mathbf{A}}\right)^2+\left(U(\mathbf{r})+E_j\right)\mathbf{I}+\mathbf{V}(\mathbf{r})\right]\vec{\psi}(\mathbf{r},t), \tag{6.6}$$

where $\vec{\mathbf{A}}=(\mathbf{A}_x,\mathbf{A}_y,\mathbf{A}_z)$ is a 3-component vector of matrices and we define the effective scalar potential

$$V_{ij}(\mathbf{r}) = \frac{1}{2m}\left(\langle\chi_i(\mathbf{r})\nabla|\right)\cdot\left(\nabla|\chi_j(\mathbf{r})\rangle\right)-\frac{1}{2m}\sum_{k=1}^{N}\vec{A}_{ik}(\mathbf{r})\cdot\vec{A}_{kj}(\mathbf{r}). \tag{6.7}$$

We can rewrite this potential by inserting the identity operator $\mathbf{I}=\sum_k|\chi_k(\mathbf{r})\rangle\langle\chi_k(\mathbf{r})|$ into the first term, where the sum is over the elements of an orthonormal basis of the *entire* Hilbert space of spin states (i.e., both the degenerate states with $i=1...N$ as well as all states non-degenerate with the atom's initial eigenstate). Thus, we obtain the expression

$$V_{ij}(\mathbf{r})=\frac{1}{2m}\sum_{k\neq 1...N}\vec{A}_{ik}(\mathbf{r})\cdot\vec{A}_{kj}(\mathbf{r}). \tag{6.8}$$

By considering Eq. (6.6) we see that the effective Schrödinger equation for the spatial wavefunction $\vec{\psi}(\mathbf{r})$ is of the form of a particle subject to an external potential $U(\mathbf{r})\mathbf{I}+\mathbf{V}(\mathbf{r})$ and a gauge field $\mathbf{A}(\mathbf{r})=(\mathbf{A}_x,\mathbf{A}_y,\mathbf{A}_z)$ whose components are $N\times N$ matrices. Thus, if there are no other eigenstates degenerate with the initial state ($N=1$) the synthetic gauge field will necessarily be Abelian. However, if $N>1$ the gauge field components will not, in general, commute (e.g., $[\mathbf{A}_x,\mathbf{A}_y]\neq 0$) so that we obtain a non-Abelian field.

Having outlined the general means by which Berry's phase can be exploited to produce an artificial gauge field, in the next section we discuss a particular optical scheme which has been proposed to realize such fields in the laboratory.

6.3 Creating an Artificial Gauge Field

As shown in the previous section, in order to simulate a non-Abelian gauge field we must prepare a system with more than one degenerate eigenstate. A system would be particularly amenable to manipulation in this context if its unperturbed eigenvalues came in degenerate sets and were easily controlled with a tunable external field. One such system, which was exploited to create the first non-Abelian artificial gauge field, is the three $F=1$ hyperfine states of ^{87}Rb [59]. In order to understand how this system can be exploited, we will briefly consider a three-state system with the "Λ-level" structure shown in Fig. 6.1, and which is subject to the electric fields of two counter-propagating lasers. In the discussion which follows we will make use of both the Schrödinger and interaction representations to express system's operators. For a review of

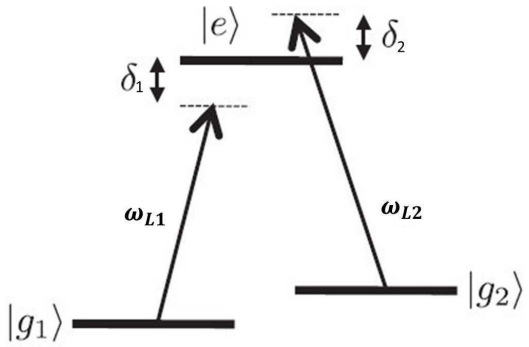

Figure 6.1: Atomic Λ-level structure with two nearly degenerate states $|g_1\rangle$ and $|g_2\rangle$, which are coupled to an excited state $|e\rangle$ by two lasers with frequencies ω_{L1} and ω_{L2}. Adapted from [56].

these representations and their connection, see [143].

6.3.1 Schrödinger Representation

Let us consider a three state atomic system which is subject to the external field of two counter-propagating lasers, one tuned to couple the states $|g_1\rangle$ and $|e\rangle$ (with frequency ω_{L1}) and the other to couple $|g_2\rangle$ and $|e\rangle$ (with frequency ω_{L2}). The system's Hamiltonian can be written in the form $H = H_A + H_{AF1} + H_{AF2}$, where H_A is the unperturbed atomic Hamiltonian and H_{AF1} and H_{AF2} are the interaction Hamiltonians describing the coupling between the atoms and the lasers. Working in the basis $\{|g_1\rangle, |e\rangle, |g_2\rangle\}$, the unperturbed Hamiltonian is of the form $H_A = \mathrm{diag}(\omega_1, \omega_e, \omega_2)$. Meanwhile, energy conservation allows us to relate the various frequencies shown in Fig. 6.1:

$$g_1 - e \text{ transition} \quad : \qquad \omega_e - \omega_1 = \omega_{L1} + \delta_1, \tag{6.9}$$

$$g_2 - e \text{ transition} \quad : \qquad \omega_e - \omega_2 = \omega_{L2} - \delta_2, \tag{6.10}$$

where the δ_i are in general position-dependent. Subtracting Eq. (6.10) from Eq. (6.9) yields

$$\delta_1 + \delta_2 \quad = \quad (\omega_{L2} - \omega_{L1}) + (\omega_2 - \omega_1), \tag{6.11}$$

which is known as the detuning of the two-photon Raman excitation (or simply Raman detuning). Alternatively, adding Eq. (6.9) and (6.10) gives

$$2\omega_e = (\omega_{L1} + \omega_{L2}) + (\omega_1 + \omega_2) + \delta_{12}, \tag{6.12}$$

where we define $\delta_{12} = \delta_1 - \delta_2$. This relation can be used to eliminate ω_e in the atomic Hamiltonian and after shifting the zero of energy so that $(H_A)_{22} = 0$ we obtain

$$H'_A = \begin{pmatrix} -(\delta_1 + \omega_{L1}) & 0 & 0 \\ 0 & 0 & 0 \\ 0 & 0 & (\delta_2 - \omega_{L2}) \end{pmatrix}. \tag{6.13}$$

Turning now to the interactions and working in the dipole approximation, the Hamiltonians due to the two lasers are

$$H_{AF1} = -\begin{pmatrix} 0 & \mathbf{d}_{21}^* & 0 \\ \mathbf{d}_{21} & 0 & 0 \\ 0 & 0 & 0 \end{pmatrix} \cdot \mathbf{E}_1 \cos(\mathbf{k}_1 \cdot \mathbf{r} - \omega_{L1} t), \tag{6.14}$$

$$H_{AF2} = -\begin{pmatrix} 0 & 0 & 0 \\ 0 & 0 & \mathbf{d}_{32}^* \\ 0 & \mathbf{d}_{32} & 0 \end{pmatrix} \cdot \mathbf{E}_2 \cos(\mathbf{k}_2 \cdot \mathbf{r} - \omega_{L2} t). \tag{6.15}$$

Defining the Rabi frequencies $\Omega_1 = -\mathbf{d}_{21} \cdot \mathbf{E}_1$ and $\Omega_2 = -\mathbf{d}_{32} \cdot \mathbf{E}_1$, and adding the interaction and atomic Hamiltonians yields the full Hamiltonian

$$H = \begin{pmatrix} -(\delta_1 + \omega_{L1}) & \Omega_1^* \cos(\mathbf{k}_1 \cdot \mathbf{r} - \omega_{L1} t) & 0 \\ \Omega_1 \cos(\mathbf{k}_1 \cdot \mathbf{r} - \omega_{L1} t) & 0 & \Omega_2^* \cos(\mathbf{k}_2 \cdot \mathbf{r} - \omega_{L2} t) \\ 0 & \Omega_2 \cos(\mathbf{k}_2 \cdot \mathbf{r} - \omega_{L2} t) & (\delta_2 - \omega_{L2}) \end{pmatrix}. \tag{6.16}$$

Having obtained the system's full Hamiltonian, we next transform to the interaction representation in order to motivate the *random wave approximation*, which we will shortly apply.

6.3.2 Interaction Representation

In order to transform to the interaction representation we must decompose the Hamiltonian in the form $H = H_0 + H'$, after which the interaction Hamiltonian will be given by $H'_I = e^{iH_0 t} H' e^{-iH_0 t}$. In order to simplify this procedure, we will choose $H_0 = -\mathrm{diag}(\omega_{L1}, 0, \omega_{L2})$ so that its exponentiation is trivial. The

remaining portion of the Hamiltonian is then

$$H' = \begin{pmatrix} -\delta_1 & \Omega_1^* \cos(\mathbf{k}_1 \cdot \mathbf{r} - \omega_{L1} t) & 0 \\ \Omega_1 \cos(\mathbf{k}_1 \cdot \mathbf{r} - \omega_{L1} t) & 0 & \Omega_2^* \cos(\mathbf{k}_2 \cdot \mathbf{r} - \omega_{L2} t) \\ 0 & \Omega_2 \cos(\mathbf{k}_2 \cdot \mathbf{r} - \omega_{L2} t) & \delta_2 \end{pmatrix}. \tag{6.17}$$

Writing the cosine terms as complex exponentials and evaluating H_I' gives

$$H_I' = \frac{1}{2} \begin{pmatrix} -2\delta_1 & \Omega_1^*(e^{-i\mathbf{k}_1 \cdot \mathbf{r}} + e^{i(\mathbf{k}_1 \cdot \mathbf{r} - 2\omega_{L1} t)}) & 0 \\ \Omega_1(e^{i\mathbf{k}_1 \cdot \mathbf{r}} + e^{-i(\mathbf{k}_1 \cdot \mathbf{r} - 2\omega_{L1} t)}) & 0 & \Omega_2^*(e^{-i\mathbf{k}_2 \cdot \mathbf{r}} + e^{i(\mathbf{k}_2 \cdot \mathbf{r} - 2\omega_{L2} t)}) \\ 0 & \Omega_2(e^{i\mathbf{k}_2 \cdot \mathbf{r}} + e^{-i(\mathbf{k}_2 \cdot \mathbf{r} - 2\omega_{L2} t)}) & 2\delta_1 \end{pmatrix}. \tag{6.18}$$

We see that in the interaction representation the Hamiltonian consists of terms that are (1) constant in time, and (2) oscillatory with frequency $2\omega_{Li}$. Since the time scale for our measurements is much longer than the period of oscillation for a visible laser with frequency $\omega_L \sim 10^{15}$ Hz we may safely replace the oscillatory terms with their average values (zero). This replacement, which is known as the rotating wave approximation yields the Hamiltonian

$$H_I'^{RWA} = \frac{1}{2} \begin{pmatrix} -2\delta_1 & \kappa_1^* & 0 \\ \kappa_1 & 0 & \kappa_2 \\ 0 & \kappa_2^* & 2\delta_2 \end{pmatrix}, \tag{6.19}$$

where we have defined the spatially-varying complex Rabi frequencies $\kappa_1 = \Omega_1 e^{i\mathbf{k}_1 \cdot \mathbf{r}}$ and $\kappa_2 = \Omega_2^* e^{-i\mathbf{k}_2 \cdot \mathbf{r}}$, which are determined by the geometry of the laser configuration. Having obtained the three state Hamiltonian, from the discussion in Section 6.2 we know that the effective gauge field will be determined by the eigenstates of the system. Unfortunately, while as the roots of a cubic polynomial it is possible to obtain a closed form expression for the eigenvalues (and the corresponding eigenstates) of Eq. (6.19), such an expression is rather opaque in the general case. However, when the system is tuned symmetrically about the average of the $g_1 - e$ and $g_2 - e$ excitations (i.e., when $\delta_1 = \delta_2 \equiv \delta$) the eigenvalues simplify considerably and it is instructive to consider this limit.

6.3.3 Abelian Gauge Field

In the case of symmetric tuning the eigenvalues of Eq. (6.19) are $E_0 = 0$ and $E_\pm = \pm\sqrt{\delta^2 + \kappa^2/2}$. If we consider two counter-propagating lasers with equal magnitude wave vectors ($\kappa_1 = \kappa_2^* \equiv \kappa e^{-ikx}$) then the

corresponding eigenstates are [140]

$$|+\rangle = \begin{pmatrix} e^{ikx}\cos^2(\theta/2) \\ -\sin(\theta)/\sqrt{2} \\ e^{-ikx}\sin^2(\theta/2) \end{pmatrix}, \qquad |0\rangle = \begin{pmatrix} e^{ikx}\sin(\theta)/\sqrt{2} \\ \cos(\theta) \\ -e^{-ikx}\sin(\theta)/\sqrt{2} \end{pmatrix}, \qquad |-\rangle = \begin{pmatrix} e^{ikx}\sin^2(\theta/2) \\ \sin(\theta)/\sqrt{2} \\ e^{-ikx}\cos^2(\theta/2) \end{pmatrix}, \quad (6.20)$$

where we define $\tan(\theta) = \kappa/\sqrt{2}\delta$. While these eigenstates are position dependent, E_- is always the ground state of the system (as long as $\kappa, \delta \neq 0$) so that applying the adiabatic theorem, an atom prepared in the (local) ground state will simply evolve continuously with $|-\rangle$. Since the ground state is unique, the synthetic gauge field is trivially Abelian and from Eq. (6.5) we obtain

$$\vec{A} = i\langle -|\nabla|-\rangle = -k\cos(\theta)\hat{\mathbf{x}}. \quad (6.21)$$

The synthetic magnetic field $\mathbf{B} = \nabla \times \mathbf{A}$ is therefore

$$\mathbf{B} = -\frac{\kappa k}{2(\delta^2 + \kappa^2/2)^{3/2}}\left(\frac{\partial \delta}{\partial z}\hat{\mathbf{y}} - \frac{\partial \delta}{\partial y}\hat{\mathbf{z}}\right). \quad (6.22)$$

We see that the components of the magnetic field are related to the spatial gradient of the detuning δ. The first synthetic gauge field realized in the laboratory consisted of a spatially uniform δ so that $\vec{A} \neq 0$, but $\mathbf{B} = 0$ [133]. Soon after, a detuning linear in y ($\delta = \alpha y$) was utilized to obtain a uniform synthetic magnetic field which manifested itself by inducing the formation of vortices in the superfluid ^{87}Rb system [54]. Having seen how an artificial Abelian gauge field can be realized by means of a spatially varying symmetric detuning, we next consider how a cold atomic gas can be utilized to simulate a non-Abelian field.

6.4 Rashba-Dresselhaus Spin-Orbit Coupling

As discussed in Section 6.2, Berry's phase is a versatile tool which can, in principle, allow for the synthetic realization of a wide variety of Abelian and non-Abelian gauge fields. In practice, however, the technical challenges to achieving these fields are quite significant and it is only slowly that progressively more complex field configurations are obtained in the laboratory. One particular class of non-Abelian gauge fields which is beginning to be realized is the Rashba-Dresselhaus spin-orbit coupling, whose Hamiltonians can be written in the form

$$H_R = v_R(k_x\sigma_y - k_y\sigma_x), \qquad H_D = v_D(k_x\sigma_x - k_y\sigma_y), \quad (6.23)$$

where $\mathbf{k}$ is the atom's momentum and $\boldsymbol{\sigma} = (\sigma_x, \sigma_y, \sigma_z)$ is the vector of Pauli matrices in hyperfine space. These Hamiltonian were first studied in the context of two dimensional semiconductors, in which the Rashba interaction stems from an inversion asymmetry of the confining potential, while the Dresselhaus interaction is brought about by an inversion asymmetry of the bulk material [57, 58]. More recently, these interactions have found renewed interest due to their relatively simple non-Abelian character and the possibility of their simulation in cold atomic gases.

While Eq. (6.23) gives the Rashba and Dresselhaus Hamiltonians in their original forms, for our purposes it will be convenient to work in a rotated coordinate system in which the hyperfine Pauli matrices become

$$\sigma_x \to \frac{\sigma_x - \sigma_y}{\sqrt{2}}, \qquad \sigma_y \to \frac{\sigma_x + \sigma_y}{\sqrt{2}}, \tag{6.24}$$

and the momentum-space axes become

$$k_x \to \frac{k_x - k_y}{\sqrt{2}}, \qquad k_y \to \frac{k_x + k_y}{\sqrt{2}}. \tag{6.25}$$

In this rotated space the RD interaction couples only momentum and spin coordinates corresponding to the same axes, taking on the simple form

$$H = \frac{\kappa}{m} k_x \sigma_x + \frac{\eta\kappa}{m} k_y \sigma_y, \tag{6.26}$$

where $\kappa = m(v_R + v_D)$ is the overall strength of the RD coupling and $\eta = (v_R - v_D)/(v_R + v_D)$ is a measure of the relative strength of the Rashba and Dresselhaus components, which we refer to as the *anisotropy* of the RD coupling. Without loss of generality we assume $\kappa > 0$ and $0 \leq \eta \leq 1$ throughout our discussion.[1]

While several experimental schemes have been proposed for creating synthetic fields of the Rashba-Dresselhaus form [136–139, 144], only the equal-Rashba-Dresselhaus (ERD) case ($\eta = 0$) has thus far been realized [54]. Here we will briefly review a proposed method for obtaining a synthetic Rashba-only (RO) field ($\eta = 1$) by means of *dark states* which follows the discussion in [56].

We consider a generalization of the atomic system discussed in Section 6.3.3 in which there are *three* nearly degenerate ground states $|g_1\rangle, |g_2\rangle, |g_3\rangle$, and one excited state $|e\rangle$. Working in the interaction representation and within the rotating wave approximation we can write the Hamiltonian in the compact form

$$H = \sum_{j=1}^{3} \left[\frac{\kappa_i}{2} |e\rangle \langle g_j| + \text{H.c.} \right], \tag{6.27}$$

[1] If either of these conditions is not met we can simply redefine our momentum-space axes such that both conditions are satisfied in the new coordinate system.

where the three κ_j are spatially-varying complex Rabi frequencies corresponding to three distinct lasers. If we choose the geometry of our system such that the lasers are positioned at the vertices of an equilateral triangle whose center is the atomic gas then we can write $\kappa_j = \kappa e^{i\mathbf{k}_j\cdot\mathbf{r}}/\sqrt{3}$ where $\mathbf{k}_j = k(-\cos\theta_j, \sin\theta_j, 0)$ and $\theta_j = 2\pi j/3$. Thus, we can recast the Hamiltonian in the form

$$H = \frac{\kappa}{2}\,|e\rangle\langle B| + \text{H.c.}, \tag{6.28}$$

where we define the *bright state* as the unique linear combination of the $|g_j\rangle$ which couples to $|e\rangle$:

$$|B\rangle = \sum_{j=1}^{3} \frac{e^{-i\mathbf{k}_j\cdot\mathbf{r}}}{\sqrt{3}}\,|g_j\rangle\,. \tag{6.29}$$

Next, we define the dark states, which form a basis for the subspace of $|g_j\rangle$ which do not couple to $|e\rangle$:

$$|D_1\rangle = \sum_{j=1}^{3} \frac{e^{i\theta_j}e^{-i\mathbf{k}_j\cdot\mathbf{r}}}{\sqrt{3}}\,|g_j\rangle\,, \qquad |D_2\rangle = \sum_{j=1}^{3} \frac{e^{2i\theta_j}e^{-i\mathbf{k}_j\cdot\mathbf{r}}}{\sqrt{3}}\,|g_j\rangle\,. \tag{6.30}$$

It is straightforward to verify that $\{|B\rangle, |e\rangle, |D_1\rangle, |D_2\rangle\}$ is an orthonormal basis for the Hilbert space of relevant states.

Since the dark states do not couple to either $|B\rangle$ or $|e\rangle$, if an atom is prepared in one of these states (or a superposition thereof), it will simply evolve within the dark subspace. From Eq. (6.5), the gauge field in this subspace is therefore

$$\begin{aligned}
A_{mn} &= i\langle D_n|\nabla|D_m\rangle\,, \\
&= i\left[\sum_{j=1}^{3} \frac{e^{-in\theta_j}e^{i\mathbf{k}_j\cdot\mathbf{r}}}{\sqrt{3}}\,\langle g_j|\right]\nabla\left[\sum_{j'=1}^{3} \frac{e^{im\theta_{j'}}e^{-i\mathbf{k}_{j'}\cdot\mathbf{r}}}{\sqrt{3}}\,|g_{j'}\rangle\right], \\
&= \frac{i}{3}\sum_{j,j'=1}^{3} e^{i(m\theta_{j'}-n\theta_j)}e^{i(\mathbf{k}_j-\mathbf{k}_{j'})\cdot\mathbf{r}}(-i\mathbf{k}_{j'})\delta_{jj'}, \\
&= \frac{1}{3}\sum_{j=1}^{3}\mathbf{k}_j e^{i(m-n)\theta_j}.
\end{aligned} \tag{6.31}$$

Substituting $\mathbf{k}_j = k(-\cos\theta_j, \sin\theta_j, 0)$ and evaluating the sum explicitly yields

$$\vec{\mathbf{A}} = -\frac{k}{2}(\sigma_x, \sigma_y, 0), \tag{6.32}$$

which is precisely the gauge field involved in RO spin-orbit coupling. As noted previously, this interaction

has not yet been realized in the laboratory, largely due to the short lifetime of particles in the dark subspace due to collisions which induce transitions to lower energy states. At least one proposal for overcoming this obstacle has been made, however, and experimentalists continue to investigates methods for realizing this interaction [139].

Having described the form of the RD interaction and the general methods by which synthetic gauge fields of this form may be realized, we now move on to construct the phase diagram of systems subject to RD spin-orbit coupling and a tunable two-body contact interaction.

6.5 Spin-Orbit Coupled Fermions with a Contact Interaction

We consider a system of two fermionic species in the presence of a (real or fictitious) magnetic field $\mathbf{h}(\mathbf{r})$ and subject to a two-body contact interaction, whose Hamiltonian density is

$$\mathcal{H}(\mathbf{r}) = \sum_{\alpha\beta} \psi_\alpha^\dagger(\mathbf{r}) \left[K_\alpha(\mathbf{r})\delta_{\alpha\beta} - \mathbf{h}(\mathbf{r})\cdot\boldsymbol{\sigma}_{\alpha\beta}\right]\psi_\beta(\mathbf{r}) + g\psi_\uparrow^\dagger(\mathbf{r})\psi_\downarrow^\dagger(\mathbf{r})\psi_\downarrow(\mathbf{r})\psi_\uparrow(\mathbf{r}), \tag{6.33}$$

where $K_\alpha = -\nabla^2/2m_\alpha - \mu_\alpha$ is the kinetic energy operator of species α with mass m_α, measured relative to its chemical potential μ_α, and $g < 0$ corresponds to an attractive interaction. In addition, while we label the species as different "spins," in ultracold gases these states are typically different hyperfine states rather than true spins.

Anticipating the effects of pairing, we define the pairing amplitude $\Delta(\mathbf{r}) = g\langle\psi_\downarrow(\mathbf{r})\psi_\uparrow(\mathbf{r})\rangle$ and approximate the two-body interaction by factoring in the following form, then neglecting quadratic fluctuations:

$$\begin{aligned}
H_{int} &= g\psi_\uparrow^\dagger(\mathbf{r})\psi_\downarrow^\dagger(\mathbf{r})\psi_\downarrow(\mathbf{r})\psi_\uparrow(\mathbf{r}), \\
&= g\Big[\langle\psi_\uparrow^\dagger(\mathbf{r})\psi_\downarrow^\dagger(\mathbf{r})\rangle + \left(\psi_\uparrow^\dagger(\mathbf{r})\psi_\downarrow^\dagger(\mathbf{r}) - \langle\psi_\uparrow^\dagger(\mathbf{r})\psi_\downarrow^\dagger(\mathbf{r})\rangle\right)\Big] \\
&\qquad\qquad \times\Big[\langle\psi_\downarrow(\mathbf{r})\psi_\uparrow(\mathbf{r})\rangle + \left(\psi_\downarrow(\mathbf{r})\psi_\uparrow(\mathbf{r}) - \langle\psi_\downarrow(\mathbf{r})\psi_\uparrow(\mathbf{r})\rangle\right)\Big], \\
&\approx g\Big[\left|\langle\psi_\downarrow(\mathbf{r})\psi_\uparrow(\mathbf{r})\rangle\right|^2 + \langle\psi_\uparrow^\dagger(\mathbf{r})\psi_\downarrow^\dagger(\mathbf{r})\rangle\left(\psi_\downarrow(\mathbf{r})\psi_\uparrow(\mathbf{r}) - \langle\psi_\downarrow(\mathbf{r})\psi_\uparrow(\mathbf{r})\rangle\right) \\
&\qquad\qquad +\langle\psi_\downarrow(\mathbf{r})\psi_\uparrow(\mathbf{r})\rangle\left(\psi_\uparrow^\dagger(\mathbf{r})\psi_\downarrow^\dagger(\mathbf{r}) - \langle\psi_\uparrow^\dagger(\mathbf{r})\psi_\downarrow^\dagger(\mathbf{r})\rangle\right)\Big], \\
&= g\Big[\langle\psi_\uparrow^\dagger(\mathbf{r})\psi_\downarrow^\dagger(\mathbf{r})\rangle\psi_\downarrow(\mathbf{r})\psi_\uparrow(\mathbf{r}) + \langle\psi_\downarrow(\mathbf{r})\psi_\uparrow(\mathbf{r})\rangle\psi_\uparrow^\dagger(\mathbf{r})\psi_\downarrow^\dagger(\mathbf{r}) - \left|\langle\psi_\downarrow(\mathbf{r})\psi_\uparrow(\mathbf{r})\rangle\right|^2\Big], \\
&= \Delta^\dagger(\mathbf{r})\psi_\downarrow(\mathbf{r})\psi_\uparrow(\mathbf{r}) + \Delta(\mathbf{r})\psi_\uparrow^\dagger(\mathbf{r})\psi_\downarrow^\dagger(\mathbf{r}) - \frac{|\Delta(\mathbf{r})|^2}{g}.
\end{aligned} \tag{6.34}$$

Next, we transform to momentum-space by defining the Fourier transforms

$$\psi_\sigma(\mathbf{r},t) = \frac{1}{\sqrt{V}}\sum_{\mathbf{k}} e^{i\mathbf{k}\cdot\mathbf{r}}\psi_{\mathbf{k}\sigma}(t), \qquad \Delta(\mathbf{r},t) = \sum_{\mathbf{q}} e^{i\mathbf{q}\cdot\mathbf{r}}\Delta_{\mathbf{q}}(t), \tag{6.35}$$

where V is the volume of the system. Thus, the Hamiltonian becomes

$$H = \sum_{\mathbf{k}\alpha\beta}\left[\xi_{\mathbf{k}\alpha}\delta_{\alpha\beta} - \mathbf{h}(\mathbf{k})\cdot\boldsymbol{\sigma}_{\alpha\beta}\right]\psi^\dagger_{\mathbf{k}\alpha}\psi_{\mathbf{k}\beta} + \sum_{\mathbf{k}\mathbf{k}'}\Delta^\dagger_{\mathbf{k}'-\mathbf{k}}\psi_{-\mathbf{k}\downarrow}\psi_{\mathbf{k}'\uparrow} + \sum_{\mathbf{k}\mathbf{k}'}\Delta_{\mathbf{k}-\mathbf{k}'}\psi^\dagger_{\mathbf{k}\uparrow}\psi^\dagger_{-\mathbf{k}'\downarrow} - \frac{V}{g}\sum_{\mathbf{q}}|\Delta_{\mathbf{q}}|^2, \tag{6.36}$$

where $\xi_{\mathbf{k}\alpha} = k^2/(2m_\alpha) - \mu_\alpha$ is the kinetic energy of an atom of species α with respect to its chemical potential. Noting that the spin-orbit field couples particles of different species (but the same momentum), while the pairing amplitude couples particles of momentum and spin $(\mathbf{k},\sigma)$ with particles of $(-\mathbf{k}',-\sigma)$ we define the Nambu-Gor'kov spinor

$$\Psi_{\mathbf{k}} = \begin{pmatrix}\psi_{\mathbf{k}\uparrow} & \psi_{\mathbf{k}\downarrow} & \psi^\dagger_{-\mathbf{k}\uparrow} & \psi^\dagger_{-\mathbf{k}\downarrow}\end{pmatrix}^T. \tag{6.37}$$

Symmetrizing the Hamiltonian with respect to the Nambu-Gor'kov components allows us to write the Hamiltonian in the form

$$H = \frac{1}{2}\sum_{\mathbf{k}\mathbf{k}'}\Psi^\dagger_{\mathbf{k}}\mathbf{H}_{\mathbf{k}\mathbf{k}'}\Psi_{\mathbf{k}'} - \frac{V}{g}\sum_{\mathbf{q}}|\Delta_{\mathbf{q}}|^2 + \sum_{\mathbf{k}}\tilde{\xi}_{\mathbf{k}+}, \tag{6.38}$$

where we define $\tilde{\xi}_{\mathbf{k}\uparrow} = \xi_{\mathbf{k}\uparrow} - h_z$, $\tilde{\xi}_{\mathbf{k}\downarrow} = \xi_{\mathbf{k}\downarrow} + h_z$, and $\tilde{\xi}_{\mathbf{k}\pm} = (\tilde{\xi}_{\mathbf{k}\uparrow} \pm \tilde{\xi}_{\mathbf{k}\uparrow})/2$, along with the Hamiltonian matrix

$$\mathbf{H}_{\mathbf{k}\mathbf{k}'} = \begin{pmatrix} (\xi_{\mathbf{k}\uparrow} - h_z)\delta_{\mathbf{k}\mathbf{k}'} & -h_\perp(\mathbf{k})\delta_{\mathbf{k}\mathbf{k}'} & 0 & \Delta_{\mathbf{k}-\mathbf{k}'} \\ -h^*_\perp(\mathbf{k})\delta_{\mathbf{k}\mathbf{k}'} & (\xi_{\mathbf{k}\downarrow} + h_z)\delta_{\mathbf{k}\mathbf{k}'} & -\Delta_{\mathbf{k}-\mathbf{k}'} & 0 \\ 0 & -\Delta^\dagger_{\mathbf{k}'-\mathbf{k}} & -(\xi_{-\mathbf{k}\uparrow} - h_z)\delta_{\mathbf{k}\mathbf{k}'} & h^*_\perp(-\mathbf{k})\delta_{\mathbf{k}\mathbf{k}'} \\ \Delta^\dagger_{\mathbf{k}'-\mathbf{k}} & 0 & h_\perp(-\mathbf{k})\delta_{\mathbf{k}\mathbf{k}'} & -(\xi_{-\mathbf{k}\downarrow} + h_z)\delta_{\mathbf{k}\mathbf{k}'} \end{pmatrix}. \tag{6.39}$$

Note that the final term in Eq. (6.38) arises from commutation of the diagonal elements of the kinetic energy operator.

The partition function of the system is $\mathcal{Z} = \int D[\Delta^\dagger, \Delta, \psi^\dagger, \psi]e^{-S_E}$, where the Euclidean action is

$$S_E = \int_0^\beta d\tau\left[\sum_\alpha \psi^\dagger_{\mathbf{k}\alpha}(\tau)\partial_\tau\psi_{\mathbf{k}\alpha}(\tau) + H\right], \tag{6.40}$$

and where $\beta = 1/T$ is the inverse temperature and $\tau = it$. Defining the Fourier transforms in (imaginary)

time

$$\psi_{k\sigma} = \frac{1}{\sqrt{\beta}} \sum_{\omega_n} e^{i\omega_n \tau} \psi_{\mathbf{k}\sigma}(\tau), \qquad \Delta_q = \sum_{\nu_n} e^{i\nu_n \tau} \Delta_{\mathbf{q}}(\tau), \tag{6.41}$$

where $\omega_n = (2n+1)\pi T$ and $\nu_n = 2n\pi T$ are the fermionic and bosonic Matsubara frequencies, respectively, we can write S_E in the form

$$S_E = \frac{\beta}{2} \sum_{kk'} \Psi_k^\dagger \mathbf{G}^{-1}_{kk'} \Psi_{k'} - \frac{\beta V}{g} \sum_q |\Delta_q|^2 + \beta \sum_k \tilde{\xi}_{\mathbf{k}+}, \tag{6.42}$$

where the single-particle Green's function is $\mathbf{G}^{-1} = i\omega_n \mathbf{I} + \mathbf{H}$:

$$\mathbf{G}^{-1}_{kk'} = \begin{pmatrix} (i\omega_n + \tilde{\xi}_{\mathbf{k}\uparrow})\delta_{kk'} & -h_\perp(\mathbf{k})\delta_{kk'} & 0 & \Delta_{k-k'} \\ -h_\perp^*(\mathbf{k})\delta_{kk'} & (i\omega_n + \tilde{\xi}_{\mathbf{k}\downarrow})\delta_{kk'} & -\Delta_{k-k'} & 0 \\ 0 & -\Delta^\dagger_{k'-k} & (i\omega_n - \tilde{\xi}_{-\mathbf{k}\uparrow})\delta_{kk'} & h_\perp^*(-\mathbf{k})\delta_{kk'} \\ \Delta^\dagger_{k'-k} & 0 & h_\perp(-\mathbf{k})\delta_{kk'} & (i\omega_n - \tilde{\xi}_{-\mathbf{k}\downarrow})\delta_{kk'} \end{pmatrix}, \tag{6.43}$$

Having cast the partition function in the form of a Gaussian integral, we can integrate over $\Psi^\dagger, \Psi$ explicitly and obtain the thermodynamic potential per unit volume $\Omega = -T \ln \mathcal{Z}/V$:

$$\Omega = -\sum_q \frac{|\Delta_q|^2}{g} - \frac{T}{2V} \operatorname{tr} \ln(\beta \mathbf{G}^{-1}) + \frac{1}{V} \sum_k \tilde{\xi}_{\mathbf{k}+}, \tag{6.44}$$

where the trace is taken over the continuous momentum variable as well as the discrete Nambu-Gor'kov and spin indices and the factor of $1/2$ in the second term comes from the double-counting of degrees of freedom inherent in the Nambu-Gor'kov formalism.[2]

Next, we expand the thermodynamic potential about the homogeneous mean field gap Δ_0 by writing $\Delta_q = \Delta_0 \delta_{q,0} + \eta_q$, where η_q is the fluctuation field. Similarly, we rewrite $\operatorname{tr} \ln(\beta \mathbf{G}^{-1})$ as

$$\begin{aligned} \operatorname{tr} \ln\left(\beta \mathbf{G}^{-1}\right) &= \operatorname{tr} \ln\left[\beta\left(\mathbf{G}_0^{-1} + \mathbf{G}_F^{-1}\right)\right], \\ &= \operatorname{tr} \ln\left(\beta \mathbf{G}_0^{-1}\right) + \operatorname{tr} \ln\left(1 + \mathbf{G}_0 \mathbf{G}_F^{-1}\right), \end{aligned} \tag{6.45}$$

[2] In integrating over $\Psi^\dagger, \Psi$ we have treated all elements of the Nambu-Gor'kov spinor as independent fields. However, as one can see from Eq. (6.37), only two of the four elements are actually independent. The factor of $1/2$ in Eq. (6.44) removes this double-counting of the system's degrees of freedom.

where $\mathbf{G}_0^{-1}$ is the inverse of the mean field Green's function:

$$\mathbf{G}_0^{-1}(k,k') = \begin{pmatrix} i\omega_n + \tilde{\xi}_{\mathbf{k}\uparrow} & -h_\perp(\mathbf{k}) & 0 & \Delta_0 \\ -h_\perp^*(\mathbf{k}) & i\omega_n + \tilde{\xi}_{\mathbf{k}\downarrow} & -\Delta_0 & 0 \\ 0 & -\Delta_0^\dagger & i\omega_n - \tilde{\xi}_{-\mathbf{k}\uparrow} & h_\perp^*(-\mathbf{k}) \\ \Delta_0^\dagger & 0 & h_\perp(-\mathbf{k}) & i\omega_n - \tilde{\xi}_{-\mathbf{k}\downarrow} \end{pmatrix} \delta_{kk'}. \tag{6.46}$$

and $\mathbf{G}_F$ is the fluctuation matrix:

$$\mathbf{G}_F^{-1}(k,k') = \begin{pmatrix} 0 & 0 & 0 & -\eta_{k-k'} \\ 0 & 0 & \eta_{k-k'} & 0 \\ 0 & \eta_{k'-k}^\dagger & 0 & 0 \\ -\eta_{k'-k}^\dagger & 0 & 0 & 0 \end{pmatrix}. \tag{6.47}$$

Thus, separating the mean field and fluctuation contributions to the thermodynamic potential we can write

$$\Omega = \Omega_0 + \Omega_F, \tag{6.48}$$

$$\Omega_0 = -\frac{|\Delta_0|^2}{g} - \frac{T}{2V}\,\mathrm{tr}\ln\left(\beta\mathbf{G}_0^{-1}\right) + \frac{1}{V}\sum_{\mathbf{k}}\tilde{K}_+, \tag{6.49}$$

$$\Omega_F = -\sum_q \frac{|\eta(q)|^2}{g} - \frac{T}{2V}\,\mathrm{tr}\ln(1 + \mathbf{G}_0\mathbf{G}_F^{-1}), \tag{6.50}$$

where the terms linear in η vanish due to the stationary condition of Ω at the mean field gap.[3] Having derived the thermodynamic potential, we now proceed to consider the mean field properties of the system, deferring a discussion of fluctuation effects to Appendix A.

6.6 Mean Field Approximation

Before constructing the mean field thermodynamic potential Ω_0 explicitly, we make two observations. First, we note that for Rashba-Dresselhaus spin-orbit fields the magnetic field strength is linear (odd) in the momentum coordinates, while the energies $\tilde{\xi}_{\mathbf{k}\alpha}$ are quadratic (even). In particular, this implies $h_\perp(-\mathbf{k}) = -h_\perp(\mathbf{k})$ and $\tilde{\xi}_{-\mathbf{k}\alpha} = \tilde{\xi}_{\mathbf{k}\alpha}$. Second, while to this point we have allowed for different masses for the two spin species, in practice a spin-orbit field is incapable of transforming an atom of one species into another species of different mass. Thus, in what follows we will discuss only the situation of equal masses, $m_\uparrow = m_\downarrow \equiv m$.[4]

[3] The mean field gap is precisely the value of Δ_0 that minimizes the thermodynamic potential. As a result, any linear terms in an expansion of Ω about the mean field configuration must vanish identically. For this reason, this approximation is often referred to as the *saddle point approximation*.

[4] It is possible that in the presence of weak spin-dependent optical lattices one may obtain different effective masses for the two hyperfine states ($m_\uparrow \neq m_\downarrow$) [62]. Such a spin-dependence would modify our starting Hamiltonian and require careful

In order to obtain the mean field thermodynamic potential we begin by computing the eigenvalues of the system by diagonalizing the mean field Hamiltonian $\mathbf{H}_0 = \mathbf{G}_0^{-1} - i\omega_n \mathbf{I}$. This yields the eigenvalue pairs

$$E_{1,2} = \sqrt{Y_+ + Y_- \pm 2\sqrt{Y_+ Y_- - |\Delta_0|^2 |h_\perp|^2}}, \tag{6.51}$$

$$E_{3,4} = -E_{1,2}, \tag{6.52}$$

where following the notation of [62] we define $Y_+ = \tilde{\xi}_{\mathbf{k}+}^2 + |\Delta_0|^2$ and $Y_- = \tilde{\xi}_{\mathbf{k}-}^2 + |h_\perp|^2$, with $\tilde{\xi}_{\mathbf{k}\pm} = (\tilde{\xi}_{\mathbf{k}\uparrow} \pm \tilde{\xi}_{\mathbf{k}\downarrow})/2$. Making use of the identity $\mathrm{tr} \ln \mathbf{A} = \ln \det \mathbf{A}$, we can express $\mathrm{tr} \ln(\beta \mathbf{G}_0^{-1})$ in terms of the system's eigenvalues as

$$\begin{aligned} \mathrm{tr} \ln \left(\beta \mathbf{G}_0^{-1}\right) &= \ln \prod_{j=1}^{4} \left[\beta \left(i\omega_n - E_j\right)\right], \\ &= \sum_{j=1}^{4} \ln \left[\beta \left(i\omega_n - E_j\right)\right]. \end{aligned} \tag{6.53}$$

Substituting this expression into Eq. (6.49) and performing the Matsubara sum (as shown in Appendix C), we obtain the mean field thermodynamic potential:

$$\Omega_0 = -\frac{|\Delta_0|^2}{g} - \frac{T}{V} \sum_{j=1}^{2} \sum_{\mathbf{k}} \left[\ln(1 + e^{-\beta E_j}) + \frac{1}{2}\beta E_j\right] + \frac{1}{V} \sum_{k} \tilde{\xi}_{\mathbf{k}+}, \tag{6.54}$$

which we have written in terms of the positive eigenvalues $E_{1,2}$. Having obtained the thermodynamic potential, we next derive the mean field gap and number equations in order to analyze the phase structure of the system.

6.6.1 Gap Equation

The mean field gap is the homogeneous configuration $\Delta(\mathbf{x}) = \Delta_0$ which minimizes the thermodynamic potential Ω_0. The trivial solution $\Delta_0 = 0$, which represents the "normal" phase of the system, is always a solution of the equation $\partial\Omega_0/\partial|\Delta_0| = 0$. The gap equation, which implicitly defines the non-trivial solution to this extremization problem, is given by $\partial\Omega_0/\partial|\Delta_0|^2$:

$$\frac{1}{g} = -\frac{1}{2V} \sum_{j=1}^{2} \sum_{\mathbf{k}} \tanh\left(\frac{\beta E_j}{2}\right) \frac{\partial E_j}{\partial |\Delta_0|^2}. \tag{6.55}$$

analysis, but spin-orbit transitions between species of different mass would remain prohibited on physical grounds. An analysis of the full implications of such spin-dependence is beyond the scope of this thesis.

Replacing the divergent bare coupling g with the s-wave scattering length via the relation

$$\frac{1}{g} = \frac{m}{4\pi a_s} - \frac{1}{V}\sum_{\mathbf{k}} \frac{1}{2\varepsilon}, \tag{6.56}$$

where $\varepsilon = k^2/2m$, and computing the eigenvalues' derivatives in Eq. (6.55) we obtain the renormalized gap equation

$$\frac{m}{4\pi a_s} = \frac{1}{V}\sum_{\mathbf{k}} \left[\frac{1}{2\varepsilon} - \left(\frac{X_1}{4E_1} + \frac{X_2}{4E_2} \right) - \frac{\tilde{\xi}^2_{\mathbf{k}-}}{\sqrt{Y_+ Y_- - |\Delta_0|^2 |h_\perp|^2}} \left(\frac{X_1}{4E_1} - \frac{X_2}{4E_2} \right) \right], \tag{6.57}$$

where we define $X_i = \tanh(\beta E_i/2)$.

6.6.2 Number Equations

The number equation for the species α is given by the thermodynamic identity $n_\alpha = -\partial\Omega_0/\partial\mu_\alpha$. Thus, differentiating Eq. (6.54) we obtain

$$n_\uparrow = \frac{1}{2V}\sum_{\mathbf{k}} \left[1 - \tilde{\xi}_{\mathbf{k}\uparrow} \left(\frac{X_1}{2E_1} + \frac{X_2}{2E_2} \right) - \frac{\tilde{\xi}_{\mathbf{k}+} Y_- + \tilde{\xi}_{\mathbf{k}-} Y_+}{\sqrt{Y_+ Y_- - |\Delta_0|^2 |h_\perp|^2}} \left(\frac{X_1}{2E_1} - \frac{X_2}{2E_2} \right) \right], \tag{6.58}$$

$$n_\downarrow = \frac{1}{2V}\sum_{\mathbf{k}} \left[1 - \tilde{\xi}_{\mathbf{k}\downarrow} \left(\frac{X_1}{2E_1} + \frac{X_2}{2E_2} \right) - \frac{\tilde{\xi}_{\mathbf{k}+} Y_- - \tilde{\xi}_{\mathbf{k}-} Y_+}{\sqrt{Y_+ Y_- - |\Delta_0|^2 |h_\perp|^2}} \left(\frac{X_1}{2E_1} - \frac{X_2}{2E_2} \right) \right]. \tag{6.59}$$

Before proceeding to solve the gap and number equations we note that by alternatively adding or subtracting subtracting Eqs. (6.58) and (6.59) we can express the total particle density in the form

$$n = \frac{1}{V}\sum_{\mathbf{k}} \left[1 - \tilde{\xi}_{\mathbf{k}+} \left(\frac{X_1}{2E_1} + \frac{X_2}{2E_2} \right) - \frac{\tilde{\xi}_{\mathbf{k}+} Y_-}{\sqrt{Y_+ Y_- - |\Delta_0|^2 |h_\perp|^2}} \left(\frac{X_1}{2E_1} - \frac{X_2}{2E_2} \right) \right], \tag{6.60}$$

and the excess density of up spins as

$$n_\uparrow - n_\downarrow = -\frac{1}{V}\sum_{\mathbf{k}} \tilde{\xi}_{\mathbf{k}-} \left[\frac{X_1}{2E_1} + \frac{X_2}{2E_2} + \frac{Y_+}{\sqrt{Y_+ Y_- - |\Delta_0|^2 |h_\perp|^2}} \left(\frac{X_1}{2E_1} - \frac{X_2}{2E_2} \right) \right]. \tag{6.61}$$

From this expression it is clear that the Zeeman field acts in the same way as a chemical potential difference between the two spin species. In particular, defining $\mu_\pm = (\mu_\uparrow \pm \mu_\downarrow)/2$, when $\tilde{\xi}_{\mathbf{k}-} = -(\mu_- + h_z) \neq 0$ the right side of Eq. (6.61) will not vanish and the system will be population imbalanced. On the other hand, for $\tilde{\xi}_{\mathbf{k}-} = 0$ the two number equations are identical and we need only solve Eqs. (6.57) and (6.60) for (Δ, μ), where $\mu = \mu_\uparrow = \mu_\downarrow$ is the two species' common chemical potential.

There are two different experimental situations that may be realized for which $\tilde{\xi}_{\mathbf{k}-} \neq 0$. On the one

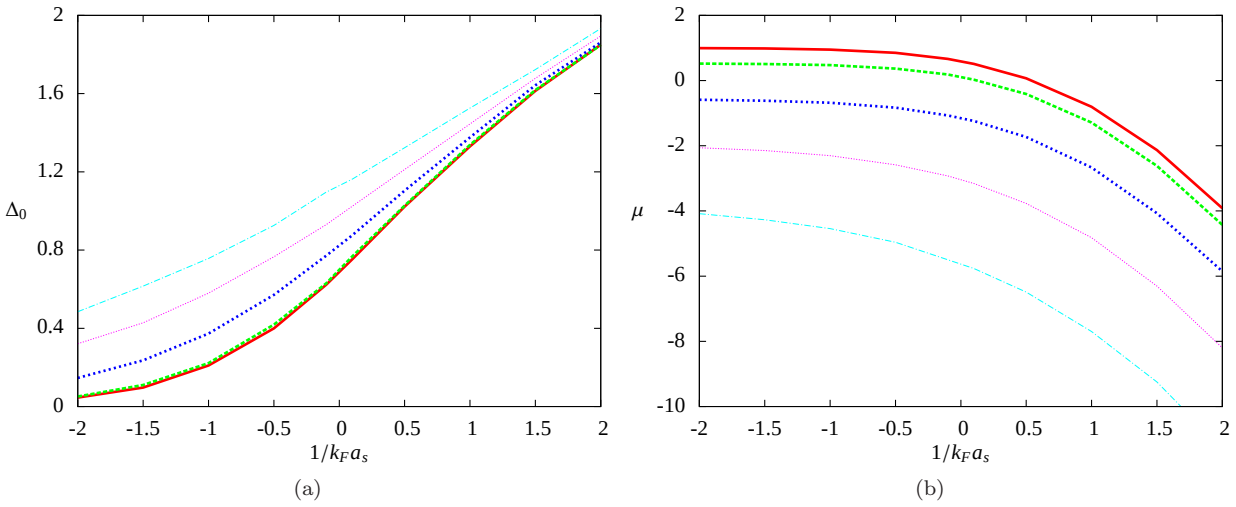

Figure 6.2: (a) Pairing gap magnitude Δ_0 and (b) chemical potential μ (in units of ε_F, the Fermi energy of the free Fermi gas) vs. inverse scattering length $(1/k_F a_s)$ at $T = 0$ in the RO case ($\eta = 1$) for $\kappa/k_F = 0$ (solid red), 0.5 (dashed green), 1.0 (dotted blue), 1.5 (thin violet), and 2.0 (dot-dashed light blue), where $k_F = \sqrt{2m\varepsilon_F}$ is the Fermi momentum. In the ERD case the gap is independent of κ and hence is identical to the $\kappa = 0$ curve in (a), while $\mu(v) = \mu(0) - \kappa^2/2m$ (see Eq. (6.62)).

hand, by applying a radio frequency (RF) field during the system's preparation it is possible to induce a specified population imbalance. In the absence of a spin-orbit field capable of transforming one hyperfine state into the another, this imbalance will persist and $\mu_\uparrow \neq \mu_\downarrow$ so that we must solve the full set of three equations (6.57), (6.58), and (6.59) for $(\Delta, \mu_\uparrow, \mu_\downarrow)$. On the other hand, in the presence of a Zeeman field the system will spontaneously develop a population imbalance due to the energy difference between the two hyperfine states, but the spin-orbit induced equilibrium between the species dictates that $\mu_\uparrow = \mu_\downarrow$. While both situations are realizable, in the following calculations we concentrate on the latter case.

In the next section we investigate the phases of the population balanced system by solving Eqs. (6.57) and (6.60) for $\tilde{\xi}_{\mathbf{k}-} = 0$. We then proceed in the following section to introduce a non-zero Zeeman field and consider the more general case $n_\uparrow \neq n_\downarrow$.

6.7 Population Balanced System

In order to solve the gap and number equations, even for a population balanced system, we must specify the two-body interaction strength (or s-wave scattering length) as well as the overall spin-orbit magnitude κ and the anisotropy η. Thus, the phase space of our system is already rather large, depending on three independent parameters. In order to render our calculations maximally useful, we therefore restrict our attention to situations which are, or we anticipate will be shortly, within the realm of experimental observation. In particular, regarding the spin-orbit coupling we will focus on the ERD ($\eta = 0$) and RO ($\eta = 1$) cases. The

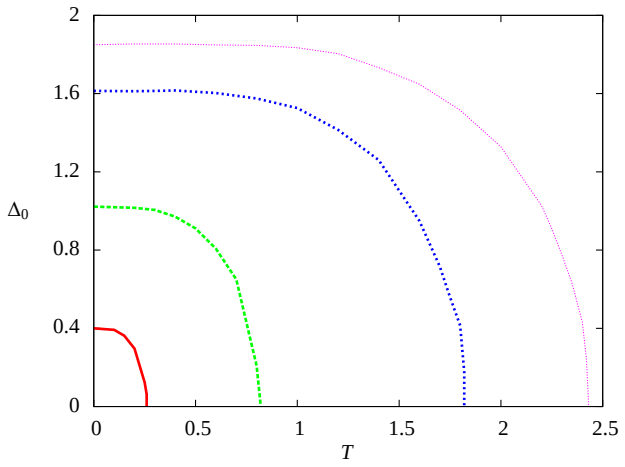

Figure 6.3: Pairing gap magnitude Δ_0 vs. T (in units of ε_F) in the case $\kappa = 0$ for $1/k_F a_s = -0.5$ (solid red), 0.5 (dashed green), 1.5 (dotted blue), and 2.0 (thin violet).

s-wave scattering length, which can be tuned arbitrarily via a Feshbach resonance, will be investigated across all parameter values.

Figure 6.2 shows the zero temperature mean field gap and chemical potential as a function of the interaction parameter $1/k_F a_s$ in the RO case, for a variety of spin-orbit couplings. We find that the gap increases with increasing κ for fixed $1/k_F a_s$, but that this effect diminishes as $1/k_F a_S \to \infty$ where the curves converge. Meanwhile, the chemical potential consistently decreases with increasing κ.

The ERD case has the important property that in the absence of a Zeeman field, Δ_0 is independent of the magnitude of the spin-orbit coupling κ, and so is simply given by the $\kappa = 0$ curve in Fig. 6.2(a). We can understand this result by considering the eigenvalues in the ERD case, which for $\tilde{\xi}_{\mathbf{k}-} = 0$ reduce to $E_{1,2} = \sqrt{(\tilde{\xi}_{\mathbf{k}+} \pm \kappa|k_x|/m)^2 + |\Delta_0|^2}$, where $\tilde{\xi}_{\mathbf{k}+} = \varepsilon - \mu$. By shifting the integral over k_x to $k'_x = k_x \pm \kappa$ we obtain

$$\tilde{\xi}_{\mathbf{k}+} \pm \frac{\kappa|k_x|}{m} \quad \longrightarrow \quad \tilde{\xi}_{\mathbf{k}'+} - \frac{\kappa^2}{2m}. \tag{6.62}$$

Thus, the entire spin-orbit dependence of the gap and number equations can be subsumed into a shift of the chemical potential to $\mu(\kappa) = \mu(0) - \kappa^2/2m$. The result is that, as observed, the gap is independent of κ, while the chemical potential has a simple quadratic dependence on κ.

Turning next to the temperature dependence of Δ_0, Fig. 6.3 shows the mean field gap in the absence of spin-orbit coupling, where the system exhibits behavior typical of second-order phase transitions with $\Delta(T) \propto \sqrt{T_c - T}$. As shown in Fig. 6.4, as κ increases in the RO case, the critical temperature also increases, as we would expect from the increased zero temperature gap observed in Fig. 6.2(a). In contrast,

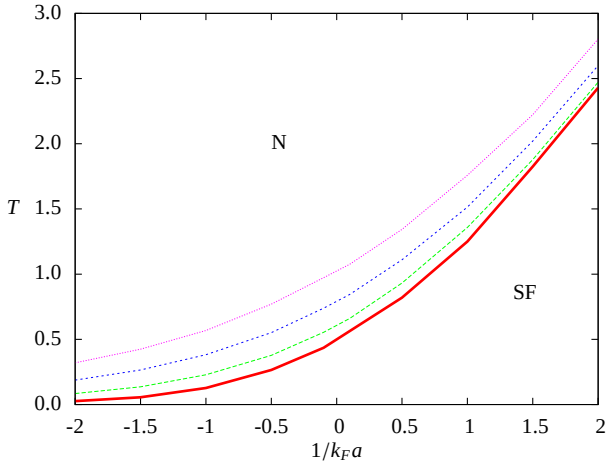

Figure 6.4: Mean field phase diagram for an RO coupled system for $\kappa/k_F = 0$ (solid red), 1.0 (dashed green), 1.5 (dotted blue), and 2.0 (thin violet). N and SF denote normal and superfluid phases, respectively. The ERD phase boundary is identical to the $\kappa = 0$ curve. The temperature is in units of ε_F.

since the zero temperature gap is independent of v in the ERD case, T_c is similarly independent of the spin-orbit coupling strength.

Figure 6.4 shows the mean field phase diagram for the population balanced system in the RO case for several values of κ. We see that the effect of $\kappa \neq 0$ is to increase the region of superfluidity by enhancing the pairing strength and thereby increasing T_c for a given interaction strength.

6.8 Population Imbalanced System

Having constructed the phase diagram for a population balanced system with $\tilde{\xi}_{\mathbf{k}-} = 0$ we now move on to consider the more general case in which $\tilde{\xi}_{\mathbf{k}-} \neq 0$. The description of imbalanced systems is complicated by the fact that for $N_\uparrow \neq N_\downarrow$ the Fermi seas of the two species are mismatched (i.e., $k_{F,\uparrow} \neq k_{F,\downarrow}$) so that the net pair condensation energy obtainable by forming spin-singlet BCS pairs is decreased [145–149]. As a result, in the absence of triplet pairing, as the population imbalance $P = (n_\uparrow - n_\downarrow)/(n_\uparrow + n_\downarrow)$ grows, the net condensation energy falls until at some critical value P_c superfluidity is destroyed altogether.

Figure 6.5 shows the mean field phase diagrams for RO coupled systems with various Zeeman fields and Rashba couplings. We see that at small κ the Zeeman field acts to suppress superfluidity by inducing a mismatch of the Fermi surfaces of the two species, thereby making pairing more difficult. However, as noted in [62], as κ increases, the pair-breaking mechanism of h_z becomes less effective, due to the emergence of a triplet component of the superfluid order parameter. Indeed, as shown for $\kappa/k_F = 1.0$, 1.5, and 2.0, the region of superfluidity actually *increases* with increasing Zeeman field. Moreover, the effect of h_z on the phase boundary is magnified as κ increases so that the curves in Fig. 6.5 spread out with increasing κ.

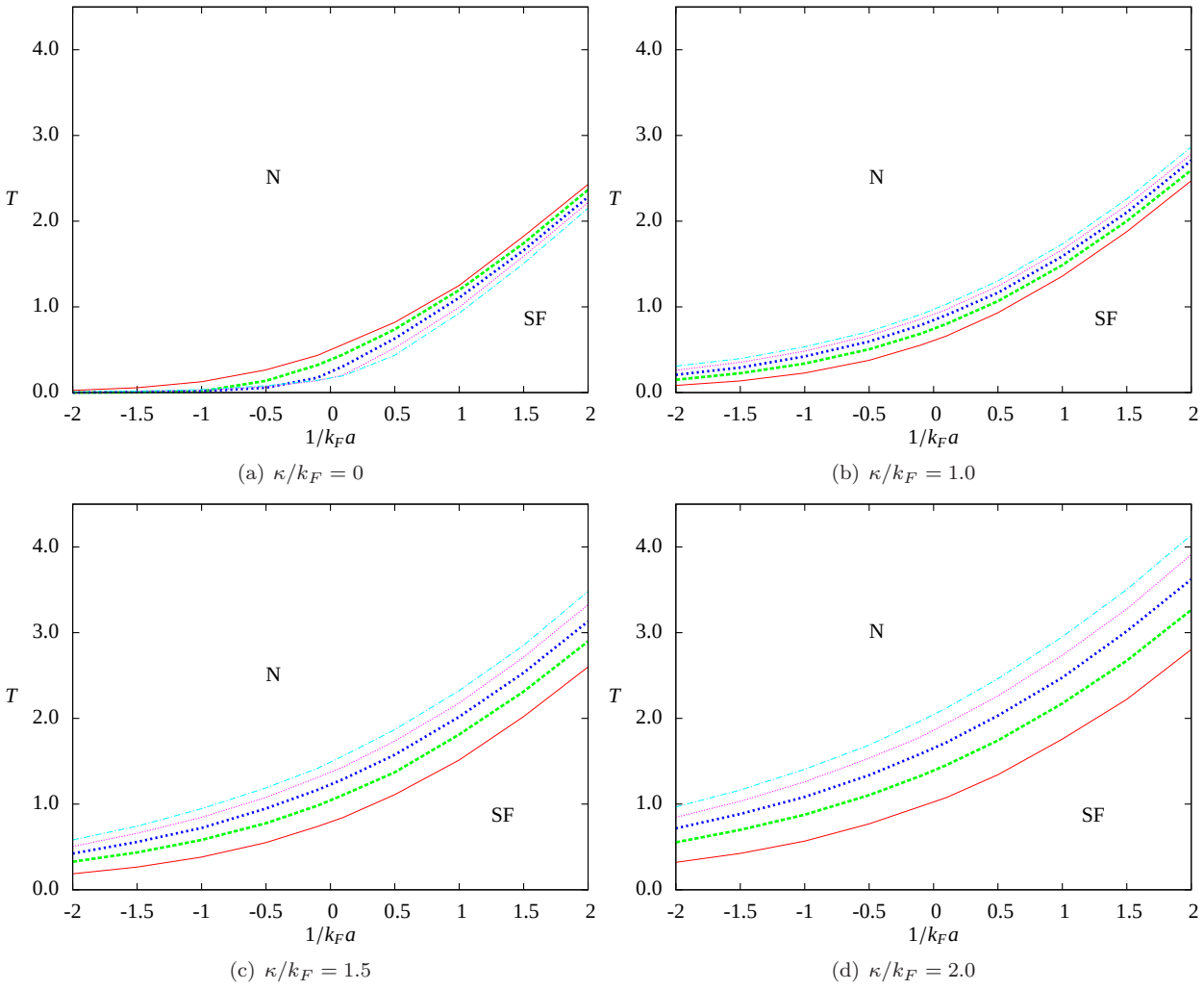

(a) $\kappa/k_F = 0$ (b) $\kappa/k_F = 1.0$

(c) $\kappa/k_F = 1.5$ (d) $\kappa/k_F = 2.0$

Figure 6.5: Mean field phase diagrams for RO coupled systems with $h_z/\varepsilon_F = 0$ (solid red), 0.25 (dashed green), 0.5 (big dotted blue), 0.75 (small dotted violet), and 1.0 (dot-dashed light blue) and various spin-orbit coupling strengths.

In Fig. 6.6 we show the phase diagrams for ERD coupled systems with various Zeeman fields and spin-orbit couplings. As shown in Eq. (6.62), for $h_z = 0$ the ERD coupling can be absorbed into a shift in the system's chemical potential so that the location of the phase boundary is independent of κ. Thus, the red curves in the four plots of Fig. 6.6 are identical. However, for $h_z \neq 0$ the κ dependence can no longer be eliminated by such a gauge transformation and the phase diagram develops a non-trivial dependence on the spin-orbit coupling. In particular, we find that the Zeeman field tends to increase T_c and its effect is magnified as the magnitude of the spin-orbit field is increased.

One common feature of the mean field phase diagrams for both RO and ERD coupled systems is the exponential increase in T_c with increasing $1/k_F a_s$. Thus, it appears that one can increase T_c arbitrarily simply by tuning the system to create strongly bound diatomic molecules ($1/k_F a_s \to \infty$). This cannot be

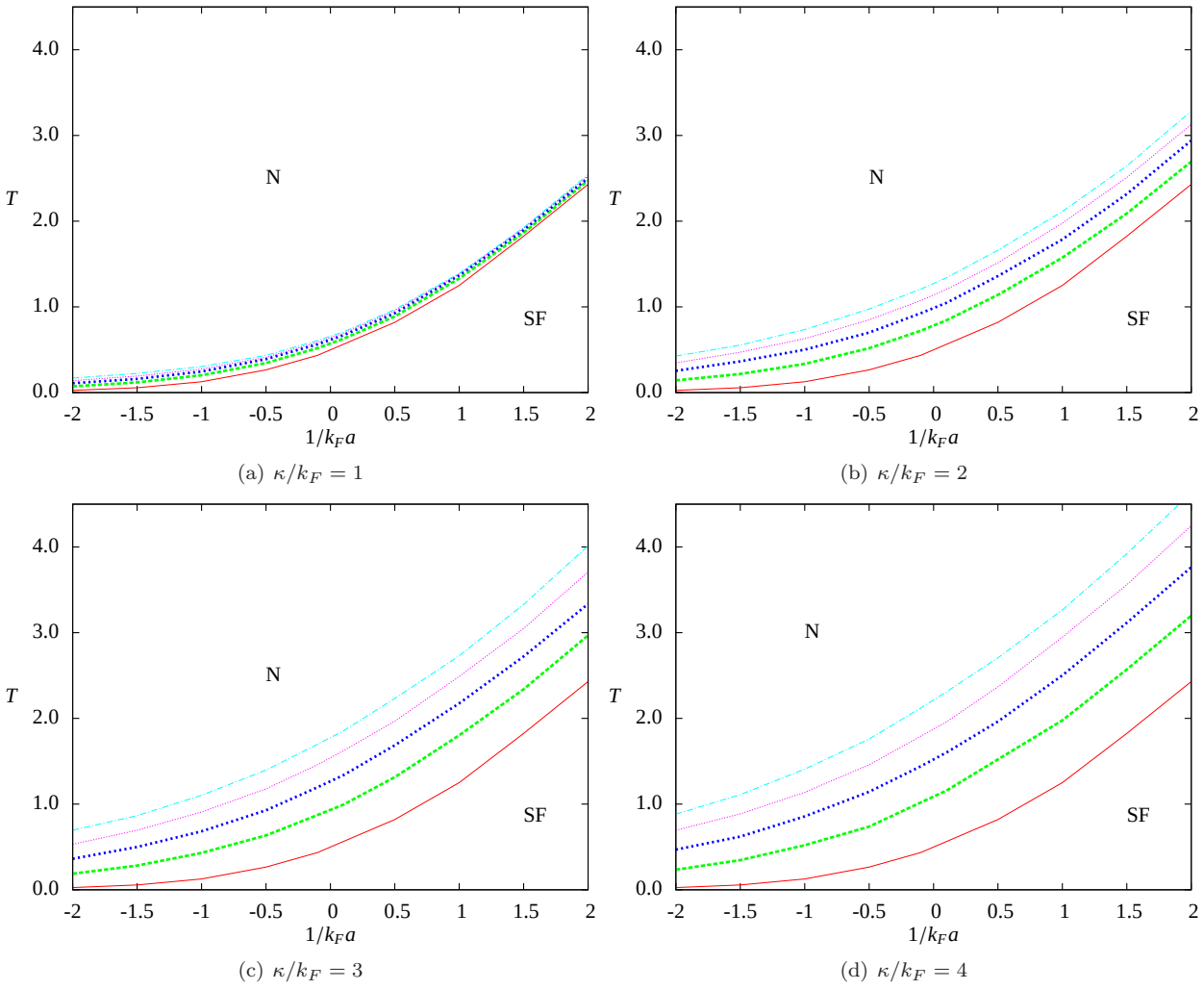

(a) $\kappa/k_F = 1$ (b) $\kappa/k_F = 2$

(c) $\kappa/k_F = 3$ (d) $\kappa/k_F = 4$

Figure 6.6: Mean field phase diagrams for ERD coupled systems with various spin-orbit coupling strengths. Line types are the same as in Fig. 6.5.

true, however, for in this BEC limit the system simply behaves as a gas of bosons with $m_B = 2m$ and $n_B = n/2$. The critical temperature for BEC formation in a *free* boson gas is [150]

$$T_c = \frac{2\pi}{m_B}\left(\frac{n_B}{\zeta(3/2)}\right)^{2/3}, \tag{6.63}$$

where $\zeta(z)$ is the Riemann zeta function and $\zeta(3/2) \approx 2.61$. Comparing this expression to the Fermi temperature ($T_F = \varepsilon_F/k_B$) of the original gas of fermions we find

$$T_c = \left(\frac{2}{9\pi\zeta(3/2)^2}\right)^{1/3} T_F \approx 0.218 T_F. \tag{6.64}$$

Thus, on physical grounds we expect that the phase boundaries shown in Figs. 6.5 and 6.6 should reach a

plateau at $T_c \sim T_F$ as $1/k_F a_s \to \infty$, rather than continuing to increase. In fact, this unphysical behavior in the BEC limit is a generic feature of our mean field treatment of the BCS-BEC crossover, independent of the spin-orbit coupling with which we are presently concerned [151–153]. This discrepancy can be traced to the number equation's failure to account for the fact that for $1/k_F a_s \gg 1$, nearly all of the fermions in the system are bound into composite bosons. In particular, in this limit the normal state should be a (composite) Bose gas, not the Fermi gas about which the mean field treatment expands. In order to account for BEC physics we must include the effects of fluctuations, which is the subject of Appendix A.

6.9 Ginzburg-Landau Thermodynamic Potential

In order to gain insight into the superfluid-normal phase transition, as well as to lay the foundation for our consideration of fluctuations in Appendix A, it will be helpful to consider the thermodynamic potential very near the phase boundary by expanding in a Ginzburg-Landau (GL) form:

$$\Omega_{GL}(\Delta_0) = \Omega_0(0) + a|\Delta_0|^2 + \frac{b}{2}|\Delta_0|^4 + \cdots , \tag{6.65}$$

where the coefficients a and b depend on μ and T. These coefficients can be computed directly by differentiating Eq. (6.54) and are

$$a(\mu,T) = -\frac{m}{4\pi a_s} + \frac{1}{V}\sum_{\mathbf{k}}\left[\frac{1}{2\varepsilon} - \left(\frac{X_1}{4E_1} + \frac{X_2}{4E_2}\right) - \frac{h_z^2}{\xi_{\mathbf{k}} h}\left(\frac{X_1}{4E_1} - \frac{X_2}{4E_2}\right)\right], \tag{6.66}$$

$$b(\mu,T) = \frac{1}{2V}\sum_{\mathbf{k}}\left[\left(1 + \frac{h_z^4}{\xi_{\mathbf{k}}^2 h^2}\right)\left(\frac{Z_{11}}{4E_1^3} + \frac{Z_{22}}{4E_2^3}\right) + \frac{2h_z^2}{\xi_{\mathbf{k}} h}\left(\frac{Z_{11}}{4E_1^3} - \frac{Z_{22}}{4E_2^3}\right) + \frac{h_z^4}{\xi_{\mathbf{k}}^3 h^3}\left(\frac{X_1}{4E_1} - \frac{X_2}{4E_2}\right)\right]. \tag{6.67}$$

where we define $Y_i = \mathrm{sech}^2(\beta E_i/2)$ and $Z_{ij} = X_i - \beta E_i Y_j/2$, and the eigenvalues are understood to be evaluated at $\Delta_0 = 0$, so that $E_{1,2} = \xi_k \pm h$, where $\xi_k = \varepsilon - \mu$ and $Y_- = h_z^2 + |h_\perp|^2 \equiv h^2$. Note also that since we have specialized to mass balanced systems in chemical equilibrium we have $\xi_{\mathbf{k}\uparrow} = \xi_{\mathbf{k}\downarrow} \equiv \xi_{\mathbf{k}}$ as well as $\tilde{\xi}_{\mathbf{k}+} = \xi_{\mathbf{k}}$ and $\xi_{\mathbf{k}-} = -h_z$.

Comparing Eqs. (6.57) and Eq. (6.66) we note that the GL coefficient $a(\mu,T)$ vanishes precisely when the gap equation is satisfied for $\Delta_0 = 0$. This is encouraging, for both of these conditions are criteria for defining the onset of pairing. In the first case, the gap equation does not in general contain the trivial solution $\Delta_0 = 0$, so that when a solution exists at all, pairing has commenced. In the second case, a negative coefficient a is precisely what is required of Ω_{GL} to produce a non-trivial minimum.

Appendix A

Effects of Fluctuations on Spin-Orbit Coupled Fermions

A.1 Introduction

In Chapter 6 we analyzed the mean field properties of ultracold fermions subject to an artificial gauge field of the Rashba-Dresselhaus form. While our results have provided insight into the generic phase structure of these systems, particularly in the weak coupling regime, we have observed that fluctuations play a crucial role in determining the location of the phase boundary in the BEC regime where the normal phase consists largely of composite bosons. Thus, in this appendix we build on our prior results by considering the effects of Gaussian fluctuations on the phase diagram of spin-orbit coupled fermions.

A.2 Fluctuation Thermodynamic Potential

In Chapter 6 we derived the thermodynamic potential for our spin-orbit coupled system, including fluctuations, which is given in Eqs. (6.49)-(6.50). However, before proceeding with our treatment of the fluctuation contribution Ω_F we make two approximations. First, we expand Ω_F in powers of the fluctuation field η and truncate the series at quartic order. Second, since we are particularly interested in the effects of fluctuations on the phase boundary of the system, where the mean field gap vanishes, we set $\Delta_0 = 0$ and henceforth denote the fluctuation field by the now identical full gap Δ.

Anticipating our expansion about $\Delta = \Delta_0 = 0$ we begin by writing $\mathbf{G}^{-1}[\Delta] = \mathbf{G}_0^{-1}[0] + \mathbf{G}_F^{-1}[\Delta]$ where the ungapped Green's function is now of the block diagonal form

$$\mathbf{G}_0^{-1}[0] = \begin{pmatrix} i\omega_n + \tilde{\xi}_{\mathbf{k}\uparrow} & -h_\perp(\mathbf{k}) & 0 & 0 \\ -h_\perp^*(\mathbf{k}) & i\omega_n + \tilde{\xi}_{\mathbf{k}\downarrow} & 0 & 0 \\ 0 & 0 & i\omega_n - \tilde{\xi}_{\mathbf{k}\uparrow} & -h_\perp^*(\mathbf{k}) \\ 0 & 0 & -h_\perp(\mathbf{k}) & i\omega_n - \tilde{\xi}_{\mathbf{k}\downarrow} \end{pmatrix} \delta_{kk'}. \tag{A.1}$$

and where the gap-dependent fluctuation matrix is given by Eq. (6.47), with $\eta = \Delta$. The tr ln term in Eq. (6.50) can be expanded as

$$\mathrm{tr}\ln\left(\beta\mathbf{G}^{-1}[\Delta]\right) \quad = \quad \mathrm{tr}\ln\left(\beta\mathbf{G}_0^{-1}[0] + \beta\mathbf{G}_F^{-1}[\Delta]\right),$$

$$
\begin{aligned}
&= \operatorname{tr}\ln\left(\beta\mathbf{G}_0^{-1}[0]\right) + \operatorname{tr}\ln\left(1+\mathbf{G}_0[0]\mathbf{G}_F^{-1}[\Delta]\right), \\
&= \operatorname{tr}\ln\left(\beta\mathbf{G}_0^{-1}[0]\right) - \frac{1}{2}\operatorname{tr}\left(\mathbf{G}_0[0]\mathbf{G}_F^{-1}[\Delta]\right)^2 - \frac{1}{4}\operatorname{tr}\left(\mathbf{G}_0[0]\delta\mathbf{G}_F^{-1}[\Delta]\right)^4 + \cdots, \quad \text{(A.2)}
\end{aligned}
$$

where we note that traces of odd powers of $\mathbf{G}[0]\mathbf{G}_F^{-1}[\Delta]$ vanish. Thus, truncating the thermodynamic potential per unit volume at fourth order we have

$$
\begin{aligned}
\Omega[\Delta] &= \Omega_0[0] + \Omega^{(2)}[\Delta] + \Omega^{(4)}[\Delta], & \text{(A.3)}\\
\Omega_0[0] &= -\frac{T}{2V}\operatorname{tr}\ln\left(\beta\mathbf{G}_0^{-1}[0]\right) + \frac{1}{V}\sum_k \tilde{\xi}_{\mathbf{k}+}, & \text{(A.4)}\\
\Omega^{(2)}[\Delta] &= -\sum_q \frac{|\Delta_q|^2}{g} + \frac{T}{4V}\operatorname{tr}\left(\mathbf{G}_0[0]\mathbf{G}_F^{-1}[\Delta]\right)^2, & \text{(A.5)}\\
\Omega^{(4)}[\Delta] &= \frac{T}{8V}\operatorname{tr}\left(\mathbf{G}_0[0]\mathbf{G}_F^{-1}[\Delta]\right)^4. & \text{(A.6)}
\end{aligned}
$$

Evaluating Eqs. (A.3)-(A.6), we will obtain the Ginzburg-Landau (GL) thermodynamic potential, which we write in the form

$$
\Omega_{GL}[\Delta] = \Omega_0[0] + \sum_q \Gamma^{-1}(q)|\Delta_q|^2 + \frac{1}{2}\sum_{q_1\cdots q_3} b(q_1,q_2,q_3)\Delta_{q_1}\Delta^\dagger_{q_2}\Delta_{q_3}\Delta^\dagger_{q_1-q_2+q_3} + \cdots \quad \text{(A.7)}
$$

Given our interest in how fluctuations affect the critical temperature of the system, our task is now to compute $\Gamma^{-1}(q)$ and $b(q_1,q_2,q_3)$ explicitly by evaluating Eq. (A.3)-(A.6) and determine how these quantities are modified from their mean field values in which $q_i = 0$. Since we are focusing on the phase boundaries of the system where $\Delta \to 0$, we treat the gap Δ, as well as the Matsubara and momentum coordinates $(q_n, \mathbf{q})$, as an expansion parameter, and in keeping with Eq. (A.7) we truncate our expansion at fourth order.

In order to assess the lowest-order corrections to the mean field action in Eq. (A.4) we must evaluate the bosonic propagator, $\Gamma^{-1}(q)$, to second order in the momentum coordinates and first order in frequency:

$$
\Gamma^{-1}(\omega,\mathbf{q}) = a + d\omega + c_i\frac{q_i^2}{2m} + \cdots, \quad \text{(A.8)}
$$

where the sum over $i = x, y, z$ is implied and we have analytically continued $\Gamma^{-1}(q_n,\mathbf{q})$ to real frequencies, as discussed in A.4. For the quartic term in Eq. (A.7), since Δ is itself an expansion parameter and we truncate at fourth order, we can set $q_1 = q_2 = q_3 = q_4 = 0$ so that $b(q_1,q_2,q_3) \sim b(0,0,0) \equiv b$ is unchanged from its mean field value at our level of approximation. In what follows, we no longer consider the term $\Omega^{(0)}_{\text{eff}}$, as it provides only an overall shift in the thermodynamic potential and is irrelevant to determining the phase boundaries of the system.

A.3 Calculation of $\Gamma^{-1}(q)$

In this section we will evaluate the quadratic portion of the thermodynamic potential, $\Omega^{(2)}[\Delta]$, from which we will extract the bosonic propagator $\Gamma^{-1}(q)$. To simplify this computation we begin by writing $\mathbf{G}_0^{-1}[0]$ and $\mathbf{G}_F^{-1}[\Delta]$ in the block matrix form:

$$\mathbf{G}^{-1}[0](k,k') = \begin{pmatrix} \mathbf{A}^{-1}(k) & \mathbf{0} \\ \mathbf{0} & -\mathbf{A}^{-1}(-k)^T \end{pmatrix} \delta_{kk'}, \quad \mathbf{G}_F^{-1}[\Delta](k,k') = \begin{pmatrix} \mathbf{0} & \mathbf{C}\Delta(k-k') \\ -\mathbf{C}\Delta^\dagger(k'-k) & \mathbf{0} \end{pmatrix}, \tag{A.9}$$

where we define the 2×2 blocks

$$\mathbf{A}^{-1}(k) = \begin{pmatrix} i\omega_n + \tilde{\xi}_{\mathbf{k}\uparrow} & -h_\perp(\mathbf{k}) \\ -h_\perp^*(\mathbf{k}) & i\omega_n + \tilde{\xi}_{\mathbf{k}\downarrow} \end{pmatrix}, \qquad \mathbf{C} = \begin{pmatrix} 0 & -1 \\ 1 & 0 \end{pmatrix}. \tag{A.10}$$

Thus, the ungapped mean field propagator may be written as

$$\mathbf{G}_0[0](k,k') = \begin{pmatrix} \mathbf{A}(k) & \mathbf{0} \\ \mathbf{0} & -\mathbf{A}(-k)^T \end{pmatrix} \delta_{kk'}, \tag{A.11}$$

where direct computation yields

$$\mathbf{A}(k) = a(k) \begin{pmatrix} i\omega_n + \tilde{\xi}_{\mathbf{k}\downarrow} & h_\perp(\mathbf{k}) \\ h_\perp^*(\mathbf{k}) & i\omega_n + \tilde{\xi}_{\mathbf{k}\uparrow} \end{pmatrix}, \tag{A.12}$$

and where we define $a(k) = \det[\mathbf{A}(k)]$, with the determinant taken over the Nambu-Gor'kov and spin indices. Given these definitions, computing the product $\mathbf{G}[0]\delta\mathbf{G}^{-1}[\Delta]$ yields

$$\begin{aligned} \left(\mathbf{G}_0[0]\mathbf{G}_F^{-1}[\Delta]\right)(k,k'') &= \sum_{k'} \begin{pmatrix} \mathbf{A}(k) & \mathbf{0} \\ \mathbf{0} & -\mathbf{A}(-k)^T \end{pmatrix} \delta_{kk'} \begin{pmatrix} \mathbf{0} & \mathbf{C}\Delta(k'-k'') \\ -\mathbf{C}\Delta^\dagger(k''-k') & \mathbf{0} \end{pmatrix}, \\ &= \begin{pmatrix} \mathbf{0} & \mathbf{A}(k)\mathbf{C}\Delta(k-k'') \\ \mathbf{A}(-k)^T\mathbf{C}\Delta^\dagger(k''-k) & \mathbf{0} \end{pmatrix}. \end{aligned} \tag{A.13}$$

Squaring this matrix and taking the trace, as appears in $\Omega^{(2)}[\Delta]$, we obtain

$$\mathrm{tr}\left(\mathbf{G}_0[0]\mathbf{G}_F^{-1}[\Delta]\right)^2 = \sum_{kk''} \mathrm{tr}\Big[\mathbf{A}(k)\mathbf{C}\mathbf{A}(-k'')^T\mathbf{C}|\Delta(k-k'')|^2 + \mathbf{A}(-k)^T\mathbf{C}\mathbf{A}(k'')\mathbf{C}|\Delta(k''-k)|^2\Big]. \tag{A.14}$$

Rewriting the second term by taking $k \leftrightarrow k''$ and using the cyclicity of the trace shows that it is identical to the first term. Thus, shifting the sum over k'' by defining $q = k - k''$, we obtain

$$\mathrm{tr}\left(\mathbf{G}_0[0]\mathbf{G}_F^{-1}[\Delta]\right)^2 = 2\sum_q |\Delta(q)|^2 \sum_k \mathrm{tr}\Big[\mathbf{A}(k)\mathbf{C}\mathbf{A}(q-k)^T\mathbf{C}\Big]. \tag{A.15}$$

Inserting this expression into Eq. (A.5) and comparing with Eq. (A.7), we find that we can write the bosonic propagator in the form

$$\Gamma^{-1}(q) = -\frac{1}{g} + \frac{T}{2V}\sum_k \mathrm{tr}\Big[\mathbf{A}(k)\mathbf{C}\mathbf{A}(q-k)^T\mathbf{C}\Big]. \tag{A.16}$$

In order to evaluate the trace in Eq. (A.16) we next obtain the diagonal elements of the product $\mathbf{A}(k)\mathbf{C}\mathbf{A}(q-k)^T\mathbf{C}$:

$$\left[\frac{\mathbf{A}(k)\mathbf{C}\mathbf{A}(q-k)^T\mathbf{C}}{a(k)a(q-k)}\right]_{11} = \left(i\omega_n + \tilde{\xi}_{\mathbf{k}\downarrow}\right)\left(i\omega_n - iq_n - \tilde{\xi}_{\mathbf{k}-\mathbf{q},\uparrow}\right) - h_\perp^*(\mathbf{k}-\mathbf{q})h_\perp(\mathbf{k}), \tag{A.17}$$

$$\left[\frac{\mathbf{A}(k)\mathbf{C}\mathbf{A}(q-k)^T\mathbf{C}}{a(k)a(q-k)}\right]_{22} = \left(i\omega_n + \tilde{\xi}_{\mathbf{k}\uparrow}\right)\left(i\omega_n - iq_n - \tilde{\xi}_{\mathbf{k}-\mathbf{q},\downarrow}\right) - h_\perp^*(\mathbf{k})h_\perp(\mathbf{k}-\mathbf{q}). \tag{A.18}$$

Substituting these expressions into Eq. (A.16) gives

$$\begin{aligned}\Gamma^{-1}(q) = -\frac{1}{g} + \frac{T}{2V}\sum_k a(k)a(q-k)\Big[&\left(i\omega_n + \tilde{\xi}_{\mathbf{k}\uparrow}\right)\left(i\omega_n - iq_n - \tilde{\xi}_{\mathbf{k}-\mathbf{q},\downarrow}\right) \\ &+ \left(i\omega_n + \tilde{\xi}_{\mathbf{k}\downarrow}\right)\left(i\omega_n - iq_n - \tilde{\xi}_{\mathbf{k}-\mathbf{q},\uparrow}\right) - h_\perp^*(\mathbf{k})h_\perp(\mathbf{k}-\mathbf{q}) - h_\perp^*(\mathbf{k}-\mathbf{q})h_\perp(\mathbf{k})\Big].\end{aligned} \tag{A.19}$$

In order to proceed, we must now evaluate the Matsubara sum over each of the terms above. The explicit calculation is given in Appendix G, the result of which can be written in the form

$$\Gamma^{-1}(q) = -\frac{1}{g} - \frac{1}{2V}\sum_{\mathbf{k}}\Big[W_{12} + W_{21} + g(k,q)\left(W_{11} - W_{12} - W_{21} + W_{22}\right)\Big], \tag{A.20}$$

where $g(k,q) = u_k^2 v_{k-q}^2 + u_{k-q}^2 v_k^2 + 2u_k v_k u_{k-q} v_{k-q}\cos(\theta_k - \theta_{k-q})$ is a function of the quasiparticle amplitudes

$$u_k^2 = \frac{1}{2}\left(1 - \frac{\tilde{\xi}_{\mathbf{k}-}(\mathbf{k})}{\sqrt{Y_-(\mathbf{k})}}\right), \qquad v_k^2 = \frac{1}{2}\left(1 + \frac{\tilde{\xi}_{\mathbf{k}-}(\mathbf{k})}{\sqrt{Y_-(\mathbf{k})}}\right), \tag{A.21}$$

as well as the spin orbit phase angle, defined via the relation $h_\perp(\mathbf{k}) = |h_\perp(\mathbf{k})|e^{i\theta_k}$, and the quantities

$$W_{ij} = \frac{1 - f(E_i(\mathbf{k})) - f(E_j(\mathbf{k}-\mathbf{q}))}{iq_n + E_i(\mathbf{k}) + E_j(\mathbf{k}-\mathbf{q})}, \tag{A.22}$$

where $E_{1,2}$ are evaluated at $\Delta_0 = 0$, and $f(E)$ is the Fermi distribution function. It is straightforward to verify that by setting $q = 0$ in Eq. (A.20) and expressing the coupling g in terms of the s-wave scattering length, one recovers the mean field Ginzburg-Landau coefficient $a(\mu, T)$ given in Eq. (6.66). Thus, having obtained a general expression for the bosonic propagator, we now proceed to perform a lowest-order frequency expansion of $\Gamma^{-1}(\omega, \mathbf{q})$.

In the calculations that follow we again specialize to the situation of mass-balanced systems ($m_\uparrow = m_\downarrow$) in chemical equilibrium ($\mu_\uparrow = \mu_\downarrow$). We will therefore drop the pseudospin indices from $\xi_{\mathbf{k}\sigma}$, and also write $\tilde{\xi}_{\mathbf{k}+} = \xi_{\mathbf{k}}$ and $\tilde{\xi}_{\mathbf{k}-} = -h_z$. This further implies $Y_- = h_z^2 + |h_\perp|^2 \equiv h^2$. Finally, since we are interested in the superfluid-normal phase boundary throughout this chapter, all quantities are understood to be evaluated at $\Delta_0 = 0$ so that $Y_+ = \xi_{\mathbf{k}}^2$ and $E_{1,2} = \xi_{\mathbf{k}} \pm h$.

A.4 Expansion of $\Gamma^{-1}(\omega, \mathbf{0})$

In order to investigate the frequency behavior of the system, we begin by analytically continuing $\Gamma^{-1}(q_n, \mathbf{0})$ to real frequency by taking $iq_n \to \omega + i\epsilon$, where $\epsilon \to 0^+$. The frequency ω appears only in the W_{ij} terms of Eq. (A.20), which can be written in the form

$$W_{ij} = \frac{X_i + X_j}{2}\left[\mathcal{P}\left(\frac{1}{\omega + E_i + E_j}\right) - i\pi\delta(\omega + E_i + E_j)\right], \tag{A.23}$$

where $\mathcal{P}$ denotes the principal value. Thus, setting $\mathbf{q} = \mathbf{0}$ and defining $Q(\omega) = \Gamma^{-1}(\omega, \mathbf{0}) - \Gamma^{-1}(0)$ we obtain $Q(\omega) = Q_R(\omega) + iQ_I(\omega)$, where the real and imaginary parts of $Q(\omega)$ are

$$\begin{aligned} Q_R(\omega) &= \frac{1}{2V}\sum_{\mathbf{k}}\Bigg\{(X_1 + X_2)\mathcal{P}\left(\frac{\omega}{2\xi_{\mathbf{k}}(\omega + 2\xi_{\mathbf{k}})}\right) + \frac{|h_\perp|^2}{h^2}\Bigg[X_1\mathcal{P}\left(\frac{\omega}{2E_1(\omega + 2E_1)}\right) \\ &\qquad + X_2\mathcal{P}\left(\frac{\omega}{2E_2(\omega + 2E_1)}\right) - (X_1 + X_2)\mathcal{P}\left(\frac{\omega}{2\xi_{\mathbf{k}}(\omega + 2\xi_{\mathbf{k}})}\right)\Bigg]\Bigg\}, \end{aligned} \tag{A.24}$$

$$\begin{aligned} Q_I(\omega) &= \frac{\pi}{2V}\sum_{\mathbf{k}}\Bigg\{(X_1 + X_2)\delta(\omega + 2\xi_{\mathbf{k}}) \\ &\qquad + \frac{|h_\perp|^2}{h^2}\Big[X_1\delta(\omega + 2E_1) + X_2\delta(\omega + 2E_2) - (X_1 + X_2)\delta(\omega + 2\xi_{\mathbf{k}})\Big]\Bigg\}. \end{aligned} \tag{A.25}$$

Having obtained $Q(\omega)$, we are in a position to analyze the low frequency fluctuations of the system by expanding to first order in ω. Writing the expansion in the form $Q(\omega) = d\omega + \cdots$, we obtain $d = d_R + id_I$ where

$$d_R(\mu, T) = \frac{1}{2V}\mathcal{P}\sum_{\mathbf{k}}\left[\left(1 + \frac{h_z^2}{\xi_{\mathbf{k}}^2}\right)\left(\frac{X_1}{4E_1^2} + \frac{X_2}{4E_2^2}\right) + \frac{2h_z^2}{\xi_{\mathbf{k}}h}\left(\frac{X_1}{4E_1^2} - \frac{X_2}{4E_2^2}\right)\right], \tag{A.26}$$

$$d_I(\mu,T) = \frac{\pi}{2}\sum_{\mathbf{k}}\left\{(X_1+X_2)\delta'(2\xi_{\mathbf{k}}) + \frac{|h_\perp|^2}{h^2}\left[X_1\delta'(2E_1)+X_2\delta'(2E_2)-(X_1+X_2)\delta'(2\xi_{\mathbf{k}})\right]\right\}, \quad \text{(A.27)}$$

where terms involving $\delta'(x) = d\delta(x)/dx$ are understood to be evaluated by integrating the associated terms by parts. As we will see in section A.6, the imaginary part of $d(\mu,T)$ determines the lifetime of the bosonic molecules while the real part plays a role in determining the Bose gas' properties in the BEC limit. Regarding the lifetime of the molecules, we note that for $1/k_F a_s \to \infty$, as $\mu \sim -E_b/2 \to -\infty$, the arguments of the δ'-functions in Eq. (A.27) are always positive so that $d_I = 0$ and the molecules' lifetime becomes $\tau_B \propto 1/d_I \to \infty$. Thus, as expected on physical grounds, for large enough $1/k_F a_s$ the system becomes a dilute gas of stable bosonic molecules.

A.5 Expansion of $\Gamma^{-1}(0,\mathbf{q})$

We now wish to assess the stability of the system to spatial inhomogeneities by expanding $\Gamma^{-1}(0,\mathbf{q})$ to second order in $\mathbf{q}$. This expansion is more tedious than the expansion in ω, as we must expand both the quasiparticle function $g(k,q)$ of Eq. (A.20) as well as the W_{ij}. Our first step is then to obtain the expansions of the quasiparticle amplitudes u_{k-q} and v_{k-q}, as well as the spin-orbit phase angle θ_{k-q}. A straightforward, though cumbersome, Taylor expansion yields

$$u_{k-q} \sim u_k + \frac{h_z}{4u_k h^3}A - \frac{h_z}{32u_k^3h^6}\left[4u_k^2h^3B + \left(h_z - 12u_k^2h^2\right)A^2\right], \quad \text{(A.28)}$$

$$v_{k-q} \sim v_k - \frac{h_z}{4v_k h^3}A + \frac{h_z}{32v_k^3h^6}\left[4v_k^2h^3B - \left(h_z + 12v_k^2\sqrt{Y_-}\right)A^2\right], \quad \text{(A.29)}$$

$$\theta_{k-q} \sim \theta_k + \frac{1}{|h_\perp|^2}C + \frac{1}{|h_\perp|^4}AC, \quad \text{(A.30)}$$

where we define the quantities

$$A = \frac{\kappa^2}{m^2}\left(k_xq_x + \eta^2k_yq_y\right), \qquad B = \frac{\kappa^2}{m^2}\left(q_x^2 + \eta^2q_y^2\right), \qquad C = \frac{\eta\kappa^2}{m^2}\left(k_xq_y - k_yq_x\right). \quad \text{(A.31)}$$

Using these expressions, the second order expansion of the function $g(k,q)$ becomes

$$g(k,q) \sim \frac{|h_\perp|^2}{h^2} - \frac{h_z^2}{h^4}A + \frac{h_z^2}{2h^6}\left[h^2B - \left(3 + \frac{h^2}{2|h_\perp|^2}\right)A^2\right] - \frac{1}{4h^2|h_\perp|^2}C^2. \quad \text{(A.32)}$$

Next, we must obtain expansions for the W_{ij}. We begin by obtaining the second order expansions of the eigenvalues $E_{1,2}(\mathbf{k}-\mathbf{q}) \sim E_{1,2}(\mathbf{k}) - D_\pm + E_\pm$, where we define the quantities

$$D_\pm = \frac{\mathbf{k}\cdot\mathbf{q}}{m} \pm \frac{A}{h} \qquad\qquad E_\pm = \frac{\mathbf{q}^2}{2m} \pm \frac{B}{2h} \mp \frac{A^2}{2h^3}. \tag{A.33}$$

From these expressions we can obtain the expansions of the Fermi distribution functions:

$$f(E_1(\mathbf{k}-\mathbf{q})) \sim f(E_1(\mathbf{k})) + \frac{\beta Y_1(D_+ - E_+)}{4} + \frac{\beta^2 X_1 Y_1 D_+^2}{8}, \tag{A.34}$$

$$f(E_2(\mathbf{k}-\mathbf{q})) \sim f(E_2(\mathbf{k})) + \frac{\beta Y_2(D_- - E_-)}{4} + \frac{\beta^2 X_1 Y_1 D_-^2}{8}, \tag{A.35}$$

Having obtained expressions for the eigenvalues and the Fermi distributions, we can now write down expansions for the W_{ij}:

$$W_{11} = \frac{X_1}{2E_1} + \frac{Z_{11}}{4E_1^2}(D_+ - E_+) + \frac{U_{11}}{8E_1^3} D_+^2, \tag{A.36}$$

$$W_{12} = \frac{X_1 + X_2}{4\xi_{\mathbf{k}}} + \frac{Z_{12} + Z_{22}}{8\xi_{\mathbf{k}}^2}(D_- - E_-) + \frac{U_{12} + U_{22}}{16\xi_{\mathbf{k}}^3} D_-^2, \tag{A.37}$$

$$W_{21} = \frac{X_1 + X_2}{4\xi_{\mathbf{k}}} + \frac{Z_{11} + Z_{21}}{8\xi_{\mathbf{k}}^2}(D_+ - E_+) + \frac{U_{11} + U_{21}}{16\xi_{\mathbf{k}}^3} D_+^2, \tag{A.38}$$

$$W_{22} = \frac{X_2}{2E_2} + \frac{Z_{22}}{4E_2^2}(D_- - E_-) + \frac{U_{22}}{8E_2^3} D_-^2, \tag{A.39}$$

where we introduce the quantities $U_{ij} = Z_{ij} - \beta^2(E_i + E_j)^2 X_j Y_j/8$. Finally, we are now in a position to obtain a second order expansion for the full bosonic propagator $\Gamma^{-1}(0,\mathbf{q})$. Substituting our expansions into Eq. (A.20) we can write the propagator in the form Eq. (A.8) with a given in Eq. (6.66) and the c_i:

$$\begin{aligned} c_x(\mu,T) = c_z + \frac{\kappa^2}{2mV}\sum_{\mathbf{k}} \Bigg\{ &\frac{1}{8h}\left(1 - \frac{k_x^2}{k_\eta^2}\right)\tilde{Z}_- - \frac{k_x^2}{8k_\eta^2}\tilde{U}_+ - \frac{k_x^2}{4\kappa k_\eta}\tilde{U}_- + \frac{4h_z^2}{h^2}\tilde{Z}_+ \\ &- \left[\frac{2h_z^2}{h^4}\left(1 - \left(3 + \frac{h^2}{2|h_\perp|^2}\right)\frac{k_x^2}{k_\eta^2}\right) - \frac{\eta^2 k_y^2}{|h_\perp|^2 k_\eta^2}\right] X_+ \Bigg\}, \end{aligned} \tag{A.40}$$

$$\begin{aligned} c_y(\mu,T) = c_z + \frac{\eta^2\kappa^2}{2mV}\sum_{\mathbf{k}} \Bigg\{ &\frac{1}{8h}\left(1 - \frac{\eta^2 k_y^2}{k_\eta^2}\right)\tilde{Z}_- - \frac{\eta^2 k_y^2}{8k_\eta^2}\tilde{U}_+ - \frac{k_y^2}{4\kappa k_\eta}\tilde{U}_- + \frac{4h_z^2}{h^2}\tilde{Z}_+ \\ &- \left[\frac{2h_z^2}{h^4}\left(1 - \left(3 + \frac{h^2}{2|h_\perp|^2}\right)\frac{\eta^2 k_y^2}{k_\eta^2}\right) - \frac{\eta^2 k_x^2}{|h_\perp|^2 k_\eta^2}\right] X_+ \Bigg\}, \end{aligned} \tag{A.41}$$

$$c_z(\mu,T) = \frac{1}{V}\sum_{\mathbf{k}} \left\{ \frac{\zeta_+}{16\xi_{\mathbf{k}}^2} - \frac{\tilde{v}_+}{16m\xi_{\mathbf{k}}^3} k_z^2 + \frac{|h_\perp|^2}{h^2}\left(Z_+ - U_+\frac{k_z^2}{m}\right) \right\}, \tag{A.42}$$

where we define the quantities $k_\eta = mh/\kappa$, $\zeta_\pm = Z_{11} + Z_{22} \pm (Z_{12} + Z_{21})$, and $\upsilon_\pm = (U_{11} + U_{22}) \pm (U_{12} + U_{21})$, as well as

$$X_+ = \frac{X_1}{4E_1} + \frac{X_2}{4E_2} - \frac{X_1 + X_2}{4\xi_{\mathbf{k}}}, \qquad Z_\pm = \frac{Z_{11}}{8E_1^2} + \frac{Z_{22}}{8E_2^2} - \frac{\zeta_\pm}{16\xi_{\mathbf{k}}^2}, \qquad U_\pm = \frac{U_{11}}{8E_1^3} + \frac{U_{22}}{8E_2^3} - \frac{\tilde{\upsilon}_\pm}{16\xi_{\mathbf{k}}^3}, \tag{A.43}$$

$$\tilde{Z}_+ = Z_+ + \frac{\kappa}{k_\eta} Z_-, \qquad \tilde{Z}_- = \frac{\zeta_-}{\xi_{\mathbf{k}}^2} + \frac{16|h_\perp|^2}{h^2} Z_-, \qquad \tilde{U}_\pm = \frac{\upsilon_\pm}{\xi_{\mathbf{k}}^3} + \frac{16|h_\perp|^2}{h^2} U_\pm. \tag{A.44}$$

Having obtained all of the LG coefficients to quartic order in Δ, we are now in a position to analyze the full time dependent GL thermodynamic potential. Thus, in the next section we first discuss the general structure of the time dependent Ginzburg Landau (TDGL) equation and then proceed to consider specifically the BEC limit.

A.6 Time-Dependent Ginzburg-Landau Functional

Returning to Eq. (A.3) with the expansions of the prior sections in hand, we are now in a position to derive the time-dependent Ginzburg-Landau (TDGL) functional. Substituting the expansion Eq. (A.8) into Eq. (A.7) and neglecting the overall constant $\Omega_0[0]$ gives the momentum-space functional

$$F[\Delta] = \sum_q \left(a + c_i \frac{q_i^2}{2m} + d\omega \right) |\Delta(q)|^2 + \frac{1}{2} \sum_{q_1, q_2, q_3} b(q_1, q_2, q_3) \Delta_{q_1} \Delta_{q_2}^\dagger \Delta_{q_3} \Delta_{q_1 - q_2 + q_3}^\dagger. \tag{A.45}$$

We now transform to real spacetime by rewriting $\Delta_q^\dagger = \sum_{q'} \Delta_{q'}^\dagger \delta_{qq'}$ in the quadratic term, while also assuming that $b(q_1, q_2, q_3) \equiv b$ is independent of momentum, so that we obtain:

$$\begin{aligned}
F[\Delta] &= \sum_{q,q'} \left(a + c_i \frac{q_i^2}{2m} + d\omega \right) \Delta_{q'}^\dagger \Delta_q \delta_{qq'} + \frac{1}{2} b |\Delta_0|^4, \\
&= \sum_{q,q'} \left(a + c_i \frac{q_i^2}{2m} + d\omega \right) \Delta_{q'}^\dagger \Delta_q \int \frac{dt}{\beta} \frac{d^3\mathbf{r}}{V} e^{i(q-q')\cdot r} + \frac{b}{2} \int \frac{dt}{\beta} \frac{d^3\mathbf{r}}{V} |\Delta(r)|^4, \\
&= \int \frac{dt}{\beta} \frac{d^3\mathbf{r}}{V} \sum_{q,q'} e^{-iq'\cdot r} \Delta_{q'}^\dagger \Delta_q \left(a - \frac{c_i}{2m} \nabla_i^2 - id\frac{\partial}{\partial t} \right) e^{iq\cdot r} + \frac{b}{2} \int \frac{dt}{\beta} \frac{d^3\mathbf{r}}{V} |\Delta(r)|^4, \\
&= \int \frac{dt}{\beta} \frac{d^3\mathbf{r}}{V} \left[\sum_{q'} e^{-iq'\cdot r} \Delta_{q'}^\dagger \right] \left(a - \frac{c_i}{2m} \nabla_i^2 - id\frac{\partial}{\partial t} \right) \left[\sum_q e^{iq\cdot r} \Delta_q \right] + \frac{b}{2} \int \frac{dt}{\beta} \frac{d^3\mathbf{r}}{V} |\Delta(r)|^4, \\
&= \int \frac{dt}{\beta} \frac{d^3\mathbf{r}}{V} \Delta^\dagger(r) \left(a - \frac{c_i}{2m} \nabla_i^2 - id\frac{\partial}{\partial t} \right) \Delta(r) + \frac{b}{2} \int \frac{dt}{\beta} \frac{d^3\mathbf{r}}{V} |\Delta(r)|^4.
\end{aligned} \tag{A.46}$$

Integrating the Laplacian term by parts yields the standard form

$$F[\Delta] = \int \frac{dt}{\beta} \frac{d^3\mathbf{r}}{V} \left(a|\Delta(r)|^2 + \frac{c_i}{2m} |\nabla_i \Delta(r)|^2 + \frac{b}{2} |\Delta(r)|^4 - id\Delta^\dagger(r) \frac{\partial}{\partial t} \Delta(r) \right). \tag{A.47}$$

This functional, which describes the low energy excitations of the system, depends on μ and T through the GL coefficients. By setting $\delta G/\delta\Delta = 0$ we obtain the equation of motion for these excitations:

$$\left(a + b|\Delta(r)|^2 - \frac{c_i}{2m}\nabla_i^2 - id\frac{\partial}{\partial t}\right)\Delta(r) = 0. \tag{A.48}$$

We note that for a static homogeneous solution this equation reduces to the familiar mean field expression $|\Delta_0| = \sqrt{-a/b}$, so that the condition for pairing is $a(\mu, T) < 0$.

A.7 BEC Limit

Having obtained the equation of motion for the low energy excitations of the system, we now consider the BEC limit in which the ground state above which these excitations exist is a dilute gas of composite bosons. In particular, by computing the effective bosonic properties of the system one can infer the critical temperature for the superfluid transition in the limit $1/k_F a_s \to \infty$.

In the BEC limit we define the bosonic "wavefunction" $\Psi = \sqrt{d}\Delta$. Substituting into Eq. (A.48) yields the equation of motion

$$\left(\frac{a}{d} + \frac{b}{d^2}|\Psi(r)|^2 - \frac{c_i}{2md}\nabla_i^2 - i\frac{\partial}{\partial t}\right)\Psi(r) = 0. \tag{A.49}$$

This equation is precisely of the form of the Gross-Pitaevski equation for a dilute Bose gas. The standard form of this equation, which describes a gas of bosons with mass m_B, chemical potential μ_B, and s-wave contact interaction strength $U = 4\pi a_B/m_B$, is

$$\left(-\mu_B + U|\Psi(r)|^2 - \frac{1}{2m_B}\nabla^2 - i\frac{\partial}{\partial t}\right)\Psi(r) = 0. \tag{A.50}$$

By equating coefficients of Eqs. (A.49) and (A.50) we find the effective bosonic parameters

$$\mu_B = -\frac{a}{d}, \qquad U = \frac{b}{d^2}, \qquad m_{B,i} = \left(\frac{d}{c_i}\right)m, \tag{A.51}$$

where we note that the anisotropy of the spin-orbit field induces different effective masses for the three spatial coordinates.

Having cast the equation of motion in BEC limit in the form of an interacting Bose gas, it is possible to compute the superfluid transition temperature by applying the results of [154]. In this earlier study no spin-orbit effects were considered, but having absorbed the spin-orbit effects into the GL coefficients, it is straightforward to make the necessary correspondences required to compute the spin-orbit-dependent

transition temperature in the BEC limit. This calculation will be the subject of a future publication.

Appendix B

Gauge Fields at Finite Temperature

In this appendix we discuss the replacements required to treat gauge fields in the standard finite temperature path integral formalism. This analysis is based largely on the very helpful work [155]. In particular, we will find that it is necessary to make the replacement $x_0 \to ix_0$ for *all* 4-vectors in the theory. In the NJL model this affects only the position 4-vector, $x_\mu = (t, \mathbf{r})$, and results in the usual replacement $t \to it$. However, in the PNJL model, having introduced the 4-vector gauge field $A_\mu = (A_0, \mathbf{0})$, we must also take $A_0 \to iA_0$. The need for this replacement can be observed most easily by considering the electromagnetic field at finite temperature.

In order to treat the electromagnetic field at finite temperature we wish to transform the path integral into the partition function by making the replacement $t = -i\beta$, where $\beta = 1/T$ is the inverse temperature:

$$\mathcal{Z} = \int [DA_\mu]\, e^{i\int_0^t dt' \int d^3\mathbf{x}\, \mathcal{L}_{EM}} \qquad \Longrightarrow \qquad \mathcal{Z} = \int [DA_\mu]\, e^{-\int_0^\beta d\tau \int d^3\mathbf{x}\, \mathcal{H}_{EM}}, \tag{B.1}$$

where $\mathcal{L}_{EM} = \frac{1}{2}(\mathcal{E}^2 - \mathcal{B}^2)$ and $\mathcal{B}_{EM} = \frac{1}{2}(\mathcal{E}^2 + \mathcal{B}^2)$ are the electromagnetic field Lagrangian and Hamiltonian densities respectively. Thus, in addition to the replacement $t \to -i\beta$, we must make an additional replacement(s) such that $\mathcal{L}_{EM} \to -\mathcal{H}_{EM}$. Clearly, the simplest manner in which this can be achieved is by ensuring $\mathcal{E} \to i\mathcal{E}$ and $\mathcal{B} \to \mathcal{B}$.

In order to determine the necessary finite temperature replacements of the gauge field components, we recall that the electric and magnetic field densities are given in terms of the gauge fields by

$$\mathcal{E} = -\nabla A_0 - \frac{\partial \mathbf{A}}{\partial t} \qquad\qquad \mathcal{B} = \nabla \times \mathbf{A}. \tag{B.2}$$

While the change of variable $t = i\tau$ in the time integral of Eq. (B.1) produces the necessary factor of i in the second term of $\mathcal{E}$, we must introduce this factor into the first term by hand. Thus, we find that the required finite temperature gauge field replacement is $(A_0, \mathbf{A}) \to (iA_0, \mathbf{A})$[1].

[1] We note that while many authors use this convention, a significant portion of the literature does not explicitly introduce the factor of i, but rather takes the field A_0 to be *anti*-Hermitian, effectively absorbing the i into a redefinition of the field. While physically equivalent, this discrepancy does lead to slightly different expressions in the literature. For the sake of clarity we will always write the factor of i explicitly and A_0 will correspondingly remain a Hermitian field.

Appendix C

Evaluation of Matsubara Sums

In this appendix we evaluate a fermionic Matsubara sum which appears frequently in the study of finite temperature field theories, namely

$$S = \sum_n \ln[\beta(i\omega_n + E)], \tag{C.1}$$

where $\omega_n = (2n+1)\pi T$ are the fermionic Matsubara frequencies, $\beta = 1/T$ is the inverse temperature, and E is a constant.

The common feature in evaluating Matsubara sums is to convert the sum into a contour integral by identifying the summand with the residues of a complex function. Having done so, we may then exchange the sum for an integral by means of Cauchy's residue theorem:

$$\oint_{\mathcal{C}} dz\, g(z) = 2\pi i \sum_n \operatorname*{res}_{z=z_n} g(z), \tag{C.2}$$

where $\{z_n\}$ are the poles of $g(z)$, and $\mathcal{C}$ is a contour enclosing the given poles. Our first step, then, is to identify a function $g(z)$ whose poles are the fermionic Matsubara frequencies $i\omega_n$ (or more precisely, $i\beta\omega_n$, since the argument of the complex function must be dimensionless) and whose residues are the terms appearing in Eq. (C.1). While there are any number of such functions, it is straightforward to verify that one such function with the correct poles is simply the analytical continuation of the Fermi distribution function

$$f(z) = \frac{1}{e^z + 1}. \tag{C.3}$$

While $f(z)$ has the correct poles, it does not have the desired residues. In fact, expanding $f(z)$ about an

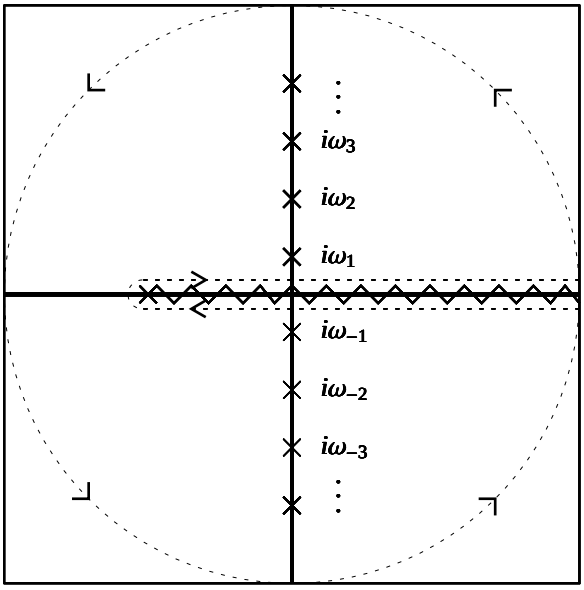

Figure C.1: Contour for the evaluation of the Matsubara sum Eq. (C.1).

arbitrary pole $z_n = \omega_n$, we obtain

$$\begin{aligned} f(z) &= \frac{1}{e^{z_n} e^{(z-z_n)} + 1}, \\ &= \frac{1}{1 - e^{(z-z_n)}}, \qquad\qquad (e^{-z_n} = -1) \\ &= \frac{1}{1 - [1 + (z - z_n) + \cdots]}, \\ &= -\frac{1}{z - z_n} + \cdots \end{aligned} \tag{C.4}$$

Thus, we can simply read off

$$\operatorname*{res}_{z=z_n} f(z) = -1. \tag{C.5}$$

In order to obtain a function $g(z)$ with the desired residues, we must therefore multiply $f(z)$ by the function $h(z) = -\ln(z + \beta E)$. Thus, defining $g(z) = f(z)h(z)$, we can rewrite Eq. (C.1) as

$$S = \frac{1}{2\pi i} \oint_{\mathcal{C}} dz\, g(z), \tag{C.6}$$

where $\mathcal{C}$ is any contour enclosing the poles of $f(z)$, which lie along the imaginary z axis.

Choosing the contour $\mathcal{C}$ as shown in Fig. (C.1), where we have introduced a branch cut from $z = -\beta E$ to $z = \infty$, we note that the contribution to the integral for $|z| \to \infty$ with $\mathrm{Re}(z) > 0$ is exponentially suppressed

by the function $f(z)$. However, the contribution from $|z| \to \infty$ with $\mathrm{Re}(z) < 0$ is divergent. In order to remedy this problem, we introduce a small (positive) number η and rewrite (C.6) as

$$S = -\lim_{\eta \to 0} \frac{1}{2\pi i} \oint_{\mathcal{C}} dz\, f(z) \ln(z + \beta E) e^{\eta z}. \tag{C.7}$$

Having accounted for the portions of $\mathcal{C}$ at infinity, the only non-zero contribution to S comes from the segments along the real axis. Taking $z = x \pm i\epsilon$ along these segments, we obtain

$$\begin{aligned} S &= -\lim_{\eta,\epsilon \to 0} \frac{1}{2\pi i} \Bigg\{ \int_{-\beta E}^{\infty} dx\, f(x + i\epsilon) \ln(x + i\epsilon + \beta E) e^{\eta(x+i\epsilon)} \\ &\qquad - \int_{-\beta E}^{\infty} dx\, f(x - i\epsilon) \ln(x - i\epsilon + \beta E) e^{\eta(x-i\epsilon)} \Bigg\}, \\ &= -\lim_{\epsilon \to 0} \frac{1}{2\pi i} \int_{-\beta E}^{\infty} dx\, f(x) \Big[\ln(x + i\epsilon + \beta E) - \ln(x - i\epsilon + \beta E) \Big], \end{aligned} \tag{C.8}$$

Next, we evaluate the term in brackets by using polar coordinates to write

$$\begin{aligned} \ln(a + i\epsilon) &= \ln(\sqrt{a^2 + \epsilon^2} e^{i\theta}) \qquad\qquad (\theta = \tan^{-1}(\epsilon/a)), \\ &= \ln(\sqrt{a^2 + \epsilon^2}) + i\theta. \end{aligned} \tag{C.9}$$

Due to the branch cut we restrict the values of θ to the interval $[0, 2\pi)$. Thus, the bracketed term in Eq. (C.8) becomes

$$\begin{aligned} \ln(x + i\epsilon + \beta E) - \ln(x - i\epsilon + \beta E) &= \ln \sqrt{(x + \beta E)^2 + \epsilon^2} + i \tan^{-1}\left(\frac{\epsilon}{x + \beta E}\right) \\ &\quad - \ln \sqrt{(x + \beta E)^2 + \epsilon^2} - i \left[2\pi - \tan^{-1}\left(\frac{\epsilon}{x + \beta E}\right) \right], \\ &= -2\pi i + 2 \tan^{-1}\left(\frac{\epsilon}{x + \beta E}\right). \end{aligned} \tag{C.10}$$

Substituting this expression into Eq. (C.8) and taking $\epsilon \to 0$ gives

$$S = \int_{-\beta E}^{\infty} \frac{dx}{e^x + 1} = \ln(1 + e^{\beta E}). \tag{C.11}$$

One final word should be said regarding the Matsubara sum just calculated. An attentive reader may be bothered by our apparently arbitrary introduction of the convergence factor $e^{\eta z}$ in Eq. (C.7), particularly because once we cited its suppression of the portion of the contour for which $Re(z) \to -\infty$, we then set $\eta = 0$ and continued as if it had never existed. Even worse, it is straightforward to show that if we had

instead used the function $F(z) = 1/(e^{-z}+1)$ to pick out the desired poles in Eq. (C.6) and then introduced the convergence factor $e^{-\eta z}$ (a procedure which is equally valid on its face), we would have obtained the result

$$S' = \ln(1 + e^{-\beta E}). \tag{C.12}$$

In other words, the value of the sum depends on the auxiliary function $f(z)$ chosen and the convergence factor it requires. Fortunately, for any physical problem, the physics itself will dictate the proper convergence factor. One is then free to choose any auxiliary function which picks out the correct poles and ensures convergence in the limit not taken care of by the physical convergence factor, and will then obtain the unique physical value for the sum.

Appendix D

Determinants of Block Matrices

In this appendix we derive an expression for the determinant of a block matrix of arbitrary partitioning in terms of its constituent blocks. This material is based on [5].

D.1 General Construction

Let $\mathbf{S}$ be an $(nN) \times (nN)$ complex matrix, which is partitioned into N^2 blocks, each of size $n \times n$, and let $\mathbf{U}$ be a lower triangular auxiliary matrix:

$$\mathbf{S} = \begin{pmatrix} \mathbf{S}_{11} & \mathbf{S}_{12} & \cdots & \mathbf{S}_{1N} \\ \mathbf{S}_{21} & \mathbf{S}_{22} & \cdots & \mathbf{S}_{2N} \\ \vdots & \vdots & \ddots & \vdots \\ \mathbf{S}_{N1} & \mathbf{S}_{N2} & \cdots & \mathbf{S}_{NN} \end{pmatrix} \qquad \mathbf{U} = \begin{pmatrix} \mathbf{I} & \mathbf{0} & \cdots & \mathbf{0} \\ \mathbf{U}_{21} & \mathbf{I} & \cdots & \mathbf{0} \\ \vdots & \vdots & \ddots & \vdots \\ \mathbf{U}_{N1} & \mathbf{U}_{N2} & \cdots & \mathbf{I} \end{pmatrix}. \tag{D.1}$$

Forming the product $\mathbf{SU}$ gives

$$\mathbf{SU} = \begin{pmatrix} \mathbf{S}_{11} + \mathbf{S}_{12}\mathbf{U}_{21} + \cdots \mathbf{S}_{1N}\mathbf{U}_{N1} & \mathbf{S}_{12} + \mathbf{S}_{13}\mathbf{U}_{32} + \cdots \mathbf{S}_{1N}\mathbf{U}_{N2} & \cdots & \mathbf{S}_{1N} \\ \mathbf{S}_{21} + \mathbf{S}_{22}\mathbf{U}_{21} + \cdots \mathbf{S}_{2N}\mathbf{U}_{N1} & \mathbf{S}_{22} + \mathbf{S}_{23}\mathbf{U}_{32} + \cdots \mathbf{S}_{2N}\mathbf{U}_{N2} & \cdots & \mathbf{S}_{2N} \\ \vdots & \vdots & \ddots & \vdots \\ \mathbf{S}_{N1} + \mathbf{S}_{N2}\mathbf{U}_{21} + \cdots \mathbf{S}_{NN}\mathbf{U}_{N1} & \mathbf{S}_{N2} + \mathbf{S}_{N3}\mathbf{U}_{32} + \cdots \mathbf{S}_{NN}\mathbf{U}_{N2} & \cdots & \mathbf{S}_{NN} \end{pmatrix}. \tag{D.2}$$

Now, let us assume that the blocks of $\mathbf{U}$ can be chosen such that the product $\mathbf{SU}$ is upper triangular. In this case, we obtain $(N^2 - N)/2$ constraint equations (the lower triangular blocks of $\mathbf{SU} = \mathbf{0}$) with $(N^2 - N)/2$ unknowns (the blocks of $\mathbf{U}$). The $N - k$ equations arising from the kth column of $\mathbf{SU}$ are

$$\begin{aligned} \mathbf{S}_{k+1,k} + \mathbf{S}_{k+1,k+1}\mathbf{U}_{k+1,k} + \cdots + \mathbf{S}_{k+1,N}\mathbf{U}_{Nk} &= \mathbf{0}, \\ \mathbf{S}_{k+2,k} + \mathbf{S}_{k+2,k+1}\mathbf{U}_{k+1,k} + \cdots + \mathbf{S}_{k+2,N}\mathbf{U}_{Nk} &= \mathbf{0}, \\ &\vdots \\ \mathbf{S}_{N,k} + \mathbf{S}_{N,k+1}\mathbf{U}_{k+1,k} + \cdots + \mathbf{S}_{NN}\mathbf{U}_{Nk} &= \mathbf{0}. \end{aligned} \tag{D.3}$$

In order to simplify our notation, we now define the block vectors

$$\mathbf{s}_{ij} = \begin{pmatrix} \mathbf{S}_{ij} \\ \mathbf{S}_{i+1,j} \\ \vdots \\ \mathbf{S}_{Nj} \end{pmatrix} \qquad \mathbf{u}_{ij} = \begin{pmatrix} \mathbf{U}_{ij} \\ \mathbf{U}_{i+1,j} \\ \cdots \\ \mathbf{U}_{Nj} \end{pmatrix} \qquad \boldsymbol{\sigma}_{ij} = \begin{pmatrix} \mathbf{S}_{ij} \\ \mathbf{S}_{i,j+1} \\ \cdots \\ \mathbf{S}_{iN} \end{pmatrix}. \tag{D.4}$$

We also let $\tilde{\mathbf{S}}_k$ represent the $k \times k$ block matrix formed from the lower-right corner of $\mathbf{S}$,

$$\tilde{\mathbf{S}}_k = \begin{pmatrix} \mathbf{S}_{N-k+1,N-k+1} & \mathbf{S}_{N-k+1,N-k+2} & \cdots & \mathbf{S}_{N-k+1,N} \\ \mathbf{S}_{N-k+2,N-k+1} & \mathbf{S}_{N-k+2,N-k+2} & \cdots & \mathbf{S}_{N-k+2,N} \\ \vdots & \vdots & \ddots & \vdots \\ \mathbf{S}_{N,N-k+1} & \mathbf{S}_{N,N-k+2} & \cdots & \mathbf{S}_{N,N} \end{pmatrix}. \tag{D.5}$$

With these definitions, we can rewrite Eqs. (D.3) in the matrix form:

$$\tilde{\mathbf{S}}_{N-k}\mathbf{u}_{k+1,k} = -\mathbf{s}_{k+1,k}. \tag{D.6}$$

Solving for the auxiliary block vector yields

$$\mathbf{u}_{k+1,k} = -\tilde{\mathbf{S}}_{N-k}^{-1}\mathbf{s}_{k+1,k}. \tag{D.7}$$

We now define $\boldsymbol{\sigma}_{ij}^T$ as the block row vector of $\mathbf{S}$ lying to the right, and inclusive of, the position (i, j) (Eq. (D.4)). Inspecting Eq. (D.2), we can express the kth diagonal element of $\mathbf{SU}$ in the form

$$\begin{aligned} (\mathbf{SU})_{kk} &= \mathbf{S}_{kk} + \boldsymbol{\sigma}_{k,k+1}^T\mathbf{u}_{k+1,k}, \\ &= \mathbf{S}_{kk} - \boldsymbol{\sigma}_{k,k+1}^T\tilde{\mathbf{S}}_{N-k}^{-1}\mathbf{s}_{k+1,k}, \\ &= \tilde{\mathbf{S}}_{N-k+1}/\tilde{\mathbf{S}}_{N-k}, \end{aligned} \tag{D.8}$$

where $\tilde{\mathbf{S}}_{N-k+1}/\tilde{\mathbf{S}}_{N-k}$ denotes the Schür complement of $\tilde{\mathbf{S}}_{N-k+1}$ with respect to $\tilde{\mathbf{S}}_{N-k}$ [156]. Next, defining the matrices

$$\begin{aligned} \boldsymbol{\alpha}_{ij}^{(0)} &= \mathbf{S}_{ij}, \\ \boldsymbol{\alpha}_{ij}^{(k)} &= \mathbf{S}_{ij} - \boldsymbol{\sigma}_{i,N-k+1}^T\tilde{\mathbf{S}}_k^{-1}\mathbf{s}_{N-k+1,j}, \qquad k \geq 1, \end{aligned} \tag{D.9}$$

we can write $(\mathbf{SU})_{kk} = \boldsymbol{\alpha}_{kk}^{(N-k)}$. Since $\mathbf{SU}$ is upper triangular by design, the determinant is simply the product of the determinants of its diagonal blocks. This, together with the fact that $\det(\mathbf{U}) = 1$ gives

$$\det(\mathbf{S}) = \prod_{k=1}^{N} \det(\boldsymbol{\alpha}_{kk}^{(N-k)}). \tag{D.10}$$

In order to express $\det(\mathbf{S})$ in terms of the blocks of $\mathbf{S}$, we must now evaluate $\tilde{\mathbf{S}}_k^{-1}$, which appears in Eq. (D.9). Rather than approaching this problem directly, we will focus on the matrices $\boldsymbol{\alpha}_{ij}^{(k)}$, and seek to find a recursive relationship between matrices of consecutive values of k. Thus, we begin by writing

$$\begin{aligned}
\boldsymbol{\alpha}_{ij}^{(k+1)} &= \mathbf{S}_{ij} - \boldsymbol{\alpha}_{i,N-k}^T \tilde{\mathbf{S}}_{k+1}^{-1} \mathbf{s}_{N-k,j}, \\
&= \mathbf{S}_{ij} - \begin{pmatrix} \boldsymbol{S}_{i,N-k} & \boldsymbol{\sigma}_{i,N-k+1}^T \end{pmatrix} \begin{pmatrix} \boldsymbol{S}_{N-k,N-k} & \boldsymbol{\sigma}_{N-k,N-k+1}^T \\ \boldsymbol{s}_{N-k+1,N-k} & \tilde{\boldsymbol{S}}_k \end{pmatrix}^{-1} \begin{pmatrix} \boldsymbol{S}_{N-k,j} \\ \boldsymbol{s}_{N-k+1,j} \end{pmatrix},
\end{aligned} \tag{D.11}$$

where we have partitioned the block vectors and matrix into sections of block length 1 and N. Next, we evaluate the inverse matrix above by making use of the Banachiewic identity [157, 158]

$$\begin{pmatrix} \mathbf{A} & \mathbf{B} \\ \mathbf{C} & \mathbf{D} \end{pmatrix}^{-1} = \begin{pmatrix} (\mathbf{A} - \mathbf{B}\mathbf{D}^{-1}\mathbf{C})^{-1} & -(\mathbf{A} - \mathbf{B}\mathbf{D}^{-1}\mathbf{C})^{-1}\mathbf{B}\mathbf{D}^{-1} \\ -\mathbf{D}^{-1}\mathbf{C}(\mathbf{A} - \mathbf{B}\mathbf{D}^{-1}\mathbf{C})^{-1} & \mathbf{D}^{-1}\left[\mathbf{I} + \mathbf{C}(\mathbf{A} - \mathbf{B}\mathbf{D}^{-1}\mathbf{C})^{-1}\mathbf{B}\mathbf{D}^{-1}\right] \end{pmatrix}. \tag{D.12}$$

Identifying this expression with the partitioned form of $\tilde{\mathbf{S}}_k^{-1}$ in Eq. (D.11), the Schür complement with respect to $\tilde{\boldsymbol{S}}_k$ becomes

$$\begin{aligned}
\mathbf{A} - \mathbf{B}\mathbf{D}^{-1}\mathbf{C} &= \mathbf{S}_{N-k,N-k} - \boldsymbol{\sigma}_{N-k,N-k+1}^T \tilde{\mathbf{S}}_k^{-1} \mathbf{s}_{N-k+1,N-k} \\
&= \boldsymbol{\alpha}_{N-k,N-k}^{(k)}.
\end{aligned} \tag{D.13}$$

Thus, evaluating the inverse matrix in Eq. (D.11), we have

$$\begin{aligned}
\boldsymbol{\alpha}_{ij}^{(k+1)} &= \mathbf{S}_{ij} - \begin{pmatrix} \boldsymbol{S}_{i,N-k} & \boldsymbol{\sigma}_{i,N-k+1}^T \end{pmatrix} \\
&\quad \times \begin{pmatrix} (\boldsymbol{\alpha}_{N-k,N-k}^{(k)})^{-1} & -(\boldsymbol{\alpha}_{N-k,N-k}^{(k)})^{-1}\boldsymbol{\sigma}_{N-k,N-k+1}^T \tilde{\boldsymbol{S}}_k^{-1} \\ -\tilde{\boldsymbol{S}}_k^{-1}\boldsymbol{s}_{N-k+1,N-k}(\boldsymbol{\alpha}_{N-k,N-k}^{(k)})^{-1} & \tilde{\boldsymbol{S}}_k^{-1}\left[\boldsymbol{I} + \boldsymbol{s}_{N-k+1,N-k}(\boldsymbol{\alpha}_{N-k,N-k}^{(k)})^{-1}\boldsymbol{\sigma}_{N-k,N-k+1}^T \tilde{\boldsymbol{S}}_k^{-1}\right] \end{pmatrix} \\
&\quad \times \begin{pmatrix} \boldsymbol{S}_{N-k,j} \\ \boldsymbol{s}_{N-k+1,j} \end{pmatrix},
\end{aligned}$$

$$
\begin{aligned}
&= \boldsymbol{S}_{ij} - \begin{pmatrix} \left(\boldsymbol{S}_{i,N-k} - \boldsymbol{\sigma}^T_{i,N-k+1}\tilde{\boldsymbol{S}}^{-1}_k \boldsymbol{s}_{N-k+1,N-k}\right)(\boldsymbol{\alpha}^{(k)}_{N-k,N-k})^{-1} \\ \boldsymbol{\sigma}^T_{i,N-k+1}\tilde{\boldsymbol{S}}^{-1}_k - \left(\boldsymbol{S}_{i,N-k} - \boldsymbol{\sigma}^T_{i,N-k+1}\tilde{\boldsymbol{S}}^{-1}_k \boldsymbol{s}_{N-k+1,N-k}\right)(\boldsymbol{\alpha}^{(k)}_{N-k,N-k})^{-1}\boldsymbol{\sigma}^T_{N-k,N-k+1}\tilde{\boldsymbol{S}}^{-1}_k \end{pmatrix} \\
&\qquad \times \begin{pmatrix} \boldsymbol{S}_{N-k,j} \\ \boldsymbol{s}_{N-k+1,j} \end{pmatrix}, \\
&= \boldsymbol{S}_{ij} - \begin{pmatrix} \boldsymbol{\alpha}^{(k)}_{i,N-k}(\boldsymbol{\alpha}^{(k)}_{N-k,N-k})^{-1} \\ \boldsymbol{\sigma}^T_{i,N-k+1}\tilde{\boldsymbol{S}}^{-1}_k - \boldsymbol{\alpha}^{(k)}_{i,N-k}(\boldsymbol{\alpha}^{(k)}_{N-k,N-k})^{-1}\boldsymbol{\sigma}^T_{N-k,N-k+1}\tilde{\boldsymbol{S}}^{-1}_k \end{pmatrix} \begin{pmatrix} \boldsymbol{S}_{N-k,j} \\ \boldsymbol{s}_{N-k+1,j} \end{pmatrix}, \\
&= \mathbf{S}_{ij} - \boldsymbol{\alpha}^{(k)}_{i,N-k}(\boldsymbol{\alpha}^{(k)}_{N-k,N-k})^{-1}\mathbf{S}_{N-k,j} - \boldsymbol{\sigma}^T_{i,N-k+1}\tilde{\mathbf{S}}^{-1}_k \mathbf{s}_{N-k+1,j} \\
&\qquad\qquad + \boldsymbol{\alpha}^{(k)}_{i,N-k}(\boldsymbol{\alpha}^{(k)}_{N-k,N-k})^{-1}\boldsymbol{\sigma}^T_{N-k,N-k+1}\tilde{\mathbf{S}}^{-1}_k \mathbf{s}_{N-k+1,j}, \\
&= \left(\mathbf{S}_{ij} - \boldsymbol{\sigma}^T_{i,N-k+1}\tilde{\mathbf{S}}^{-1}_k \mathbf{s}_{N-k+1,j}\right) - \boldsymbol{\alpha}^{(k)}_{i,N-k}(\boldsymbol{\alpha}^{(k)}_{N-k,N-k})^{-1}\left(\mathbf{S}_{N-k,j} - \boldsymbol{\sigma}^T_{N-k,N-k+1}\tilde{\mathbf{S}}^{-1}_k \mathbf{s}_{N-k+1,j}\right), \\
&= \boldsymbol{\alpha}^{(k)}_{ij} - \boldsymbol{\alpha}^{(k)}_{i,N-k}(\boldsymbol{\alpha}^{(k)}_{N-k,N-k})^{-1}\boldsymbol{\alpha}^{(k)}_{N-k,j}. \qquad \text{(D.14)}
\end{aligned}
$$

We can therefore express the $\boldsymbol{\alpha}^{(k)}_{ij}$ in the recursive form:

$$
\begin{aligned}
\boldsymbol{\alpha}^{(0)}_{ij} &= \mathbf{S}_{ij}, \\
\boldsymbol{\alpha}^{(k+1)}_{ij} &= \boldsymbol{\alpha}^{(k)}_{ij} - \boldsymbol{\alpha}^{(k)}_{i,N-k}(\boldsymbol{\alpha}^{(k)}_{N-k,N-k})^{-1}\boldsymbol{\alpha}^{(k)}_{N-k,j}, \qquad k \geq 1. \qquad \text{(D.15)}
\end{aligned}
$$

Given this recursive relationship, the matrix $\boldsymbol{\alpha}^{(0)}_{ij}$ can be read off directly from $\mathbf{S}$, and all higher order $\boldsymbol{\alpha}^{(k)}_{ij}$ can be calculated iteratively. Finally, the determinant may be computed via Eq. (D.10).

D.2 Simple Cases

Having derived an expression for the determinant of an $N \times N$ complex block matrix, it will be useful to examine the result for a few specific values of N. We choose to consider $N = 2$ and $N = 3$, as the first is a well-known result and the second gives a clear picture of what sort of objects our result actually involves. Larger values of N quickly become cumbersome to write down, but the procedure for their calculation will be made clear. Lastly, we present a "real world" application of our result by calculating the determinant of a 48×48 matrix, which arises in the study of quark matter.

D.2.1 2×2 Block Matrices

In the case $N = 2$, Eq. (D.10) reduces to

$$
\det(\mathbf{S}) = \det(\boldsymbol{\alpha}^{(1)}_{11})\det(\boldsymbol{\alpha}^{(0)}_{22}), \qquad \text{(D.16)}
$$

while Eqs. (D.15) become

$$\boldsymbol{\alpha}_{ij}^{(0)} = \mathbf{S}_{ij} \qquad \boldsymbol{\alpha}_{ij}^{(1)} = \mathbf{S}_{ij} - \mathbf{S}_{i2}\mathbf{S}_{22}^{-1}\mathbf{S}_{21}. \tag{D.17}$$

Thus, we obtain the result

$$\det(\mathbf{S}) = \det(\mathbf{S}_{11} - \mathbf{S}_{12}\mathbf{S}_{22}^{-1}\mathbf{S}_{21})\det(\mathbf{S}_{22}). \tag{D.18}$$

It is instructive to combine the two determinants in this expression and rewrite it in the alternate forms

$$\begin{aligned} \det(\mathbf{S}) &= \det(\mathbf{S}_{11}\mathbf{S}_{22} - \mathbf{S}_{12}\mathbf{S}_{22}^{-1}\mathbf{S}_{21}\mathbf{S}_{22}), \\ &= \det(\mathbf{S}_{22}\mathbf{S}_{11} - \mathbf{S}_{22}\mathbf{S}_{12}\mathbf{S}_{22}^{-1}\mathbf{S}_{21}). \end{aligned} \tag{D.19}$$

In these forms, it is clear that when either $\mathbf{S}_{12}$ or $\mathbf{S}_{21}$ commute with $\mathbf{S}_{22}$ our expression reduces to:

$$\begin{aligned} \mathbf{S}_{12}\mathbf{S}_{22} = \mathbf{S}_{22}\mathbf{S}_{12} \quad &: \quad \det(\mathbf{S}) = \det(\mathbf{S}_{22}\mathbf{S}_{11} - \mathbf{S}_{12}\mathbf{S}_{21}), \\ \mathbf{S}_{21}\mathbf{S}_{22} = \mathbf{S}_{21}\mathbf{S}_{22} \quad &: \quad \det(\mathbf{S}) = \det(\mathbf{S}_{11}\mathbf{S}_{22} - \mathbf{S}_{12}\mathbf{S}_{21}). \end{aligned} \tag{D.20}$$

Alternatively, for anti-commuting matrices, which often arise in the study of fermionic systems, the signs in (D.20) become positive.

D.2.2 3×3 Block Matrices

In the case $N = 3$, Eq. (D.10) reduces to

$$\det(\mathbf{S}) = \det(\boldsymbol{\alpha}_{11}^{(2)})\det(\boldsymbol{\alpha}_{22}^{(1)})\det(\boldsymbol{\alpha}_{33}^{(0)}), \tag{D.21}$$

while Eqs. (D.15) become

$$\begin{aligned} \boldsymbol{\alpha}_{ij}^{(0)} = \mathbf{S}_{ij}, \qquad \boldsymbol{\alpha}_{ij}^{(1)} = \mathbf{S}_{ij} - \mathbf{S}_{i3}\mathbf{S}_{33}^{-1}\mathbf{S}_{31}, \\ \boldsymbol{\alpha}_{ij}^{(2)} = \left(\mathbf{S}_{ij} - \mathbf{S}_{i3}\mathbf{S}_{33}^{-1}\mathbf{S}_{3j}\right) - \left(\mathbf{S}_{i2} - \mathbf{S}_{i3}\mathbf{S}_{33}^{-1}\mathbf{S}_{32}\right)\left(\mathbf{S}_{22} - \mathbf{S}_{23}\mathbf{S}_{33}^{-1}\mathbf{S}_{32}\right)^{-1}\left(\mathbf{S}_{2j} - \mathbf{S}_{23}\mathbf{S}_{33}^{-1}\mathbf{S}_{3j}\right). \end{aligned} \tag{D.22}$$

Thus, we obtain the result

$$\begin{aligned}\det(\mathbf{S}) &= \det\left[\left(\mathbf{S}_{11}-\mathbf{S}_{13}\mathbf{S}_{33}^{-1}\mathbf{S}_{31}\right)-\left(\mathbf{S}_{12}-\mathbf{S}_{13}\mathbf{S}_{33}^{-1}\mathbf{S}_{32}\right)\left(\mathbf{S}_{22}-\mathbf{S}_{23}\mathbf{S}_{33}^{-1}\mathbf{S}_{32}\right)^{-1}\left(\mathbf{S}_{21}-\mathbf{S}_{23}\mathbf{S}_{33}^{-1}\mathbf{S}_{31}\right)\right] \\ &\quad\times\det\left(\mathbf{S}_{22}-\mathbf{S}_{23}\mathbf{S}_{33}^{-1}\mathbf{S}_{32}\right)\det(\mathbf{S}_{33}). \end{aligned} \tag{D.23}$$

Analogously to the $N=2$ case, the commutation of certain blocks (e.g., $\mathbf{S}_{33}$ and $\mathbf{S}_{3j}$, $\alpha_{12}^{(1)}$ with $\alpha_{22}^{(1)}$) allows this expression to be simplified.

D.3 Eigenvalues of the two-flavor NJL model

Having considered the general form of the determinant of 2×2 and 3×3 block matrices, we now consider an application of our result by calculating the eigenenergies of quark matter in the two flavor Nambu–Jona-Lasinio model [15, 16, 21]. In this model, the energies are the roots of the equation $\det\mathbf{S}=0$, where

$$\mathbf{S}=\begin{pmatrix} \not{k}+\mu\gamma^0-M & \Delta\gamma_5\tau_2\lambda_2 \\ -\Delta^*\gamma_5\tau_2\lambda_2 & \not{k}-\mu\gamma^0-M \end{pmatrix}, \tag{D.24}$$

and where M is the effective quark mass, μ is the chemical potential, Δ is the color superconducting pairing gap, $\not{k}\equiv E\gamma^0-\boldsymbol{\gamma}\cdot\mathbf{k}$, where $\mathbf{k}=(k_1,k_2,k_3)^T$ is the quark momentum and the γ^ν ($\nu=0...3$) are the 4×4 Dirac matrices:

$$\gamma^0=\begin{pmatrix}\mathbf{I} & \mathbf{0}\\ \mathbf{0} & -\mathbf{I}\end{pmatrix}, \qquad \gamma^i=\begin{pmatrix}\mathbf{0} & \boldsymbol{\sigma}_i\\ -\boldsymbol{\sigma}_i & \mathbf{0}\end{pmatrix}, \tag{D.25}$$

with $\boldsymbol{\sigma}=(\sigma_x,\sigma_y,\sigma_z)^T$ representing the vector of Pauli matrices:

$$\sigma_x=\begin{pmatrix}0&1\\1&0\end{pmatrix}, \qquad \sigma_y=\begin{pmatrix}0&-i\\i&0\end{pmatrix}, \qquad \sigma_z=\begin{pmatrix}1&0\\0&-1\end{pmatrix}. \tag{D.26}$$

In addition, $\gamma_5\equiv i\gamma^0\gamma^1\gamma^2\gamma^3$, τ_2 is the second Pauli matrix in flavor space, and λ_2 is the second Gell-Mann matrix in color space:

$$\lambda_2=\begin{pmatrix}0&-i&0\\i&0&0\\0&0&0\end{pmatrix}. \tag{D.27}$$

Thus, while we have written Eq. (D.24) in 2×2 block form, each block is itself a 24×24 matrix (2 (flavor) $\times$ 3 (color) $\times$ 4 (Dirac)).

Before constructing the determinant from Eq. (D.10), we must choose how we wish to partition $\mathbf{S}$. We could, for instance, choose to begin with the 2×2 block form shown in Eq. (D.24), in which case the $\boldsymbol{\alpha}^{(k)}$ would be 24×24 matrices, which we would partition further, repeating the process until we have eliminated all indices. While this choice has the advantage of requiring the construction of only a single $\boldsymbol{\alpha}^{(k)}$ ($\boldsymbol{\alpha}^{(1)}$) for the first step (Eq. (D.16)), the price is that correspondingly more steps are required to finally obtain $\det \mathbf{S}$.

As a middle ground, balancing the number of $\boldsymbol{\alpha}^{(k)}$'s which must be constructed in each step with the number of steps, we will partition $\mathbf{S}$ into a 6×6 block matrix, with each block of size 8×8. We achieve this partitioning by writing out the color indices explicitly, while leaving the Dirac and flavor indices intact. Thus, the non-zero blocks of $\mathbf{S}$ become

$$\begin{aligned}
\mathbf{S}_{11} &= \mathbf{S}_{22} = \mathbf{S}_{33} = \not{k} + \mu\gamma^0 - M, \\
\mathbf{S}_{44} &= \mathbf{S}_{55} = \mathbf{S}_{66} = \not{k} - \mu\gamma^0 - M, \\
\mathbf{S}_{24} &= -\mathbf{S}_{15} = i\Delta\gamma_5\tau_2, \\
\mathbf{S}_{42} &= -\mathbf{S}_{51} = i\Delta^*\gamma_5\tau_2.
\end{aligned} \tag{D.28}$$

We now must construct $\boldsymbol{\alpha}^{(1)} \cdots \boldsymbol{\alpha}^{(5)}$. From Eq. (D.15), we see that $\boldsymbol{\alpha}_{ij}^{(k+1)}$ will be equal to $\boldsymbol{\alpha}_{ij}^{(k)}$ unless both $\boldsymbol{\alpha}_{i,N-k}^{(k)}$ and $\boldsymbol{\alpha}_{N-k,j}^{(k)}$ are non-zero. As a result, since $\mathbf{S}_{i6} = \mathbf{S}_{6j} = \mathbf{0}$ for $i, j \neq 6$, we find

$$\boldsymbol{\alpha}_{ij}^{(1)} = \mathbf{S}_{ij}, \quad 1 \leq i, j \leq 5. \tag{D.29}$$

Next, we note that $\mathbf{S}_{15}$ and $\mathbf{S}_{51}$ are the only non-zero blocks with a row or column index of 5. Thus, the only $\boldsymbol{\alpha}_{ij}^{(2)}$ which differs from $\boldsymbol{\alpha}_{ij}^{(1)}$ is

$$\boldsymbol{\alpha}_{11}^{(2)} = \mathbf{S}_{11} - \mathbf{S}_{15}\mathbf{S}_{55}^{-1}\mathbf{S}_{51}. \tag{D.30}$$

A straightforward application of the Banachiewicz identity (Eq. (D.12)) yields $\mathbf{S}_{55}^{-1}$:

$$\mathbf{S}_{55}^{-1} = \frac{\not{k} - \mu\gamma^0 + M}{(E-\mu)^2 - E_k^2}, \tag{D.31}$$

where $E_k \equiv \sqrt{\mathbf{k}^2 + M^2}$. Substituting this expression into Eq. (D.30) yields

$$\begin{aligned} \boldsymbol{\alpha}_{11}^{(2)} &= \not{k} + \mu\gamma^0 - M - (-i\Delta\gamma_5\tau_2)\left[\frac{\not{k} - \mu\gamma^0 + M}{(E-\mu)^2 - E_k^2}\right](-i\Delta\gamma_5\tau_2), \\ &= \not{k} + \mu\gamma^0 - M - |\Delta|^2\,\frac{\not{k} - \mu\gamma^0 - M}{(E-\mu)^2 - E_k^2}, \end{aligned} \tag{D.32}$$

where we have used the fact that $\tau_2^2 = \mathbf{I}$ and $\gamma_5\gamma^\mu = -\gamma^\mu\gamma_5$. Meanwhile, the rest of the $\boldsymbol{\alpha}_{ij}^{(2)} = \boldsymbol{\alpha}_{ij}^{(1)} = \mathbf{S}_{ij}$, so that

$$\boldsymbol{\alpha}_{ij}^{(2)} = \begin{cases} \not{k} + \mu\gamma^0 - M - |\Delta|^2\,\frac{\not{k} - \mu\gamma^0 - M}{(E-\mu)^2 - E_k^2} & \text{if } i,j = 1, \\ \mathbf{S}_{ij} & \text{else } (1 \le i,j \le 4). \end{cases} \tag{D.33}$$

Constructing $\boldsymbol{\alpha}^{(3)}$, we note that $\boldsymbol{\alpha}_{24}^{(2)}$ and $\mathbf{S}_{42}$ are the only non-zero blocks in the fourth row or column of $\boldsymbol{\alpha}^{(2)}$. As a result, we find

$$\begin{aligned} \boldsymbol{\alpha}_{22}^{(3)} &= \boldsymbol{\alpha}_{22}^{(2)} - \boldsymbol{\alpha}_{24}^{(2)}\left(\boldsymbol{\alpha}_{44}^{(2)}\right)^{-1}\boldsymbol{\alpha}_{42}^{(2)}, \\ &= \mathbf{S}_{11} - (-\mathbf{S}_{15})(\mathbf{S}_{55})^{-1}(-\mathbf{S}_{51}), \\ &= \mathbf{S}_{11} - \mathbf{S}_{15}\mathbf{S}_{55}^{-1}\mathbf{S}_{51}, \\ &= \boldsymbol{\alpha}_{11}^{(2)}. \end{aligned} \tag{D.34}$$

The rest of the $\boldsymbol{\alpha}_{ij}^{(3)}$ are equal to $\boldsymbol{\alpha}_{ij}^{(2)}$ so we find

$$\boldsymbol{\alpha}_{ij}^{(3)} = \begin{cases} \not{k} + \mu\gamma^0 - M - |\Delta|^2\,\frac{\not{k} - \mu\gamma^0 - M}{(E-\mu)^2 - E_k^2} & \text{if } i,j = 1 \text{ or } i,j = 2, \\ \mathbf{S}_{ij} & \text{else } (1 \le i,j \le 3). \end{cases} \tag{D.35}$$

Since $\boldsymbol{\alpha}_{33}^{(3)} = \mathbf{S}_{33}$ is the only non-zero block in the third row/column, we have

$$\boldsymbol{\alpha}_{ij}^{(4)} = \boldsymbol{\alpha}_{ij}^{(3)}, \qquad 1 \le i,j \le 2. \tag{D.36}$$

Finally, since $\boldsymbol{\alpha}_{12}^{(4)} = \boldsymbol{\alpha}_{21}^{(4)} = \mathbf{S}_{12} = \mathbf{S}_{21} = \mathbf{0}$, we find that the sole block of $\boldsymbol{\alpha}^{(5)}$ is

$$\begin{aligned} \boldsymbol{\alpha}_{11}^{(5)} &= \boldsymbol{\alpha}_{11}^{(4)} = \boldsymbol{\alpha}_{11}^{(3)}, \\ &= \not{k} + \mu\gamma^0 - M - |\Delta|^2\,\frac{\not{k} - \mu\gamma^0 - M}{(E-\mu)^2 - E_k^2}. \end{aligned} \tag{D.37}$$

Having constructed the necessary determinants, Eq. (D.10) gives

$$\begin{aligned}\det(\mathbf{S}) &= \det(\boldsymbol{\alpha}_{11}^{(5)})\det(\boldsymbol{\alpha}_{22}^{(4)})\det(\boldsymbol{\alpha}_{33}^{(3)})\det(\boldsymbol{\alpha}_{44}^{(2)})\det(\boldsymbol{\alpha}_{55}^{(1)})\det(\boldsymbol{\alpha}_{66}^{(0)}), \\ &= \det_{f,D}\left(\not{k}+\mu\gamma^0-M-|\Delta|^2\,\frac{\not{k}-\mu\gamma^0-M}{(E-\mu)^2-E_k^2}\right)^2 \det_{f,D}(\not{k}+\mu\gamma^0-M)\det_{f,D}(\not{k}-\mu\gamma^0-M)^3, \quad \text{(D.38)}\end{aligned}$$

where the subscript of f, D on the determinant indicates that the remaining determinant is to be taken over flavor and Dirac indices.

Thus, we have eliminated 6 of the original 48 indices, and have only the Dirac and flavor indices remaining. In fact, the flavor indices are now trivial, having vanished upon squaring the matrix τ_2 (see Eq. (D.32)), so that

$$\det(\mathbf{S}) = \det_{D}\left(\not{k}+\mu\gamma^0-M-|\Delta|^2\,\frac{\not{k}-\mu\gamma^0-M}{(E-\mu)^2-E_k^2}\right)^4 \det_{D}(\not{k}+\mu\gamma^0-M)^2\det_{D}(\not{k}-\mu\gamma^0-M)^6 \quad \text{(D.39)}$$

Computing $\det(\not{k}\pm\mu\gamma^0-M)$ yields

$$\begin{aligned}\det(\not{k}\pm\mu\gamma^0-M) &= \det\begin{pmatrix}(E\pm\mu)-M & -\boldsymbol{\sigma}\cdot\mathbf{k} \\ \boldsymbol{\sigma}\cdot\mathbf{k} & -(E\pm\mu)-M\end{pmatrix}, \\ &= \left[-(E\pm\mu)^2+M^2+(\sigma\cdot\mathbf{k})^2\right]^2, \\ &= \left[(E\pm\mu)^2-E_k^2\right]^2, \\ &= \left[E+(E_k\pm\mu)\right]^2\left[E-(E_k\mp\mu)\right]^2, \quad \text{(D.40)}\end{aligned}$$

where we have used the fact that $(\boldsymbol{\sigma}\cdot\mathbf{k})^2=\mathbf{k}^2$.

Finally, computing the remaining determinant from Eq. (D.39), we find

$$\begin{aligned}&\det\left(\not{k}+\mu\gamma^0-M-|\Delta|^2\,\frac{\not{k}-\mu\gamma^0-M}{(E-\mu)^2-E_k^2}\right) \\ &\quad= \left\{-\left[(E+\mu)-|\Delta|^2\frac{E-\mu}{(E-\mu)^2-E_k^2}\right]^2+\left[1-\frac{|\Delta|^2}{(E-\mu)^2-E_k^2}\right]^2E_k^2\right\}^2, \\ &\quad= \frac{[E^2-(E_k+\mu)^2-|\Delta|^2]^2[E^2-(E_k-\mu)^2-|\Delta|^2]^2}{(E-E_k-\mu)^2(E+E_k-\mu)^2}. \quad \text{(D.41)}\end{aligned}$$

Inserting Eq. (D.40) and (D.41) into Eq. (D.39), we obtain the result

$$\begin{aligned}\det(\mathbf{S}) &= \left[E+\sqrt{(E_k+\mu)^2+|\Delta|^2}\right]^8\left[E+\sqrt{(E_k-\mu)^2+|\Delta|^2}\right]^8\left[E-\sqrt{(E_k+\mu)^2+|\Delta|^2}\right]^8 \\ &\quad\times\left[E-\sqrt{(E_k-\mu)^2+|\Delta|^2}\right]^8(E+E_k+\mu)^4(E-E_k-\mu)^4 \\ &\quad\times(E+E_k-\mu)^4(E-E_k+\mu)^4. \end{aligned} \tag{D.42}$$

Finally, then, we can read off the eigenenergies, which are the absolute values of the roots of $\det(\mathbf{S})=0$:

$$\begin{aligned} E_1 &= |E_k+\mu| && \text{(multiplicity 8)}, \\ E_2 &= |E_k-\mu| && \text{(multiplicity 8)}, \\ E_3 &= \sqrt{(E_k+\mu)^2+|\Delta|^2} && \text{(multiplicity 16)}, \\ E_4 &= \sqrt{(E_k-\mu)^2+|\Delta|^2} && \text{(multiplicity 16)}. \end{aligned} \tag{D.43}$$

Indeed, these are the correct eigenenergies, as reported previously by Rossner [21].

Appendix E

NJL Model Code

The code below, written in C, minimizes the thermodynamic potential of the three flavor Nambu–Jona-Lasinio model, including the axial anomaly, with massless bare quarks. This system was considered by Abuki *et al.* and is a precursor to the model studied in Chapters 3 and 4. The algorithms employed are part of the GNU Scientific Library (GSL), release gsl-1.15 [159]. Note that some of the spacing and line-breaks have been modified in order to comply with formatting requirements.

```
//  File: NJLAAmin.c
//  Author: Philip D. Powell
//  Date Created: November 8, 2011
//  Date Last Modified: November 8, 2011

////////////////////////////////////////////////////////////////////////
//                                                                    //
//   This program is designed to minimize the thermodynamic potential //
//   for the Nambu—Jona-Lasinio (NJL) model including the effects of  //
//   the QCD axial anomaly.  For a given chemical potential (mu) and  //
//   temperature (T) it minimizes the thermodynamic potential with    //
//   respect to the chiral condensate (sigma) and diquark condensate  //
//   (d).  The code allows the chemical potential and temperature to  //
//   be varied, and therefore to compute the equilibrium values of    //
//   the condensates at any point in the phase diagram (mu,T).        //
//                                                                    //
////////////////////////////////////////////////////////////////////////

#include <stdlib.h>
#include <stdio.h>
#include "gsl/gsl_vector.h"
#include "gsl/gsl_integration.h"
#include "gsl/gsl_multimin.h"

// Define dimensionless couplings (scaled by Lambda)
double G = 1.926;
double K = 12.36;
double Kp = 12.36 * 4.2;
double H = 1.74;
double Lambda = 602.3;   // 3-momentum cutoff in units of MeV

double my_f (const gsl_vector *v, void *params);
double integrand1 (double x, void * params);
```

```
struct rparams
{
  double a;             //used for storing sigma
  double b;             //used for storing d
  double d;             //used for storing mu
  double f;             //used for storing t
};

struct mut
{
  double T;
  double MU;
};


int main ()
{
        FILE *file;
        file = fopen("njl-data","wt");  // open file to store results

        size_t iter = 0;
        int status, j, k;
        double size;

        double mu_min = 0.0 / Lambda;
        double mu_max = 600.0 / Lambda;
        double T_min = 1.0 / Lambda;
        double T_max = 600.0 / Lambda;

        double temp = 0.5;              // initialize temperature
        double mu1 = 0.0 / Lambda;      // initialize chemical potential

        struct mut Mut = {temp,mu1};

        const gsl_multimin_fminimizer_type *T =
                        gsl_multimin_fminimizer_nmsimplex2;
        gsl_multimin_fminimizer *s = NULL;
        gsl_vector *ss, *x;
        gsl_multimin_function my_func;

        my_func.n = 2;
        my_func.f = my_f;
        my_func.params = &Mut;

        s = gsl_multimin_fminimizer_alloc (T,2);

        // vector of unknown variables (sigma, d)
        x = gsl_vector_alloc (2);
        ss = gsl_vector_alloc (2);
```

```
for (k = 0; k < 601; k++) {
for (j = 0; j < 155; j++)
{
  iter = 0;

  Mut.MU = ( 1.0 * k ) / Lambda;          // set the chemical potential
  Mut.T = ( 1.0 + 1.0 * j ) / Lambda;     // set the temperature

  gsl_vector_set_all (ss, 0.001);

  // Check to see if mu and T are in the desired range
  if( (Mut.MU >= mu_min) && (Mut.MU <= mu_max)
                         && (Mut.T >= T_min) && (Mut.T <= T_max) )
  {
    if( Mut.T * Lambda < 180)
    {
      // initial guess for minimizer
      gsl_vector_set (x, 0, -0.047);
      gsl_vector_set (x, 1, 0.00);
    }
    else
    {
      gsl_vector_set (x, 0, 0.0);
      gsl_vector_set (x, 1, 0.0);
    }

    gsl_multimin_fminimizer_set (s, &my_func, x, ss);

    do
    {
      iter++;
      status = gsl_multimin_fminimizer_iterate (s);

      if (status)
        break;

      size = gsl_multimin_fminimizer_size (s);
      status = gsl_multimin_test_size (size, 1e-7);

      if (status == GSL_SUCCESS)
        fprintf(file, "%.1f      %.1f      %.6f      %.6f      %.9f \n",
                Mut.MU*Lambda, Mut.T*Lambda,
               -gsl_vector_get(s->x,0)/0.063565,
                fabs(gsl_vector_get(s->x,1))/0.054760,s->fval)
    }
    while (status == GSL_CONTINUE && iter < 4000);

    if(status != GSL_SUCCESS)
      fprintf(file,"%.1f      %.1f      %.6f      %.6f      %.9f \n",
              Mut.MU*Lambda, Mut.T*Lambda, 7.777777, 7.777777,
              7.777777777);
```

```
            else
              fprintf(file, "%.1f      %.1f      %.6f      %.6f      %.9f \n",
                      Mut.MU*Lambda, Mut.T*Lambda, 9.999999, 9.999999,
                      9.999999999);
          }
        }

        gsl_vector_free (x);
        gsl_vector_free (ss);
        gsl_multimin_fminimizer_free (s);

        fclose(file);

        return 0;
}


// Returns the value of Omega
double my_f (const gsl_vector *v, void *params)
{
        // initialize variables
        double V = 0.0;
        double Omega = 0.0;

        // absolute error limit for integrals
        double abserror = 1e-10;

        const struct mut Mut = *(struct mut *)params;
        double mu = Mut.MU;
        double t = Mut.T;

        const double Sigma = gsl_vector_get (v, 0);
        const double D = gsl_vector_get (v, 1);

        gsl_integration_workspace *w1 =
                gsl_integration_workspace_alloc(1000);

        double result1, error1;

        struct rparams Vars = {Sigma, D, mu, t};

        gsl_function F;
        F.function = &integrand1;
        F.params = &Vars;

        gsl_integration_qags(&F,0,1,0,abserror,0.0,w1,&result1,&error1);

        V = 6 * G * pow(Sigma,2) + 3 * H * pow(D,2) - 4 * K * pow(Sigma,3)
                - 3 * Kp * Sigma * pow(D,2) / 2;

        double DiracSea = 3.0 * (3.0 + pow(mu,4) ) / (4.0 * pow(M_PI,2));
```

```
        Omega = V - t * result1 / pow(M_PI,2) + DiracSea;

        gsl_integration_workspace_free (w1);

        return Omega;
}

double integrand1 (double x, void * params)
{
        double *p = (double *)params;
        double sigma = p[0];
        double d = p[1];
        double mu = p[2];
        double t = p[3];

        double M = - 4 * (G - K * sigma / 2) * sigma + Kp * pow(d,2) / 4;
        double delta = - 2 * (H - Kp * sigma / 4) * d;
        double Ek = sqrt( pow(x,2) + pow(M,2));

        double E1 = sqrt( pow(Ek + mu,2) + pow(delta,2));
        double E2 = sqrt( pow(Ek - mu,2) + pow(delta,2));
        double E3 = sqrt( pow(Ek + mu,2) + 4 * pow(delta,2));
        double E4 = sqrt( pow(Ek - mu,2) + 4 * pow(delta,2));

        double logsum = 8 * log(1 + pow(M_E, -E1/t))
                        + 8 * log(1 + pow(M_E, -E2/t))
                        + log(1 + pow(M_E, -E3/t))
                        + log(1 + pow(M_E, -E4/t));

        double nonlogsum = 1.0/(2*t) * (8 * E1 + 8 * E2 + E3 + E4);

        return pow(x,2) * (logsum + nonlogsum);
}
```

Appendix F

Gap and Number Equations Code

The code below, written in C, solves the gap and number equation(s) for the system considered in Chapter 6 and Appendix A. The algorithms employed are part of the GNU Scientific Library (GSL), release gsl-1.15 [159]. Note that some of the spacing and line-breaks have been modified in order to comply with formatting requirements.

```
//  File: CASolve.c
//  Author: Philip D. Powell
//  Date Created: April 1, 2013
//  Date Last Modified: April 4, 2013

////////////////////////////////////////////////////////////////////////
//                                                                    //
//   This program is designed to solve the gap and number equation(s) //
//   for a system of a mixture of two species of spin-orbit coupled   //
//   fermions, with spin-orbit coupling of a Rashba-Dresselhaus form. //
//   The program takes as inputs the temperature (T), Rashba and      //
//   Dresselhaus coupling strengths (vR and vD), Zeeman field (hz),   //
//   and population imbalance (P = (n_up - n_down)/(n_up + n_down)),  //
//   and outputs the equilibrium chemical potentials (mu_up and       //
//   mu_down) and BCS pairing gap (Delta).                            //
//                                                                    //
////////////////////////////////////////////////////////////////////////


#include <stdlib.h>
#include <gsl/gsl_monte_vegas.h>
#include <gsl/gsl_vector.h>
#include <gsl/gsl_multiroots.h>
#include <gsl/gsl_monte_miser.h>

// Integrands for gap and number equations
double gap_int (double *k, size_t dim, void *params);
double num_int_1 (double *k, size_t dim, void *params);
double num_int_2 (double *k, size_t dim, void *params);

// Gap and number equations
int gapNnums (const gsl_vector * x, void *params, gsl_vector * f);

// Auxiliary function to print iteration data
int print_state (size_t iter, gsl_multiroot_fsolver * s);
```

```
struct Params
{
        double T;               // temperature
        double vD;              // Dresselhaus coupling coefficient
        double vR;              // Rashba coupling coefficient
        double hz;              // Zeeman field
        double mu_up;           // spin up chemical potential
        double mu_down;         // spin down chemical potential
        double Delta;           // BCS gap
};

struct rparams
{
        double T;
        double vD;
        double vR;
        double hz;
        double as;      // s-wave scattering length
        double P;       // population inbalance
};

// Specify integration method for 3-momentum integrals
const char integration_method = 'm';

int main ()
{
        FILE *file;
        file = fopen("CAdata","wt");    // open file to write results

        const gsl_multiroot_fsolver_type *T;
        gsl_multiroot_fsolver *s;

        // vector for gap & number equation(s)
        gsl_vector *F = gsl_vector_alloc(2);
//      gsl_vector *F = gsl_vector_alloc(3);

        int status;
        size_t i, iter = 0;

        double myDelta = 0.0;
        double myMu = 0.0;

        const size_t n = 2;     // #vars in gap & number equations
//      const size_t n = 3;

        double Temp = 2.35;
        double vD = 0.0;
        double vR = 0.0;
        double hz = 0.0;
        double as = 1.0/(2.0);
        double P = 0.0;
```

```
        struct rparams p = {Temp, vD, vR, hz, as, P};
        gsl_multiroot_function f = {&gapNnums, n, &p};

        // initial guess (Delta, mu_up, mu_down)
        double x_init[2] = {0.7,-3.8};
//      double x_init[3] = {1.2,-0.5,-0.5};

        gsl_vector *x = gsl_vector_alloc (n);

        gsl_vector_set (x, 0, x_init[0]);
        gsl_vector_set (x, 1, x_init[1]);
//      gsl_vector_set (x, 2, x_init[2]);

        T = gsl_multiroot_fsolver_hybrids;
        s = gsl_multiroot_fsolver_alloc (T, 2);
//      s = gsl_multiroot_fsolver_alloc (T, 3);
        gsl_multiroot_fsolver_set (s, &f, x);
        print_state (iter, s);

        do
        {
                iter++;
                status = gsl_multiroot_fsolver_iterate (s);

                print_state (iter, s);

                // stop solver routine when gap and number equation(s)
                // are less than 5e-3
                if (status)   // check if solver is stuck
                        break;
                status = gsl_multiroot_test_residual (s->f, 5e-3);
        }
        while (status == GSL_CONTINUE && iter < 50);

        printf ("status = %s\n", gsl_strerror (status));

        gsl_multiroot_fsolver_free (s);
        gsl_vector_free (x);

        return 0;
}


double gap_int (double *k, size_t dim, void *params)
{
// map integration from (-infty..infty) (in p) to (0,1) (in k)
// this is necessary because the GSL Monte Carlo integration
// routines require a finite domain of integration
        double px, py, pz;
        px = k[0]/(1-k[0]);
        py = k[1]/(1-k[1]);
        pz = k[2]/(1-k[2]);
```

```
        // Jacobian for the integration variable change
        double jacobian = 1.0 / (pow(1-k[0],2) * pow(1-k[1],2)
                                 * pow(1-k[2],2) );

        double integrand = 0.0;

        double *p = (double *)params;
        double T = p[0];
        double vD = p[1];
        double vR = p[2];
        double hz = p[3];
        double mu_up = p[4];
        double mu_down = p[4];
//      double mu_down = p[5];
        double Delta = p[6];

// define auxiliary quantities which make the equations managable
        double v_plus = vD + vR;
        double v_minus = vD - vR;

        double mu_plus = (mu_up + mu_down) / 2;
        double mu_minus = (mu_up - mu_down) / 2;

        double Kt_plus = pow(px,2) + pow(py,2) + pow(pz,2) - mu_plus;
        double Kt_minus = - (hz + mu_minus);

        double hp = 2 * pow( pow(v_plus * px,2) + pow(v_minus * py,2), 0.5);

        double Y_plus = pow(Kt_plus,2) + pow(Delta,2);
        double Y_minus = pow(Kt_minus,2) + pow(hp,2);

        double E1 = pow( Y_plus + Y_minus + 2 * pow( Y_plus * Y_minus
                                 - pow(Delta,2) * pow(hp,2), 0.5), 0.5);
        double E2 = pow( Y_plus + Y_minus - 2 * pow( Y_plus * Y_minus
                                 - pow(Delta,2) * pow(hp,2), 0.5), 0.5);

        double X1 = tanh(E1/(2*T));
        double X2 = tanh(E2/(2*T));

        // this condition avoids "nan" values resulting near 0/0 division
        if(Y_plus * Y_minus - pow(Delta,2) * pow(hp,2) > 1e-4)
                integrand = 1.0 / (pow(px,2) + pow(py,2) + pow(pz,2))
                             - X1/(2*E1) - X2/(2*E2) - pow(Kt_minus,2) /
                             pow( Y_plus * Y_minus - pow(Delta,2)
                                * pow(hp,2), 0.5) * (X1/(2*E1) - X2/(2*E2));
        else
                integrand = 1.0 / (pow(px,2) + pow(py,2) + pow(pz,2))
                                 - X1/(2*E1) - X2/(2*E2);

        return integrand * jacobian;
}
```

```
double num_int_1 (double *k, size_t dim, void *params)
{
        double px, py, pz;
        px = k[0]/(1-k[0]);
        py = k[1]/(1-k[1]);
        pz = k[2]/(1-k[2]);

        double jacobian = 1.0 / (pow(1-k[0],2) * pow(1-k[1],2)
                                 * pow(1-k[2],2) );

        double integrand = 0.0;

        double *p = (double *)params;
        double T = p[0];
        double vD = p[1];
        double vR = p[2];
        double hz = p[3];
        double mu_up = p[4];
        double mu_down = p[4];
//      double mu_down = p[5];
        double Delta = p[6];

        double v_plus = vD + vR;
        double v_minus = vD - vR;

        double mu_plus = (mu_up + mu_down) / 2;
        double mu_minus = (mu_up - mu_down) / 2;

        double Kt_plus = pow(px,2) + pow(py,2) + pow(pz,2) - mu_plus;
        double Kt_minus = - (hz + mu_minus);

        double Kt_up = Kt_plus + Kt_minus;
        double Kt_down = Kt_plus - Kt_minus;

        double hp = 2 * pow( pow(v_plus * px,2) + pow(v_minus * py,2), 0.5);
        double Y_plus = pow(Kt_plus,2) + pow(Delta,2);
        double Y_minus = pow(Kt_minus,2) + pow(hp,2);

        double E1 = pow( Y_plus + Y_minus + 2 * pow( Y_plus * Y_minus
                                 - pow(Delta,2) * pow(hp,2), 0.5), 0.5);
        double E2 = pow( Y_plus + Y_minus - 2 * pow( Y_plus * Y_minus
                                 - pow(Delta,2) * pow(hp,2), 0.5), 0.5);

        double X1 = tanh(E1/(2*T));
        double X2 = tanh(E2/(2*T));


        if(Y_plus * Y_minus - pow(Delta,2) * pow(hp,2) > 1e-4)
                integrand = 1 - Kt_up * (X1/(2*E1) + X2/(2*E2))
                              - (Kt_up * Y_minus + Kt_minus * Y_plus)
                              / pow( Y_plus * Y_minus - pow(Delta,2)
```

```
                                * pow(hp,2), 0.5) * (X1/(2*E1) - X2/(2*E2));
        else
                integrand = 1 - Kt_up * (X1/(2*E1) + X2/(2*E2));

        return integrand * jacobian;
}

double num_int_2 (double *k, size_t dim, void *params)
{
        double px, py, pz;
        px = k[0]/(1-k[0]);
        py = k[1]/(1-k[1]);
        pz = k[2]/(1-k[2]);

        double jacobian = 1.0 / (pow(1-k[0],2) * pow(1-k[1],2)
                                 * pow(1-k[2],2) );
        double integrand = 0.0;

        double *p = (double *)params;
        double T = p[0];
        double vD = p[1];
        double vR = p[2];
        double hz = p[3];
        double mu_up = p[4];
        double mu_down = p[4];
//      double mu_down = p[5];
        double Delta = p[6];

        double v_plus = vD + vR;
        double v_minus = vD - vR;

        double mu_plus = (mu_up + mu_down) / 2;
        double mu_minus = (mu_up - mu_down) / 2;

        double Kt_plus = pow(px,2) + pow(py,2) + pow(pz,2) - mu_plus;
        double Kt_minus = - (hz + mu_minus);

        double Kt_up = Kt_plus + Kt_minus;
        double Kt_down = Kt_plus - Kt_minus;

        double hp = 2 * pow( pow(v_plus * px,2) + pow(v_minus * py,2), 0.5);

        double Y_plus = pow(Kt_plus,2) + pow(Delta,2);
        double Y_minus = pow(Kt_minus,2) + pow(hp,2);

        double E1 = pow( Y_plus + Y_minus + 2 * pow( Y_plus * Y_minus
                                - pow(Delta,2) * pow(hp,2), 0.5), 0.5);
        double E2 = pow( Y_plus + Y_minus - 2 * pow( Y_plus * Y_minus
                                - pow(Delta,2) * pow(hp,2), 0.5), 0.5);

        double X1 = tanh(E1/(2*T));
        double X2 = tanh(E2/(2*T));
```

```
        if(Y_plus * Y_minus - pow(Delta,2) * pow(hp,2) > 1e-4)
                integrand = 1 - Kt_down * (X1/(2*E1) + X2/(2*E2))
                              - (Kt_up * Y_minus - Kt_minus * Y_plus)
                              / pow( Y_plus * Y_minus - pow(Delta,2)
                              * pow(hp,2), 0.5) * (X1/(2*E1) - X2/(2*E2));
        else
                integrand = 1 - Kt_down * (X1/(2*E1) + X2/(2*E2));

        return integrand * jacobian;
}

int gapNnums (const gsl_vector * x, void *params, gsl_vector * f)
{
        double *p = (double *)params;
        double Mu_down;

        const double Delta = gsl_vector_get (x, 0);
        const double mu_up = gsl_vector_get (x, 1);
        const double mu_down = gsl_vector_get (x, 1);
//      const double mu_down = gsl_vector_get (x, 2);


        double T = p[0];
        double vD = p[1];
        double vR = p[2];
        double hz = p[3];
        double as = p[4];
        double P = p[5];

        // variables for storing integral values and errors
        double res1, err1, res2, err2;
        double res3, err3;

        // lower and upper limits of integration in {px,py,pz}
        double xl[3] = { 0.0, 0.0, 0.0 };
        double xu[3] = { 1.0, 1.0, 1.0 };

        double gap_equation, num_equation_1;
//      double num_equation_2;

        const gsl_rng_type *T1, *T2;
//      const gsl_rng_type *T3;
        gsl_rng *r1, *r2;
        gsl_rng *r3;

        struct Params parameters = {T, vD, vR, hz, mu_up, mu_down, Delta};

        gsl_monte_function F1 = { &gap_int, 3, &parameters };
        gsl_monte_function F2 = { &num_int_1, 3, &parameters };
//        gsl_monte_function F3 = { &num_int_2, 3, &parameters };
```

```
        // number of function calls in Monte-Carlo integration procedure
        size_t calls = 100000;

        gsl_rng_env_setup ();

        T1 = gsl_rng_default;
        r1 = gsl_rng_alloc (T1);

        T2 = gsl_rng_default;
        r2 = gsl_rng_alloc (T1);

//        T3 = gsl_rng_default;
//        r3 = gsl_rng_alloc (T1);

        gsl_monte_vegas_state *s1 = gsl_monte_vegas_alloc (3);
        gsl_monte_vegas_state *s2 = gsl_monte_vegas_alloc (3);
//      gsl_monte_vegas_state *s3 = gsl_monte_vegas_alloc (3);

        gsl_monte_miser_state *S1 = gsl_monte_miser_alloc (3);
        gsl_monte_miser_state *S2 = gsl_monte_miser_alloc (3);
//      gsl_monte_miser_state *S3 = gsl_monte_miser_alloc (3);

        if(integration_method == 'v')
        {
                do
                {
                        gsl_monte_vegas_integrate
                         (&F1, xl, xu, 3, calls, r1, s1, &res1, &err1);
                }
                while (fabs (gsl_monte_vegas_chisq (s1) - 1.0) > 0.5);

                do
                {
                        gsl_monte_vegas_integrate
                         (&F2, xl, xu, 3, calls, r2, s2, &res2, &err2);
                }
                while (fabs (gsl_monte_vegas_chisq (s2) - 1.0) > 0.5) ;
/*
                do
                {
                        gsl_monte_vegas_integrate
                         (&F3, xl, xu, 3, calls, r3, s3, &res3, &err3);
                }
                while (fabs (gsl_monte_vegas_chisq (s3) - 1.0) > 0.5);
*/
        }
        else
        {
                gsl_monte_miser_integrate
                 (&F1, xl, xu, 3, calls, r1, S1, &res1, &err1);
                gsl_monte_miser_integrate
                 (&F2, xl, xu, 3, calls, r2, S2, &res2, &err2);
//              gsl_monte_miser_integrate
```

```
//                (&F3, xl, xu, 3, calls, r3, S3, &res3, &err3);
//                printf("gap_int = %f +/- %f\n",res1,err1);
//                printf("num_int = %f +/- %f\n",res2,err2);
        }

        gsl_monte_vegas_free (s1);
        gsl_monte_vegas_free (s2);
//      gsl_monte_vegas_free (s3);

        gsl_monte_miser_free (S1);
        gsl_monte_miser_free (S2);
//      gsl_monte_miser_free (S3);

        gsl_rng_free (r1);
        gsl_rng_free (r2);
//      gsl_rng_free (r3);

        gap_equation = pow(M_PI,2) / (4*as) - res1;
        num_equation_1 = M_PI * (1 + P) / 3 - res2;

        gsl_vector_set (f, 0, gap_equation);
        gsl_vector_set (f, 1, num_equation_1);
//      gsl_vector_set (f, 2, num_equation_2);

        return 0;
}



int print_state (size_t iter, gsl_multiroot_fsolver * s)
{
//      printf ("iter = %3u   Delta = % .3f   mu_up = % .3f   mu_down = %.3f
                f1 = %.3f   f2 = %.3f   f3 = %.3f \n", iter,
                gsl_vector_get (s->x, 0), gsl_vector_get (s->x, 1),
                gsl_vector_get (s->x, 2), gsl_vector_get (s->f, 0),
                gsl_vector_get (s->f, 1), gsl_vector_get (s->f, 2));
        printf ("iter = %3u   Delta = % .6f   mu = % .6f   f1 = %.6f
                f2 = %.6f \n", iter, gsl_vector_get (s->x, 0),
                gsl_vector_get (s->x, 1), gsl_vector_get (s->f, 0),
                gsl_vector_get (s->f, 1));
}
```

Appendix G

Evaluation of Matsubara sums in $\Gamma^{-1}(q)$

In this appendix we explicitly evaluate the Matsubara sums appearing in the bosonic propagator $\Gamma^{-1}(q_n, \mathbf{q})$, which is given in Eq. (A.19). In order to facilitate a comparison with [62] we use the notation $\tilde{K}_\alpha(\mathbf{k})$ in place of $\tilde{\xi}_{\mathbf{k}\alpha}$, which is used in Chapter 6.

G.1 Mean Field Eigenvalues

Before evaluating the Matsubara sums of Eq. (A.19), we will find it useful to compute the eigenvalues of the ungapped system, which are the poles of $\mathbf{G}[0]$ (Eq. (A.1)), or alternatively, the roots of the equation $\det(\mathbf{G}^{-1}[0]) = 0$. Due to the block diagonal structure of $\mathbf{G}^{-1}[0]$, the determinant is straight-forward to compute and is simply

$$\det\left(\mathbf{G}^{-1}[0]\right) = -\frac{1}{a(k)a(-k)}, \tag{G.1}$$

where $a(k)$ is defined below Eq. (A.12). Thus, two of the eigenvalues are the roots of the equation

$$\begin{aligned}
0 &= \frac{1}{a(k)}, \\
&= [i\omega_n + \tilde{K}_\uparrow(\mathbf{k})][i\omega_n + \tilde{K}_\downarrow(\mathbf{k})] - |h_\perp(\mathbf{k})|^2, \\
&= \left[i\omega_n + \frac{\tilde{K}_\uparrow(\mathbf{k}) + \tilde{K}_\downarrow(\mathbf{k})}{2}\right]^2 - \left[\frac{\tilde{K}_\uparrow(\mathbf{k}) + \tilde{K}_\downarrow(\mathbf{k})}{2}\right]^2 + \tilde{K}_\uparrow(\mathbf{k})\tilde{K}_\downarrow(\mathbf{k}) - |h_\perp(\mathbf{k})|^2, \\
&= [i\omega_n + \tilde{K}_+(\mathbf{k})]^2 - \tilde{K}_-(\mathbf{k})^2 - |h_\perp(\mathbf{k})|^2, \\
&= \left[i\omega_n + \tilde{K}_+(\mathbf{k}) + \sqrt{Y_-(\mathbf{k})}\right]\left[i\omega_n + \tilde{K}_+(\mathbf{k}) - \sqrt{Y_-(\mathbf{k})}\right],
\end{aligned} \tag{G.2}$$

where we have defined $\tilde{K}_- = (\tilde{K}_\uparrow - \tilde{K}_\downarrow)/2$ and $Y_- = \tilde{K}_-^2 + |h_\perp|^2$. Thus, defining the eigenvalues

$$E_1(\mathbf{k}) = \tilde{K}_+(\mathbf{k}) + \sqrt{Y_-(\mathbf{k})}, \tag{G.3}$$

$$E_2(\mathbf{k}) = \tilde{K}_+(\mathbf{k}) - \sqrt{Y_-(\mathbf{k})}, \tag{G.4}$$

we can express $a(k)$ in the form

$$a(k) = \frac{1}{[i\omega_n + E_1(\mathbf{k})][i\omega_n + E_2(\mathbf{k})]}. \tag{G.5}$$

The remaining two eigenvalues, which solve the equation $1/a(-k) = 0$ are simply $E_{3,4} = -E_{1,2}$ so that we can write

$$a(-k) = \frac{1}{[i\omega_n - E_1(\mathbf{k})][i\omega_n - E_2(\mathbf{k})]}. \tag{G.6}$$

G.2 Term 1

With the above expression for $a(k)$, we can now write the first term in Eq. (A.19) as

$$\begin{aligned}
\text{term } 1 &= \sum_k a(k)a(q-k)[i\omega_n + \tilde{K}_\uparrow(\mathbf{k})][i\omega_n - iq_n - \tilde{K}_\downarrow(\mathbf{k}-\mathbf{q})], \\
&= \sum_k \frac{i\omega_n + \tilde{K}_\uparrow(\mathbf{k})}{i\omega_n + E_1(\mathbf{k})} \frac{1}{i\omega_n + E_2(\mathbf{k})} \frac{i\omega_n - iq_n - \tilde{K}_\downarrow(\mathbf{k}-\mathbf{q})}{i\omega_n - iq_n - E_1(\mathbf{k}-\mathbf{q})} \frac{1}{i\omega_n - iq_n - E_2(\mathbf{k}-\mathbf{q})}, \\
&= \sum_k \left(1 + \frac{\tilde{K}_\uparrow(\mathbf{k}) - E_1(\mathbf{k})}{i\omega_n + E_1(\mathbf{k})}\right) \frac{1}{i\omega_n + E_2(\mathbf{k})} \left(1 + \frac{E_1(\mathbf{k}-\mathbf{q}) - \tilde{K}_\downarrow(\mathbf{k}-\mathbf{q})}{i\omega_n - iq_n - E_1(\mathbf{k}-\mathbf{q})}\right) \\
&\qquad \times \frac{1}{i\omega_n - iq_n - E_2(\mathbf{k}-\mathbf{q})}, \\
&= \sum_k \left(1 + \frac{\tilde{K}_-(\mathbf{k}) - \sqrt{Y_-(\mathbf{k})}}{i\omega_n + E_1(\mathbf{k})}\right) \frac{1}{i\omega_n + E_2(\mathbf{k})} \left(1 + \frac{\tilde{K}_-(\mathbf{k}-\mathbf{q}) + \sqrt{Y_-(\mathbf{k}-\mathbf{q})}}{i\omega_n - iq_n - E_1(\mathbf{k}-\mathbf{q})}\right) \\
&\qquad \times \frac{1}{i\omega_n - iq_n - E_2(\mathbf{k}-\mathbf{q})}.
\end{aligned} \tag{G.7}$$

Expanding this expression yields

$$\begin{aligned}
\text{term } 1 &= \sum_k \frac{1}{i\omega_n + E_2(\mathbf{k})} \frac{1}{i\omega_n - iq_n - E_2(\mathbf{k}-\mathbf{q})} \\
&\quad + \left[\tilde{K}_-(\mathbf{k}) - \sqrt{Y_-(\mathbf{k})}\right] \sum_k \frac{1}{i\omega_n + E_1(\mathbf{k})} \frac{1}{i\omega_n + E_2(\mathbf{k})} \frac{1}{i\omega_n - iq_n - E_2(\mathbf{k}-\mathbf{q})} \\
&\quad + \left[\tilde{K}_-(\mathbf{k}-\mathbf{q}) + \sqrt{Y_-(\mathbf{k}-\mathbf{q})}\right] \sum_k \frac{1}{i\omega_n + E_2(\mathbf{k})} \frac{1}{i\omega_n - iq_n - E_1(\mathbf{k}-\mathbf{q})} \frac{1}{i\omega_n - iq_n - E_2(\mathbf{k}-\mathbf{q})} \\
&\quad + \left[\tilde{K}_-(\mathbf{k}) - \sqrt{Y_-(\mathbf{k})}\right] \left[\tilde{K}_-(\mathbf{k}-\mathbf{q}) + \sqrt{Y_-(\mathbf{k}-\mathbf{q})}\right] \\
&\qquad \times \sum_k \frac{1}{i\omega_n + E_1(\mathbf{k})} \frac{1}{i\omega_n + E_2(\mathbf{k})} \frac{1}{i\omega_n - iq_n - E_1(\mathbf{k}-\mathbf{q})} \frac{1}{i\omega_n - iq_n - E_2(\mathbf{k}-\mathbf{q})}
\end{aligned} \tag{G.8}$$

Next, we will perform partial fraction decomposition on each of the four terms above, after which we will evaluate the sums directly.

The first component of term 1 is

$$\begin{aligned}
\text{term } 1_1 &= \sum_k \frac{1}{i\omega_n + E_2(\mathbf{k})} \frac{1}{i\omega_n - iq_n - E_2(\mathbf{k}-\mathbf{q})} \\
&= \frac{1}{iq_n + E_2(\mathbf{k}) + E_2(\mathbf{k}-\mathbf{q})} \sum_k \left[\frac{1}{i\omega_n - iq_n - E_2(\mathbf{k}-\mathbf{q})} - \frac{1}{i\omega_n + E_2(\mathbf{k})}\right], \\
&= \frac{1}{iq_n + E_2(\mathbf{k}) + E_2(\mathbf{k}-\mathbf{q})} \left[\sum_{k'} \frac{1}{i\omega_{n'} - E_2(\mathbf{k}-\mathbf{q})} - \sum_k \frac{1}{i\omega_n + E_2(\mathbf{k})}\right], \\
&= \frac{\beta}{iq_n + E_2(\mathbf{k}) + E_2(\mathbf{k}-\mathbf{q})} \left[f(E_2(\mathbf{k}-\mathbf{q})) - \frac{1}{2} - f(-E_2(\mathbf{k})) + \frac{1}{2}\right], \\
&= -\beta \frac{1 - f(E_2(\mathbf{k})) - f(E_2(\mathbf{k}-\mathbf{q}))}{iq_n + E_2(\mathbf{k}) + E_2(\mathbf{k}-\mathbf{q})},
\end{aligned} \tag{G.9}$$

where we have suppressed the sum over $\mathbf{k}$ for notational simplicity. In addition, in evaluating the second sum above we have shifted the summand by defining $\omega_{n'} = \omega_n - q_n$. This is permissible, as the difference between a fermionic and bosonic frequency is another fermionic frequency. The second component of term

1 is

$$\begin{aligned}
\text{term } 1_2 &= \left[\tilde{K}_-(\mathbf{k}) - \sqrt{Y_-(\mathbf{k})}\right] \sum_k \frac{1}{i\omega_n + E_1(\mathbf{k})} \frac{1}{i\omega_n + E_2(\mathbf{k})} \frac{1}{i\omega_n - iq_n - E_2(\mathbf{k}-\mathbf{q})}, \\
&= \left[\tilde{K}_-(\mathbf{k}) - \sqrt{Y_-(\mathbf{k})}\right] \sum_k \left[\frac{1}{E_1(\mathbf{k}) - E_2(\mathbf{k})} \frac{1}{iq_n + E_1(\mathbf{k}) + E_2(\mathbf{k}-\mathbf{q})} \frac{1}{i\omega_n + E_1(\mathbf{k})} \right. \\
&\qquad - \frac{1}{E_1(\mathbf{k}) - E_2(\mathbf{k})} \frac{1}{iq_n + E_2(\mathbf{k}) + E_2(\mathbf{k}-\mathbf{q})} \frac{1}{i\omega_n + E_2(\mathbf{k})} \\
&\qquad \left. + \frac{1}{iq_n + E_1(\mathbf{k}) + E_2(\mathbf{k}-\mathbf{q})} \frac{1}{iq_n + E_2(\mathbf{k}) + E_2(\mathbf{k}-\mathbf{q})} \frac{1}{i\omega_n - iq_n - E_2(\mathbf{k}-\mathbf{q})} \right], \\
&= \beta \left[\tilde{K}_-(\mathbf{k}) - \sqrt{Y_-(\mathbf{k})}\right] \left[\frac{\frac{1}{2} - f(E_1(\mathbf{k}))}{2\sqrt{Y_-(\mathbf{k})}} \frac{1}{iq_n + E_1(\mathbf{k}) + E_2(\mathbf{k}-\mathbf{q})} \right. \\
&\qquad - \frac{\frac{1}{2} - f(E_2(\mathbf{k}))}{2\sqrt{Y_-(\mathbf{k})}} \frac{1}{iq_n + E_2(\mathbf{k}) + E_2(\mathbf{k}-\mathbf{q})} \\
&\qquad \left. + \frac{f(E_2(\mathbf{k}-\mathbf{q})) - \frac{1}{2}}{2\sqrt{Y_-(\mathbf{k})}} \left(\frac{1}{iq_n + E_2(\mathbf{k}) + E_2(\mathbf{k}-\mathbf{q})} - \frac{1}{iq_n + E_1(\mathbf{k}) + E_2(\mathbf{k}-\mathbf{q})} \right) \right], \\
&= \beta \frac{\tilde{K}_-(\mathbf{k}) - \sqrt{Y_-(\mathbf{k})}}{2\sqrt{Y_-(\mathbf{k})}} \left[\frac{1 - f(E_1(\mathbf{k}) - f(E_2(\mathbf{k}-\mathbf{q})}{iq_n + E_1(\mathbf{k}) + E_2(\mathbf{k}-\mathbf{q})} - \frac{1 - f(E_2(\mathbf{k})) - f(E_2(\mathbf{k}-\mathbf{q}))}{iq_n + E_2(\mathbf{k}) + E_2(\mathbf{k}-\mathbf{q})} \right]. \quad \text{(G.10)}
\end{aligned}$$

The third component of term 1 is

$$\begin{aligned}
\text{term } 1_3 &= \left[\tilde{K}_-(\mathbf{k}-\mathbf{q}) + \sqrt{Y_-(\mathbf{k}-\mathbf{q})}\right] \\
&\qquad \times \sum_k \frac{1}{i\omega_n + E_2(\mathbf{k})} \frac{1}{i\omega_n - iq_n - E_1(\mathbf{k}-\mathbf{q})} \frac{1}{i\omega_n - iq_n - E_2(\mathbf{k}-\mathbf{q})}, \\
&= \left[\tilde{K}_-(\mathbf{k}-\mathbf{q}) + \sqrt{Y_-(\mathbf{k}-\mathbf{q})}\right] \\
&\qquad \times \sum_k \left[\frac{1}{iq_n + E_2(\mathbf{k}) + E_1(\mathbf{k}-\mathbf{q})} \frac{1}{iq_n + E_2(\mathbf{k}) + E_2(\mathbf{k}-\mathbf{q})} \frac{1}{i\omega_n + E_2(\mathbf{k})} \right. \\
&\qquad + \frac{1}{E_1(\mathbf{k}-\mathbf{q}) - E_2(\mathbf{k}-\mathbf{q})} \frac{1}{iq_n + E_2(\mathbf{k}) + E_1(\mathbf{k}-\mathbf{q})} \frac{1}{i\omega_n - iq_n - E_1(\mathbf{k}-\mathbf{q})} \\
&\qquad \left. - \frac{1}{E_1(\mathbf{k}-\mathbf{q}) - E_2(\mathbf{k}-\mathbf{q})} \frac{1}{iq_n + E_2(\mathbf{k}) + E_2(\mathbf{k}-\mathbf{q})} \frac{1}{i\omega_n - iq_n - E_2(\mathbf{k}-\mathbf{q})} \right] \\
&= \beta \left[\tilde{K}_-(\mathbf{k}-\mathbf{q}) + \sqrt{Y_-(\mathbf{k}-\mathbf{q})}\right] \\
&\qquad \times \left[\frac{\frac{1}{2} - f(E_2(\mathbf{k}))}{2\sqrt{Y_-(\mathbf{k}-\mathbf{q})}} \left(\frac{1}{iq_n + E_2(\mathbf{k}) + E_2(\mathbf{k}-\mathbf{q})} - \frac{1}{iq_n + E_2(\mathbf{k}) + E_1(\mathbf{k}-\mathbf{q})} \right) \right. \\
&\qquad + \frac{f(E_1(\mathbf{k}-\mathbf{q})) - \frac{1}{2}}{2\sqrt{Y_-(\mathbf{k}-\mathbf{q})}} \frac{1}{iq_n + E_2(\mathbf{k}) + E_1(\mathbf{k}-\mathbf{q})} \\
&\qquad \left. - \frac{f(E_2(\mathbf{k}-\mathbf{q})) - \frac{1}{2}}{2\sqrt{Y_-(\mathbf{k}-\mathbf{q})}} \frac{1}{iq_n + E_2(\mathbf{k}) + E_2(\mathbf{k}-\mathbf{q})} \right], \\
&= \beta \frac{\tilde{K}_-(\mathbf{k}-\mathbf{q}) + \sqrt{Y_-(\mathbf{k}-\mathbf{q})}}{2\sqrt{Y_-(\mathbf{k}-\mathbf{q})}} \left[- \frac{1 - f(E_2(\mathbf{k})) - f(E_1(\mathbf{k}-\mathbf{q}))}{iq_n + E_2(\mathbf{k}) + E_1(\mathbf{k}-\mathbf{q})} \right. \\
&\qquad \left. + \frac{1 - f(E_2(\mathbf{k})) - f(E_2(\mathbf{k}-\mathbf{q}))}{iq_n + E_2(\mathbf{k}) + E_2(\mathbf{k}-\mathbf{q})} \right]. \quad \text{(G.11)}
\end{aligned}$$

The fourth component of term 1 is

$$\begin{aligned}
\text{term } 1_4 &= \left[\tilde{K}_-(\mathbf{k}) - \sqrt{Y_-(\mathbf{k})}\right]\left[\tilde{K}_-(\mathbf{k}-\mathbf{q}) + \sqrt{Y_-(\mathbf{k}-\mathbf{q})}\right] \\
&\quad \times \sum_k \frac{1}{i\omega_n + E_1(\mathbf{k})}\frac{1}{i\omega_n + E_2(\mathbf{k})}\frac{1}{i\omega_n - iq_n - E_1(\mathbf{k}-\mathbf{q})}\frac{1}{i\omega_n - iq_n - E_2(\mathbf{k}-\mathbf{q})} \\
&= \beta\left[\tilde{K}_-(\mathbf{k}) - \sqrt{Y_-(\mathbf{k})}\right]\left[\tilde{K}_-(\mathbf{k}-\mathbf{q}) + \sqrt{Y_-(\mathbf{k}-\mathbf{q})}\right] \\
&\quad \times \Bigg[\frac{1}{2\sqrt{Y_-(\mathbf{k})}}\frac{\frac{1}{2} - f(E_2(\mathbf{k}))}{2\sqrt{Y_-(\mathbf{k}-\mathbf{q})}}\left(\frac{1}{iq_n + E_2(\mathbf{k}) + E_2(\mathbf{k}-\mathbf{q})} - \frac{1}{iq_n + E_2(\mathbf{k}) + E_1(\mathbf{k}-\mathbf{q})}\right) \\
&\qquad + \frac{f(E_1(\mathbf{k}-\mathbf{q})) - \frac{1}{2}}{2\sqrt{Y_-(\mathbf{k}-\mathbf{q})}}\frac{1}{2\sqrt{Y_-(\mathbf{k})}}\left(\frac{1}{iq_n + E_2(\mathbf{k}) + E_1(\mathbf{k}-\mathbf{q})} - \frac{1}{iq_n + E_1(\mathbf{k}) + E_1(\mathbf{k}-\mathbf{q})}\right) \\
&\qquad - \frac{\frac{1}{2} - f(E_1(\mathbf{k}))}{2\sqrt{Y_-(\mathbf{k})}}\frac{1}{2\sqrt{Y_-(\mathbf{k}-\mathbf{q})}}\left(\frac{1}{iq_n + E_1(\mathbf{k}) + E_2(\mathbf{k}-\mathbf{q})} - \frac{1}{iq_n + E_1(\mathbf{k}) + E_1(\mathbf{k}-\mathbf{q})}\right) \\
&\qquad - \frac{f(E_2(\mathbf{k}-\mathbf{q})) - \frac{1}{2}}{2\sqrt{Y_-(\mathbf{k}-\mathbf{q})}}\frac{1}{2\sqrt{Y_-(\mathbf{k})}}\left(\frac{1}{iq_n + E_2(\mathbf{k}) + E_2(\mathbf{k}-\mathbf{q})} - \frac{1}{iq_n + E_1(\mathbf{k}) + E_2(\mathbf{k}-\mathbf{q})}\right)\Bigg], \\
&= \beta\frac{\tilde{K}_-(\mathbf{k}) - \sqrt{Y_-(\mathbf{k})}}{2\sqrt{Y_-(\mathbf{k})}}\frac{\tilde{K}_-(\mathbf{k}-\mathbf{q}) + \sqrt{Y_-(\mathbf{k}-\mathbf{q})}}{2\sqrt{Y_-(\mathbf{k}-\mathbf{q})}} \\
&\quad \times \Bigg[\frac{1 - f(E_1(\mathbf{k})) - f(E_1(\mathbf{k}-\mathbf{q}))}{iq_n + E_1(\mathbf{k}) + E_1(\mathbf{k}-\mathbf{q})} - \frac{1 - f(E_1(\mathbf{k})) - f(E_2(\mathbf{k}-\mathbf{q}))}{iq_n + E_1(\mathbf{k}) + E_2(\mathbf{k}-\mathbf{q})} \\
&\qquad - \frac{1 - f(E_2(\mathbf{k})) - f(E_1(\mathbf{k}-\mathbf{q}))}{iq_n + E_2(\mathbf{k}) + E_1(\mathbf{k}-\mathbf{q})} + \frac{1 - f(E_2(\mathbf{k})) - f(E_2(\mathbf{k}-\mathbf{q}))}{iq_n + E_2(\mathbf{k}) + E_2(\mathbf{k}-\mathbf{q})}\Bigg]. \qquad \text{(G.12)}
\end{aligned}$$

Next, in order to simplify our notation we define the quantities

$$u_k^2 = \frac{1}{2}\left(1 - \frac{\tilde{K}_-(\mathbf{k})}{\sqrt{Y_-(\mathbf{k})}}\right), \qquad v_k^2 = \frac{1}{2}\left(1 + \frac{\tilde{K}_-(\mathbf{k})}{\sqrt{Y_-(\mathbf{k})}}\right). \qquad \text{(G.13)}$$

along with the quantities

$$W_{ij} = \frac{1 - f(E_i(\mathbf{k})) - f(E_j(\mathbf{k}-\mathbf{q}))}{iq_n + E_i(\mathbf{k}) + E_j(\mathbf{k}-\mathbf{q})}. \qquad \text{(G.14)}$$

In terms of these quantities, combining the four components of term 1, we obtain

$$\begin{aligned}
\text{term } 1 &= -\beta W_{22} - \beta u_k^2\left(W_{12} - W_{22}\right) + \beta v_{k-q}^2\left(W_{22} - W_{21}\right) = -\beta u_k^2 v_{k-q}^2\left(W_{11} - W_{12} - W_{21} + W_{22}\right), \\
&= -\beta\Big[u_k^2 v_{k-q}^2 W_{11} + u_k^2(1 - v_{k-q}^2)W_{12} + (1 - u_k^2)v_{k-q}^2 W_{21} + (1 - u_k^2)(1 - v_{k-q}^2)W_{22}\Big]., \\
&= -\beta\Big[u_k^2 v_{k-q}^2 W_{11} + u_k^2 u_{k-q}^2 W_{12} + v_k^2 v_{k-q}^2 W_{21} + u_{k-q}^2 v_k^2 W_{22}\Big]. \qquad \text{(G.15)}
\end{aligned}$$

G.3 Term 2

Looking at Eq. (A.19), we note that the second term may be obtained from the first by simply taking $\uparrow\leftrightarrow\downarrow$, which implies $\tilde{K}_- \to -\tilde{K}_-$ and therefore $u_k^2 \leftrightarrow v_k^2$. Thus, we have

$$\text{term } 2 = -\beta\Big[u_{k-q}^2 v_k^2 W_{11} + v_k^2 v_{k-q}^2 W_{12} + u_k^2 u_{k-q}^2 W_{21} + u_k^2 v_{k-q}^2 W_{22}\Big]. \qquad \text{(G.16)}$$

G.4 Terms 3 and 4

The third and fourth terms in Eq. (A.19) are

$$\text{terms } 3\&4 = -\left[h_\perp^*(\mathbf{k})h_\perp(\mathbf{k}-\mathbf{q}) + h_\perp^*(\mathbf{k}-\mathbf{q})h_\perp(\mathbf{k})\right]\sum_k a(k)a(q-k). \tag{G.17}$$

This sum is precisely the sum evaluated in term 1_4 (Eq. (G.12)), so we obtain

$$\text{term } 3\&4 = -\beta\,\frac{h_\perp^*(\mathbf{k})h_\perp(\mathbf{k}-\mathbf{q}) + h_\perp^*(\mathbf{k}-\mathbf{q})h_\perp(\mathbf{k})}{4\sqrt{Y_-(\mathbf{k})Y_-(\mathbf{k}-\mathbf{q})}}\left(W_{11} - W_{12} - W_{21} + W_{22}\right). \tag{G.18}$$

From the definition of u_k and v_k we see that

$$u_k v_k = \sqrt{\frac{\sqrt{Y_-(\mathbf{k})} - \tilde{K}_-(\mathbf{k})}{2\sqrt{Y_-(\mathbf{k})}}\,\frac{\sqrt{Y_-(\mathbf{k})} + \tilde{K}_-(\mathbf{k})}{2\sqrt{Y_-(\mathbf{k})}}} = \sqrt{\frac{Y_-(\mathbf{k}) - \tilde{K}_-(\mathbf{k})^2}{4\sqrt{Y_-(\mathbf{k})}}} = \frac{|h_\perp(\mathbf{k})|}{2\sqrt{Y_-(\mathbf{k})}}. \tag{G.19}$$

Thus, writing $h_\perp(\mathbf{k}) = |h_\perp(\mathbf{k})|e^{i\theta_k}$, we can rewrite terms 3&4 as

$$\text{terms } 3\&4 = -2\beta u_k v_k u_{k-q} v_{k-q}\cos\left(\theta_k - \theta_{k-q}\right)\left(W_{11} - W_{12} - W_{21} + W_{22}\right). \tag{G.20}$$

G.5 Constructing $\Gamma^{-1}(q)$

Substituting the expressions for terms 1-4 into Eq. (A.19), the full expression for $\Gamma^{-1}(q)$ becomes

$$\begin{aligned}\Gamma^{-1}(q) \;=\; -\frac{1}{g} - \frac{1}{2V}\sum_{\mathbf{k}}\Bigg\{&\left[u_k^2 v_{k-q}^2 + u_{k-q}^2 v_k^2 + 2u_k v_k u_{k-q} v_{k-q}\cos(\theta_k - \theta_{k-q})\right](W_{11} + W_{22}) \\ &+\left[u_k^2 u_{k-q}^2 + v_k^2 v_{k-q}^2 - 2u_k v_k u_{k-q} v_{k-q}\cos(\theta_k - \theta_{k-q})\right](W_{12} + W_{21})\Bigg]\Bigg\}.\end{aligned} \tag{G.21}$$

We can simplify this expression slightly by noting that the two bracketed terms sum to one (a fact which follows from the condition $|u_k|^2 + |v_k|^2 = 1$) so that by defining the function

$$g(k,q) = u_k^2 v_{k-q}^2 + u_{k-q}^2 v_k^2 + 2u_k v_k u_{k-q} v_{k-q}\cos(\theta_k - \theta_{k-q}), \tag{G.22}$$

we can express $\Gamma^{-1}(q)$ in the form

$$\Gamma^{-1}(q) \;=\; -\frac{1}{g} - \frac{1}{2V}\sum_{\mathbf{k}}\Big[W_{12} + W_{21} + g(k,q)\left(W_{11} - W_{12} - W_{21} + W_{22}\right)\Big]. \tag{G.23}$$

Finally, replacing the coupling strength g with the s-wave scattering length via Eq. (6.56) we obtain the renormalized expression

$$\Gamma^{-1}(q) \;=\; -\frac{m}{4\pi a_s} + \frac{1}{2V}\sum_{\mathbf{k}}\left\{\frac{1}{\varepsilon} - \Big[W_{12} + W_{21} + g(k,q)\left(W_{11} - W_{12} - W_{21} + W_{22}\right)\Big]\right\}. \tag{G.24}$$

Appendix H

Green's Functions for Spin-Orbit Coupled Fermions

In this appendix we construct the Green's functions relevant to Chapter 6 and Appendix A, whose Hamiltonian is $H = H_0 + H_{so} + H_{int}$, where

$$H_0 = \sum_{\mathbf{k}\alpha} \xi_{\mathbf{k}\alpha} \psi^\dagger_{\mathbf{k}\alpha} \psi_{\mathbf{k}\alpha}, \tag{H.1}$$

$$H_{so} = -\sum_{\mathbf{k}\alpha\beta} \mathbf{h}(\mathbf{k}) \cdot \boldsymbol{\sigma}_{\alpha\beta} \psi^\dagger_{\mathbf{k}\alpha} \psi_{\mathbf{k}\beta}, \tag{H.2}$$

$$H_{int} = \frac{g}{V} \sum_{\mathbf{k}_1 \cdots \mathbf{k}_4} \psi^\dagger_{\mathbf{k}_1\uparrow} \psi^\dagger_{\mathbf{k}_2\downarrow} \psi_{\mathbf{k}_3\downarrow} \psi_{\mathbf{k}_4\uparrow} \delta_{\mathbf{k}_1+\mathbf{k}_2-\mathbf{k}_3-\mathbf{k}_4}, \tag{H.3}$$

where α, β are spin indices, $\mathbf{h}$ is a spin-orbit field, $\xi_{\mathbf{k}\alpha} = k^2/2m_\alpha - \mu_\alpha$, $g < 0$ corresponds to an attractive two-body contact interaction, and V is the volume of the system. In order to obtain the Green's functions, we will first compute the equations of motion for the operators $\psi_{\mathbf{k}\alpha}$, from which the equations of motion for the Green's functions will be derived.

H.1 Equation of motion for $\psi_{\mathbf{k}\sigma}(t)$

The equation of motion for the operator $\psi_{\mathbf{k}\sigma}(t)$ is given by the standard expression

$$i \frac{\partial \psi_{\mathbf{k}\sigma}(t)}{\partial t} = [\psi_{\mathbf{k}\sigma}(t), H(t)]. \tag{H.4}$$

For simplicity, in the following calculations we suppress the explicit time dependence of the operators when no confusion will arise. Unless otherwise noted, all operators are evaluated at the same time t. Taking the commutator of $\psi_{\mathbf{k},\sigma}$ with the free-particle Hamiltonian, we obtain

$$\begin{aligned}
[\psi_{\mathbf{k}\sigma}, H_0] &= \sum_{\mathbf{k}'\alpha} \xi_{\mathbf{k}'\alpha} [\psi_{\mathbf{k}\sigma}, \psi^\dagger_{\mathbf{k}'\alpha} \psi_{\mathbf{k}'\alpha}], \\
&= \sum_{\mathbf{k}'\alpha} \xi_{\mathbf{k}'\alpha} \left([\psi_{\mathbf{k}\sigma}, \psi^\dagger_{\mathbf{k}'\alpha}] \psi_{\mathbf{k}'\alpha} + \psi^\dagger_{\mathbf{k}'\alpha} [\psi_{\mathbf{k}\sigma}, \psi_{\mathbf{k}'\alpha}] \right), \\
&= \sum_{\mathbf{k}'\alpha} \xi_{\mathbf{k}'\alpha} \left[\left(\{\psi_{\mathbf{k}\sigma}, \psi^\dagger_{\mathbf{k}'\alpha}\} - 2\psi^\dagger_{\mathbf{k}'\alpha} \psi_{\mathbf{k}\sigma} \right) \psi_{\mathbf{k}'\alpha} + \psi^\dagger_{\mathbf{k}'\alpha} \left(\{\psi_{\mathbf{k}\sigma}, \psi_{\mathbf{k}'\alpha}\} - 2\psi_{\mathbf{k}'}\psi_{\mathbf{k}\sigma} \right) \right], \\
&= \sum_{\mathbf{k}'\alpha} \xi_{\mathbf{k}'\alpha} \left[\delta_{\mathbf{k}\mathbf{k}'} \delta_{\sigma\alpha} \psi_{\mathbf{k}'\alpha} - 2\psi^\dagger_{\mathbf{k}'\alpha} \{\psi_{\mathbf{k}\sigma}, \psi_{\mathbf{k}'\alpha}\} \right], \\
&= \xi_{\mathbf{k}\sigma} \psi_{\mathbf{k}\sigma}.
\end{aligned} \tag{H.5}$$

Similarly, taking the commutator with the spin-orbit Hamiltonian yields

$$\begin{aligned}
[\psi_{\mathbf{k}\sigma}, H_{so}] &= -\sum_{\mathbf{k}'\alpha\beta} h_i(\mathbf{k}') \sigma_{i,\alpha\beta} [\psi_{\mathbf{k}\sigma}, \psi^\dagger_{\mathbf{k}'\alpha} \psi_{\mathbf{k}'\beta}], \\
&= -\sum_{\mathbf{k}'\alpha\beta} h_i(\mathbf{k}') \sigma_{i,\alpha\beta} \left([\psi_{\mathbf{k}\sigma}, \psi^\dagger_{\mathbf{k}'\alpha}] \psi_{\mathbf{k}'\beta} + \psi^\dagger_{\mathbf{k}'\alpha} [\psi_{\mathbf{k}\sigma}, \psi_{\mathbf{k}'\beta}] \right),
\end{aligned}$$

$$
\begin{aligned}
&= -\sum_{\mathbf{k}'\alpha\beta} h_i(\mathbf{k}')\sigma_{i,\alpha\beta}\left[\left(\delta_{\mathbf{k}\mathbf{k}'}\delta_{\sigma\alpha} - 2\psi^\dagger_{\mathbf{k}'\alpha}\psi_{\mathbf{k}\sigma}\right)\psi_{\mathbf{k}'\beta} + 2\psi^\dagger_{\mathbf{k}'\alpha}\psi_{\mathbf{k}\sigma}\psi_{\mathbf{k}'\beta}\right], \\
&= -\sum_{\beta}\mathbf{h}(\mathbf{k})\cdot\boldsymbol{\sigma}_{\sigma\beta}\psi_{\mathbf{k}\beta}. \qquad \text{(H.6)}
\end{aligned}
$$

Finally, the commutator with the two-body interaction gives

$$
\begin{aligned}
[\psi_{\mathbf{k}\sigma}, H_{int}] &= \frac{g}{V}\sum_{\mathbf{k}_1\cdots\mathbf{k}_4}[\psi_{\mathbf{k}\sigma},\psi^\dagger_{\mathbf{k}_1\uparrow}\psi^\dagger_{\mathbf{k}_2\downarrow}\psi_{\mathbf{k}_3\downarrow}\psi_{\mathbf{k}_4\uparrow}]\delta_{\mathbf{k}_1+\mathbf{k}_2-\mathbf{k}_3-\mathbf{k}_4}, \\
&= \frac{g}{V}\sum_{\mathbf{k}_1\cdots\mathbf{k}_4}\left([\psi_{\mathbf{k}\sigma},\psi^\dagger_{\mathbf{k}_1\uparrow}\psi^\dagger_{\mathbf{k}_2\downarrow}]\psi_{\mathbf{k}_3\downarrow}\psi_{\mathbf{k}_4\uparrow} + \psi^\dagger_{\mathbf{k}_1\uparrow}\psi^\dagger_{\mathbf{k}_2\downarrow}[\psi_{\mathbf{k}\sigma},\psi_{\mathbf{k}_3\downarrow}\psi_{\mathbf{k}_4\uparrow}]\right)\delta_{\mathbf{k}_1+\mathbf{k}_2-\mathbf{k}_3-\mathbf{k}_4}, \\
&= \frac{g}{V}\sum_{\mathbf{k}_1\cdots\mathbf{k}_4}\left([\psi_{\mathbf{k}\sigma},\psi^\dagger_{\mathbf{k}_1\uparrow}]\psi^\dagger_{\mathbf{k}_2\downarrow} + \psi^\dagger_{\mathbf{k}_1\uparrow}[\psi_{\mathbf{k}\sigma},\psi^\dagger_{\mathbf{k}_2\downarrow}]\right)\psi_{\mathbf{k}_3\downarrow}\psi_{\mathbf{k}_4\uparrow}\delta_{\mathbf{k}_1+\mathbf{k}_2-\mathbf{k}_3-\mathbf{k}_4}, \\
&= \frac{g}{V}\sum_{\mathbf{k}_1\cdots\mathbf{k}_4}\left[\left(\delta_{\mathbf{k}\mathbf{k}_1}\delta_{\sigma\uparrow} - 2\psi^\dagger_{\mathbf{k}_1\uparrow}\psi_{\mathbf{k}\sigma}\right)\psi^\dagger_{\mathbf{k}_2\downarrow} + \psi^\dagger_{\mathbf{k}_1\uparrow}\left(\delta_{\mathbf{k}\mathbf{k}_2}\delta_{\sigma\downarrow} - 2\psi^\dagger_{\mathbf{k}_2\downarrow}\psi_{\mathbf{k}\sigma}\right)\right] \\
&\qquad\qquad \times\psi_{\mathbf{k}_3\downarrow}\psi_{\mathbf{k}_4\uparrow}\delta_{\mathbf{k}_1+\mathbf{k}_2-\mathbf{k}_3-\mathbf{k}_4}, \\
&= \frac{g}{V}\sum_{\mathbf{k}_1\cdots\mathbf{k}_4}\left(\delta_{\mathbf{k}\mathbf{k}_1}\delta_{\sigma\uparrow}\psi^\dagger_{\mathbf{k}_2\downarrow} + \delta_{\mathbf{k}\mathbf{k}_2}\delta_{\sigma\downarrow}\psi^\dagger_{\mathbf{k}_1\uparrow} - 2\psi^\dagger_{\mathbf{k}_1\uparrow}\{\psi_{\mathbf{k}\sigma},\psi^\dagger_{\mathbf{k}_2\downarrow}\}\right)\psi_{\mathbf{k}_3\downarrow}\psi_{\mathbf{k}_4\uparrow}\delta_{\mathbf{k}_1+\mathbf{k}_2-\mathbf{k}_3-\mathbf{k}_4}, \\
&= \frac{g}{V}\sum_{\mathbf{k}_1\cdots\mathbf{k}_4}\left(\delta_{\mathbf{k}\mathbf{k}_1}\delta_{\sigma\uparrow}\psi^\dagger_{\mathbf{k}_2\downarrow} - \delta_{\mathbf{k}\mathbf{k}_2}\delta_{\sigma\downarrow}\psi^\dagger_{\mathbf{k}_1\uparrow}\right)\psi_{\mathbf{k}_3\downarrow}\psi_{\mathbf{k}_4\uparrow}\delta_{\mathbf{k}_1+\mathbf{k}_2-\mathbf{k}_3-\mathbf{k}_4}, \\
&= \gamma_\sigma\frac{g}{V}\sum_{\mathbf{k}_2\cdots\mathbf{k}_4}\psi^\dagger_{\mathbf{k}_2,-\sigma}\psi_{\mathbf{k}_3\downarrow}\psi_{\mathbf{k}_4\uparrow}\delta_{\mathbf{k}+\mathbf{k}_2-\mathbf{k}_3-\mathbf{k}_4}, \qquad \text{(H.7)}
\end{aligned}
$$

where we have introduced the quantity $\gamma_{\uparrow,\downarrow} = \pm 1$ in the last line. Combining the three commutators, after a trivial relabeling of indices we obtain the equation of motion

$$
i\frac{\partial\psi_{\mathbf{k}\sigma}}{\partial t} = \xi_{\mathbf{k}\sigma}\psi_{\mathbf{k}\sigma} - \sum_\alpha \mathbf{h}(\mathbf{k})\cdot\boldsymbol{\sigma}_{\sigma\alpha}\psi_{\mathbf{k}\alpha} + \gamma_\sigma\frac{g}{V}\sum_{\mathbf{k}_1\cdots\mathbf{k}_3}\psi^\dagger_{\mathbf{k}_1,-\sigma}\psi_{\mathbf{k}_2\downarrow}\psi_{\mathbf{k}_3\uparrow}\delta_{\mathbf{k}+\mathbf{k}_1-\mathbf{k}_2-\mathbf{k}_3}. \qquad \text{(H.8)}
$$

In order to proceed we next group the first two terms of Eq. (H.8) and rewrite the third term so that we obtain

$$
i\frac{\partial\psi_{\mathbf{k}\sigma}}{\partial t} = \sum_\alpha\left[\xi_{\mathbf{k}\sigma}\delta_{\sigma\alpha} - \mathbf{h}(\mathbf{k})\cdot\boldsymbol{\sigma}_{\sigma\alpha}\right]\psi_{\mathbf{k}\alpha} + \gamma_\sigma\frac{g}{V}\sum_{\mathbf{k}_1}\psi^\dagger_{\mathbf{k}_1,-\sigma}\sum_{\mathbf{k}_2}\psi_{\mathbf{k}_2\downarrow}\psi_{\mathbf{k}+\mathbf{k}_1-\mathbf{k}_2,\uparrow}. \qquad \text{(H.9)}
$$

Next, we introduce the momentum-space pairing amplitude

$$
\Delta_{\mathbf{q}} = \frac{g}{V}\sum_{\mathbf{k}}\langle\psi_{\mathbf{k}\downarrow}\psi_{\mathbf{q}-\mathbf{k}\uparrow}\rangle, \qquad \text{(H.10)}
$$

and approximate the interaction term in Eq. (H.8) by replacing the sum over $\mathbf{k}_2$ by its thermal expectation value. Thus, after making the trivial replacement $\mathbf{k}_1 \to -\mathbf{k}'$ in the final sum we obtain

$$
i\frac{\partial\psi_{\mathbf{k}\sigma}}{\partial t} = \sum_\alpha\left[\xi_{\mathbf{k}\sigma}\delta_{\sigma\alpha} - \mathbf{h}(\mathbf{k})\cdot\boldsymbol{\sigma}_{\sigma\alpha}\right]\psi_{\mathbf{k}\alpha} + \gamma_\sigma\sum_{\mathbf{k}'}\Delta_{\mathbf{k}-\mathbf{k}'}\psi^\dagger_{-\mathbf{k}',-\sigma}. \qquad \text{(H.11)}
$$

We see that the spin-orbit field couples particles of different species, allowing for transitions between the two, while the two-body interaction couples particles of momentum and spin $(\mathbf{k},\sigma)$ and holes with $(\text{-}\mathbf{k},-\sigma)$. In order to obtain a closed set of equations we must therefore obtain the equations of motion for the hole operators ($\psi^\dagger_{\mathbf{k}\sigma}$ as well. Taking the Hermitian conjugate of Eq. (H.11), taking $(\mathbf{k},\sigma) \to (-\mathbf{k},-\sigma)$, and

making the replacement $\mathbf{k}' \to -\mathbf{k}'$ in the last sum yields

$$i\,\frac{\partial \psi^\dagger_{-\mathbf{k}\sigma}}{\partial t} = -\sum_\alpha \left[\xi_{-\mathbf{k}\sigma}\delta_{\sigma\alpha} - \mathbf{h}^*(-\mathbf{k})\cdot\boldsymbol{\sigma}_{\sigma\alpha}\right]\psi^\dagger_{-\mathbf{k}\alpha} - \gamma_\sigma \sum_{\mathbf{k}'} \Delta^*_{\mathbf{k}'-\mathbf{k}}\psi_{\mathbf{k}',-\sigma}. \tag{H.12}$$

Defining the Nambu-Gor'kov spinor $\Psi_{\mathbf{k}} = \begin{pmatrix}\psi_{\mathbf{k}\uparrow} & \psi_{\mathbf{k}\downarrow} & \psi^\dagger_{-\mathbf{k}\uparrow} & \psi^\dagger_{-\mathbf{k}\downarrow}\end{pmatrix}^T$, by combining Eqs. (H.11) and (H.12) we can write the equation of motion of $\Psi_{\mathbf{k}}(t)$ in the matrix form

$$i\,\frac{\partial \Psi_{\mathbf{k}}(t)}{\partial t} = \sum_{\mathbf{k}'} \mathbf{M}_{\mathbf{k}\mathbf{k}'}\Psi_{\mathbf{k}'}(t), \tag{H.13}$$

where we define the matrix $\mathbf{M}_{\mathbf{k}\mathbf{k}'}$:

$$\mathbf{M}_{\mathbf{k}\mathbf{k}'} = \begin{pmatrix} (\xi_{\mathbf{k}\uparrow}-h_z)\delta_{\mathbf{k}\mathbf{k}'} & -h_\perp(\mathbf{k})\delta_{\mathbf{k}\mathbf{k}'} & 0 & \Delta_{\mathbf{k}-\mathbf{k}'} \\ -h^*_\perp(\mathbf{k})\delta_{\mathbf{k}\mathbf{k}'} & (\xi_{\mathbf{k}\downarrow}+h_z)\delta_{\mathbf{k}\mathbf{k}'} & -\Delta_{\mathbf{k}-\mathbf{k}'} & 0 \\ 0 & -\Delta^*_{\mathbf{k}'-\mathbf{k}} & -(\xi_{-\mathbf{k}\uparrow}-h_z)\delta_{\mathbf{k}\mathbf{k}'} & h^*_\perp(-\mathbf{k})\delta_{\mathbf{k}\mathbf{k}'} \\ \Delta^*_{\mathbf{k}'-\mathbf{k}} & 0 & h_\perp(-\mathbf{k})\delta_{\mathbf{k}\mathbf{k}'} & -(\xi_{-\mathbf{k}\downarrow}+h_z)\delta_{\mathbf{k}\mathbf{k}'} \end{pmatrix}, \tag{H.14}$$

and where $h_\perp = h_x - ih_y$. Having obtained the equations of motion for the single particle operators $\psi_{\mathbf{k}\sigma}$ and $\psi^\dagger_{\mathbf{k}\sigma}$, we now move on to consider the single-particle Green's functions.

H.2 Equation of motion for $G_{\alpha\beta}(\mathbf{k};t_1,t_2)$

The momentum-space single-particle Green's functions are defined by

$$G_{\alpha\beta}(\mathbf{k};t_1,t_2) = -i\left\langle T\left(\psi_{\mathbf{k}\alpha}(t_1)\psi^\dagger_{\mathbf{k}\beta}(t_2)\right)\right\rangle, \tag{H.15}$$

where T is the fermionic time-ordering operator, which we define as

$$T(AB) = \begin{cases} AB & \text{if } t_A > t_B \\ -BA & \text{if } t_A < t_B \end{cases}. \tag{H.16}$$

In terms of the Nambu-Gor'kov spinor defined in the prior section, we also define the matrix Green's function

$$\mathcal{G}_{ij}(\mathbf{k};t_1,t_2) = -i\left\langle T\left(\Psi_{\mathbf{k}i}(t_1)\Psi^\dagger_{\mathbf{k}j}(t_2)\right)\right\rangle, \tag{H.17}$$

where $i,j = 1...4$ are Nambu-Gor'kov indices. In matrix form, this Green's function can be written as

$$\boldsymbol{\mathcal{G}}(\mathbf{k};t_1,t_2) = -i\left\langle T\begin{pmatrix} \psi_{\mathbf{k}\uparrow}(t_1)\psi^\dagger_{\mathbf{k}\uparrow}(t_2) & \psi_{\mathbf{k}\uparrow}(t_1)\psi^\dagger_{\mathbf{k}\downarrow}(t_2) & \psi_{\mathbf{k}\uparrow}(t_1)\psi_{-\mathbf{k}\uparrow}(t_2) & \psi_{\mathbf{k}\uparrow}(t_1)\psi_{-\mathbf{k}\downarrow}(t_2) \\ \psi_{\mathbf{k}\downarrow}(t_1)\psi^\dagger_{\mathbf{k}\uparrow}(t_2) & \psi_{\mathbf{k}\downarrow}(t_1)\psi^\dagger_{\mathbf{k}\downarrow}(t_2) & \psi_{\mathbf{k}\downarrow}(t_1)\psi_{-\mathbf{k}\uparrow}(t_2) & \psi_{\mathbf{k}\downarrow}(t_1)\psi_{-\mathbf{k}\downarrow}(t_2) \\ \psi^\dagger_{-\mathbf{k}\uparrow}(t_1)\psi^\dagger_{\mathbf{k}\uparrow}(t_2) & \psi^\dagger_{-\mathbf{k}\uparrow}(t_1)\psi^\dagger_{\mathbf{k}\downarrow}(t_2) & \psi^\dagger_{-\mathbf{k}\uparrow}(t_1)\psi_{-\mathbf{k}\uparrow}(t_2) & \psi^\dagger_{-\mathbf{k}\uparrow}(t_1)\psi_{-\mathbf{k}\downarrow}(t_2) \\ \psi^\dagger_{-\mathbf{k}\downarrow}(t_1)\psi^\dagger_{\mathbf{k}\uparrow}(t_2) & \psi^\dagger_{-\mathbf{k}\downarrow}(t_1)\psi^\dagger_{\mathbf{k}\downarrow}(t_2) & \psi^\dagger_{-\mathbf{k}\downarrow}(t_1)\psi_{-\mathbf{k}\uparrow}(t_2) & \psi^\dagger_{-\mathbf{k}\downarrow}(t_1)\psi_{-\mathbf{k}\downarrow}(t_2) \end{pmatrix}\right\rangle, \tag{H.18}$$

In order to obtain the equation of motion for $\boldsymbol{\mathcal{G}}(\mathbf{k};t_1,t_2)$ we write out the action of the time-ordering operator explicitly and differentiate Eq. (H.17) with respect to t_1:

$$\begin{aligned} i\,\frac{\partial}{\partial t_1}\mathcal{G}_{ij}(\mathbf{k};t_1,t_2) &= \frac{\partial}{\partial t_1}\left[\theta(t_1-t_2)\left\langle\Psi_{\mathbf{k}i}(t_1)\Psi^\dagger_{\mathbf{k}j}(t_2)\right\rangle - \theta(t_2-t_1)\left\langle\Psi^\dagger_{\mathbf{k}j}(t_2)\Psi_{\mathbf{k}i}(t_1)\right\rangle\right], \\ &= \delta(t_1-t_2)\left\langle\left\{\Psi_{\mathbf{k}i}(t_1),\Psi^\dagger_{\mathbf{k}j}(t_2)\right\}\right\rangle - i\left\langle T\left(i\,\frac{\partial\Psi_{\mathbf{k}i}(t_1)}{\partial t_1}\,\Psi^\dagger_{\mathbf{k}j}(t_2)\right)\right\rangle, \\ &= \delta(t_1-t_2) - i\left\langle T\left(i\,\frac{\partial\Psi_{\mathbf{k}i}(t_1)}{\partial t_1}\,\Psi^\dagger_{\mathbf{k}j}(t_2)\right)\right\rangle. \end{aligned} \tag{H.19}$$

Substituting Eq. (H.13) into this expression gives

$$\begin{aligned} i\frac{\partial}{\partial t_1}\mathcal{G}_{ij}(\mathbf{k};t_1,t_2) &= \delta(t_1-t_2) - i\left\langle T\left(\sum_{\mathbf{k}'l} M_{\mathbf{k}\mathbf{k}',il}\Psi_{\mathbf{k}'l}(t_1)\Psi^\dagger_{\mathbf{k}j}(t_2)\right)\right\rangle, \\ &= \delta(t_1-t_2) + \sum_{\mathbf{k}'l} M_{\mathbf{k}\mathbf{k}',il}(-i)\left\langle T\left(\Psi_{\mathbf{k}'l}(t_1)\Psi^\dagger_{\mathbf{k}j}(t_2)\right)\right\rangle. \end{aligned} \tag{H.20}$$

If we work in the mean field level, assuming a spatially homogeneous pairing gap, then $\mathbf{M}_{\mathbf{k}\mathbf{k}'} \equiv \mathbf{M}_{\mathbf{k}}\delta_{\mathbf{k}\mathbf{k}'}$ and Eq. (H.20) simplifies to

$$i\frac{\partial}{\partial t_1}\mathcal{G}_{0,ij}(\mathbf{k};t_1,t_2) = \delta(t_1-t_2) + \sum_l M_{\mathbf{k},il}\mathcal{G}_{0,lj}(\mathbf{k};t_1,t_2), \tag{H.21}$$

or, in matrix form:

$$i\frac{\partial}{\partial t_1}\boldsymbol{\mathcal{G}}_0(\mathbf{k};t_1,t_2) = \delta(t_1-t_2)\mathbf{I} + \mathbf{M}_{\mathbf{k}}\boldsymbol{\mathcal{G}}_0(\mathbf{k};t_1,t_2), \tag{H.22}$$

where $\mathbf{I}$ is the identity matrix in Nambu-Gor'kov space. Having obtained the equation of motion for $\boldsymbol{\mathcal{G}}_0(\mathbf{k};t_1,t_2)$, we are now in a position to evaluate the single-particle Green's functions.

H.3 Single-Particle Green's Functions

In order to solve Eq. (H.22) we define the frequency space matrix Green's function $\boldsymbol{\mathcal{G}}(\omega,\mathbf{k})$, where

$$\boldsymbol{\mathcal{G}}(\mathbf{k};t_1,t_2) = \int \frac{d\omega}{2\pi}\, e^{-i\omega(t_1-t_2)}\boldsymbol{\mathcal{G}}(\omega,\mathbf{k}). \tag{H.23}$$

Thus, Fourier transforming Eq. (H.22), we obtain

$$\boldsymbol{\mathcal{G}}_0(\omega,\mathbf{k}) = \left(\omega\mathbf{I} - \mathbf{M}_{\mathbf{k}}\right)^{-1}. \tag{H.24}$$

Before writing out this expression explicitly, we define the quantities $\tilde{\xi}_{\mathbf{k}\uparrow} = \xi_{\mathbf{k}\uparrow} - h_z$ and $\tilde{\xi}_{\mathbf{k}\downarrow} = \xi_{\mathbf{k}\downarrow} + h_z$ and note that for the Rashba-Dresselhaus coupling with which we are concerned, $h_\perp(-\mathbf{k}) = -h_\perp(\mathbf{k})$. Thus, combining Eqs. (H.14) and (H.24) we find

$$\boldsymbol{\mathcal{G}}_0^{-1}(\omega,\mathbf{k}) = \begin{pmatrix} \omega - \tilde{\xi}_{\mathbf{k}\uparrow} & h_\perp(\mathbf{k}) & 0 & -\Delta_0 \\ h_\perp^*(\mathbf{k}) & \omega - \tilde{\xi}_{\mathbf{k}\downarrow} & \Delta_0 & 0 \\ 0 & \Delta_0^* & \omega + \tilde{\xi}_{\mathbf{k}\uparrow} & h_\perp^*(\mathbf{k}) \\ -\Delta_0^* & 0 & h_\perp(\mathbf{k}) & \omega + \tilde{\xi}_{\mathbf{k}\downarrow} \end{pmatrix}. \tag{H.25}$$

This expression can be inverted by applying the Banachiewic identity, Eq. (D.12):[1]

$$\begin{pmatrix} \mathbf{A} & \mathbf{B} \\ \mathbf{C} & \mathbf{D} \end{pmatrix}^{-1} = \begin{pmatrix} \left(\mathbf{A} - \mathbf{B}\mathbf{D}^{-1}\mathbf{C}\right)^{-1} & \left(\mathbf{C} - \mathbf{D}\mathbf{B}^{-1}\mathbf{A}\right)^{-1} \\ \left(\mathbf{B} - \mathbf{A}\mathbf{C}^{-1}\mathbf{D}\right)^{-1} & \left(\mathbf{D} - \mathbf{C}\mathbf{A}^{-1}\mathbf{B}\right)^{-1} \end{pmatrix}, \tag{H.26}$$

where $\mathbf{A}$, $\mathbf{B}$, $\mathbf{C}$, and $\mathbf{D}$ are the 2×2 constituent blocks of $\boldsymbol{\mathcal{G}}_0^{-1}(\omega,\mathbf{k})$. Using the notation $k = (\omega,\mathbf{k})$ we can express these blocks as

$$\mathbf{A}(k) = -\mathbf{D}^\dagger(-k) = \begin{pmatrix} \omega - \tilde{\xi}_{\mathbf{k}\uparrow} & h_\perp(\mathbf{k}) \\ h_\perp^*(\mathbf{k}) & \omega - \tilde{\xi}_{\mathbf{k}\downarrow} \end{pmatrix}, \qquad \mathbf{B} = \mathbf{C}^\dagger = \begin{pmatrix} 0 & -\Delta_0 \\ \Delta_0 & 0 \end{pmatrix}. \tag{H.27}$$

[1] Note that the form of the Banachiewic identity used here is slightly different than that of Eq. (D.12). This is due to the fact that the latter form is valid as long as $\mathbf{D}$ is invertible, while the simpler form used here requires all of the constituent blocks be invertible. It is straightforward to verify, however, that our results will be independent of this requirement.

In order to write the elements of $\boldsymbol{\mathcal{G}}_0(\omega,\mathbf{k})$ explicitly we define the quantities $\tilde{\xi}_{\mathbf{k}\pm} = (\tilde{\xi}_{\mathbf{k}\uparrow} \pm \tilde{\xi}_{\mathbf{k}\downarrow})/2$, $Y_+ = \tilde{\xi}^2_{\mathbf{k}+} + |\Delta_0|^2$, and $Y_- = \tilde{\xi}^2_{\mathbf{k}-} + |h_\perp(\mathbf{k})|^2$. Inverting Eq. (H.25) then yields

$$
\begin{aligned}
\det[\boldsymbol{\mathcal{G}}_0^{-1}(\omega,\mathbf{k})]\boldsymbol{\mathcal{G}}_0(\omega,\mathbf{k})_{11} &= \omega\left[(\omega+\tilde{\xi}_{\mathbf{k}+})^2 - Y_- - |\Delta_0|^2\right] - \left[(\omega+\tilde{\xi}_{\mathbf{k}+})^2 - Y_- + |\Delta_0|^2\right]\tilde{\xi}_{\mathbf{k}\downarrow},\\
\det[\boldsymbol{\mathcal{G}}_0^{-1}(\omega,\mathbf{k})]\boldsymbol{\mathcal{G}}_0(\omega,\mathbf{k})_{12} &= -h_\perp(\mathbf{k})\left[(\omega+\tilde{\xi}_{\mathbf{k}+})^2 - Y_- - |\Delta_0|^2\right],\\
\det[\boldsymbol{\mathcal{G}}_0^{-1}(\omega,\mathbf{k})]\boldsymbol{\mathcal{G}}_0(\omega,\mathbf{k})_{13} &= 2\Delta_0 h_\perp(\mathbf{k})\tilde{\xi}_{\mathbf{k}\downarrow},\\
\det[\boldsymbol{\mathcal{G}}_0^{-1}(\omega,\mathbf{k})]\boldsymbol{\mathcal{G}}_0(\omega,\mathbf{k})_{14} &= \Delta_0\left[(\omega+\tilde{\xi}_{\mathbf{k}-})^2 - Y_+ - |h_\perp(\mathbf{k})|^2\right],\\
\det[\boldsymbol{\mathcal{G}}_0^{-1}(\omega,\mathbf{k})]\boldsymbol{\mathcal{G}}_0(\omega,\mathbf{k})_{21} &= -h^*_\perp(\mathbf{k})\left[(\omega+\tilde{\xi}_{\mathbf{k}+})^2 - Y_- - |\Delta_0|^2\right],\\
\det[\boldsymbol{\mathcal{G}}_0^{-1}(\omega,\mathbf{k})]\boldsymbol{\mathcal{G}}_0(\omega,\mathbf{k})_{22} &= \omega\left[(\omega+\tilde{\xi}_{\mathbf{k}+})^2 - Y_- - |\Delta_0|^2\right] - \left[(\omega+\tilde{\xi}_{\mathbf{k}+})^2 - Y_- + |\Delta_0|^2\right]\tilde{\xi}_{\mathbf{k}\uparrow},\\
\det[\boldsymbol{\mathcal{G}}_0^{-1}(\omega,\mathbf{k})]\boldsymbol{\mathcal{G}}_0(\omega,\mathbf{k})_{23} &= -\Delta_0\left[(\omega-\tilde{\xi}_{\mathbf{k}-})^2 - Y_+ - |h_\perp(\mathbf{k})|^2\right],\\
\det[\boldsymbol{\mathcal{G}}_0^{-1}(\omega,\mathbf{k})]\boldsymbol{\mathcal{G}}_0(\omega,\mathbf{k})_{24} &= -2\Delta_0 h^*_\perp(\mathbf{k})\tilde{\xi}_{\mathbf{k}\uparrow},\\
\det[\boldsymbol{\mathcal{G}}_0^{-1}(\omega,\mathbf{k})]\boldsymbol{\mathcal{G}}_0(\omega,\mathbf{k})_{31} &= 2\Delta^*_0 h^*_\perp(\mathbf{k})\tilde{\xi}_{\mathbf{k}\downarrow},\\
\det[\boldsymbol{\mathcal{G}}_0^{-1}(\omega,\mathbf{k})]\boldsymbol{\mathcal{G}}_0(\omega,\mathbf{k})_{32} &= -\Delta^*_0\left[(\omega-\tilde{\xi}_{\mathbf{k}-})^2 - Y_+ - |h_\perp(\mathbf{k})|^2\right],\\
\det[\boldsymbol{\mathcal{G}}_0^{-1}(\omega,\mathbf{k})]\boldsymbol{\mathcal{G}}_0(\omega,\mathbf{k})_{33} &= \omega\left[(\omega-\tilde{\xi}_{\mathbf{k}+})^2 - Y_- - |\Delta_0|^2\right] + \left[(\omega-\tilde{\xi}_{\mathbf{k}+})^2 - Y_- + |\Delta_0|^2\right]\tilde{\xi}_{\mathbf{k}\downarrow},\\
\det[\boldsymbol{\mathcal{G}}_0^{-1}(\omega,\mathbf{k})]\boldsymbol{\mathcal{G}}_0(\omega,\mathbf{k})_{34} &= -h^*_\perp(\mathbf{k})\left[(\omega-\tilde{\xi}_{\mathbf{k}+})^2 - Y_- - |\Delta_0|^2\right],\\
\det[\boldsymbol{\mathcal{G}}_0^{-1}(\omega,\mathbf{k})]\boldsymbol{\mathcal{G}}_0(\omega,\mathbf{k})_{41} &= \Delta^*_0\left[(\omega+\tilde{\xi}_{\mathbf{k}-})^2 - Y_+ - |h_\perp(\mathbf{k})|^2\right],\\
\det[\boldsymbol{\mathcal{G}}_0^{-1}(\omega,\mathbf{k})]\boldsymbol{\mathcal{G}}_0(\omega,\mathbf{k})_{42} &= -2\Delta^*_0 h_\perp(\mathbf{k})\tilde{\xi}_{\mathbf{k}\uparrow},\\
\det[\boldsymbol{\mathcal{G}}_0^{-1}(\omega,\mathbf{k})]\boldsymbol{\mathcal{G}}_0(\omega,\mathbf{k})_{43} &= -h_\perp(\mathbf{k})\left[(\omega-\tilde{\xi}_{\mathbf{k}+})^2 - Y_- - |\Delta_0|^2\right],\\
\det[\boldsymbol{\mathcal{G}}_0^{-1}(\omega,\mathbf{k})]\boldsymbol{\mathcal{G}}_0(\omega,\mathbf{k})_{44} &= \omega\left[(\omega-\tilde{\xi}_{\mathbf{k}+})^2 - Y_- - |\Delta_0|^2\right] + \left[(\omega-\tilde{\xi}_{\mathbf{k}+})^2 - Y_- + |\Delta_0|^2\right]\tilde{\xi}_{\mathbf{k}\uparrow}.
\end{aligned}
$$

References

[1] D. Rumsfeld, "Department of Defense News Briefing, February 12, 2002." "http://www.defense.gov/Transcripts/Transcript.aspx?TranscriptID=2636", 2002.

[2] P. D. Powell and G. Baym, "The axial anomaly and three-flavor NJL model with confinement: constructing the QCD phase diagram," *Phys. Rev. D* **85**, 074003 (2012).

[3] P. D. Powell and G. Baym, "Asymmetric pairing of realistic mass quarks and color neutrality in the Polyakov–Nambu–Jona-Lasinio model of QCD," *To appear in Phys. Rev. D* (2013).

[4] P. D. Powell, G. Baym, K. Masuda, and T. Hatsuda, "Effects of a vector coupling on the stability of massive hybrid quark stars," *To be published* (2013).

[5] P. D. Powell, "An analytical method for calculating the determinants of block matrices," `arXiv:math-gm:0381775`.

[6] C. Gattringer and C. B. Lang, *Quantum Chromodynamics on the Lattice: An Introductory Presentation*, vol. 788 of *Lecture Notes in Physics*. Springer, 2010.

[7] S. Muroya, A. Nakamura, C. Nonaka, and T. Takaishi, "Lattice QCD at Finite Density: An Introductory Review," *Prog. Theor. Phys.* **110**, 615–668 (2003).

[8] F. Karsch, "Lattice QCD at Finite Temperature," *AIP Conf. Proc.* **631**, 112–141 (2002).

[9] Y. Aoki, Z. Fodor, S. D. Katz, and K. K. Szabó, "The QCD transition temperature: Results with physical masses in the continuum limit," *Phys. Lett. B* **643**, 46–54 (2006).

[10] Y. Aoki, S. Borsányi, S. Dürr, Z. Fodor, S. D. Katz, S. Krieg, and K. Szabó, "The QCD transition temperature: results with physical masses in the continuum limit II," *J. High Energy Phys.* **88**, (2009).

[11] Y. Nambu and G. Jona-Lasinio, "Dynamical Model of Elementary Particles Based on an Analogy with Superconductivity I," *Phys. Rev.* **122**, 345–358 (1961).

[12] Y. Nambu and G. Jona-Lasinio, "Dynamical Model of Elementary Particles Based on an Analogy with Superconductivity II," *Phys. Rev.* **124**, 246–254 (1961).

[13] M. K. Volkov and A. E. Radzhabov, "The Nambu–Jona-Lasinio model and its development," *Sov. Phys. Usp.* **49**, 51–561 (2006).

[14] T. Hatsuda and T. Kunihiro, "QCD phenomenology based on a chiral effective Lagrangian," *Phys. Rep.* **247**, 221–367 (1994).

[15] S. P. Klevansky, "The Nambu–Jona-Lasinio model of quantum chromodynamics," *Rev. Mod. Phys.* **64**, 649–708 (1992).

[16] M. Buballa, "NJL-model analysis of dense quark matter," *Phys. Rep.* **407**, 205–376 (2005).

[17] K. Fukushima, "Chiral effective model with the Polyakov loop," *Phys. Lett. B* **591**, 277–284 (2004).

[18] T. Hatsuda, M. Tachibana, N. Yamamoto, and G. Baym, "New Critical Point Induced By the Axial Anomaly in Dense QCD," *Phys. Rev. Lett.* **97**, 122001 (2006).

[19] K. Fukushima, "Phase diagrams in the three-flavor NambuJona-Lasinio model with the Polyakov loop," *Phys. Rev. D* **77**, 114028 (2008).

[20] H. Abuki, G. Baym, T. Hatsuda, and N. Yamamoto, "Nambu–Jona-Lasinio model of dense three-flavor matter with axial anomaly: The low temperature critical point and BEC-BCS diquark crossover," *Phys. Rev. D* **81**, 125010 (2010).

[21] S. Rößner, C. Ratti, and W. Weise, "Polyakov loop, diquarks and the two-flavour phase diagram," *Phys. Rev. D* **75**, 034007 (2007).

[22] C. Sasaki, B. Friman, and K. Redlich, "Susceptibilities and the phase structure of a chiral model with Polyakov loops," *Phys. Rev. D* **75**, 074013 (2007).

[23] F. Halzen and A. D. Martin, *Quarks & Leptons: An Introductory Course in Modern Particle Physics*. John Wiley & Sons, 1984.

[24] J. Beringer and others (Particle Data Group), "The Review of Particle Physics," *Phys. Rev. D* **86**, 010001 (2012).

[25] G. 't Hooft, "Symmetry breaking through Bell-Jackiw anomalies," *Phys. Rev. Lett.* **37**, 8–11 (1976).

[26] C. M. Institute, "The Millennium Problems." "http://www.claymath.org/millennium/Yang-Mills_Theory/", 2013.

[27] A. Polyakov, "Thermal properties of gauge fields and quark liberation," *Phys. Lett. B* **72**, 477–480 (1978).

[28] B. Svetitsky, "Symmetry aspects of finite-temperature confinement transitions," *Phys. Rep.* **132**, 1–53 (1986).

[29] E. Megias, E. R. Arriola, and L. Salcedo, "Polyakov loop in chiral quark models at finite temperature," *Phys. Rev. D* **74**, 065005 (2006).

[30] K. Fukushima and T. Hatsuda, "The phase diagram of dense QCD," *Rep. Prog. Phys.* **74**, 014001 (2011).

[31] R. E. Rutledge, D. B. Fox, and A. H. Shevchuk, "Discovery of an Isolated Compact Object at High Galactic Latitude," *Astrophys. J.* **672**, 1137–1143 (2008).

[32] A. S. H. Shevchuk, D. B. Fox, and R. E. Rutledge, "Chandra Observations of 1RXS J141256.0+792204 (Calvera)," *Astrophys. J.* **705**, 391–397 (2009).

[33] P. Demorest, T. Pennucci, S. M. Ransom, R. M. S. E., and J. W. T. Hessels, "A two-solar-mass neutron star measured using Shapiro delay," *Nature (London)* **467**, 1081 (2010).

[34] C. J. Pethick, "Cooling of neutron stars," *Rev. Mod. Phys.* **64**, 1133–1140 (1992).

[35] J. Madsen, "Probing Strange Stars and Color Superconductivity by r-Mode Instabilities in Millisecond Pulsars," *Phys. Rev. Lett.* **85**, 10–13 (2000).

[36] F. Özel, G. Baym, and T. Güver, "Astrophysical measurement of the equation of state of neutron star matter," *Phys. Rev. D* **82**, 010301(R) (2010).

[37] J. Oppenheimer and G. Volkoff, "On Massive Neutron Star Cores," *Phys. Rev.* **55**, 374–381 (1939).

[38] R. C. Tolman, "Static Solutions of Einstein's Field Equations for Spheres of Fluid," *Phys. Rev.* **55**, 364–373 (1939).

[39] S. Chandrasekhar, "The Density of White Dwarf Stars," *Philos. Mag.* **11**, 592–596 (1931).

[40] Chandrasekhar, S., "The maximum mass of ideal white dwarfs," *Astrophys. J.* **74**, 81–82 (1931).

[41] R. W. Romani, A. V. Filippenko, J. M. Silverman, S. B. Cenko, J. Greiner, A. Rau, J. Elliott, and H. J. Pletsch, "PSR J13113430: A heaviweight neutron star with a flyweight helium companion," *Astrophys. J. Lett.* **760**, L36 (2012).

[42] J. Antoniadis, P. C. C. Freire, N. Wex, T. M. Tauris, R. S. Lynch, M. H. van Kerkwijk, M. Kramer, C. Bassa, V. S. Dhillon, T. Driebe, J. W. T. Hessels, V. M. Kaspi, V. I. Kondratiev, N. Langer, T. R. Marsh, M. A. McLaughlin, T. T. Pennucci, S. M. Ransom, I. H. Stairs, J. van Leeuwen, J. P. W. Verbiest, and D. G. Whelan, "A Massive Pulsar in a Compact Relativistic Binary," *Science* **340**, 1233232 (2013).

[43] B. Freedman and L. McLerran, "Quark star phenomenology," *Phys. Rev. D* **17**, 1109–1122 (1978).

[44] H. Heiselberg, C. Pethick, and E. Staubo, "Quark matter droplets in neutron stars," *Phys. Rev. Lett.* **70**, 1355–1359 (1993).

[45] "The Nobel Prize in Physics 1997."
"http://www.nobelprize.org/nobel"prizes/physics/laureates/1997/", 1997.

[46] K. Davis, M. Mewes, M. Andrews, N. van Druten, D. Durfee, D. Kurn, and K. W., "Bose-Einstein condensation in a gas of sodium atoms," *Phys. Rev. Lett.* **75**, 3969–3973 (1995).

[47] B. Demarco and D. Jin, "Onset of Fermi Degeneracy in a Trapped Atomic Gas," *Science* **285**, 1703–1706 (1999).

[48] S. Bose, "Plancks Gesetz und Lichtquantenhypothese," *Zeitschrift fr Physik* **26**, 178–181 (1924).

[49] A. Einstein, "Quantentheorie des einatomigen idealen Gases," *Sitzungsberichte der Preussischen Akademie der Wissenschaften* **1**, 3 (1925).

[50] H. Feshbach, "Unified Theory of Nuclear Reactions," *Ann. Phys.* **6**, 357–399 (1958).

[51] S. Inouye, M. Andrews, J. Stenger, H. Miesner, D. Stamper-Kurn, and W. Ketterle, "Observation of Feshbach resonances in a BoseEinstein condensate," *Nature (London)* **392**, 151–154 (1998).

[52] C. Regal, C. Ticknor, J. Bohn, and D. Jin, "Creation of ultracold molecules from a Fermi gas of atoms," *Nature (London)* **424**, 47–50 (2003).

[53] M. Greiner, C. A. Regal, and D. Jin, "Emergence of a molecular Bose-Einstein condensate from a Fermi gas," *Nature (London)* **426**, 537–540 (2003).

[54] Y. Lin, R. Compton, K. Jiménez-García, J. Porto, and I. Spielman, "Synthetic magnetic fields for ultracold neutral atoms," *Nature (London)* **462**, 638–632 (2009).

[55] Y. Lin, R. Compton, K. Jiménez-García, W. Phillips, J. Porto, and I. Spielman, "A synthetic electric force acting on neutral atoms," *Nature Physics (London)* **7**, 531–534 (2011).

[56] J. Dalibard, F. Gerbier, G. Juzeliūnas, and P. Öhberg, "Artificial gauge potentials for neutral atoms," *Rev. Mod. Phys.* **83**, 1523–1543 (2011).

[57] G. Dresselhaus, "Spin-orbit coupling effects in zinc blende structures," *Phys. Rev.* **100**, 580–586 (1955).

[58] E. Rashba, "Properties of semiconductors with an extremum loop I. cyclotron and combinational resonance in a magnetic field perpendicular to the plane of the loop," *Fizika Tverdogo Tela* **2**, 1224–1238 (1960).

[59] Y. Lin, K. Jiménez-García, and I. Spielman, "Spin-orbit-coupled Bose-Einstein condensates," *Nature (London)* **471**, 83–86 (2011).

[60] M. Iskin and C. Sá de Melo, "Ultracold fermions in real or fictitious magnetic fields: BCS-BEC evolution and type-I–type-II transition," *Phys. Rev. A* **83**, 045602 (2011).

[61] K. Seo, L. Han, and C. Sá de Melo, "Emergence of Majorana and Dirac Particles in Ultracold Fermions via Tunable Interactions, Spin-Orbit Effects, and Zeeman Fields," *Phys. Rev. Lett.* **109**, 105303 (2012).

[62] K. Seo, L. Han, and C. Sá de Melo, "Topological phase transitions in ultracold Fermi superfluids: The evolution from Bardeen-Cooper-Schrieffer to Bose-Einstein-condensate superfluids under artificial spin-orbit fields," *Phys. Rev. A* **85**, 033601 (2012).

[63] L. Han and C. Sá de Melo, "Evolution from BCS to BEC superfluidity in the presence of spin-orbit coupling," *Phys. Rev. A* **85**, 011606(R) (2012).

[64] H. Abuki and T. Kunihiro, "Extensive study of phase diagram for charge-neutral homogeneous quark matter affected by dynamical chiral condensation: unified picture for thermal unpairing transitions from weak to strong coupling," *Nucl. Phys. A* **768**, 118–159 (2006).

[65] T. Schäfer, "Phases of QCD," `arXiv:hep-ph:0509068`.

[66] M. Alford, "Color-superconducting quark matter," *Annu. Rev. Nucl. Part. Sci.* **51**, 131–160 (2001).

[67] M. Alford, K. Rajagopal, Schaefer, T. Schäfer, and A. Schmitt, "Color superconductivity in dense quark matter," *Rev. Mod. Phys.* **80**, 1455–1515 (2008).

[68] A. W. Steiner, S. Reddy, and M. Prakash, "Color-neutral superconducting quark matter," *Phys. Rev. D* **66**, 094007 (2002).

[69] D. B. Kaplan and S. Reddy, "Novel phases and transitions in color flavor locked matter," *Phys. Rev. D* **65**, 054042 (2002).

[70] M. Alford, J. A. Bowers, and K. Rajagopal, "Crystalline color superconductivity," *Phys. Rev. D* **63**, 074016 (2001).

[71] M. Alford, K. Rajagopal, S. Reddy, and F. Wilczek, "Minimal color-flavor-lockednuclear interface," *Phys. Rev. D* **64**, 074017 (2001).

[72] C. Ratti and W. Weise, "Thermodynamics of two-color QCD and the Nambu Jona-Lasinio model," *Phys. Rev. D* **70**, 054013 (2004).

[73] C. Ratti, M. A. Thaler, and W. Weise, "Phases of QCD: Lattice thermodynamics and a field theoretical model," *Phys. Rev. D* **73**, 014019 (2006).

[74] A. Dumitru, R. D. Pisarski, and D. Zschiesche, "Dense quarks, and the fermion sign problem, in a SU(N) matrix model," *Phys. Rev. D* **72**, 065008 (2005).

[75] S. K. Ghosh, T. K. Mukherjee, M. G. Mustafa, and R. Ray, "Susceptibilities and speed of sound from the Polyakov-Nambu-Jona-Lasinio model," *Phys. Rev. D* **73**, 114007 (2006).

[76] Z. Zhang and Y.-X. Liu, "Coupling of pion condensate, chiral condensate and Polyakov loop in an extended NJL model," *Phys. Rev. C* **75**, 064910 (2007).

[77] S. Rößner, T. Hell, C. Ratti, and W. Weise, "The chiral and deconfinement crossover transitions: PNJL model beyond mean field," *Nucl. Phys. A* **814**, 118–143 (2008).

[78] H. Abuki, M. Ciminale, R. Gatto, G. Nardulli, and M. Ruggieri, "Enforced neutrality and color-flavor unlocking in the three-flavor Polyakov-loop NambuJona-Lasinio model," *Phys. Rev. D* **77**, 074018 (2008).

[79] H. Abuki and K. Fukushima, "Gauge dynamics in the PNJL model: Color neutrality and Casimir scaling," *Phys. Lett. B* **676**, 57–62 (2009).

[80] T. Brauner, K. Fukushima, and Y. Hidaka, "Two-color quark matter: $U(1)_A$ restoration, superfluidity, and quarkyonic phase," *Phys. Rev. D* **80**, 074035 (2009).

[81] S. Imai, H. Toki, and W. Weise, "Quark-Hadron Matter at Finite Temperature and Density in a Two-Color PNJL model," `arXiv:nucl-th:1210.1307`.

[82] F. Karsch, E. Laermann, and A. Peikert, "Quark mass and flavour dependence of the QCD phase transition," *Nucl. Phys. B* **605**, 579–599 (2001).

[83] L. McLerran and R. D. Pisarski, "Phases of dense quarks at large N_c," *Nucl. Phys. B* **796**, 83–100 (2007).

[84] Y. Hidaka, L. McLerran, and R. D. Pisarski, "Baryons and the phase diagram for a large number of colors and flavors," *Nucl. Phys. A* **808**, 117–123 (2008).

[85] N. Yamamoto, M. Tachibana, T. Hatsuda, and G. Baym, "Phase structure, collective modes, and the axial anomaly in dense QCD," *Phys. Rev. D* **76**, 074001 (2007).

[86] R. D. Pisarski and F. Wilczek, "Remarks on the chiral phase transition in chromodynamics," *Phys. Rev. D* **29**, 338–341 (1984).

[87] M. Kobayashi and T. Maskawa, "Chiral Symmetry and η-χ Mixing," *Prog. Theor. Phys.* **44**, 1422–1424 (1970).

[88] D. B. Blaschke, F. Sandin, V. Skokov, and S. Typel, "Accessibility of color superconducting quark matter phses in heavy-ion collisions," *Acta Phys. Pol. B Proc. Suppl.* **3**, 741–745 (2010).

[89] D. G. Dumm, D. B. Blaschke, A. Grunfeld, and N. Scoccola, "Color neutrality effects in the phase diagram of the Polyakov–Nambu–Jona-Lasinio model," *Phys. Rev. D* **78**, 114021 (2008).

[90] S. Carignano, D. Nickel, and M. Buballa, "Influence of vector interaction and Polyakov loop dynamics on inhomogeneous chiral symmetry breaking phases," *Phys. Rev. D* **82**, 054009 (2010).

[91] T. Kojoa, Y. Hidakab, K. Fukushima, L. D. McLerrana, and R. D. Pisarski, "Interweaving chiral spirals," *Nucl. Phys. A* **875**, 94–138 (2012).

[92] H. Basler and M. Buballa, "Role of two-flavor color superconductor pairing in a three-flavor NambuJona-Lasinio model with axial anomaly," *Phys. Rev. D* **82**, 094004 (2010).

[93] E. Gubankova, W. V. Liu, and F. Wilczek, "Breached Pairing Superfluidity: Possible Realization in QCD," *Phys. Rev. Lett.* **91**, 032001 (2003).

[94] W. V. Liu, F. Wilczek, and P. Zoller, "Spin-dependent Hubbard model and a quantum phase transition in cold atoms," *Phys. Rev. A* **70**, 033603 (2004).

[95] M. M. Forbes, E. Gubankova, W. V. Liu, and F. Wilczek, "Stability Criteria for Breached-Pair Superfluidity," *Phys. Rev. Lett.* **94**, 017001 (2005).

[96] A. Gerhold and A. Rebhan, "Gauge dependence identities for color superconducting QCD," *Phys. Rev. D* **68**, 011502 (2003).

[97] D. Dietrich and D. Rischke, "Gluons, tadpoles, and color neutrality in a two-flavor color superconductor," *Prog. Part. Nucl. Phys.* **53**, 305–316 (2004).

[98] K. Iida and G. Baym, "Superfluid phases of quark matter: Ginzburg-Landau theory and color neutrality," *Phys. Rev. D* **63**, 074018 (2001).

[99] M. Buballa and I. A. Shovkovy, "Note on color neutrality in Nambu-Jona-Lasinio-type models," *Phys. Rev. D* **72**, 097501 (2005).

[100] P. F. Bedaque, H. Caldas, and G. Rupak, "Phase Separation in Asymmetrical Fermion Superfluids," *Phys. Rev. Lett.* **91**, 247002 (2003).

[101] H. Caldas, "Cold asymmetrical fermion superfluids," *Phys. Rev. A* **69**, 063602 (2004).

[102] M. Gyulassy and L. McLerran, "New forms of QCD matter discovered at RHIC," *Nucl. Phys. A* **750**, 30–63 (2004).

[103] T. Hirano and M. Gyulassy, "Perfect fluidity of the quark gluon plasma core as seen through its dissipative hadronic corona," *Nucl. Phys. A* **769**, 71–94 (2005).

[104] R. A. Lacey, A. Taranenko, N. Ajitanand, and J. Alexander, "Initial indications for the production of a strongly coupled plasma in Pb+Pb collisions at $\sqrt{s_{NN}} = 2.76$ TeV," *Phys. Rev. C* **83**, 031901 (2010).

[105] W. Horowitz and M. Gyulassy, "The Surprising Transparency of the sQGP at LHC," *Nucl. Phys. A* **872**, 265–285 (2011).

[106] J. A. C. Shukraft, "First Results from the ALICE experiment at the LHC," *Nucl. Phys. A* **862–863**, 78–84 (2011).

[107] U. Heinz, C. Shen, and H.-C. Song, "The viscosity of quark-gluon plasma at RHIC and the LHC," *AIP Conf. Proc.* **1441**, 766–770 (2011).

[108] P. C. Joss and S. A. Rappaport, "Neutron Stars in Interacting Binary Systems," *Ann. Rev. Astron. Astrophys.* **22**, 537–592 (1984).

[109] V. Pandarhpande, "Hyperonic matter," *Nucl. Phys. A* **178**, 123–144 (1971).

[110] G. Baym, C. Pethick, and P. Sutherland, "The ground state of matter at high densities: equation of state and stellar models," *Astrophys. J.* **170**, 299 (1971).

[111] A. Akmal, V. Pandharipande, and D. Ravenhall, "Equation of state of nucleon matter and neutron star structure," *Phys. Rev. C* **58**, 1804–1828 (1998).

[112] M. Baldo, G. Burgio, and H. Schulze, "Hyperon stars in the Brueckner-Bethe-Goldstone theory," *Phys. Rev. C* **61**, 055801 (2000).

[113] S. Nishizaki, Y. Yamamoto, and T. Takatsuka, "Effective YN and YY Interactions and Hyperon-Mixing in Neutron Star Matter," *Prog. Theor. Phys.* **105**, 607–626 (2001).

[114] S. Nishizaki, Y. Yamamoto, and T. Takatsuka, "Hyperon-Mixed Neutron Star Matter and Neutron Stars," *Prog. Theor. Phys.* **108**, 703–718 (2002).

[115] H. Schulze and T. Rijken, "Maximum mass of hyperon stars with the Nijmegen ESC08 model," *Phys. Rev. C* **84**, 035801 (2011).

[116] A. W. Steiner, J. M. Lattimer, and E. F. Brown, "The Neutron Star Mass-Radius Relation and the Equation of State of Dense Matter," *Astrophys. J. Lett.* **765**, L5 (2013).

[117] J. Collins and M. Perry, "Superdense Matter: Neutrons or Asymptotically Free Quarks," *Phys. Rev. Lett.* **34**, 1353–1356 (1975).

[118] A. Peisher, Kämpfer, and G. Soff, "Equation of state of deconfined matter at finite chemical potential in a quasiparticle description," *Phys. Rev. C* **61**, 045203 (2000).

[119] M. Alford and S. Reddy, "Compact stars with color superconducting quark matter," *Phys. Rev. D* **67**, 074024 (2003).

[120] K. Masuda, T. Hatsuda, and T. Takatsuka, "Hadron-quark crossover and massive hybrid stars with strangeness," *Astrophys. J.* **764**, 12 (2013).

[121] K. Masuda, T. Hatsuda, and T. Takatsuka, "Hadron-Quark Crossover and Massive Hybrid Stars," `arXiv:nucl-th:1212.6803v2`.

[122] E. Farhi and R. L. Jae, "Strange matter," *Phys. Rev. D* **30**, 2379–2390 (1984).

[123] A. Bodmer, "Collapsed Nuclei," *Phys. Rev. D* **4**, 1601–1606 (1971).

[124] E. Witten, "Cosmic separation of phases," *Phys. Rev. D* **30**, 272–285 (1984).

[125] J. G. Coelho, C. H. Lenzi, M. Malheiro, R. M. Marinho Jr., C. Providncia, and M. Fiolhais, "Quark stars in SU(2) Nambu-Jona-Lasinio model with vector coupling," *Nucl. Phys. B Proc. Suppl.* **199**, 325–328 (2010).

[126] N. Bratovic, T. Hatsuda, and W. Weise, "Role of Vector Interaction and Axial Anomaly in the PNJL Modeling of the QCD Phase Diagram," *Phys. Lett. B* **719**, 131–135 (2012).

[127] G. Gamow and M. Schoenberg, "Neutrino Theory of Stellar Collapse," *Phys. Rev.* **59**, 539–547 (1941).

[128] H. Bethe, "Supernova mechanisms," *Rev. Mod. Phys.* **62**, 801–866 (1990).

[129] S. Woosley, A. Heger, and T. Weaver, "The evolution and explosion of massive stars," *Rev. Mod. Phys.* **74**, 1015–1071 (2002).

[130] K. Langanke and Martínez-Pinedo, "Nuclear weak-interaction processes in stars," *Rev. Mod. Phys.* **75**, 819–862 (2003).

[131] I. Bloch, J. Dalibard, and W. Zwerder, "Many-body physics with ultracold gases," *Rev. Mod. Phys.* **80**, 885–964 (2008).

[132] S. Giorgini, L. P. Pitaevskii, and S. Stringari, "Theory of ultracold atomic Fermi gases," *Rev. Mod. Phys.* **80**, 1215–1274 (2008).

[133] Y. Lin, R. Compton, A. Perry, W. Phillips, J. Porto, and I. Spielman, "Bose-Einstin condensate in a uniform light-induced vector potential," *Phys. Rev. Lett.* **102**, 130401 (2009).

[134] M. A. Aidelsburger, S. Nascimbène, S. Trotzky, Y. Chen, and I. Bloch, "Experimental realization of strong effective magnetic fields in an optical lattice," *Phys. Rev. Lett.* **107**, 255301 (2011).

[135] R. Williams, L. LeBlanc, Jiménez-García, M. Beeler, A. Perry, W. Phillips, and I. Spielman, "Synthetic partial waves in ultracold atomic colisions," *Science* **335**, 314–317 (2012).

[136] J. Ruseckas, G. Juzeliunas, P. Öhberg, and M. Fleischhaur, "Non-Abelian gauge potentials for ultracold atoms with degenerate dark states," *Phys. Rev. Lett.* **95**, 010404 (2005).

[137] X. Liu, M. Borunda, X. Liu, and J. Sinova, "Effect of induced spin-orbit coupling for atoms via laser fields," *Phys. Rev. Lett.* **102**, 046402 (2009).

[138] G. Juzeliunas, J. Reseckas, and J. Dalibard, "Generalized Rashba-Dresselhaus spin-orbit coupling for cold atoms," *Phys. Rev. A* **81**, 053403 (2010).

[139] D. Campbell, G. Juzeliunas, and I. Spielman, "Realistic Rashba and Dresselhaus spin-orbit coupling for neutral atoms," *Phys. Rev. A* **84**, 025602 (2011).

[140] T. Ozawa, *Topics in Multi-Component Ultracold Gases and Gauge Fields.* PhD thesis, University of Illinois at Urbana-Champaign, 2012.

[141] M. Berry, "Quantal phase factors accompanying adiabatic changes," *Proc. R. Soc. London A* **392**, 45–57 (1984).

[142] D. Rohrlich, "Berry's Phase,", in *Compendium of Quantum Physics*, D. Greenberger, K. Hentschel, and F. Weinert, eds. Berlin & Heidelberg: Springer, 2009.

[143] G. Baym, *Lectures on Quantum Mechanics.* Lecture Notes and Supplements in Physics. Westview Press, 1969.

[144] S. Zhu, H. Fu, C. Wu, S. Zhang, and L. Duan, "Spin Hall effects for cold atoms in a light-induced gauge potential," *Phys. Rev. Lett.* **97**, 240401 (2006).

[145] M. Iskin and C. Sá de Melo, "Two-Species Fermion Mixtures with Population Imbalance," *Phys. Rev. Lett.* **97**, 100404 (2006).

[146] J. Kinnunen, L. M. Jensen, and P. Törmä, "Strongly Interacting Fermi Gases with Density Imbalance," *Phys. Rev. Lett.* **96**, 110403 (2006).

[147] M. W. Zwierlein, C. H. Schunck, A. Schirotzek, and W. Ketterle, "Direct observation of the superfluid phase transition in ultracold Fermi gases," *Nature (London)* **442**, 54–58 (2006).

[148] K. Gubbels and H. Stoof, "Imbalanced Fermi Gases at Unitarity," `arXiv:cond-mat:1205.0568`.

[149] M. Tinkham, *Introduction to Superconductivity*. Dover Publications, second ed., 2004.

[150] C. J. Pethick and H. Smith, *Bose-Einstein Condensation in Dilute Gases*. New York: Cambridge University Press, second ed., 2008.

[151] P. Nozières and S. Schmitt-Rink, "Bose Condensation in an Attractive Fermion Gas: From Weak to Strong Coupling Superconductivity," *J. Low Temp. Phys.* **59**, 195–211 (1985).

[152] A. J. Leggett, "Diatomic molecules and Cooper pairs," in *Modern Trends in the Theory of Condensed Matter*, A. Pękalski and J. A. Przystawa, eds., vol. 115 of *Lecture Notes in Physics*. Berlin & Heidelberg: Springer, 1980.

[153] C. Sá de Melo, M. Randeria, and Engelbrecht, "Crossover from BCS to Bose Superconductivity: Transition Temperature and Time-Dependent Ginzburg-Landau Theory," *Phys. Rev. Lett.* **71**, 3202–3205 (1993).

[154] G. Baym, J.-P. Blaizot, M. Holzmann, F. Laloë, and D. Vautherin, "The Transition Temperature of the Dilute Interacting Bose Gas," *Phys. Rev. Lett.* **83**, 1703–1706 (1999).

[155] T. Gjestland, "Gauge theories at finite temperature," Master's thesis, Norwegian Institute of Science and Technology, 2007.

[156] C. A. Felippa, "Introduction to Finite Element Methods (Appendix P)." Unpublished lecture notes, 2004.

[157] T. Banachiewicz, "Zur Berechnung der Determinanten, wie auch der Inversen, und zur darauf basierten Auösung der Systeme linearer Gleichungen," *Acta Astron.* **3**, 41–67 (1937).

[158] R. A. Frazer, W. J. Duncan, and A. R. Collar, eds., *Elementary Matrices and Some Applications to Dynamics and Differential Equations*. Cambridge: Cambridge University Press, 1938.

[159] "GNU Scientific Library, release gsl-1.15." "http://www.gnu.org/software/gsl/", May, 2011.